Effect of the Environment on Fluxonium Qubits and Thermodynamics of Quantum Measurement

Jeremy Stevens

Numéro National de Thèse : 2021LYSEN043

THESE DE DOCTORAT DE L'UNIVERSITE DE LYON
opérée par
l'Ecole Normale Supérieure de Lyon

Ecole Doctorale N°52
Physique et Astrophysique de Lyon (PHAST)

Discipline : Physique

Soutenue publiquement le 27/09/2021, par :
Jeremy STEVENS

Effect of the Environment on Fluxonium Qubits and Thermodynamics of Quantum Measurement

Effet de l'Environnement sur les Qubits Fluxonium et Thermodynamique des Mesures Quantiques

---

Devant le jury composé de :

BLAIS, Alexandre	Professeur, Université de Sherbrooke	Rapporteur
POP, Ioan	Professeur, Karlsruhe Institut für Technologie	Rapporteur
DEGIOVANNI, Pascal	Directeur de Recherche, ENS de Lyon	Examinateur
DOTSENKO, Igor	Maître de Conférences, Collège de France	Examinateur
HAACK, Géraldine	Professeure, Université de Genève	Examinatrice
BIENFAIT, Audrey	Chargée de Recherche, ENS de Lyon	Co-encadrante
HUARD, Benjamin	Professeur des Universités, ENS de Lyon	Directeur de thèse

EFFECT OF THE ENVIRONMENT ON FLUXONIUM QUBITS AND THERMODYNAMICS OF QUANTUM MEASUREMENT

JEREMY STEVENS

Directed by Benjamin Huard

École Normale Supérieure de Lyon

August 2021

ABSTRACT

Superconducting qubits are at the heart of many experiments exploring elementary quantum mechanics and are one of the principal candidates for use in a future quantum computer. In both cases, a high level of control over both the quantum system and its environment is necessary. The first chapters of this thesis describe several techniques used to engineer the effect of the environment in circuit QED with a focus on the promising Fluxonium qubit. We give a detailed treatment of the theoretical basis for protected qubits and analyse device design and dilution refrigerator wiring from the perspective of environment noise reduction.

As an application of these methods, we reproduce state of the art conditions for Fluxonium experiments in order to study the effect of the environment on the qubit. We show how photons in the cavity used to measure the quantum bit and a high temperature of the dilution refrigerator in which the device is placed can have detrimental effects on the stability of the quantum state. Critically, this shows that there remain several problems still to solve regarding the dispersive readout of Fluxoniums before using them as the basis for a quantum computer.

Theoretically, the decoherence of a qubit can be broken down into many coherent exchanges with the qubit environment about which the observer has no information. In the last part of the thesis, we show the results of an experiment providing insight into the thermodynamics of quantum measurement and operations by observing the coherent energy exchange between a propagating field and a qubit under measurement. We provide an interpretation of the preparation of a qubit state by a coherent light pulse as a weak measurement of the pulse by the qubit.

RÉSUMÉ

Les qubits supraconducteurs sont au cœur de nombreuses expériences de mécanique quantique élémentaire et sont l'un des prétendants principaux pour le futur ordinateur quantique. Dans les deux cas, un haut niveau de contrôle, à la fois sur le qubit et son environnement, est essentiel. Les premiers chapitres de cette thèse décrivent plusieurs méthodes qui peuvent servir à concevoir l'effet de l'environnement sur les circuits supraconducteurs, et en particulier sur le très prometteur qubit Fluxonium. Nous détaillons la théorie des qubits protégés et traitons la conception des appareils quantiques, ainsi que le câblage des réfrigérateurs à dilution avec l'objectif de réduire le bruit de l'environnement.

En utilisant ces méthodes, nous créons des conditions permettant des expériences pour étudier l'effet de l'environnement sur le qubit Fluxonium. Nous montrons que les photons présents dans la cavité utilisée pour mesurer le qubit, ainsi qu'un réfrigérateur à dilution avec une température trop élevée, peuvent avoir des effets néfastes sur la stabilité de l'état quantique. Cette expérience met également en lumière les problèmes qui restent à résoudre concernant la lecture dispersive des Fluxoniums avant de les utiliser comme élément de base dans un ordinateur quantique.

La décohérence quantique d'un qubit peut être décrite par les nombreuses interactions cohérentes avec l'environnement au sujet desquelles l'observatrice n'a aucune information. Dans la dernière partie de la thèse, nous présentons des résultats permettant de mieux comprendre la thermodynamique des mesures et des opérations quantiques, en observant l'échange cohérent d'énergie entre un champ propageant et un qubit que l'on mesure. Nous interprétons la préparation de l'état du qubit par un pulse cohérent comme une mesure faible du pulse par le qubit.

A PERSONAL NOTE

PhD stands for Doctor of Philosophy (from the latin *Philosophiae Doctor*). While the meaning of doctor can be summed up as someone who is highly competent in a given subject, according to the Oxford English Dictionary the meaning of philosophy is rather more poetic. Aside from its modern interpretation as the academic "study of the fundamental nature of knowledge", a rarer and more historical interpretation is the "love or pursuit of wisdom". The research presented in this thesis is admittedly extremely specific and concerns a fairly narrow field, yet this meaning of PhD resonates strongly when I look back on the last four years. Firstly, I think I can claim to be an expert of superconducting circuits. This has material consequences, namely some very exciting career prospects, mostly due to a 'right place, right time' type of circumstance over which I have little control. Yet, by becoming an expert, I feel I have foremostly acquired some of the traits suggested by the definition of the academic title I will (hopefully!) be discerned. I feel more humble, being able to better distinguish where my knowledge ends and where my ignorance begins. This means I am also better prepared to face something unfamiliar in the future: awareness of what you don't know helps you ask more pertinent questions. I further believe that I have broadened my interests and horizons during my time as a PhD student, in a way only possible through long periods of reflection, enormous creative freedom and stimulating discussions. I owe this increased intellectual curiosity - "love or pursuit of wisdom" - to the people who I have met, both within and outside the physics community, whose intelligence and perspectives have helped my personality mature. These interactions have often been jovial and pleasant, making my time at ENS Lyon not only serious but also joyful. These conditions have set the stage of various personal achievements, namely becoming a fully qualified ski instructor and entertaining a long distance relationship between Paris and Lyon. I hope to convey some of the gratitude I feel for these things in the next few words as well as doing some storytelling to give a feeling of the mood of these last years.

Frankly, I had many reasons for joining the Quantum Circuit Group in 2017, many of which were not for the "love of wisdom". I wanted french citizenship, flexible hours to be able to concentrate on other projects, I wanted to be surrounded by smart people and if this could all be done whilst studying for a physics PhD, then why not? In case I didn't enjoy it in Lyon, I asked for a one year contract as an 'ingénieur d'études' with an agreement from my future advisor, Benjamin, that if I wanted, I would be able to stay on for three years extra to complete my PhD. After three months, still only knowing a small amount about the research in the lab, I told him I would continue. The people I had met were simply too bright, friendly and relaxed to let go of.

I must first extend many thanks to Benjamin, whose role has been perhaps larger than anyone's in writing this thesis. Within two weeks of my arrival in the group, I was in your office asking to take seven weeks leave over winter to prepare for my ski

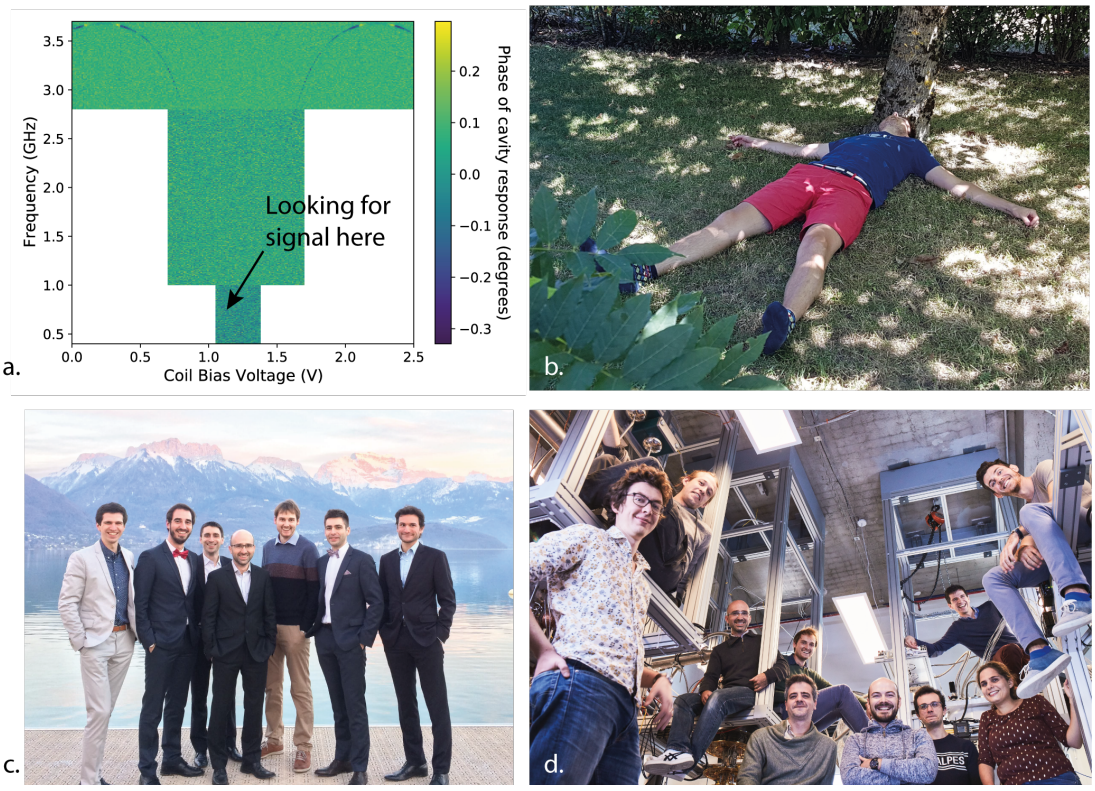

Figure 0.1: A visual summary of my PhD. a. A typical two-tone spectroscopy during the first runs of the Fluxonium experiment. Although at low frequencies it looks like a screenshot from a badly connected analog TV screen, this is in fact measurement data in which we expected to see some dark blue line corresponding to the qubit frequency. b. I seek comfort and inpiration in the shade of a tree in my father's garden when struggling with some python code. c. A group photograph from Quentin's wedding in January 2019. From left to right: Antoine, Nath, Théau, Benjamin, me, Quentin and Raphaël Lescanne from the group in Paris. d. A group photo shot in October 2020. From left to right: Rémy, Arne, Benjamin, Daniel, me, Alexis, Réouven, Antoine, Audrey and Antoine M.

instructor exams. Having only worked with me for a few weeks up until then, your lack of hesitation when giving me the go ahead was remarkable. I'm grateful that you gave me the freedom I needed to go about my other passions and the confidence you showed in me to get things done. You always provided the resources needed to succeed, both materially and socially, by making sure the atmosphere in the group was friendly and productive. I appreciate that you treated me as an equal and challenged my ideas without jugement, while letting me convince you when you thought my reasoning was sound. Your curiosity, your obsessive quest for excellence and your humility are quite inspiring.

When I started, we were only four: Nath, Quentin, Théau and I soon to be joined by Antoine six months later. I remember a fair amount of laughter, music in the evening once 'the boss' had left, and some pretty heated debates. Our relationship with Nath was pretty explosive, sometimes over little things. I'm going to put this down to our passion for measuring Fluxoniums, rather than what others may have called bad temperament. When the debates got out of hand, the other members' moods varied from

annoyed to indifferent, with Théau sometimes moving in as a mediator (or is it manager?) to try and diffuse things, and Antoine and Quentin living their own blasé agrégé life calling all the instruments (and occasionally each other) 'Michel'. My frustrating scientific results of that year (despite my best intentions) were turned into a running joke about Fluxonium experiments, the different features of white noise and random number generators (see Fig. 0.1a.). To this day I can correctly make out resonances where no one else believes there to be anything, and Antoine is still allowed his one Fluxonium joke a day. Thanks Nath, Quentin and Théau for taking me into your great group (Fig. 0.1c.) and teaching me how to measure!

With Antoine and I remaining once the others had left (although Théau hung around to write his thesis), the group changed dimension with the arrival of Rémy, Réouven, Daniel, Audrey, Arne, Alexis and Antoine M. It was now Antoine and I who were in charge of keeping group traditions alive. I think we did a good job, making sure to organise outings to Ninkasi and that people brought in cakes for birthdays and publications. Well except Réouven. You still haven't brought in a cake, but your scientific contributions and willingness to help more than compensate.
I was lucky enough to be teamed up with two post-docs, Daniel and Alexis on the thermodynamics and fluxonium experiments respectively. Alexis, you really helped me with the Fluxonium data analysis when I was submerged by my own python code (Fig. 0.1b.). Thanks for playing the 'yellow duck' and forcing me to organise my ideas by writing my problems and their solutions down. I really enjoyed teaching you about Fluxonium qubits when you arrived. I also learnt a lot from our healthy, albeit long, discussions about quantum physics and superconductivity and I'm excited to see someone taking over the Fluxonium experiments. Daniel, I enjoyed our debates about the meaning of the post-selection measurements as we worked out where the energy was going during qubit gates. It was also refreshing to chat about what was going on around the world around the inevitable 4 o'clock bag of m&ms.
With the group having grown so much I didn't have the opportunity to work closely with everyone though. Thanks to you, Audrey, for teaching me how to use Solidworks and your insights about the experiments. I'm really impressed by how fast you set up the nanoESR project with Arne and your knowledge of the literature in the community. Arne, your skills in the workshop blow my laithe coil winding out of the water and your enthusiasm for caving is always really motivating. Rémy, thanks for often helping us debug our setups and for laughing at my often poor jokes. Antoine M., you inherit the HDAWG, good luck! Thanks to all the interns and students who passed through, with a special mention for Meghan and Stefan who I worked with the closest.
Of course, I cannot forget the eternal 'stagiaire' Antoine (actually 'professeur agrégé stagiaire'), who has been my partner in crime during our PhDs in parallel. It has been a relief to have someone to share some struggles with or, as exemplified by 5 minute parties in Benasque or Génépi tasting in Les Houches, someone to enjoy the perks of academia with. Thanks to you all for making the group such a great place to work in (Fig. 0.1d.).

Of course the microcosm of a research group is dependent on the institutions which support it. I thank the members of the Laboratoire de Physique for being so welcoming and approachable, making it an ideal place to conduct high level research. A special mention goes to Fatiha Bouchneb. You had my paperwork ready from day one, making sure everything went smoothly and your efficiency and administrative intelligence is legendary. Thank you for helping us all concentrate on our research, I don't think we could bake enough cakes to repay you. Thanks to the cleanroom staff at ENS and around Lyon, Vincent, Jérôme, Radek, Joëlle... without you, a number of projects wouldn't have started.

Thanks to my parents, sister and family for their never ending support. You are are always there when I need guidance or have doubts. Thanks to my friends, who provide a refreshingly different perspective on life, with whom I share my ideas and interests and whose company helps me unwind and find new motivation. Thanks to the Chaygneaud-Dupuy family for accepting an english speaking physicist/engineer who likes snow, despite their better jugement. Lastly, thanks to Raphaëlle who weathered the emotional ups and downs which come with research and a PhD, as well as the burden of constant trips from Paris to Lyon and back. Your relentless enthusiasm, emotional intelligence and constant suggestions for activities (visits to expositions, taking a trip for the weekend, walking to a library, building furniture...) have a lot to do with my relative sanity over the last few years. Discovering you and your interests has also been part of my PhD.

Thank you to the members of the jury who accepted to read and review my thesis.

Lyon, September 2021 *Jeremy Stevens*

CONTENTS

LIST OF FIGURES

LIST OF TABLES

1 INTRODUCTION

1.1 THE BIG PICTURE

Quantum mechanics has been an immensely successful theory. What spawned from the mysteries of the ultraviolet catastrophe and the photoelectric effect, led to a formalism enabling awesome improvements in human technology. Of the inventions of the first quantum revolution, the transistor is perhaps the most important. In recognition of this, the 1956 Nobel prize was awarded to Bardeen[1], Brattain and Schockley "for the discovery of the transistor effect" [2]. Transistors are the non-linear element at the core of every electronics device. Gates, the elementary operations which modify the billions of electronic states in computers, are implemented using transistors, and we understand how transistors work because we know how electrons collectively behave in semiconductors thanks to quantum theory. From a physics point of view, we can see the democratisation of information technology over the course of the second half of the 20^{th} century as a giant experimental verification of the collective behaviour of particles underwritten by the laws of quantum mechanics. Ironically though, in its simplest form, quantum mechanics makes statements about isolated degrees of freedom, about single electrons and photons for example and about what happens when they are observed ('de-isolated' in a sense). Checking these predictions was for a long time far from trivial. As Erwin Schrödinger put it in 1952: "it is fair to state that we are not experimenting with single particles, any more than we can raise Ichthyosauria in the zoo" [3]. The issue is that isolating a degree of freedom is exceptionally difficult, as is demonstrated by the fact that in our day to day, we are unaware of quantum mechanics. The difficulty is such that even experiments designed so that a single degree of freedom is easy to isolate only really became feasible in the 1980s, becoming mainstream a decade later. Two of the protagonists of this experimental progress, David Wineland and Serge Haroche, were awarded the 2012 Nobel prize "for ground-breaking experimental methods that enable measuring and manipulation of individual quantum systems" [4]. The reason why these results had not been achieved before, is because key technologies had not yet been invented. The experiments of Haroche and Wineland were made possible by the technological progress due to the very theory their experiments were seeking to verify. The fact that Wineland and his team needed lasers to cool atoms using radiation pressure for the first time illustrates this perfectly [5].

This brief historical approach offers some perspective to the works realised in this thesis. Computers and lasers are significantly more complex than the electrons and photons that constitute them, and building computers and isolating single ions do not

1 If proof was needed that this physicist had certainly understood some of the subtleties of quantum machanics, Bardeen was later awarded a second physics Nobel prize, the only person to recieve it twice, this time for the microscopic theory of superconductivity, together with Cooper and Schrieffer [1].

require the same techniques, formalisms or even administrative structures. In this respect, the advancement of our understanding of quantum mechanics came about thanks to a productive exchange between research and technology and the mastery of effects at different scales. Inspired by this, this thesis positions itself at a series of interfaces. The interface between the physics of single excitations and that of collective properties. The interface between research and technology. The interface between theory, experiments and applications. The interface between isolated and open systems. Having the ability to focus on one point of view and then being able to switch perspective at the opportune time, will be essential to many of the results presented here.

1.2 SUPERCONDUCTING MICROWAVE CIRCUITS

Ions and Rydberg atoms are naturally quantum. The orbitals of electrons around the nucleus are very well described by Schrödinger's equation and on the ladder of quantum complexity, ions and Rydberg atoms sit on the second rung, just above a single particle. This 'natural quantumness' has its disadvantages though. Atoms cannot be tweaked or tuned. Each atom of an element is identical and immutable. If we restrict ourselves to single elements, the number of choices for experiments is constrained by the periodic table and its properties. Freedom from Nature's rules about matter can only come by changing scale[2]. This is the idea of superconducting microwave circuits, known also as cQED (circuit Quantum ElectroDynamics).

Overall, the field of superconducting circuits deals with isolating and controlling macroscopic degrees of freedom emerging from the interaction of a large number of microscopic particles. To do this, we use electrical circuits made out of superconductors whose charges and currents oscillate at microwave frequencies. At the lowest level, electrons in the superconductor start exhibiting collective behaviour by forming Cooper pairs once the temperature drops below the critical temperature [6]. At that point, the geometry of the circuit favours certain configurations called eigenmodes which can be described quantum mechanically (Chapter 2,[7]). This illustrates how, by actually increasing the number of microscopic degrees of freedom we have managed to isolate a single macroscopic one. These eigenmodes can have linear properties, creating microwave resonators or transmission lines [8], but there are also non-linear components called Josephson junctions [9, 10]. These non-linearities allow the properties of certain eigenmodes to depend on the state of other modes in the circuit, including their own. Finally, a fortuitous intersection of multiple criteria (the superconducting gap and junction plasmon frequency among others) make microwave frequency circuits (100 MHz to 20 GHz) an ideal choice. Moreover, the quantitative description of these eigenmodes depends entirely on our own choice of how to draw the circuit. Superconducting circuits therefore have that property unknown to the astro- or particle physicist. The experimentalist becomes more than just an observer of the distant stars or the infinitely small,

2 This is essentially a reformulation that as the number of constituents increases, the number of microstates increases (super-)exponentially. In more everyday terms, there are an immense number of possible castles to build with 1000 identical Lego bricks. The incredible diversity of different animal and plant species in the natural world is also a good example.

contenting themselves with the explanation of their recordings. They can now claim to truely design, at the quantum level, the experiments they would like to work on. The experimentalist can, without blushing, be considered both physicist and engineer. This exciting ability has been fully exploited over the last two decades, making superconducting microwave circuits a test bed for a number of fundamental experiments in quantum mechanics [11, 12, 13].

With such a high level of quantum control, many technologists believe that cQED is a platform which could find itself at the core of future quantum computers envisioned already in the 1980s [14, 15]. If a single experiment was to exemplify the reason why superconducting circuits seem so promising for this application, it might be the 2004 work by Wallraff et al. who dispersively coupled a Transmon qubit to a microwave resonator [16, 17, 18]. Qubits (or quantum bits) are quantum information storage devices, similar to classical bits on a hardrive up to the fact that the state of a qubit is described by a superposition of 0 and 1, not just one or the other. By coupling a qubit to a microwave mode, Wallraff and his collaborators showed two things. The first is that superconducting qubits can be readout in a straightforward quantum non-demolition (QND) manner [19, 20], using a pulse at a frequency different from the qubit transition, so that the qubit can be reused immediately after measurement. The second is that qubits could be interfaced with the techniques of microwave engineering, a subject area which had been developped for miltary reasons since the world wars and with a large amount of technological and industrial knowhow. Thus, by the beginning of the 2010s, the trio of QND readout, coherent control (demonstrated by Nakamura et al. in 1999 [21]) and long storage times [22] were available in a (sort of) scalable platform[3]. With Google's claim of "quantum supremacy" in 2019 [23], superconducting microwave circuits appear as a clear contender in the race for the quantum computer. The race is far from won, with other plaforms like Rydberg atoms [24], trapped ions [25], photonics [26] or single electrons [27, 28] with their own advantages. For circuit QED, like for the other platforms, there are still a number of open problems still to solve though, and in the spirit of the field up until now, academic research still plays a leading role in supporting the industrialisation, notably with novel quantum error correction protocols [29, 30] or remote entanglement [31].

1.3 THE EFFECT OF THE ENVIRONMENT

Research and industrial interests happen to be aligned in the search for better gates, better readout and better storage. Indeed, whilst these are necessary to run quantum algorithms, minimising operation errors in experiments is crucial in observing more and more elusive quantum mechanical effects. Unfortunately, improving the operation of quantum circuits often runs into what appear to be conflicting requirements. Quantum storage for example becomes perfect when the degree of freedom in which the infor-

3 The parallel between those three ingredients and the gates, storage and readout trio materialised in classical computer hardware by transistors, the magnetic domains of hardrives, and hardrive read-heads is striking.

mation is encoded is fully isolated from its environment. Yet, if we are to measure the state of the qubit, it must be in interaction with our measurement apparatus. Storage and readout thus appear incompatible.

Working on this from a systemic point of view was one of the main objectives of this thesis. From the get go, we chose the Fluxonium qubit because of its ability to combine good storage properties with excellent readout fidelity. The Fluxonium qubit consists of a single Josephson junction shunted by a capacitance and an inductance formed by a chain of junctions[4] [32]. Its energy level structure means that the subspace in which the qubit's state is encoded is at much lower frequencies than the other energy levels. This offers it some level of protection from bit-flip errors for reasons associated with the density of states of the environment. Phase-flip errors, the error type not present in classical computers which describes a loss of information on the phase of a quantum superposition, are also reduced by working in a parameter regime called the sweet-spot. The protection from phase-flips, in opposition to bit-flip protection, comes from internal properties of the qubit. Another consequence of the energy level structure is that the transition frequency within the computational subspace plays almost no part in the qubit's coupling rate to a readout resonator. This way we can determine the quantum state when necessary without continuously disturbing the qubit. As of June 2021, Fluxonium qubits are the most coherent and well controlled superconducting qubits [33] with state of the art readout fidelities [34]. These ideas and the reasons for Fluxonium's success are developed in detail in Chapter 3.

Although an error symptom is determined at the level of the qubit, its cause may be located in a galaxy far far away[5]. Chapters 4 and 5 try to fight quantum errors at the level of the entire experimental setup. We characterise the qubit's environment by looking at the losses of the materials surrounding it and at different sources of stray radiation which might affect the quantum state. Moreover, because circuit geometry is under our control, we present some techniques which can be used to design quantum systems with the Hamiltonians we would like to implement. We also review the literature for the best materials to use for fabricating superconducting circuits. Regarding the effects of radiation, we show that in some setups, even with state-of-the-art shielding, there can be unknown effects which dominate the qubit losses. This underlines the necessity to juggle between microscopic and macroscopic concepts, as losses due to quasiparticles can only be understood using BCS-theory, yet the change which brought the greatest improvement in coherence times in this thesis was changing dilution refrigerator. In conclusion to this part dedicated to controlling external factors, we demonstrate a number of ways to mitigate the thermal effects of the environment by purifying the state of the qubit before operation, something of particular interest for devices whose transition frequency is so low that a photon is less energetic than the thermal energy $k_{\mathrm{B}}T$.

4 The collective property of a chain of individual junctions, to go from a non-linear object to something mostly linear, is another example of a change of scale.

5 In the case of cosmic rays [35, 36].

The experimentalist is of course an integral part of the environment. Their role is especially pronounced at the time of readout, during which the qubit is entangled with the probe to which they have access. Ideally, readout should be done in a QND manner so that two successive readouts of the qubit state yield the same result. While there is no theoretical reason to believe that this should not be the case in the dispersive limit of circuit QED, experiments with Fluxoniums have often shown a number of non-QND effects when their state is readout [34, 37, 38]. We realised during this thesis that these effects were a real limitation for experimental progress, especially for devices where the number of qubits exceeds one. In Chapter 6 we provide one of the few quantitative measurements of these effects as the amplitude of the field used to ascertain the qubit state increases and at different flux biases. For this purpose, we developed a novel scheme for the identification of the qubit state from the histograms of measurement outcomes. We also diagonalised the Hamiltonian of two capacitively coupled Fluxoniums coupled to the same cavity. Then, in an experiment with no qubit gates, we extract the transition rates between the two qubit states using quantum jump trajectories. By utilising the information contained in the full jump trajectory, we improve our estimates for these transition rates, despite the imperfect measurement. We show that the transition rates between qubit states in presence of the drive vary significantly when the control parameters, flux and amplitude, are changed. In a last part, we simulate realistic quantum jump trajectories, thereby providing a partial explanation for some of the structure of the noise in our experiment. Our hope is that by quantifying the effect of the readout pulse on the Fluxonium qubits systematically, theorists will be able to determine which features to look for and may provide suggestions on how to avoid these effects.

1.4 THERMODYNAMICS OF QUANTUM MEASUREMENT

The very last chapter of the thesis continues to deal with the topic of quantum measurement, but this time at a fundamental level. Of all the strangeness associated with quantum mechanics, the measurement postulate is perhaps the most unnerving. It can be summarised by this statement attributed to Alexander Korotkov: “In quantum mechanics, you don’t see what you get. You get what you see!”. Why is there a collapse of the wavefunction? Why is there measurement backaction? We choose the engineer’s (politician’s?) perspective here and choose not to answer, but accept the experimental evidence. There is a collapse. There is backaction. In Chapter 7 we construct an example where a measurement apparatus appears to exchange energy with the qubit, despite it being QND. The explanation we propose is in the spirit of this thesis. It requires taking into account the measurement protocol as a whole, considering in particular the entire procedure leading to the state measured by the QND apparatus. By recording the energy inside the pulse reflected off the qubit which was used to prepare its state, we recover a scenario where no energy is provided by the measurement. In doing so, we make evident the entanglement between qubit and driving mode, manifesting itself experimentally through the anomalous weak values of the qubit operators [39]. The records of the driving mode post-selected on the result of a strong qubit measurement after interaction further reveals the backaction of the measurement process on the propagating field. A model, exploiting the properties of Bayesian probabilities, helps give

an intuition for the results of the experiment.

Obviously, this work has research implications for quantum thermodynamics, which questions how to harness the random outcomes of quantum measurements as a resource [40]. Surprisingly, this experiment is also strongly related to the more applied uses of circuit QED. Indeed, understanding that the state of the combined system has, from the very beginning, no uniquely defined energy is critical for high fidelity quantum gates and so is the number of photons in the pulse. Moreover, resolving the issue of energy exchanges in qubit control and measurement is essential in figuring out how much energy will be required to run a quantum processor. With potentially many millions of qubits this is a very real unsolved problem [41].

1.5 CLOSING REMARKS

In both Chapter 6 and Chapter 7 we use the past quantum state formalism [42] as a tool for the calculation of some of the main results of the thesis. This formalism helps predict the statistics of the unknown measurement outcome using both knowledge about the system's state preceding and following the time of measurement. It can be thought of as trying to make predictions about the future and inferences about the past coincide. Despite the formulas being relegated to an appendix, I think it can serve here as a commentary for this thesis as a whole.

The thesis project started with the amibition of showing effective Fluxonium resets, moving on to two qubit experiments and thermodynamics with Fluxonium. The realities of experimental physics force us to change course sometimes, and instead we focused on the readout problem and thermodynamics with a Transmon. With the thesis written up, another a posteriori interpretation for this work could be to have explored and engineered the effect of measurement on superconducting qubits. Limiting unmonitored measurement by the environment which leads to decoherence (Chapters 3 to 5), benchmarking non-QNDness (Chapter 6), and observing the energetics of measurement (Chapter 7). Different observers can have different past quantum states, reflecting their own observations, their own point of view, yet all are correct. In this introduction I chose to highlight the parallels between applied and fundamental physics on different scales in my work. This shows that, despite Science's idealisation of objectivity, there is a certain amount of editorialising to a thesis. This is certainly not the only way this work could have been presented, only my own take on the work done. I hope the choices made in the following pages will be instructive.

2

SUPERCONDUCTING CIRCUITS FOR QUANTUM COMPUTING

2.1 INTRODUCTION

The goal of the following section is to give a short introduction to the superconducting circuits platform and the theoretical and experimental techniques which describe the most simple experiments in circuit QED. We will discuss the basic building blocks which are microwave cavities (harmonic oscillators), the heavily used Transmon qubit (anharmonic oscillators) and the procedure with which we can control the states of qubits (Rabi oscillations) as well as measure the state of the qubit (dispersive readout). Each of these topics will only be convered briefly, with details given in later chapters. Many texts cover the material of this chapter, but a very thorough treatement of some of the theory can be found in S. Girvin's lecture notes from the Les Houches summer school of 2011 [43]. For a more thorough review of the current state of the art, a number of reviews have been published in recent years. Two excellent references are those by Blais et al. [44] and Krantz et al. [45]. For a more quantum computation focused review, the 2017 work by Wendin [46] is also a good place to look.

2.2 HARMONIC OSCILLATORS - MICROWAVE RESONATORS

2.2.1 *Theory*

We start by considering one of the most well understood systems in physics: the harmonic oscillator. Consider the LC circuit presented in Fig. 2.1a. A classical description can be derived using the Langrangian of the circuit

$$\mathcal{L} = \frac{L\dot{Q}^2}{2} - \frac{Q^2}{2C} \,, \tag{2.1}$$

where Q is the charge on the capacitance plates, C is its capacitance and L is the inductance of the circuit. A Legendre transform yields the quadratic Hamiltonian

$$H = \frac{\Phi^2}{2L} + \frac{Q^2}{2C} \,, \tag{2.2}$$

where we have introduced the generalised flux $\Phi = L\dot{Q} = \int V \mathrm{d}t$, which is the canonically conjugate variable to the charge on the capacitor. V is the voltage across the inductor or capacitor. Equivalently, we could have written the Langrangian as a function of the generalised flux

$$\mathcal{L} = \frac{C\dot{\Phi}^2}{2} - \frac{\Phi^2}{2L} \,, \tag{2.3}$$

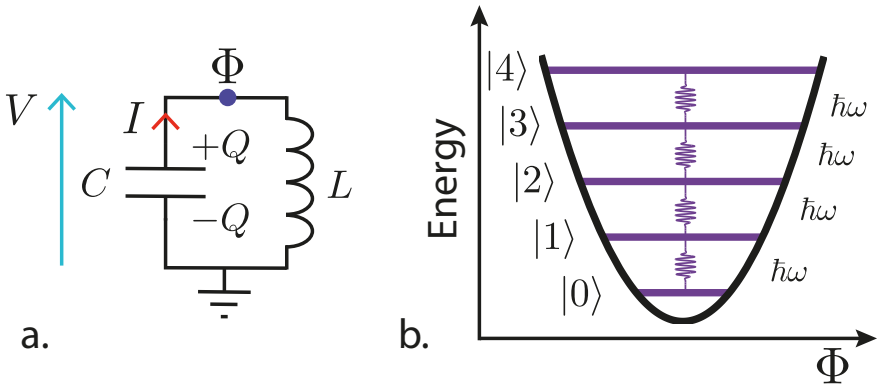

Figure 2.1: a. A parallel LC circuit. Here Q is the charge on one of the capacitance plates, I is the current in the loop, V is the voltage across the capacitance or inductance, C is the capacitance and L the inductance of the circuit. b. An illustration of the spectrum of the harmonic oscillator. The black line corresponds to a potential given by the Φ^2 term in the Hamiltonian. The energy eigenstates in purple are equally spaced by an energy $\hbar\omega$.

and obtained the same Hamiltonian. Classically, we now have everything we need to describe the circuit, and Hamilton's equations immediately yield the equation of motion

$$\ddot{Q} + \omega^2 Q = 0 \ , \tag{2.4}$$

which describes harmonic oscillations where energy is in turn stored in the electric field of the capacitance and then in the magnetic field of the inductance. We introduced the characteristic frequency of the circuit $\omega = \frac{1}{\sqrt{LC}}$ which has units of $\mathrm{rad\,s^{-1}}$.

In the quantum mechanical case, our general objective is to solve the Schrödinger equation

$$i\hbar \frac{\partial |\psi\rangle}{\partial t} = \hat{H} |\psi\rangle \ , \tag{2.5}$$

where the Hamiltonian has become an operator $\hat{H}$ acting on the state $|\psi\rangle$.

$$\hat{H} = \frac{\hat{\Phi}^2}{2L} + \frac{\hat{Q}^2}{2C} \ , \tag{2.6}$$

is identical to the classical case but for the canonical commutation relation $[\hat{\Phi}, \hat{Q}] = i\hbar$ - a manifestation that simultaneous strong measurements of the charge on the capacitance and the generalised flux are impossible[1]. Because $\hat{H}$ does not depend on time, (2.5) is separable and comes down to solving

$$\hat{H} |\psi_n\rangle = E_n |\psi_n\rangle \ , \tag{2.7}$$

where E_n and $|\psi_n\rangle$ are the eigenenergies and eigenstates of $\hat{H}$ respectively. Because there are many possible solutions, $|\psi_n\rangle$ is indexed by n and its time evolution is given

1 Simultaneous weak measurements are possible though, as was demonstrated in [47, 48]

by $|\psi_n(t)\rangle = e^{-iE_n t/\hbar}|\psi_n(0)\rangle$ at time t. The standard technique for solving (2.5) (see any quantum mechanics textbook, [49] or [50] for example) involves introducing the ladder operators

$$\hat{a} = \frac{1}{\sqrt{2\hbar Z}}\left(\hat{\Phi} + iZ\hat{Q}\right) , \tag{2.8}$$

$$\hat{a}^\dagger = \frac{1}{\sqrt{2\hbar Z}}\left(\hat{\Phi} - iZ\hat{Q}\right) , \tag{2.9}$$

where $Z = \sqrt{\frac{L}{C}}$ is the circuit impedance. Conversely

$$\hat{\Phi} = \sqrt{\frac{\hbar}{2}} \cdot \sqrt{Z}(\hat{a}^\dagger + \hat{a}) = \Phi_{\text{ZPF}}(\hat{a}^\dagger + \hat{a}) , \tag{2.10}$$

$$\hat{Q} = i\sqrt{\frac{\hbar}{2}} \cdot \frac{1}{\sqrt{Z}}(\hat{a}^\dagger - \hat{a}) = iQ_{\text{ZPF}}(\hat{a}^\dagger - \hat{a}) . \tag{2.11}$$

The prefactors Φ_{ZPF} and Q_{ZPF} are called the "Zero Point Fluctuations" of flux and charge and correspond to the excursions of the two variables around zero in the ground-state. The Hamiltonian can be written in a diagonal form using these operators as

$$\hat{H} = \hbar\omega(\hat{a}^\dagger\hat{a} + \frac{1}{2}) . \tag{2.12}$$

The eigenstates of the Hamiltonian in this form are indexed by the quantum number $n \in \mathbb{N}$ and written $|n\rangle$. Application of the operators follows the rules $\hat{a}^\dagger|n\rangle = \sqrt{n+1}\,|n+1\rangle$ and $\hat{a}|n\rangle = \sqrt{n}\,|n-1\rangle$, such that $\hat{a}$ and $\hat{a}^\dagger$ let us move up and down the ladder of states indexed by n. Importantly, the energy difference $\langle n|\hat{H}|n\rangle - \langle n-1|\hat{H}|n-1\rangle$ is constant: the 'rungs' of the ladder are separated by the constant energy $\hbar\omega$ (see Fig. 2.1b).

2.2.2 *Hardware*

Two conditions were necessary for the theoretical description above to be valid.

- The availability of a system which can be described as a simple combination of an inductance and a capacitance in parallel.
- The availability of such a system with negligeable losses.

Indeed, our circuit description did not allow for the presence of losses, which would have been modelled by a resistance somewhere in the circuit. This observation (among others) motivates the use of superconductors for the physical implementation of our quantum circuits. Below their critical temperature, around 1.2K for aluminium [51], these materials oppose strictly zero resistance to DC electrical current [6]. We can implement close to ideal LC oscillator circuits in two or three dimensions. In 3D, the electromagnetic modes of a metal cavity can be modelled by LC oscillators with different characteristic frequencies in the GHz frequency range. For the TE_{110} we can see the opposite sides of the cavity as the plates of a capacitance and the metallic sidewalls as an inductance as is clear from the distributions of current and charge in electromagnetic simulations of a 3D cavity in HFSS (Fig. 2.2c&d). In 2D, the resonator can either be

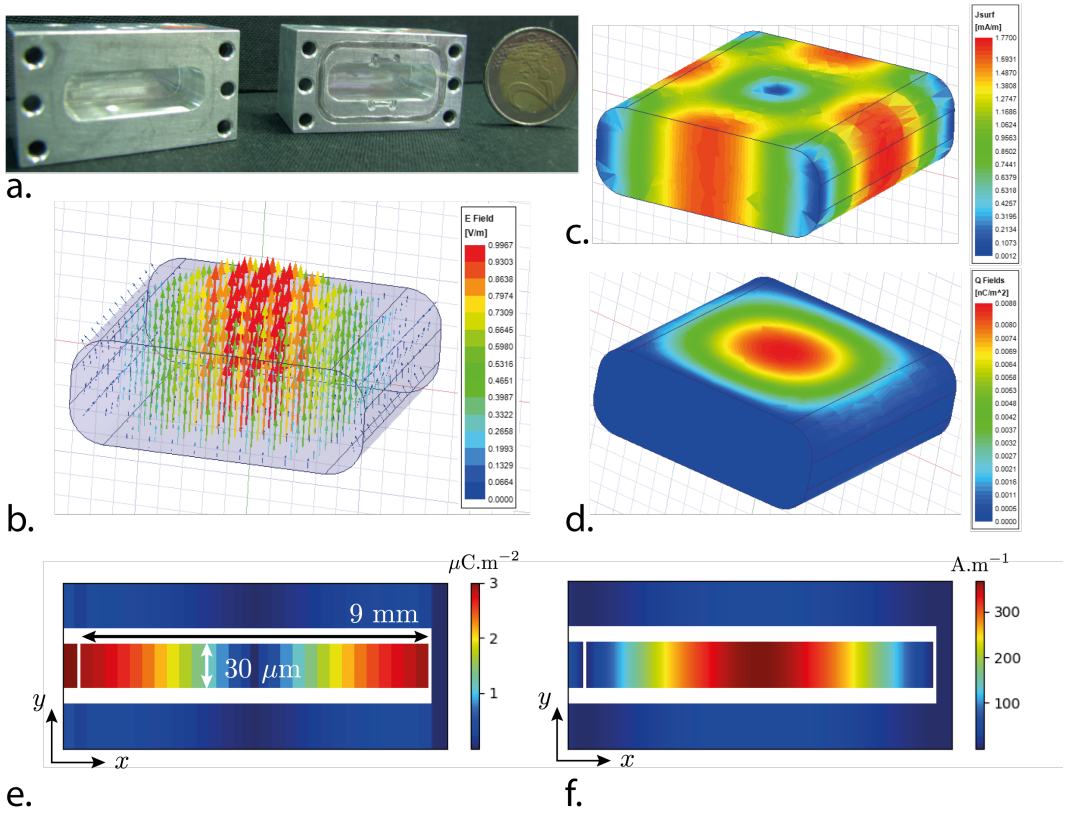

Figure 2.2: a. 3D aluminium cavity with a 2 euro coin for scale. Because the cavity is made out of aluminium, it is almost lossless at dilution refrigerator temperatures. b-c-d. Electromagnetic simulations of the cavity using HFSS. b. Shows the electric field at the lowest frequency 8.1 GHz cavity eigenmode TE_{110}. c. Current distribution of the mode, illustrating how the sidewalls of the cavity form the inductors of the equivalent LC circuit. d. Charge distribution of the mode, showing how the opposing faces of the cavity act as a parallel plate capacitor. e. Charge distribution in a Sonnet simulation of a single port $\lambda/2$ co-planar waveguide (CPW) resonator at 7.1 GHz. The two gaps at either end of the resonator separate it from the tranmission line on the left and the ground plane on the right. Notice how the charges accumulate at either end of the resonator, illustrating the capacitance of the mode. For clarity, the x and y scales are different. f. Current distribution for the same distributed resonator. The highest current density is found at the centre of the resonator, illustrating the inductance of the mode.

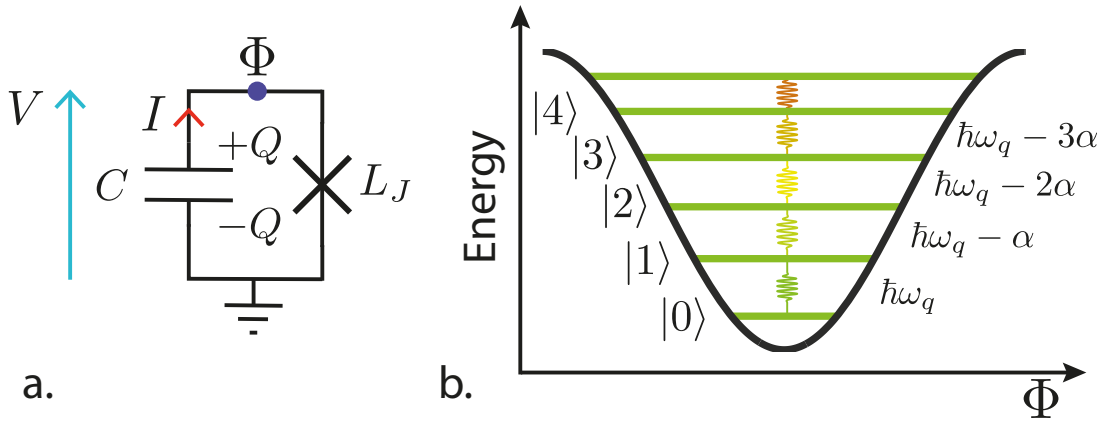

Figure 2.3: a. Equivalent circuit of a Transmon qubit. Here Q is the charge on one of the superconducting islands, I the current through the junction, V is the voltage across the junction, C is the effective capacitance and L_J the Josephson inductance of the junction. b. An illustration of the spectrum of the Transmon. The black line corresponds to the cosine potential given by the Josephson Hamiltonian (2.17). The energy eigenstates in green are no longer equally spaced because of the widening of the potential at higher energies.

implemented in a lumped element fashion with an interdigitated capacitance and meander or spiral inductance for example; or we can use a distributed element version where the resonator is a finite length transmission line where reflections at either end create an interference pattern only allowing standing waves [8]. The validity of the lumped element circuit model with a single capacitance and inductance is again illustrated by electromagnetic simulations in Sonnet for example (Fig. 2.2e&f).

2.3 ANHARMONIC OSCILLATORS - THE TRANSMON QUBIT

We need to introduce a non-linearity to harness the full toolbox of quantum information. On the one hand, this non-linearity will allow us to manipulate our quantum system and prepare non-classical states, opening the possibilities of quantum control. On the other hand, having a non-linearity will help us design a device with energy levels which are not equally spaced. Because of the anharmonic level spacing, this device is often approximated as a simple two level system or qubit. In the next section we introduce the Transmon.

2.3.1 *Theory*

Josephson junctions, named after the physicist Brian Josephson, are the basic non-linear building blocks of cQED. They are made of a superconducting/insulating/superconducting tunnel barrier shown schematically in Fig. 2.4a. The phenomenological

equations Josephson derived to describe the physics of these junctions (equations which earned him the Nobel prize in 1973 [9]) are

$$V = \frac{\Phi_0}{2\pi}\frac{\mathrm{d}\varphi}{\mathrm{d}t} , \tag{2.13}$$

$$I = I_0 \sin\varphi . \tag{2.14}$$

V and I are respectively the voltage across and the current through the junction, φ is the phase difference between the two superconductors and I_0 is the critical current of the junction above which it becomes resistive. The superconducting flux quantum $\Phi_0 = \frac{h}{2e}$ also appears in the Josephson relations. From these macroscopic equations, we can calculate the Hamiltonian describing the junction, where the superconducting leads are considered islands, disconnected from the surroundings. Conventionally, the potential term comes from the tunneling of Cooper pairs through the junction and can be derived in a simple manner by integrating the power dissipated in the junction over time

$$E_{\mathrm{pot}} = \int VI\mathrm{d}t = \frac{\Phi_0 I_0}{2\pi}\int \frac{\mathrm{d}\varphi}{\mathrm{d}t}\sin\varphi \ \mathrm{d}t = -\frac{\Phi_0 I_0}{2\pi}\cos\varphi . \tag{2.15}$$

Integrating the first Josephson relation (2.14) we can see that φ is related to the generalised flux Φ by

$$\varphi = 2\pi\frac{\Phi}{\Phi_0} , \tag{2.16}$$

so that

$$E_{\mathrm{pot}} = -E_J\cos\varphi = -E_J\cos\left(2\pi\frac{\Phi}{\Phi_0}\right) , \tag{2.17}$$

where we have defined $E_J = \frac{\Phi_0 I_0}{2\pi}$ or, in terms of the junction inductance $L_J = \frac{\Phi_0}{2\pi I_0}$, $E_J = \frac{\Phi_0^2}{4\pi^2 L_J}$. The capacitive term, which is due to the non-zero physical size of the junction and is traditionally associated with a kinetic energy, can be expressed using C the total capacitance between the superconducting leads

$$E_{\mathrm{capa}} = \frac{(Q-Q_g)^2}{2C} = \frac{4e^2(n-n_g)^2}{2C} = 4E_C(n-n_g)^2 . \tag{2.18}$$

$2(Q-Q_g)$ is the charge difference between either side of the junction expressed as a function of the number of Cooper pairs $n-n_g$ carrying charge $2e$ and $E_C = \frac{e^2}{2C}$. The total Hamiltonian of the Josephson junction, schematically represented by the circuit in Fig. 2.3a, can thus be written

$$\hat{H}_{\mathrm{Transmon}} = 4E_C(\hat{n}-n_g)^2 - E_J\cos\hat{\varphi} . \tag{2.19}$$

Q_g and n_g are here to take into account the offset charge of the islands. As suggested by the lack of 'hat', Q_g and n_g are classical variables which do not have to take integer values. They can be thought of as thermodynamic quantities whose value depends on the electrochemical potential of each island. Indeed, external electric fields, either controlled by the experimentalist in the case of an engineered voltage gate or uncontrolled, like charge fluctuations due to the environment around the qubit, can affect

the charge equilibrium point across the junction and thus the value of the offset charge. Additionally, Q_g and n_g encompass the effect of fluctuations in the background charge distribution on each island. Although the offset charge will prove to be of critical importance later on (see Chapter 3.1.1), it does not play any role in the discussion about the dynamics of the Transmon we want to have here. For this reason, we choose to omit it for the time being.

The charge number and phase operators do not commute. The commutation relation $[\hat{n}, \hat{\varphi}] = -i$ can be derived using the definitions of $\hat{Q}$ and $\hat{\Phi}$. In the case of the Transmon qubit [18] we design the capacitance C and inductance L_J of the junction so that $E_J > 50E_C$. Intuitively, this means that changing the tunneling rate of Cooper pairs (the current) through the junction is very costly compared to changing the number of charges on either superconducting islands. The lowest energy levels of the Hamiltonian will be separated only by small changes in $\hat{\varphi}$ but by large changes of $\hat{n}$. The energy of $\hat{H}_{\text{Transmon}}$ is minimised when $\hat{\varphi}$ is close to 0 independently of the value of[2] $\hat{n}$. This motivates a series expansion of the cosine around 0 to obtain the linearised Hamiltonian $\hat{H}_{\text{lin}} = 4E_C\hat{n}^2 + \frac{1}{2}E_J\hat{\varphi}^2$ which has a form identical to the harmonic oscillator of Sec. 2.2.1[3]. We will see that the corrections to the harmonic spectrum due to the cosine term are small, so that the Transmon qubit is dubbed an anharmonic oscillator. Including terms up to fourth order in the cosine expansion

$$\hat{H}_{\text{Transmon}} \approx \hbar\omega_Q \hat{a}^\dagger \hat{a} - \frac{E_C}{12}\left(\hat{a} + \hat{a}^\dagger\right)^4 . \tag{2.20}$$

We diagonalised the terms to second order using the definitions of (2.8) and (2.9), and $\omega_Q = \frac{\sqrt{8E_C E_J}}{\hbar}$ the plasmon frequency of the qubit. Treating the fourth order term as a perturbation allows us to calculate the correction of the cosine term on the energies of the harmonic ladder for the lowest energy eigenstates

$$E_{|1\rangle} - E_{|0\rangle} = \hbar\omega_Q - E_C , \tag{2.21}$$

$$E_{|2\rangle} - E_{|1\rangle} = \hbar\omega_Q - 2E_C . \tag{2.22}$$

The difference in energy differences between the three lowest energy states is called the anharmonicity and is noted α. Here $\alpha = E_C$, but for general qubit architectures this is not necessarily the case. Also note that the qubit frequency, initially equal to the plasmon frequency, is renormalised by the fourth order cosine term. In the following we will abuse notation and ω_Q will denote both the plasmon frequency and the true qubit frequency as the difference will be clear from context. The fact that we now have an anharmonic spectrum (see Fig. 2.3b) is critical for defining the two level subspace which we will consider our qubit. Because the energy separation between the two lowest energy states is unique, we can be certain that a probe at the transition frequency $(E_{|1\rangle} - E_{|0\rangle})/h$ cannot excite the Transmon outside the computational subspace as long as its amplitude does not imply Rabi rotations at frequencies larger than α.

2 Because of the cosine term in the Hamiltonian, the state $|\varphi + 2\pi\rangle$ can be identified with the state $|\varphi\rangle$. It is thus sufficient to restrict ourselves to the interval $]-\pi, \pi]$ for the values of φ. For further discussion of this fundamental issue, see [43].

3 We have neglected the constant energy offset coming from the 0^{th} order of the cosine, as it does not change the dynamics of the system.

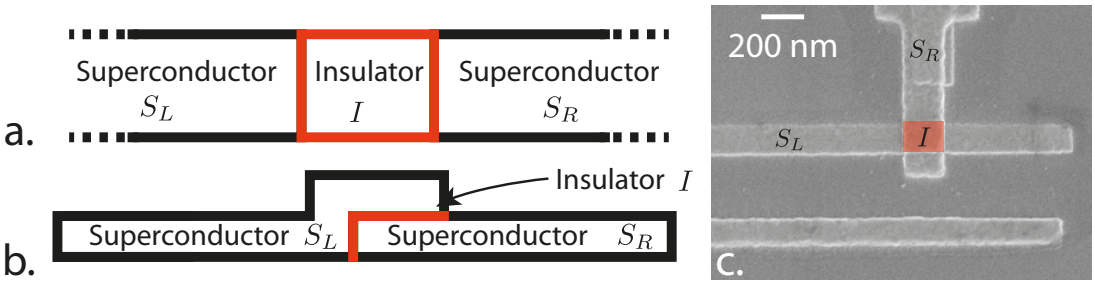

Figure 2.4: a. Basic schematic of a Josephson junction. The insulating tunnel barrier is highlighted in red. b. Cross section schematic of a Josephson junction fabricated by overlapping two layers of superconducting material separated by an oxide layer (red). Most junctions use aluminium as a superconductor and aluminium oxide for the insulator. c. SEM picture of a junction fabricated on silicon using a 30 keV e-beam lithography machine. The doubling of the junction fingers comes from the Dolan bridge fabrication technique. The slight darkening of the silicon around the aluminium pads is due to chemical treatment of the silicon substrate with HF before the deposition of aluminium.

2.3.2 *Hardware*

Here we give a brief overview of the fabrication process for Transmon qubits. More details about the basic fabrication techniques can be found in [52] for example, and a discussion of the tradeoffs between the Hamiltonian parameters will follow in the next section. Very generally we want Transmon frequencies close to, but slightly detuned from, the cavity frequency in the $4-8$ GHz range (the reason for this proximity will become clear in the discussion of the dispersive readout in Section 2.4.3). We obtain the correct frequencies through fine control of C and L_J thanks to various fabrication steps. In practice, the capacitance C can be decomposed into the sum of two capacitances C_J and C_{pads}. C_J corresponds to the direct overlap between the superconducting islands separated by the insulating barrier. This interface is highlighted in red in Fig. 2.4b. The second part of the capacitance, C_{pads}, is given by the geometrical capacitance assigned to the superconducting islands either side of the junction. The superconducting islands also have a dual purpose, as they act as an antenna for the electromagnetic fields which will be used for qubit control and readout. Engineering E_C requires taking into account the contribution of C_J when designing the size of the superconducting islands. E_J, or equivalently L_J, on the other hand is engineered by tuning the thickness and surface area of the oxide layer. The superconducting pads can be fabricated using standard optical lithography techniques because the characteristic size of these is around 10 µm to 10 mm. Sometimes though, to reduce fabrication steps, the pads are fabricated with the junction itself using e-beam lithography allowing minimum feature sizes of the order of tens of nanom. The oxide layer is obtained using a Dolan bridge technique [53] and double angle evaporation which allows a non-conductive overlap of the two superconducting wires (see Fig. 2.4c).

2.4 CONTROL AND READOUT OF A TWO-LEVEL SYSTEM

In the previous section we showed how a realisable macroscopic physical system could be described as a (quasi-)two-level system. Here we explore how to control and readout the state of this two level system, showing that we can manipulate and observe the information contained within the qubit.

2.4.1 *Two-level system basics*

In full generality, the quantum state of a two-level system can be described by

$$|\psi\rangle = \alpha\,|0\rangle + \beta\,|1\rangle \ , \tag{2.23}$$

with $\alpha, \beta \in \mathbb{C}$ and $|\alpha|^2 + |\beta|^2 = 1$. By setting the unphysical global phase of the wavefunction to 0, we can write

$$|\psi\rangle = \cos\frac{\theta}{2}\,|0\rangle + \sin\frac{\theta}{2}e^{i\phi}\,|1\rangle \ , \tag{2.24}$$

where $\theta \in [0, \pi]$ and $\phi \in [0, 2\pi]$. $|0\rangle$ and $|1\rangle$ are the eigenstates of the Hamiltonian

$$\hat{H} = \frac{\hbar}{2}\omega_Q\hat{\sigma}^z \ , \tag{2.25}$$

with eigenenergies $\pm\frac{\hbar}{2}\omega_Q$. $\hat{\sigma}^z$ is part of the basis of SU(2) spanned by the unitary operators of dimension 2 called the Pauli matrices. In the representation $|0\rangle = (0,1)^T, |1\rangle = (1,0)^T$, the Pauli operators take the form

$$\mathbb{1} = \begin{pmatrix} 1 & 0 \\ 0 & 1 \end{pmatrix} \ , \quad \hat{\sigma}^x = \begin{pmatrix} 0 & 1 \\ 1 & 0 \end{pmatrix} \ , \quad \hat{\sigma}^y = \begin{pmatrix} 0 & -i \\ i & 0 \end{pmatrix} \ , \quad \hat{\sigma}^z = \begin{pmatrix} 1 & 0 \\ 0 & -1 \end{pmatrix} \ . \tag{2.26}$$

Two other useful operators are $\hat{\sigma}^+ = \frac{1}{2}(\hat{\sigma}^x + i\hat{\sigma}^y) = \left(\begin{smallmatrix} 0 & 1 \\ 0 & 0 \end{smallmatrix}\right)$ and $\hat{\sigma}^- = \frac{1}{2}(\hat{\sigma}^x - i\hat{\sigma}^y) = \left(\begin{smallmatrix} 0 & 0 \\ 1 & 0 \end{smallmatrix}\right)$ which have the same incrementation properties as the ladder operators introduced before, but simply restricted to the two-level subspace: $\hat{\sigma}^+\,|0\rangle = |1\rangle$ and $\hat{\sigma}^-\,|1\rangle = |0\rangle$.

A convenient visual representation of 2.24 is the Bloch vector

$$\vec{u}_{|\psi\rangle} = \begin{pmatrix} \langle\hat{\sigma}^x\rangle_{|\psi\rangle} \\ \langle\hat{\sigma}^y\rangle_{|\psi\rangle} \\ \langle\hat{\sigma}^z\rangle_{|\psi\rangle} \end{pmatrix} = \begin{pmatrix} \cos\phi\sin\theta \\ \sin\phi\sin\theta \\ \cos\theta \end{pmatrix} \ , \tag{2.27}$$

of norm $\left\|\vec{u}_{|\psi\rangle}\right\| = 1$. In 3 dimensional euclidean space it describes all the positions on a sphere with radius 1 (Fig. 2.5). With this description, there is a bijective map between the vectors on the Bloch sphere and the possible states of a qubit.

2.4.2 *Control Pulses*

We can understand how to control the state of the two level system by considering the equivalent circuit of Fig. 2.6a. The Hamiltonian of this circuit is [7]

$$\hat{H} = \frac{\hat{Q}^2}{2(C + C_c)} - E_J\cos\left(2\pi\frac{\hat{\Phi}}{\Phi_0}\right) + \frac{C_c}{C_c + C}\hat{Q}V_d(t) \ , \tag{2.28}$$

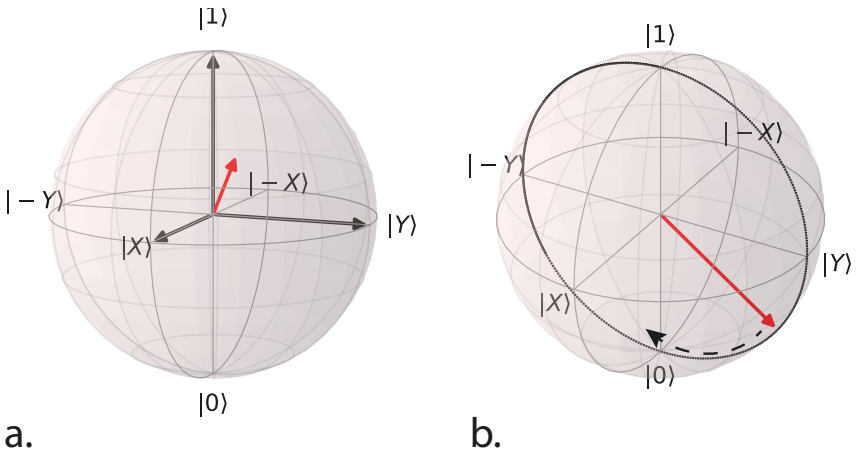

Figure 2.5: a. Bloch sphere representation of the state $|\psi\rangle = \frac{1}{2}|0\rangle + e^{-i\frac{\pi}{6}}\frac{\sqrt{3}}{2}|1\rangle$ (red vector). b. Bloch sphere representation of Rabi oscillations around the x-axis. The trajectory of a pure state with $\langle\hat{\sigma}^x\rangle_{|\psi\rangle} = 0$ (red vector) is given using the black dotted line.

which corresponds to a Transmon qubit coupled capacitively to an external drive. We limit ourselves to the low energy subspace spanned by the states $|0\rangle$ and $|1\rangle$ by replacing the ladder operators $\hat{a}$ and $\hat{a}^\dagger$ with the spin operators $\hat{\sigma}^-$ and $\hat{\sigma}^+$. The Transmon term is diagonalised straightforwardly using this correspondence and with the definition $Z = \sqrt{\frac{L_J}{C+C_c}}$. We obtain

$$\hat{H} = \frac{\hbar\omega_Q}{2}\hat{\sigma}^z + i\frac{C_c}{C_c+C}V_d(t)\frac{1}{\sqrt{Z}}(\hat{\sigma}^+ - \hat{\sigma}^-)\ . \tag{2.29}$$

Note that this is a good example of how the effective capacitance of the Transmon can be decomposed into various terms as described in Sec. 2.3.2: here the coupling to the drive adds a contribution to the capacitance seen by the junction. At this point it is useful to go to a frame rotating at the frequency of the drive ω_d. We assume the voltage drive evolves sinusoidally as a function of time with amplitude V_0, $V_d(t) = V_0\sin(\omega_d t + \phi)$ The Hamiltonian in the rotating frame $\tilde{H}$ under the unitary transformation $\hat{U} = e^{i\omega_d\hat{\sigma}^z t/2}$ is given by

$$\tilde{H} = \hat{U}\hat{H}\hat{U}^\dagger + i\hbar\frac{\mathrm{d}\hat{U}}{\mathrm{d}t}\hat{U}^\dagger = \frac{\hbar\delta\omega}{2}\hat{\sigma}^z + i\frac{C_c}{C_c+C}V_d(t)\frac{1}{\sqrt{Z}}\left(\hat{\sigma}^+e^{i\omega_Q t} - \hat{\sigma}^-e^{-i\omega_Q t}\right)\ , \tag{2.30}$$

where $\delta\omega = \omega_Q - \omega_d$. After some algebra and under the rotating wave approximation (RWA) which eliminates the rapidly rotating terms

$$\tilde{H} \approx -\frac{\hbar\Omega}{2}\left[\hat{\sigma}^x\cos(\phi) + \hat{\sigma}^y\sin(\phi)\right] + \frac{\hbar\delta\omega}{2}\hat{\sigma}^z. \tag{2.31}$$

We have defined the Rabi frequency $\Omega = V_0\frac{C_c}{C_c+C}\frac{1}{\sqrt{Z}} \propto V_0$. Through this simple model we were able to derive the Hamiltonian describing rotations around all three axes of the Bloch sphere. The detuning controls the rotation around $\hat{\sigma}^z$ and the phase of the drive controls the rotation around $\hat{\sigma}^x$ or $\hat{\sigma}^y$. As an illustration, starting in the state $|0\rangle$ and with $\phi = \pi$ and $\delta\omega = 0$, the time evolution of the qubit state is given by

$$|\psi(t)\rangle = \cos\left(\frac{\Omega}{2}t\right)|0\rangle - i\sin\left(\frac{\Omega}{2}t\right)|1\rangle\ . \tag{2.32}$$

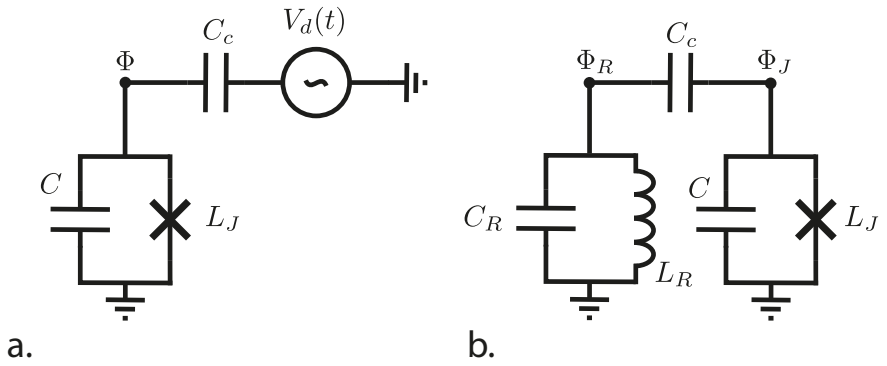

Figure 2.6: a. Equivalent circuit of a Transmon coupled to an external drive. The coupling capacitance C_c mediates the oscillating voltage drive on the right. b. Equivalent circuit of a Transmon coupled to a cavity. The coupling capacitance C_c is materialised by the antennas of the junction placed inside the standing mode of the resonator field.

After a time $\frac{\pi}{2\Omega}$ we obtain the state $\left|\psi\left(\frac{\pi}{2\Omega}\right)\right\rangle = \frac{1}{\sqrt{2}}|0\rangle - i|1\rangle = |-Y\rangle$, the eigenstate of $\hat{\sigma}^y$ with eigenvalue -1. We recognise the famous Rabi oscillations, here rotating left handedly around the x-axis, represented on the Bloch sphere in Fig. 2.5.

In practice the circuit diagram of Fig. 2.6a is materialised by letting the qubit interact with a propagating electromagnetic field generated by a RF frequency source. The pads of the junction act as an antenna which couples the qubit capacitively to the field. When placed inside a cavity, the antenna has the additionnal advantage of coupling the qubit to the resonator mode allowing the readout of the qubit state.

2.4.3 *Qubit readout*

To readout the state of the qubit, we couple it to a readout cavity, usually capacitively. The circuit model which best describes this is given in Fig. 2.6b. It is easiest to write the Lagrangian using the matrix and vector

$$C_M = \begin{pmatrix} C_R + C_c & -C_c \\ -C_c & C + C_c \end{pmatrix} \ , \ \Phi = \begin{pmatrix} \Phi_R \\ \Phi_J \end{pmatrix} \ . \tag{2.33}$$

With these definitions

$$\mathcal{L} = \frac{1}{2}\dot{\Phi}^T C_M \dot{\Phi} - \frac{1}{2L_R}\Phi_R^2 + E_J \cos\left(2\pi\frac{\Phi_J}{\Phi_0}\right) \ . \tag{2.34}$$

Defining the resonator and qubit frequencies $\omega_R = \frac{1}{L_R}\left(C_M^{-1}\right)_{11}$ and $\omega_Q = \frac{1}{L_J}\left(C_M^{-1}\right)_{22}$ as well as the coupling $g = \frac{\left(C_M^{-1}\right)_{12}+\left(C_M^{-1}\right)_{21}}{4\sqrt{L_R L_J \omega_R \omega_Q}}$, the Hamiltonian is

$$\hat{H} = \frac{1}{2}L_R\omega_R^2 Q_R^2 + \frac{\Phi_R^2}{2L_R} + \frac{1}{2}L_J\omega_Q^2 Q_J^2 - E_J\cos\left(2\pi\frac{\Phi_J}{\Phi_0}\right) + 2g\sqrt{L_R L_J \omega_R \omega_Q}\hat{Q}_R\hat{Q}_J \ , \tag{2.35}$$

where the indices of C_M^{-1} correspond to the matrix elements of the inverse of C_M. Here again we see that the first two terms correspond to a harmonic oscillator, the next two

to the Transmon mode and the last one to the capacitive coupling between the two. Thus, to 4$^{\text{th}}$ order in the Transmon cosine term and introducting the cavity operators $\hat{c}$ and $\hat{c}^\dagger$

$$\hat{H} \approx \hbar\omega_R \hat{c}^\dagger \hat{c} + \hbar\omega_Q \hat{a}^\dagger \hat{a} - \frac{E_C}{12}\left(\hat{a} + \hat{a}^\dagger\right)^4 - \hbar g(\hat{c}^\dagger - \hat{c})(\hat{a}^\dagger - \hat{a}) \ , \tag{2.36}$$

with $\omega_Q = \sqrt{8E_C E_J}/\hbar$. A simplification can be obtained by going to a frame rotating at the qubit and cavity frequencies ($\hat{U} = \exp\left[i\omega_R \hat{c}^\dagger \hat{c}t + i\omega_Q \hat{a}^\dagger \hat{a}t\right]$) and applying the RWA. This eliminates the terms $\hat{c}^\dagger \hat{a}^\dagger$ and $\hat{c}\hat{a}$ in (2.36).

$$\hat{H} = \underbrace{\hbar\omega_R \hat{c}^\dagger \hat{c} + \hbar\omega_Q \hat{a}^\dagger \hat{a} + \hbar g(\hat{c}^\dagger \hat{a} + \hat{c}\hat{a}^\dagger)}_{\text{linear}} \underbrace{- \frac{E_C}{12}\left(\hat{a} + \hat{a}^\dagger\right)^4}_{\text{non-linear}} \ . \tag{2.37}$$

We can diagonalise the linear part of the Hamiltonian, by using the Bogoliubov transformation [44] $\hat{U} = e^{\Lambda(\hat{c}^\dagger \hat{a} - \hat{c}\hat{a}^\dagger)}$ with $\Lambda = \frac{1}{2}\arctan(2g/\Delta)$ and $\Delta = (\omega_Q - E_C/\hbar) - \omega_R$. In the dispersive limit, where $g \ll |\Delta|$, the Hamiltonian becomes

$$\hat{H}_{\text{dispersive}} = \hbar\tilde{\omega}_R \hat{c}^\dagger \hat{c} + \hbar\tilde{\omega}_Q \hat{a}^\dagger \hat{a} + \frac{\hbar K_R}{2}(\hat{c}^\dagger)^2 \hat{c}^2 + \frac{\hbar K_Q}{2}(\hat{a}^\dagger)^2 \hat{a}^2 + \hbar\chi_{RQ} \hat{c}^\dagger \hat{c} \hat{a}^\dagger \hat{a}. \tag{2.38}$$

The dressed frequencies of the cavity and qubit are

$$\tilde{\omega}_R = \frac{1}{2}\left(\omega_R + \omega_Q - E_C/\hbar - \sqrt{\Delta^2 + 4g^2}\right) \ , \tag{2.39}$$

$$\tilde{\omega}_Q = \frac{1}{2}\left(\omega_R + \omega_Q - E_C/\hbar + \sqrt{\Delta^2 + 4g^2}\right) \ . \tag{2.40}$$

Eq. (2.38) is a fundamental result of circuit QED and deserves some time spent explaining it. In (2.36) there were two coupled modes, one linear and one with a cosine non-linearity, in (2.38), the cosine has been replaced by only second order non-linearities and the cavity has inherited some of the non-linearity of the junction. The frequency of the cavity depends on the number of excitations inside it and increases by $K_R = -\frac{E_C}{2\hbar}\left(\frac{g}{\Delta}\right)^4$ for each additional excitation. We also retrieve the anharmonicity of the Transmon $K_Q = -\frac{E_C}{\hbar}$. Note that the Transmon is much more anharmonic than the cavity, as is evident from the factor $\left(\frac{g}{\Delta}\right)^4$ which must be very small in the dispersive limit. In many cases this justifies neglecting the cavity non-linearity and limiting the Transmon ladder to its two lowest eigenenergies by replacing $\hat{a}$ and $\hat{a}^\dagger$ with $\hat{\sigma}^-$ and $\hat{\sigma}^+$. In that case,

$$\hat{H}_{\text{dispersive}} = \hbar\tilde{\omega}_R \hat{c}^\dagger \hat{c} + \hbar\frac{\tilde{\omega}_Q}{2}\hat{\sigma}^z + \hbar\frac{\chi_{RQ}}{2}\hat{c}^\dagger \hat{c}\hat{\sigma}^z. \tag{2.41}$$

We recover the coupling between cavity and qubit in the last term where $\chi_{RQ} = -\frac{2g^2 E_C}{\hbar\Delta(\Delta - E_C/\hbar)}$ is called the dispersive shift or cross-Kerr rate. This last term provides a good interpretation of the dispersive regime: the interaction strength between cavity and qubit is not sufficient to hybridise the two modes (the 'quton-phobit' regime) but is enough for each mode to 'feel' the presence of the other. Here, 'feeling' the presence of the other mode means that the cavity frequency is shifted by the state of the qubit (called the 'pull' of the qubit) or vice versa. So, to determine the state of the qubit, it is sufficient to determine the resonance frequency of the cavity. This is made easy with a vector network analyser which is able to quickly measure the response function of

the circuit at different frequencies. Moreover, because the interaction term $\hbar\frac{\chi_{RQ}}{2}\hat{c}^\dagger\hat{c}\hat{\sigma}^z$ commutes with the energy term of the qubit $\hbar\frac{\tilde{\omega}_Q}{2}\hat{\sigma}^z$, dispersive measurement of the qubit is naturally QND (Quantum Non-Demolition) as there is no exchange of energy between cavity and qubit. These details will become important later when we discuss experiments demonstrating explicit non-QNDness and quantum thermodynamics.

2.5 OPEN QUANTUM SYSTEMS

As is clear from the previous study of qubit control and readout, it is impossible to consider the qubits used in circuit QED as isolated quantum systems. They are in fact in constant interaction with their environment in both a coherent and incoherent manner. On the one hand, when the interaction is coherent and controlled, this is something useful, allowing us to access the quantum systems we design. On the other hand, when the interation is uncontrolled or incoherent, it can be detrimental to the objective of preserving and knowing the state of our system at all time. In this section we describe the dynamics of a qubit coupled to it's uncontrolled environment.

2.5.1 *Density Matrices*

Quantum mechanics accurately describes degrees of freedom isolated from their environment. When information about the quantum system starts to leak out to uncontrolled degrees of freedom, an observer with information about the supposedly isolated system only must consider that degree of freedom as becoming more and more classical. There is thus a continuous transition between the quantum state $|\psi\rangle$ of (2.24) determined by two real variables θ and ϕ, and a classical bit described by a single probability p of measuring the value "0" akin to the value $\frac{1+\cos\theta}{2}$. The density matrix introduced by Von Neumann in 1927, generally denoted by ρ, allows us to consistently describe quantum systems for which we only know partial information. For a pure state whose evolution is given by the Schrödinger equation, $\rho = |\psi\rangle\langle\psi|$. More generally though, a density matrix on a Hilbert space $\mathcal{H}$ is a hermitian, positive semi-definite operator of unit trace. In the basis $(|\lambda\rangle\,|\lambda \in \{1,\dots,\dim\mathcal{H}\})$ in which ρ is diagonal, $\rho = \sum_\lambda p_\lambda |\lambda\rangle\langle\lambda|$ and p_λ is the probability of obtaining the state $|\lambda\rangle$ after measurement. The expectation value of any operator $\hat{o}$ is given by

$$\langle\hat{o}\rangle_\rho = \mathrm{tr}\left[\rho\hat{o}\right] \ . \tag{2.42}$$

Finally, the equivalent of the Schrödinger equation for $|\psi\rangle$ is given by

$$\frac{\mathrm{d}\rho}{\mathrm{d}t} = -\frac{i}{\hbar}[\hat{H},\rho] \tag{2.43}$$

for the density matrix.

2.5.2 *Decoherence and energy-decay*

Let us focus now again on the description of a qubit. In full equivalence to Sec. 2.4.1 we can define a Bloch vector $\vec{u}_\rho = \left(\langle\hat{\sigma}^x\rangle_\rho \langle\hat{\sigma}^y\rangle_\rho \langle\hat{\sigma}^z\rangle_\rho\right)^T$, but whose norm is only max-

imised to 1 for a pure state, $\|\vec{u}_\rho\| \leq 1$. This gives us a pratical representation of the 'quantumness' of a state of a qubit: the further the Bloch vector is from the z-axis of the sphere, the less it can be totally described by the probability of its measurement outcomes along $\hat{\sigma}^z$. Being on the z-axis is mathematically equivalent to saying that the off-diagonal terms of ρ in the basis $(|0\rangle, |1\rangle)$ - the coherences - are 0. The characteristic time over which these coherences disappear (the rate at which the Bloch vector moves towards the $\hat{\sigma}^z$ axis) when the initially isolated quantum system is put in contact with its environment is called the decoherence time and is noted T_2. The decoherence time contains two contributions: the energy-decay time T_1 and the pure dephasing time T_ϕ related to T_2 by

$$\frac{1}{T_2} = \frac{1}{T_\phi} + \frac{1}{2T_1} \ . \tag{2.44}$$

T_ϕ is called the pure dephasing time, whereas T_1 measures the speed of energy tunneling between the two states $|0\rangle$ and $|1\rangle$. Note that T_ϕ has no classical counterpart, as there is no such thing as the phase of a superpostion in the classical case. This is not true for T_1 though, as a transition between two classical states of different energies separated by a potential barrier is possible, and can be activated by statistical fluctuations at non-zero temperature like the Arrhenius equation or Kramers escape for example [54]. In the language of quantum computing, T_1 is a measure of the bit-flip rate and T_2 a measure of the phase-flip rate. Because in the case of a bit-flip the energy of the qubit changes, there must be some energy exchange with the environment. This can happen in two ways: either the qubit gains energy at a rate $\Gamma_\uparrow$, or it can lose energy to the environment at rate $\Gamma_\downarrow$. Thus

$$\frac{1}{T_1} = \Gamma_1 = \Gamma_\uparrow + \Gamma_\downarrow \ . \tag{2.45}$$

The temperature of the bath to which the qubit is connected determines the balance between $\Gamma_\uparrow$ and $\Gamma_\downarrow$. At $T = 0$, $\Gamma_\uparrow = 0$ because the environment cannot give any energy to the qubit. As $T \to \infty$, $\frac{\Gamma_\uparrow}{\Gamma_\downarrow} \to 1^-$ because the bath becomes able to give and take energy equally. The ratio of the rates follow the detailed balance relation

$$\frac{\Gamma_\uparrow}{\Gamma_\downarrow} = e^{-\hbar\omega_Q/k_B T} \ , \tag{2.46}$$

where $k_B = 1.38 \times 10^{-23} \mathrm{J\,K^{-1}}$ is Boltzmann's constant and T is the temperature of the environment with which the qubit is interacting. $\Gamma_\uparrow$, $\Gamma_\downarrow$ and Γ_ϕ are thus the decay mechanisms which affect the qubit state when interacting with an uncontrolled bath. These concepts can be formalised through to arbitrary quantum systems, which is the subject of the next section.

2.5.3 *Lindblad master equation and Bloch equations*

An open quantum system in interaction with a number of uncontrolled degrees of freedom can often be accurately described by the Lindblad master equation [55]

$$\frac{\mathrm{d}\rho}{\mathrm{d}t} = -\frac{i}{\hbar}[\hat{H}, \rho] + \sum_i \gamma_i D[\hat{L}_i](\rho) \ , \tag{2.47}$$

where $\hat{H}$ is the Hamiltonian of the system and D is called the Lindblad superoperator. This equation holds under the Markov approximation. In other words the bath must be memoryless. This means that the correlation time of the bath must be much shorter than any of the dynamics of the quantum system with which it is interacting. Given a jump operator $\hat{L}$ acting on the quantum system

$$D[\hat{L}](\rho) = \hat{L}\rho\hat{L}^\dagger - \frac{1}{2}\rho\hat{L}^\dagger\hat{L} - \frac{1}{2}\hat{L}^\dagger\hat{L}\rho \ . \tag{2.48}$$

The first term of (2.47) corresponds to the deterministic evolution of the quantum state due to the Hamiltonian $\hat{H}$. The second term contains the description of the incoherent interaction with the bath modes. Each interaction channel i is given a rate γ_i at which information about the system leaks out into the environment through $\hat{L}_i$. Determining the correct jump operators $\hat{L}_i$ is thus critical in obtaining a correct decription of the open system dynamics.

It helps to have an example to understand the terms in more detail. We can consider a qubit which interacts with the environment through three channels: energy absorption, energy emission and dephasing at rates $\Gamma_\uparrow$, $\Gamma_\downarrow$ and Γ_ϕ respectively. The Lindblad master equation for this system can be written

$$\frac{\mathrm{d}\rho}{\mathrm{d}t} = -\frac{i}{\hbar}[\hat{H},\rho] + \frac{\Gamma_\phi}{2}D[\hat{\sigma}^z](\rho) + \Gamma_\downarrow D[\hat{\sigma}^-](\rho) + \Gamma_\uparrow D[\hat{\sigma}^+](\rho) \ . \tag{2.49}$$

We associate $\hat{\sigma}^+$ and $\hat{\sigma}^-$ to the energy absorption and emission respectively since they transform state $|1\rangle$ into $|0\rangle$ and vice versa. $\hat{\sigma}^z$ is associated with dephasing because it changes the sign of the superposition of $|1\rangle$ and $|0\rangle$: $\hat{\sigma}^z\frac{1}{\sqrt{2}}(|1\rangle + |0\rangle) = \frac{1}{\sqrt{2}}(|1\rangle - |0\rangle)$. It will be useful to write down (2.49) for the Rabi Hamiltonian $\hat{H} = \hbar\frac{\Omega}{2}\hat{\sigma}^y$ as a function of the coordinates of the Bloch vector. We obtain the Bloch equations from NMR (Nuclear Magnetic Resonance)

$$\frac{\mathrm{d}}{\mathrm{d}t}\begin{pmatrix}\langle\hat{\sigma}^x\rangle\\ \langle\hat{\sigma}^y\rangle\\ \langle\hat{\sigma}^z\rangle\end{pmatrix} = \begin{pmatrix}-\Gamma_2 & 0 & \Omega\\ 0 & -\Gamma_2 & 0\\ -\Omega & 0 & -\Gamma_1\end{pmatrix}\begin{pmatrix}\langle\hat{\sigma}^x\rangle\\ \langle\hat{\sigma}^y\rangle\\ \langle\hat{\sigma}^z\rangle\end{pmatrix} + \begin{pmatrix}0\\ 0\\ \Gamma_\uparrow - \Gamma_\downarrow\end{pmatrix} \ , \tag{2.50}$$

which describe Rabi oscillations of the Bloch vector around the y-axis at the frequency $\Omega_R = \sqrt{\Omega^2 - \frac{(\Gamma_1-\Gamma_2)^2}{4}}$ decaying at a rate $\Gamma_R = \frac{\Gamma_2+\Gamma_1}{2}$. A detailed solution to these equations is given in appendix A.

2.5.4 *Input - Output theory of a cavity connected to a transmission line*

So far, as an example of an open quantum system, we have studied a qubit interacting with its environment whose density matrix follows the evolution given by the Lindblad master equation. The modes of a microwave cavity can also be described using the Lindblad master equation. In that case, for a mode of frequency ω_R described by an annihilation operator $\hat{a}$ interacting with a bath at zero temperature, the master equation reads

$$\frac{\mathrm{d}\rho}{\mathrm{d}t} = -\frac{i}{\hbar}[\hat{H},\rho] + \kappa D[a](\rho) \ , \tag{2.51}$$

where ρ is the density matrix of the mode over the infinite dimension Hilbert space spanned by the Fock states $|n\rangle$ of the mode, and κ is the loss rate to the environment. When the cavity is connected to a transmission line, the loss rate to the environment can be separated into two components $\kappa = \kappa_i + \kappa_c$. The first, κ_i, corresponds to the intrinsic loss of the cavity due to uncontrolled sources (surface losses, uncontrolled radiative losses...). κ_c is the rate at which the cavity decays into the transmission line. The main difference between the two cases is that the information on the cavity that leaks into the transmission line can in principle be at least partially retrieved, whereas this is not possible for the other decay channels to which we do not have access. This observation also suggests that we can send signals into the cavity through the same tranmission line decay channel. Input-output theory allows us to formalise these thoughts. Using many of the same techniques used to derive the Lindblad equation [56] we can derive the quantum Langevin equation for the cavity operator $\hat{a}$ in the Heisenberg picture [57]

$$\frac{\mathrm{d}\hat{a}}{\mathrm{d}t} = -i\omega_R\hat{a} - \frac{\kappa}{2}\hat{a} + \sqrt{\kappa_c}\hat{a}_{\mathrm{in}} \ . \tag{2.52}$$

In the above equation $-i\omega_R\hat{a}$ corresponds to the evolution of $\hat{a}$ given by the Heisenberg equation of motion. The term $-\frac{\kappa}{2}\hat{a}$ represents the decay of the field inside the cavity given by the decay channels explicited above. The last term, introduces the ability for an incoming propagating field $\hat{a}_{\mathrm{in}}$ in the transmission line to interact with the cavity mode. Note that $\hat{a}_{\mathrm{in}}$ has units of $\sqrt{\mathrm{Hz}}$ and only describes the part of the transmission line field propagating towards the cavity. A time-reversed Langevin equation considering the field propagating away from the cavity can equally be derived

$$\frac{\mathrm{d}\hat{a}}{\mathrm{d}t} = -i\omega_R\hat{a} + \frac{\kappa}{2}\hat{a} - \sqrt{\kappa_c}\hat{a}_{\mathrm{out}} \ , \tag{2.53}$$

such that we obtain the input-output relation

$$\hat{a}_{\mathrm{out}} - \hat{a}_{\mathrm{in}} = \sqrt{\kappa_c}\hat{a} \tag{2.54}$$

showing how all three operators are connected. Conveniently, if the cavity has multiple ports, these equations can be generalised by adding a term $\sqrt{\kappa_{c,j}}\hat{a}_{\mathrm{in},j}$ for each additional port in (2.52) and (2.53) and making sure (2.54) holds true for each port j. We also need to update our definition of the total loss rate $\kappa = \kappa_i + \sum_j \kappa_{c,j}$

We can connect the operator relations above to the response of the cavity seen by a vector network anaylser through the transmission lines by assuming the operators are classical ($\hat{a} \to \alpha$) and going to frequency space [58]

$$S_{jj}(\omega) = \frac{\alpha_{\mathrm{out},j}}{\alpha_{\mathrm{in},j}} = \frac{2\kappa_{c,j} - \kappa + 2i(\omega - \omega_R)}{\kappa - 2i(\omega - \omega_R)} \ , \tag{2.55}$$

$$S_{kj}(\omega) = \frac{\alpha_{\mathrm{out},k}}{\alpha_{\mathrm{in},j}} = \frac{2\sqrt{\kappa_{c,j}\kappa_{c,k}}}{\kappa - 2i(\omega - \omega_R)} \ . \tag{2.56}$$

Finally, we define the quality factor of any loss mechanism l as $Q_l = \frac{\omega_R}{\kappa_l}$. For a cavity, the total quality factor $Q = \frac{\omega_R}{\kappa}$ is a measure of the characteristic number of times the photon in the resonator 'bounces' back and forth between both sides of the box before

exiting the cavity through some mechanism. We can rewrite the expressions for $S_{jj}(\omega)$ and $S_{kj}(\omega)$ as a function of the quality factors defined above

$$S_{jj}(\omega) = \frac{\left(2\frac{Q}{Q_{c,j}} - 1\right) + 2iQ\frac{\omega-\omega_R}{\omega_R}}{1 + 2iQ\frac{\omega-\omega_R}{\omega_R}} , \tag{2.57}$$

$$S_{kj}(\omega) = \frac{2Q}{\sqrt{Q_{c,j}Q_{c,k}}} \cdot \frac{1}{1 + 2iQ\frac{\omega-\omega_R}{\omega_R}} . \tag{2.58}$$

A standard experiment to calibrate a cQED setup is to measure the reflection off or transmitted through a microwave cavity. For low loss cavities with ports 1 and 2, S_{11} only contains information about ω_R and κ in the phase ($|S_{11}| \approx 1$), whereas information can be extracted from both the absolute value and the phase in the case of a measurement in transmission of S_{21}.

2.6 EXPERIMENTAL METHODS OF CIRCUIT QED

2.6.1 *Cryogenics*

Working with superconductors means working at temperatures below the critical temperature T_c of the metals involved. Given that the junctions are made out of aluminium, it is imperative make sure the device is below 1 K at all times. Additionally, it is desirable to lower the temperature as far as possible, to make sure that thermal effects are not dominant and that we do not need to go through exhaustive state preparation to obtain a pure state. Ideally we should be in the regime

$$T_{\text{fridge}} \ll \frac{\hbar\omega}{k_B} , \tag{2.59}$$

where $k_B = 1.38 \times 10^{-23}\,\text{J K}^{-1}$ is Boltzmann's constant, ω is the characteristic frequency of the system and T_{fridge} is the temperature at which we operate the device. For $\omega/2\pi$ in the range 4 GHz to 8 GHz, the temperature needs to be in the mK range. For frequencies much lower than this, we will have to resort to state preparation techniques if we want a pure state. To achieve these low temperatures, we place our ciruits at the base plate of a dilution refrigerator, a picture of which is shown in Fig. 2.7. Dry dilution refrigerators function by combining two different cryogenic technologies. A pulse tube, which uses the compression and decompression cycle of helium to take heat away from the fridge, initially brings the temperature to ~ 4 K. To bring the temperature to below 1 K, the thermodynamic properites of the two phases of a ^{3}He-^{4}He mixture (at the lowest temperature, one phase is almost pure ^{3}He, the other is around 93% ^{4}He) are exploited. Passing ^{3}He rich phase through the dilute phase in the mixing chamber is an endothermic process which happens at the base plate of the dilution refrigerator, bringing the temperature down to between 10 and 40 mK. Because the cooling power of the mixing chamber is small ($\sim 14\,\mu$W at 20 mK), the refrigerator is organised into several stages so that each level can be well thermal isolated from the others. The stages are shown in Fig. 2.7. The cold side of the pulse tube cryocooler is attached to the 4 K stage and provides a cooling power of around 1 mW. Below it we find the

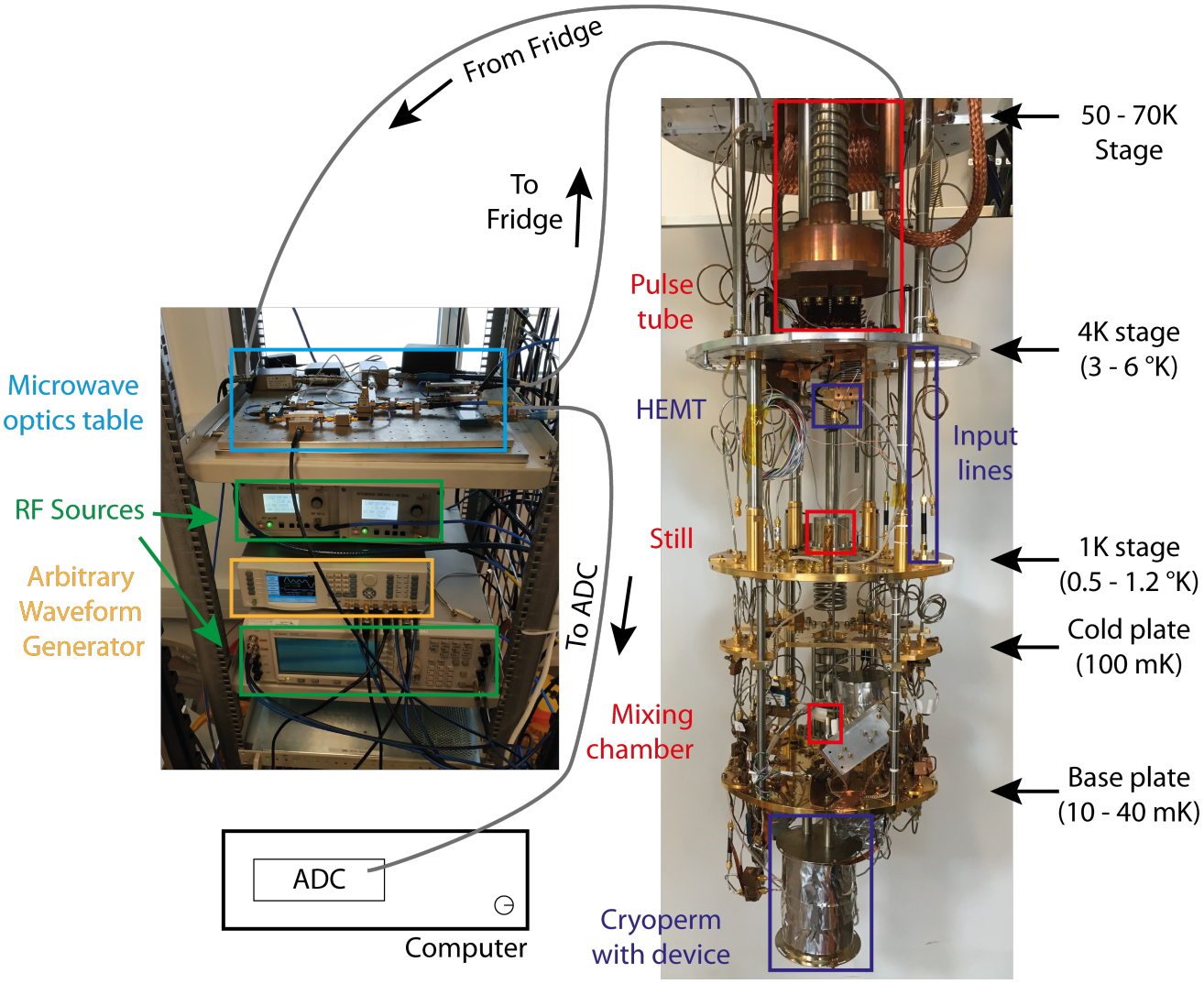

Figure 2.7: Typical circuit QED experimental setup. Signals generated by the RF sources and AWG (Arbitrary Waveform Generator) are mixed on the microwave optics table before being sent to the dilution refrigerator. They are attenuated and reach the base plate of the fridge where they interact with the qubit and cavity. Signals coming from the device are amplified and routed up the different stages, then sent to the microwave optics table again. The ouput signal is down-converted and sent to the ADC (Analog to Digital Converter) for acquisition.

1 K stage attached to the still filled with liquid ^{4}He. Below this, at the 100 mK stage, downwards flowing warm ^{3}He is cooled through heat exchangers by upwards flowing cold ^{3}He. Finally, the lowest stage is the mixing chamber stage. To prevent any thermal shorts the dilution refrigerator is operated under vacuum and the different stages are physically connected by heat switches which can be turned on and off during cooldown, warmup or standard operation. Different shields (not present in Fig. 2.7) protect lower stages from heating up because of the radiation of the higher temperature stages.

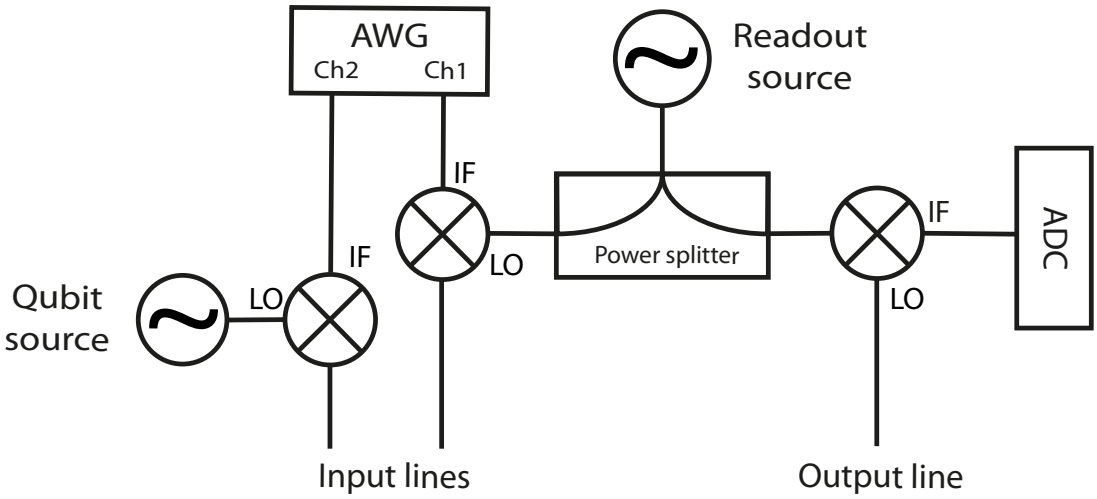

Figure 2.8: Schematic of the basic structure of the microwave optics table. The circles with crosses are single sideband mixers.

2.6.2 *Qubit control and signal acquisition*

We control the devices placed at the base plate of the dilution refrigerator with microwave frequency signals prepared at room temperature. Initially, carrier frequencies ($\sim$ GHz) are generated by RF sources shown in Fig. 2.7 and drawn schematically in Fig. 2.8. These signals are continuous waveforms and need to be amplitude modulated to obtain time resolved qubit control. For this we use high frequency Arbitary Waveform Generators (AWGs) which provide arbitrary signals at lower frequencies ($\sim$ MHz). On the microwave optics table these signals can be split and mixed depending on the different experimental requirements. Mixing the RF source output (called local oscillator - LO) with the AWG signal (called intermediate frequency - IF) gives us a modulated signal at RF frequencies[4] which is sent into the fridge (see Fig. 2.8). Signals propagating down the input lines are then attenutated down to the single excitation level inside the dilution refrigerator (more about this in Chapter 5) before interacting with the device placed inside a cryoperm shield like the one visible in Fig. 2.7. Readout signals coming from the device are routed up through the dilution refrigerator stages and are amplified above the room temperature noise at the entrance of the ADC by a High Electron Mobility Transitor amplifier (HEMT) at the 4K stage. At room temperature, the readout signal is down-converted using the same local oscillator as the input readout pulse was generated with to ensure phase stability. The now low frequency signals ($\sim$ MHz) are then acquired by a Analog to Digital Converter (ADC) at a high sampling rate to be treated numerically on a computer.

4 It is possible to do without this step for low frequencies which can be generated directly by the AWG. The Fluxonium qubits measured in this thesis were indeed often driven directly by signals generated by an Zurich Instruments HDAWG. AWGs at GHz frequencies are available but still expensive.

2.6.3 *Heterodyne detection*

We know from Sec. 2.4.3 that the cavity frequency changes depending on the qubit state. For a measurement in reflection and in the low loss limit $\kappa_c = \kappa$, this means that the phase of a fixed frequency signal at $\omega_{\mathrm{RO}} \approx \tilde{\omega}_R$ reflected off the readout cavity will depend on the qubit state. For a measurement in transmission, both the phase and amplitude can change. Measuring these changes is the way we determine the quantum state of the qubit(s). So as to consistently use the same vocabulary through the thesis, we present here the principle of the readout of the qubit state.

To measure the state of the qubit, we want to either monitor the reflection off the input port or the transmission between the input and output ports depending on the experimental setup. To do this, we generate a square pulse with the AWG modulated at the frequency ω_{IF} and mix it with a tone from an RF source at frequency $\omega_{\mathrm{RO}} + \omega_{\mathrm{IF}}$. In the case of a single sideband mixer which selects only the lower sideband, the square pulse sent into the experiment input lines is now modulated at frequency ω_{RO}. This pulse is called the readout pulse and its phase and amplitude are set by the control parameters of the instruments used to generate it. Physically it corresponds to a time dependent modulation of the electric field, or equivalently voltage, between the two conductors of a transmission line. Within a time defined by the rectangular envelope, the amplitude of the voltage difference at a given point along the input transmission lines can be described by

$$V_{\mathrm{in}}(t) = I_{\mathrm{in}} \cos(\omega_{\mathrm{RO}} t) + Q_{\mathrm{in}} \sin(\omega_{\mathrm{RO}} t) = V_{\mathrm{in}} \cos(\omega_{\mathrm{RO}} t + \phi_{\mathrm{in}}) = \mathrm{Re}\left[V_{\mathrm{in}} e^{i\omega_{\mathrm{RO}} t + i\phi_{\mathrm{in}}}\right] , \tag{2.60}$$

where I_{in} and Q_{in} are the amplitudes of the in and out of phase quadratures of the oscillating field and $V_{\mathrm{in}} = \sqrt{I_{\mathrm{in}}^2 + Q_{\mathrm{in}}^2}$ and $\phi_{\mathrm{in}} = \arctan \frac{Q_{\mathrm{in}}}{I_{\mathrm{in}}}$. We have some freedom on the choice of the global phase reference, so the phase ϕ_{in} only makes sense when comparing it to some other known oscillator. A convenient representation of $V(t)$ in the frame rotating at a frequency ω_{RO} is the IQ-plane (also known as Fresnel plane) shown in Fig. 2.9. The x-axis is given by the magnitude of the I quadrature, and the y-axis by the Q quadrature. We have represented the uncertainty on I_{in} and Q_{in} due to noise by a circle surrounding their mean values. This noise can be of classical origin, but there exists a fundamental limit on the minimum noise because of the Heisenberg uncertainty relation. In this representation, a change of phase of the oscillation corresponds to a rotation around the origin and a change of amplitude to a change along the radial direction. We can understand the scattering parameters $S(\omega_{\mathrm{RO}})$ as relating the voltage wave $V_{\mathrm{in}}(t)$ in the input line to the outgoing one $V_{\mathrm{out}}(t)$ in the output lines as [8]

$$V_{\mathrm{out}}(t) = S(\omega_{\mathrm{RO}}) V_{\mathrm{in}}(t) \ . \tag{2.61}$$

If the qubit's state does not change during the measurement of the scattering coefficient, $S(\omega_{\mathrm{RO}})$ can be chosen as $S_{11}(\omega_{\mathrm{RO}})$ or $S_{21}(\omega_{\mathrm{RO}})$ depending on the experimental setup. In the most general case though, the qubit state is not stationary, and we refer to $S(\omega_{\mathrm{RO}})$ as the transmission or reflection coefficient only. Thanks to this, we can see

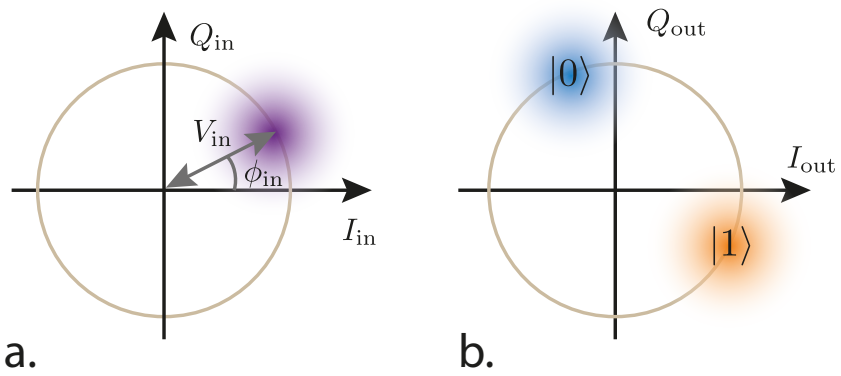

Figure 2.9: IQ-plane representation of the propagating voltage. a. $V_{\text{in}}(t)$ described by its I_{in} and Q_{in} coordinates in the frame rotating at ω_{RO}. The beige circle denotes all the possible mean IQ-coordinates for a wave of amplitude $|V_{\text{in}}|$. The purple histogram represents the distribution of IQ quadratures one would obtain if repeatedly measuring the the wave of amplitude $|V_{\text{in}}|$. b. Outgoing field at $\omega_{\text{RO}} \approx \tilde{\omega}_R$ after reflecting off a lossless cavity containing a single qubit. The phase of the outgoing field depends on the state of the qubit inside the cavity.

that $V_{\text{out}}(t)$ will obtain some phase and amplitude relative to $V_{\text{in}}(t)$ depending on the state of the qubit, due to presence of the scattering parameter $S(\omega_{\text{RO}})$ in (2.61). The distribution of $V_{\text{out}}(t)$ in the IQ-plane is thus different whether the qubit is in $|0\rangle$ or $|1\rangle$ (see Fig. 2.9).

We can determine the I and Q quadratures experimentally of the outgoing signal through heterodyne measurement. First the signal coming from the experiment is down-converted to MHz frequencies by demodulating using the local oscillator signal provided by the split RF source (see Fig. 2.8). By power splitting the same RF source for modulation and demodulation we preserve the phase coherence between the modulated input signal and demodulated output signal up to the phase variations in the cables. The down-converted signal V_{demod} is now at the frequency of the AWG waveform ω_{IF} (often around 50 MHz). Although the period of 20 ns for $\omega_{\text{IF}} = 50\,\text{MHz}$ modulation is longer than it would be for signals in the GHz range, it is not usually a limiting factor for resolving the qubit dynamics. The MHz signal is then digitized by an ADC at a sampling rate of around 1GS/s. At this point, the digitised signal is compared numerically with the voltage of a local oscillator $V_{\text{LO}}^{\phi}(t)$ whose phase ϕ and amplitude V_{LO} are well known and whose frequency is equal to ω_{IF}

$$V_{\text{LO}}^{\phi}(t) = V_{\text{LO}} \cos(\omega_{\text{IF}} t + \phi) \ . \tag{2.62}$$

If the readout pulse is square, then, by taking $T = \frac{2\pi}{\omega_{\text{IF}}}$ the period of the downconverted signal frequency, we define

$$I_{\text{out}}(t) = \frac{2}{T} \int_0^T V_{\text{demod}}(t) V_{\text{LO}}^{0}(t) \mathrm{d}t \ , \tag{2.63}$$

$$Q_{\text{out}}(t) = \frac{2}{T} \int_0^T V_{\text{demod}}(t) V_{\text{LO}}^{\frac{\pi}{2}}(t) \mathrm{d}t \ . \tag{2.64}$$

In general, the pulse may not be square or the qubit state not stationary, so $I_{\text{out}}(t)$ and $Q_{\text{out}}(t)$ can vary in time. In that case, because the integral must be taken over a full period of the oscillation, the minium time step over which the values of $I_{\text{out}}(t)$ and $Q_{\text{out}}(t)$ are decorrelated is T.

Of course, the noise in the experiment, whether quantum or classical, limits our ability to discriminate the qubit state owing to a possible overlap between distributions in the IQ-plane shown in Fig. 2.9. It is thus important to gain some statistics about the values of I_{out} and Q_{out}. We can do this by measuring an entire measurement record in the IQ-plane $\{Z^n_{\text{out}} = I^n_{\text{out}} + iQ^n_{\text{out}} | n \in \{0, \ldots, N-1\}\}$ where

$$I^n_{\text{out}} = \frac{2}{T}\int_0^T V_{\text{out}}(nT+t)V^0_{\text{LO}}(nT+t)\mathrm{d}t \ , \tag{2.65}$$

$$Q^n_{\text{out}} = \frac{2}{T}\int_0^T V_{\text{out}}(nT+t)V^{\frac{\pi}{2}}_{\text{LO}}(nT+t)\mathrm{d}t \ . \tag{2.66}$$

This comes down to sending a readout pulse of duration $N \times T$ and recording the noisy values of I and Q at each period of the IF. By taking the average $\bar{Z}_{\text{out}} = \bar{I}_{\text{out}} + i\bar{Q}_{\text{out}}$

$$\bar{I}_{\text{out}} = \frac{1}{N}\sum_{n=0}^{N-1} I^n_{\text{out}} \ , \tag{2.67}$$

$$\bar{Q}_{\text{out}} = \frac{1}{N}\sum_{n=0}^{N-1} Q^n_{\text{out}} \ , \tag{2.68}$$

we can reduce the noise of the readout significantly. To reduce the noise further, experiments and the subsequent readout pulses are repeated $M \sim 10^4 - 10^6$ times. In Fig. 2.10a. we show a histogram of the values of $\bar{Z}_{\text{out}}$ in the IQ-plane obtained from the heterodyne measurement of a readout pulse transmitted through a cavity coupled to a single qubit. The units of the axes are mV as this corresponds to the units used by the acquisition card. When we can distinguish the distributions attributed to the qubit states $|0\rangle$ and $|1\rangle$, as is the case in Fig. 2.10a., we say that we have a single-shot measurement of the qubit within the readout time defined by the duration of the pulse. Mathematically, this can be expressed by

$$\sigma_{\text{IQ}} < \left| \bar{Z}^{|0\rangle}_{\text{out}} - \bar{Z}^{|1\rangle}_{\text{out}} \right| \ , \tag{2.69}$$

where σ_{IQ} is the measurement duration dependent standard deviation of the distributions corresponding to each qubit state $|i\rangle$ and $\bar{Z}^{|i\rangle}_{\text{out}}$ is the center of the distribution if the qubit state is prepared perfectly in state $|i\rangle$.

Often, the histograms of $\bar{Z}_{\text{out}}$ are bipartite because there are only two qubit states. In that case, all the information about the qubit population is contained along a line going through $\bar{Z}^{|0\rangle}_{\text{out}}$ and $\bar{Z}^{|1\rangle}_{\text{out}}$. By finding the principal axis of the distribution of results in the IQ-plane by diagonalising its covariance matrix, we can rotate the distribution around the centre of the IQ-plane by multiplying $\bar{Z}_{\text{out}}$ by some phase factor so that this principal axis lies parallel to the x-axis. Such a transformation is shown in Fig. 2.10b. Notice how the lobes of the single quadrature distributions in the subpanels are now

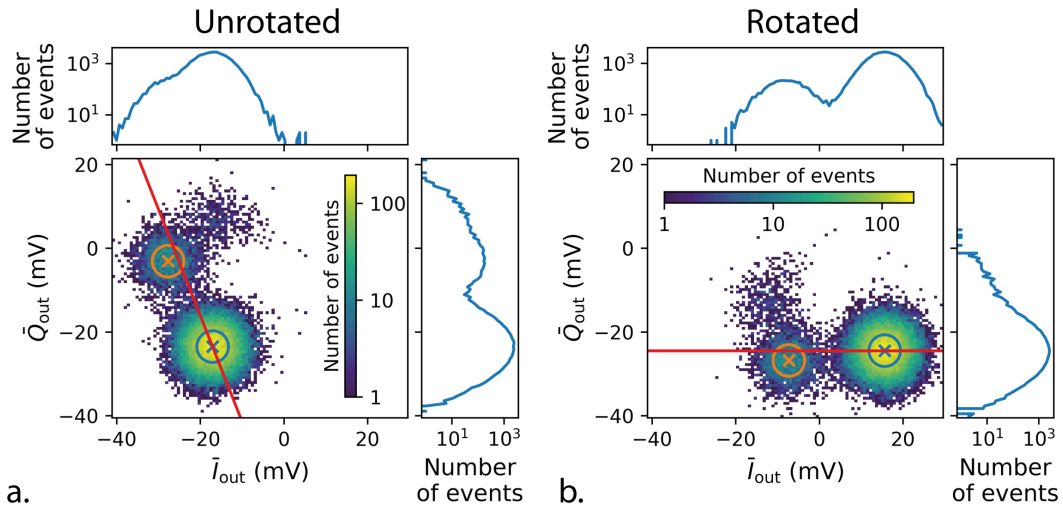

Figure 2.10: Histograms of the distribution of $\bar{Z}_{\text{out}}$ for 40000 repetitions of a 700 ns square readout pulse transmitted through a cavity dispersively coupled to a Transmon. a. (Main panel) distribution of the values of $\bar{Z}_{\text{out}}$ in the IQ-plane as obtained directly by the procedure described above. The red line corresponds to the principal axis of the distribution, the blue and orange crosses to $\bar{Z}_{\text{out}}^{|0\rangle}$ and $\bar{Z}_{\text{out}}^{|1\rangle}$ respectively. The coloured circles extend a distance σ_{IQ} around each $\bar{Z}_{\text{out}}^{|i\rangle}$. The cloud of points in the top right of the distribution corresponds to higher excited states of the qubit. (Minor panels) Marginals of the distributions of $\bar{I}_{\text{out}}$ (top) and $\bar{Q}_{\text{out}}$ (right). b. Same as figure a, but with the results rotated so the principal axis of the distribution coincides with the x-axis.

better defined. The information about the state of the qubit is almost entirely along the $\bar{I}_{\text{out}}$ axis in Fig. 2.10b., whereas is it is distributed along both quadratures in Fig. 2.10a. The slight discrepancy between the principal axis and the line going through $\bar{Z}_{\text{out}}^{|0\rangle}$ and $\bar{Z}_{\text{out}}^{|1\rangle}$ is due to the presence of the higher excited state of the Transmon. Thus, note that in general, for IQ-plane distributions made of many Gaussian distributions, the principal axis may not be aligned with the axis along which changes happen to the qubit in the experimental pulse sequence, but often rotating the data helps. In graphs where a single pulse sequence parameter P is varied (time, amplitude, phase...), and the axes are not calibrated to the number of photons in the cavity, we will label the y-axis with the label "I (mV)" showing the units of the acquisition card. This is to be understood as showing the average $\langle \bar{I}_{\text{out}} \rangle$ of the outgoing I quadrature taken over all the realisations of the experiment where P is fixed and after the readout results have been rotated so the principal axis is aligned with x. Because the rotation around the origin is unphysical, the absolute offset of the value of $\langle \bar{I}_{\text{out}} \rangle$ in mV is also irrelevant and cannot be compared from experiment to experiment. Furthermore the scale of the variations of the measurement signal along $\langle \bar{I}_{\text{out}} \rangle$, depend strongly on the settings of the AWG and the experimental setup. They should therefore also not be compared between experiments.

2.7 CONCLUSION

By introducing microwave cavities and Josephson junctions we were able to present harmonic oscillators and the Josephson Hamiltonian as the basis for circuit QED. We used the methods of circuit quantisation to derive some basic results concerning the Transmon qubit, Rabi oscillations and dispersive readout. As these calculations showed us, it is necessary to let the quantum system interact with the environment so we can control the qubit coherently and determine its state. We took into account the losses ensued because of this through the Lindblad master equation. In the last part of the chapter, we gave a short introduction to the experimental techniques of circuit QED. Signals are generated and manipulated at room temperature, interact with the devices at the base plate of a dilution refrigerator and information about the qubit state is determined by a homodyne measurement of the outgoing field at room temperature. In the next chapter we will look at how to design effective two-level systems which are intrinsically protected to the noise sources we introduced to control and readout the qubit state.

3

THE FLUXONIUM, A PROTECTED QUBIT

Now we have established the basics of superconducting circuits and their description. It's time to explore in detail what makes a useful qubit. This chapter will, in a sense, follow the historical evolution of a subset of superconducting qubits - inductively shunted Josephson junctions - whose figurehead is the Fluxonium qubit. Chronology shouldn't be seen as the only factor linking the different discussions below though. Indeed, we will see that a modern take, reinterpreting successive inventions as a quest for extended decoherence times, convieniently and elegantly links the different qubits in this chapter. We start by exposing the advantages and limitations of the Transmon as an introduction to the concepts we will need throughout. In a second part we focus on Fluxonium, the centrepiece of this chapter. The intuition and theory developped here will be essential to understand the experimental results of the following chapters. The chapter ends with a discussion about protected qubits and how they can be implemented using dual-mode circuits like the "$0-\pi$" qubit.

3.1 BEYOND THE TRANSMON

3.1.1 *Protection from Decoherence*

Let's delve deeper into the properties of the Transmon qubit in order to illustrate the reasons why it is so ubiquitous, yet imperfect. Consider again the harmonic oscillator of Eq. (2.6). The expectation values $\left\langle \hat{Q}^2 \right\rangle_\psi$ and $\left\langle \hat{\Phi}^2 \right\rangle_\psi$ are measures of the variance of the charge and flux variables respectively, giving a measure of the spread of their probability distribution in the state $|\psi\rangle$. Intuitively, $\sqrt{\left\langle \hat{\Phi}^2 \right\rangle_\psi}$ is the quantum mechanical analog of the average height of a classical skater in a halfpipe. In the energy basis

$$\left\langle \hat{Q}^2 \right\rangle_n = \frac{\hbar}{2Z}(2n+1) \ , \tag{3.1}$$

$$\left\langle \hat{\Phi}^2 \right\rangle_n = \frac{\hbar Z}{2}(2n+1) \ . \tag{3.2}$$

Now say that in the Transmon Hamiltonian we expand the $\cos(\hat{\varphi})$ to second order, without à priori justifying the expansion. We can in this case express the characteristic impedance

$$Z = \sqrt{\frac{L_j}{C}} = \frac{R_Q}{\pi}\sqrt{\frac{2E_C}{E_J}}, \tag{3.3}$$

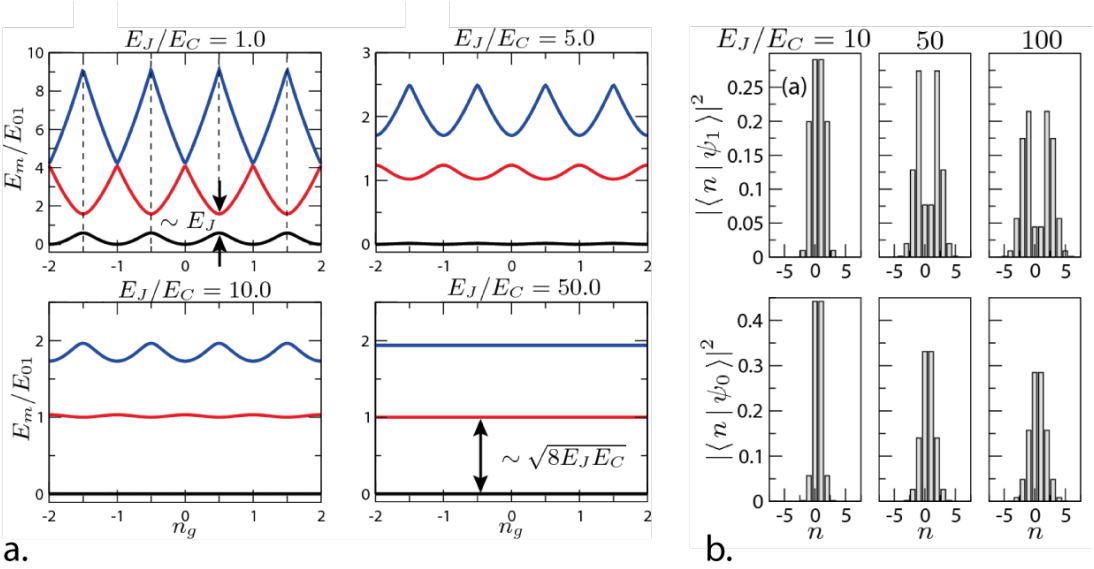

Figure 3.1: Figures adapted from [18]. Eigenenergies for the first three levels of the Transmon Hamiltonian 3.6 as a function of the offset charge n_g for different ratios E_J/E_C. Energies are given in units of the transition energy E_{01}, evaluated at the point $n_g = 0.5$. Notice how as the ratio E_J/E_C becomes large the eigenenrgies dependent less and less on the offset charge. b. The two lowest energy eigenstates $|\psi_0\rangle$ and $|\psi_1\rangle$ represented in the charge basis for $n_g = 0.5$. Notice how the eigenstates become more and more delocalised as E_J/E_C increases.

where $R_Q = \frac{h}{4e^2} = 6.45\,\mathrm{k}\Omega$ is the superconducting resistance quantum which will come in useful later. Replacing Z in the variances above we obtain

$$\sqrt{\left\langle \hat{Q}^2 \right\rangle_n} = \frac{e}{\left(\frac{2E_C}{E_J}\right)^{1/4}} \sqrt{2n+1} \Leftrightarrow \sqrt{\langle \hat{n}^2 \rangle_n} = \frac{1}{2\left(\frac{2E_C}{E_J}\right)^{1/4}} \sqrt{2n+1}\,, \tag{3.4}$$

$$\sqrt{\left\langle \hat{\Phi}^2 \right\rangle_n} = \frac{\Phi_0}{2\pi} \left(\frac{2E_C}{E_J}\right)^{1/4} \sqrt{2n+1} \Leftrightarrow \sqrt{\langle \hat{\varphi}^2 \rangle_n} = \left(\frac{2E_C}{E_J}\right)^{1/4} \sqrt{2n+1}\,. \tag{3.5}$$

In the case where $E_J > 50E_C$ the average phase excursion is much smaller than 2π for n small, which justifies our expansion self-consistently. Moreover, the spread of $\hat{n}$ increases with the ratio E_J/E_C, suggesting that the charge information is delocalised in the lowest energy states of the transmon (see Fig. 3.1b). Of course, this is just another way of expressing the Heisenberg uncertainty relation between two conjugate operators. If the phase $\hat{\varphi}$ is localised then the number of Cooper paires $\hat{n}$ must be delocalised. It is critical that the wavefunction be spread over multiple charge modes to protect it from dephasing: the environment is not able to determine the state of the Transmon by a measurement of the charges within the islands [59]. Equivalently, and taking the historical perspective, the delocalisation of the state across many charge modes gives the Transmon exponential insensitivity to charge noise [18].

To understand this, recall the Hamiltonian of 2.19 which took into account the effect of an external electric potential on the Josephson junction through the term n_g

$$\hat{H} = 4E_C(\hat{n} - n_g)^2 - E_J \cos\hat{\varphi}\,. \tag{3.6}$$

Whilst accounting for n_g was not necessary to understand the level structure of the Transmon, it is critical for understanding the effect of charge noise on decoherence. Indeed, whilst the average value of n_g can be controlled using a voltage bias (see Fig. 2.6 for example), fluctuations of the electrochemical potential around the qubit are uncontrolled and are repercussed as fluctuations δn_g of n_g around its average value. We can calculate the effect of variations of n_g on the qubit coherence Γ_ϕ to first order using the formula

$$\Gamma_\phi \propto \left|\frac{\partial \omega_q}{\partial n_g}\right|^2 , \tag{3.7}$$

which is to say that the qubit frequency should be first order insensitive to the noise. In the case where E_C is comparable to or larger than E_J, the energy eigenstates of (3.6) are very close to eigenstates of the charge operator. At the sweet spot $n_g = 0.5$, and because of the non-zero tunneling rate given by the cosine term, the charge eigenstates $|n=0\rangle$ and $|n=1\rangle$ hybridise into the energy eigenstates $|\pm\rangle = \frac{1}{\sqrt{2}}|n=0\rangle \pm |n=1\rangle$ [60]. We calculate the derivative of the Hamiltonian with respect to the offset charge

$$\frac{\partial \hat{H}}{\partial n_g} = -8E_C(\hat{n} - n_g) , \tag{3.8}$$

so that

$$\begin{aligned}\left|\frac{\partial \omega_q}{\partial n_g}\right|^2 &= \frac{1}{\hbar^2}\left|\langle +|\frac{\partial \hat{H}}{\partial n_g}|+\rangle - \langle -|\frac{\partial \hat{H}}{\partial n_g}|-\rangle\right|^2 \\ &= \frac{1}{\hbar^2}|-8E_C(\langle +|\hat{n}-n_g|+\rangle - \langle -|\hat{n}-n_g|-\rangle)|^2 = 0 , \text{ for } n_g = 0.5 ,\end{aligned} \tag{3.9}$$

because each expectation value vanishes independently. The fact that the qubit frequency is first order insensitive to charge noise is clearly visible in Fig. 3.1a. When $E_J/E_C = 1$, a smooth minimum of the transition frequency is visible at $n_g = 0.5$. In fact, the ability to set n_g to 0.5 using an on chip gate was a major innovation from the Saclay team when they developped the Quantronium qubit [61]. The previous Cooper-Pair Box (CPB) qubit, on which the first coherent measurements were demonstrated ([21]) only showed coherence times of the order of a few ns compared to the µs times exhibited by Quantronium. When $E_J > 50E_C$ the charge noise becomes irrelevant, as the energy eigenstates are no longer very sensitive to the value of n_g because of their spread in charge space.

$$\left|\frac{\partial \omega_q}{\partial n_g}\right|^2 = |-8E_C(\langle \phi_{\text{ground}}|\hat{n}-n_g|\phi_{\text{ground}}\rangle - \langle \phi_{\text{excited}}|\hat{n}-n_g|\phi_{\text{excited}}\rangle)|^2 = 0 , \ \forall n_g , \tag{3.10}$$

because, again, each expectation value vanishes independently. Indeed, the expectation value of $\hat{n}$ is equal to n_g for the two lowest energy eigenstates in the harmonic limit.

It is interesting from a historical point of view to clarify that the Quantronics team had in 2002 already understood that increasing E_J would solve the problem of charge noise: "The amplitude of the charge noise is in agreement with measurements of $1/f$

charge noise, and its effect could be minimized by increasing the E_J/E_{CP} ratio" [61]. The issue at the time was the inability to readout the qubit state if the ratio was too large. It was thus the idea of coupling the qubit to a cavity in 2004 [16], leading to the dispersive readout scheme, which truely allowed the development of the Transmon.

3.1.2 *Limitations of the Transmon*

Since it's inception, the Transmon qubit has received the lion's share of research on superconducting circuits. It's popularity can be traced back to it's insensitivity to charge noise, the simplicity of it's fabrication, the ease of state readout and the availability of exact yet simple mathematical formulas describing it's behaviour. State of the art Transmons can achieve T_1 and T_2 in the range $100 - 500\,\mu s$ [62]. This improvement from the µs level in the first Transmon experiments [63] can be attributed to a single generic mechanism: the reduction of environmental noise sources.
Consider $H = A\hat{O}\hat{X}$ the Hamiltonian coupling the Transmon to an external energy bath. $\hat{O}$ is a dimensionless qubit operator like $\hat{n}$ or $\hat{\varphi}$ for example. The physical process to which the (dimension-full) noise operator $\hat{X}$ is coupled - a current, a voltage - is encapsulated by the constant A which has a certain dimensionality. The energy decay rate of the qubit into the bath is given by

$$\Gamma_{1\to 0} = \frac{A^2}{\hbar^2}\left|\langle 0|\hat{O}|1\rangle\right|^2 \cdot S_{XX}(\omega_{01}) \ , \tag{3.11}$$

called Fermi's golden rule.

$$S_{XX}(\omega_{01}) = \int_{-\infty}^{\infty} \mathrm{d}t e^{i\omega_{01}t}\left\langle \hat{X}(t)\hat{X}(0)\right\rangle \tag{3.12}$$

is the quantum noise spectral density of the operator $\hat{X}$ [20] (more details on Fermi's golden rule in 3.2.2). Fermi's golden rule (3.11) explicitly contains two contributions. The first, the matrix element $\langle 0|\hat{O}|1\rangle$, defines the ability of the operator $\hat{O}$, coupling the qubit to the noise, to make the two level system transition from the $|0\rangle$ to the $|1\rangle$ state or vice versa. In the case of charge noise this operator is

$$\hat{O} = \frac{\partial H}{\partial n_g} = -8E_C(\hat{n} - n_g) \ ; \tag{3.13}$$

the first term in a Taylor expansion of the Hamiltonian around $n_g = 0$. In contrast to the case of decoherence, the matrix elements $\langle 0|\hat{n}|1\rangle$ are non-zero in the case of the Transmon. Charge noise can still cause energy loss but only if the modes of the environment can give or take energy at the qubit frequency. This condition is encompassed in the spectral density $S_{XX}(\omega_{01})$. Increasing T_1 and T_2 in Transmon qubits has been the exclusive effort of reducing the value of the $S_{XX}(\omega_{01})$ term [59].

A second weakness of Transmon qubits is their low anharmonicity. In increasing the ratio E_J/E_C we exponentially reduced decoherence due to charge noise, but sacrificed anharmonicity in polynomial fashion [18]. Yet anharmonicity poses a fundamental limit on qubit gate speed

$$T_{\text{gate}} \gtrsim C \cdot \frac{2\pi}{\alpha} \ . \tag{3.14}$$

For reasonable fidelities, $C \approx 1.36$ was shown numerically [64]. If this limit is surpassed, the width in frequency space of the pulse defining the gate becomes great enough to start exciting the $|1\rangle - |2\rangle$ transition. Given that Transmon anharmonicity is generally of the order of a few hundred MHz, this suggests that high fidelity gates with durations much below 10 ns will be challenging for Transmons, as is illustrated by the current state of the art [65].

3.1.3 *Characteristic Impedance: a Unifying Vision*

As a conclusion to the discussion on Transmon qubits and as an introduction to the next part, we introduce the concept of characteristic impedance as a unifying method of thinking about noise insensitivity. Consider again the expressions (2.11) and (2.10). The expressions for the zero point fluctuations can be rewritten as [43, 66]

$$\Phi_{\text{ZPF}} = \sqrt{\frac{\hbar Z}{2}} = \Phi_0 \sqrt{\frac{1}{4\pi}\frac{Z}{R_Q}} = \frac{\Phi_0}{2\pi}\left(\frac{2E_C}{E_J}\right)^{1/4}, \tag{3.15}$$

$$Q_{\text{ZPF}} = \sqrt{\frac{\hbar}{2Z}} = 2e\sqrt{\frac{1}{4\pi}\frac{R_Q}{Z}} = 2e\left(\frac{E_J}{32E_C}\right)^{1/4}. \tag{3.16}$$

In the case of the Cooper Pair Box, $E_C \gtrsim E_J$ leading to $Q_{\text{ZPF}} < 2e$. The charge is well localised [32]. The impedance Z of the circuit is greater than the resistance quantum R_Q. For the Transmon, $E_J > 50E_C \Leftrightarrow Z \ll R_Q$, and the charge is delocalised, providing noise insensitivity. Thus, looking at the characteristic impedance is a useful way to determine the sensitivity to noise in charge and flux.

We now list three observations which will help in designing a qubit which can solve some of the issues of the Transmon.

1. There exists a duality between charge and flux, $\hat{n}$ and $\hat{\varphi}$. Describing the physics of superconducting circuits using the charge basis is equivalent to a description in the flux basis.

2. Creating circuits with characteristic impedance above the resistance quantum is difficult [67, 68].

3. Experimentally, charge noise measured in units of $2e$ is around 2 orders of magnitude greater than flux noise measured in units of Φ_0 in superconducting circuit experiments [59].

The first observation motivates the design of a circuit which is the dual of the Transmon in phase space. It consists of a Transmon qubit shunted by an additional large inductance L_{shunt} such that $Z = \sqrt{\frac{L_{\text{shunt}}+L_J}{C}} > R_Q$ (Fig. 3.2a), delocalising the phase variable and protecting it from flux noise. This 'hypothetical' qubit is naturally protected from charge noise, because the two superconducting islands of the Transmon are now DC connected to each other, rendering it insensitive to charge offsets.
Unfortunately, creating such a large inductance is difficult (our second observation). In fact for a long time it was considered impossible to surpass the value of R_Q with

a purely geometrical inductance. Indeed, in a geometrical inductor, the electrical and magnetic fields live in vacuum or in materials with $\epsilon_r > 1$, such that their impedance is generally bound the impedance of free space $Z_0 \approx 377\,\Omega$ [32, 69]. Up until recently, surpassing Z_0 required using the kinetic inductance of materials like NbN, granular alumnium or the effective kinetic inductance of a chain of Josephson junctions. Only in 2018 was the first geometrical inductor with $Z > R_Q$ demonstrated [70] and the bound was widely improved in 2020 thanks to extreme miniaturisation and careful substrate engineering [68]. Kinetic inductance is still of prime importance though. It was the kinetic inductor formed by a suspended chain of Josephson junctions, removing the impedance reducing spurious self-capacitance of the chain by moving the dielectric further away from the chain currents ($\epsilon_r \to 1$), which in 2019 allowed the realisation of our hypothetical Transmon dual: the Blochnium qubit [67]. An impressive breakthrough in circuit fabrication at the university of Maryland was key in achieving this design.
As is evident, designing the dual circuit to the Transmon is challenging, only being realised for the first time during the duration of this thesis and so far only consistently mastered by a single research group worldwide. Thankfully we can exploit our last observation, the charge/flux noise asymmetry, to design a qubit which will solve some of the issues of the Transmon. To understand why charge noise is greater than flux noise, we can consider the ratio

$$\frac{R_Q}{Z} = \frac{1}{8\alpha}\frac{Z_0}{Z}\ , \tag{3.17}$$

where $\alpha \approx 1/137$ is the fine structure constant. It we imagine the noise of the environment as an ensemble of LC fluctuators in vacuum, the characteristic impedance of these modes is Z_0. So the ratio of the noise in flux to the noise in charge is given by the ratio of the environment mode's zero point fluctuations measured in the natural units Φ_0 and $2e$

$$\frac{\Phi_{\text{ZPF}}/\Phi_0}{Q_{\text{ZPF}}/2e} = 8\alpha \approx 0.06\ . \tag{3.18}$$

We approximately retrieve the order of magnitude observed experimentally. Concretely, this asymmetry between charge and flux noise means that it can still be advantageous to shunt the Transmon with a large inductance even if we are not completely in the regime where the phase is delocalised. Obviously, this will solve the charge offset problem, but will also increase the anharmonicity dramatically as well as reduce the value of $S_{XX}(\omega_{01})$. In the next section we will detail the physics of the Fluxonium qubit.

3.2 FLUXONIUM THEORY

3.2.1 *Fluxonium Hamiltonian*

The basic circuit model for Fluxonium qubits is given in Fig. 3.2a, looking like a Transmon shorted by an inductance as mentioned before. The value of E_J is defined by the small junction in the top left corner of the SEM image of Fig. 3.2b. $E_L = \frac{\Phi_0^2}{4\pi^2 L}$ is given by the value of the inductance L formed by the junction chain in the same figure. Finally, E_C is given by the combination in parallel of the capacitance of the small junction

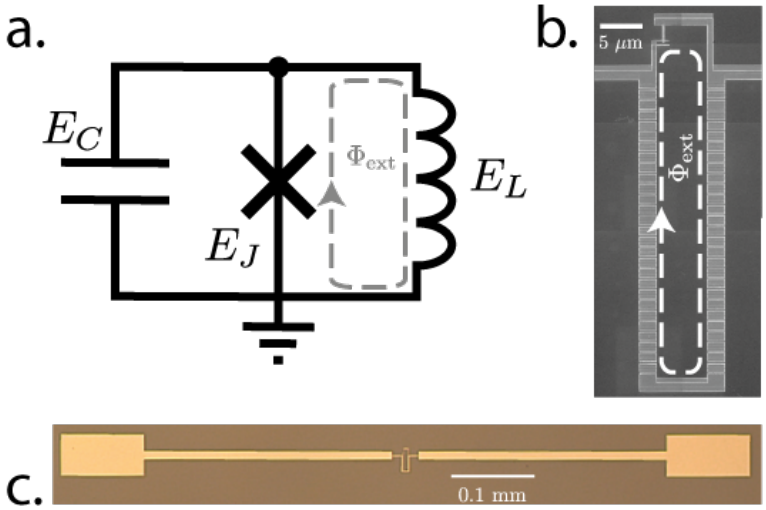

Figure 3.2: a. Generic circuit model for the Hamiltonian given in (3.19). In the closed loop formed by the junction and the inductance we can couple an external magnetic field given symbolised here by the external flux Φ_{ext}. b. An SEM image of the small junction (top left) and the superinductance formed by a chain of Josephson junctions. c. Image of a full 3D Fluxonium circuit taken with an optical microscope. The two pads either side of the loop in the centre of the image serve a double purpose: dominating the capacitive energy E_C and coupling to the cavity field in which they are placed. Images b and c were taken at the University of Maryland, where our Fluxonium qubits were fabricated.

and the capacitance of the antennas in Fig. 3.2c. That a chain of Josephson junctions should effectively form a large inductance is not an entirely trivial statement. Several conditions need to be met: the junctions must be physcially large (small inductance, large capacitance), exponentially suppressing phase slips across junctions in the chain; the chain must contain a sufficient number of junctions to be considered a linear element; the chain must be short enough so that transmission line modes allowed by the spurious capacitances to ground do not resonate at the same frequency as the modes of interest in the Fluxonium; the operation frequency of the chain must be well below the plasma frequency of the individual junctions [32, 66, 71, 72, 73]. It should also be noted that it is possible to create Fluxoniums with disordered superconductors with high kinetic inductance such as granular aluminium (GrAl) [74], or using a nanowire superinductance as was demonstrated in [75].

The generic Hamiltonian of the circuit model of Fig. 3.2a is

$$\hat{H} = 4E_C\hat{n}^2 + \frac{1}{2}E_L\hat{\varphi}^2 - E_J\cos\left(\hat{\varphi} - 2\pi\frac{\Phi_{\text{ext}}}{\Phi_0}\right) . \tag{3.19}$$

It is possible to thread an external magnetic flux Φ_{ext} through the closed loop, displacing the cosine potential of the junction with respect to the harmonic potential of the inductor. The n_g term which was problematic for Transmon devices has disappeared because the two sides of the small junction are galvanically connected. Furthermore, the flux potential is no longer 2π periodic allowing the charge number $\hat{n}$ to take continous values

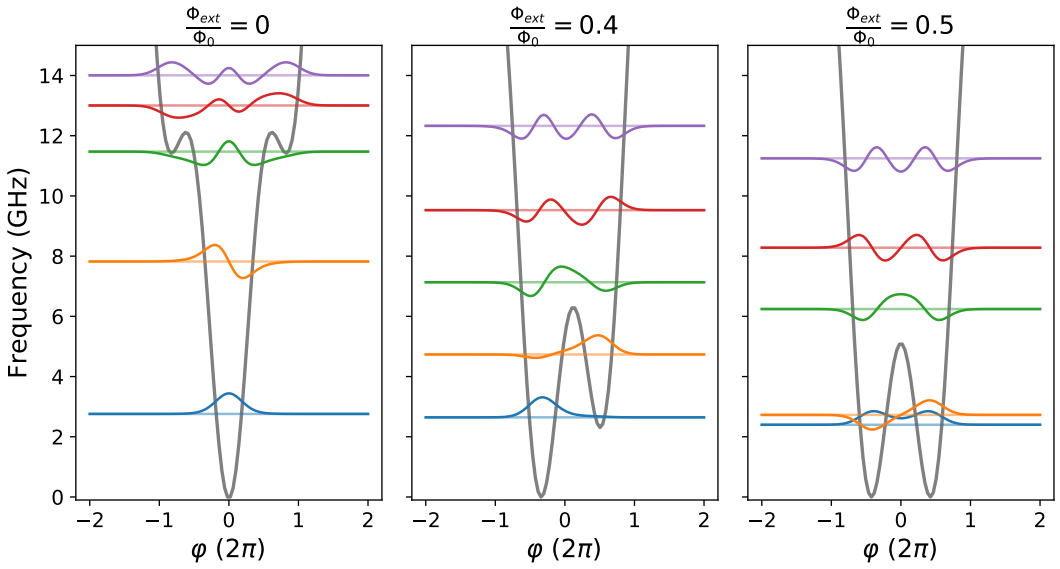

Figure 3.3: Fluxonium wavefunctions and energy levels at different external fluxes for the parameters $E_C = 0.97\,\text{GHz}$, $E_L = 0.69\,\text{GHz}$, $E_J = 4\,\text{GHz}$ as a function of the phase φ. The wavefunctions of the first 5 energy levels are plotted with solid coloured lines, offset by corresponding eigenenergies given in GHz (pale coloured lines). In gray we show the potential given by $\frac{1}{2}E_L\varphi^2 - E_J\cos\left(\varphi - 2\pi\frac{\Phi_{\text{ext}}}{\Phi_0}\right)$.

instead of being quantised as in the Transmon case [43]. The usual parameters of Fluxonium devices puts them in the regime $E_J \gg E_L$ and $\frac{E_J}{E_C} \sim 1-10$ [66, 76]. Concretely, for the superinductance, we need to make chains with inductance $L_J^{\text{chain}} = 1-5\,\text{nH}$ per junction with around $50-200$ junctions so that $E_L/h = 0.5-1\,\text{GHz}$. The tunneling energy is set by the inductance $L_J = 10-40\,\text{nH}$ of the small junction such that $E_J/h = 2-20\,\text{GHz}$. Finally we aim for a capacitive energy of $E_C/h = 0.5-5\,\text{GHz}$ corresponding to capacitances of the order of $C = 5-50\,\text{fF}$. These capacitance values are well above the capacitance C_J of the small junction, which is defined by the surface area of the junction and the oxidation parameters during the fabrication of the oxide layer. In standard devices $C_J = 0.5-3\,\text{fF}$, so that the main contribution to E_C must come from the capacitance of the antennas (Fig. 3.2c) or from the difficultly controllable capacitance to ground if the circuit is in 2D.

A good way to understand the spectrum of (3.19) is to do some numerics (more details on this later). In Fig. 3.3 we show the wavefunctions, energy levels and potential of the Fluxonium qubit in phase representation. At $\Phi_{\text{ext}} = 0$, the spectrum resembles that of a Transmon circuit. At low energies the potential is quasi-harmonic and the energy levels are approximately separated by the Lamb shifted plasmon frequency $\omega_Q = \frac{\sqrt{8E_C(E_J+E_L)}-E_C}{\hbar}$. Transitions between levels are called plasmons because the average value of the flux does not change during the transition. At this working point, Fluxoniums exhibit very little difference from Transmon qubits. As we move towards the half flux point, at $\Phi_{\text{ext}} = 0.4\Phi_0$ in the 2$^{\text{nd}}$ panel, the two wells corresponding to the closest minima of the cosine to $\hat{\varphi} = 0$ and house the two lowest energy states $|0\rangle$ and $|1\rangle$.

The transition between these two levels is called a fluxon because it requires changing the value of $\hat{\varphi}$. When the two energy levels exhibit disjoint support like in this case, T_1 is strongly enhanced because a local operator $\hat{O}$ cannot effectively induce a transition between the two levels [59]. Equivalently, the matrix element $\langle 0|\hat{O}|1\rangle$ of (3.11) is very small. Finally, we consider the spectrum at $\Phi_{\text{ext}} = 0.5\Phi_0$ called the sweet spot and the standard working point for Fluxonium qubits. At this value of external flux, the energy levels within both wells are degenerate, a degeneracy lifted by the $4E_C\hat{n}^2$ term of the Hamiltonian. Noting $|\circlearrowleft\rangle$ the state localised in the well on the left, and $|\circlearrowright\rangle$ the state localised in the well on the right, the first 2 energy levels are given by symmetric and antisymmetric superpositions of these states

$$|0\rangle = \frac{|\circlearrowleft\rangle + |\circlearrowright\rangle}{\sqrt{2}} \ , \tag{3.20}$$

$$|1\rangle = \frac{|\circlearrowleft\rangle - |\circlearrowright\rangle}{\sqrt{2}} \ . \tag{3.21}$$

This notation is useful in reminding us of the physical manifestation of these energy states as superpositions of currents circulating clockwise and anticlockwise in the loop formed by the junction and inductor. Because the transition frequency at the sweet spot is given by the lifting of a degeneracy of a double well potential, the ratio of E_C to E_J plays a central role in determining the qubit frequency. Intuitively, E_J sets the height of the barrier between the two wells and E_C sets the tunneling rate. When E_C reduces compared to E_J, the qubit frequency drops as the level splitting decreases [77]. If the ratio E_J/E_C decreases (eventually becoming smaller than 1), the qubit frequency will increase as the levels repel each other. In practice, the frequency of the $|0\rangle - |1\rangle$ transition can be anywhere between 10 MHz and 1 GHz, depending on the qubit parameters [32, 74, 75, 77, 67, 78]. For the Fluxoniums used in this thesis $\omega_{01}/2\pi = 100 - 500$ MHz and $\omega_{12}/2\pi \sim 5$ GHz at the sweet spot, exhibiting extremely large anharmonicity. Furthermore, as is clear from the symmetry of the 3$^{\text{rd}}$ panel of Fig. 3.3, Fluxoniums are insensitive to flux noise at[1] $\Phi_{\text{ext}} = 0.5\Phi_0$, strongly enhancing their T_2. A typical T_2 measurement as a function of flux is shown in Fig. 3.4 where this enhancement is visible. Interestingly, it is the same mechanism protecting T_1 for $\Phi_{\text{ext}} \neq 0.5\Phi_0$ that protects T_2 at the sweet spot. A phase-flip, measured at a rate $1/T_2$, occurs when $|+X\rangle$ is transformed into $|-X\rangle$. Yet in the Fluxonium qubit, the states $|\pm X\rangle = \frac{|0\rangle \pm |1\rangle}{\sqrt{2}}$ are in fact just the clockwise and anticlockwise current states $|\circlearrowleft\rangle$ and $|\circlearrowright\rangle$. These states are localised in the degenerate left and right potential wells such that their support is disjoint. A local operator thus cannot induce a phase-flip. Does this mean that T_1 is now unprotected? In the wavefunction support sense, yes, but because the qubit frequency is an order of magnitude lower than in Transmons (0.5 vs. 5 GHz), $S_{XX}(\omega_{01})$ is also reduced for most lost mechanisms.

1 This is also true at $\Phi_{\text{ext}} = 0\Phi_0$.

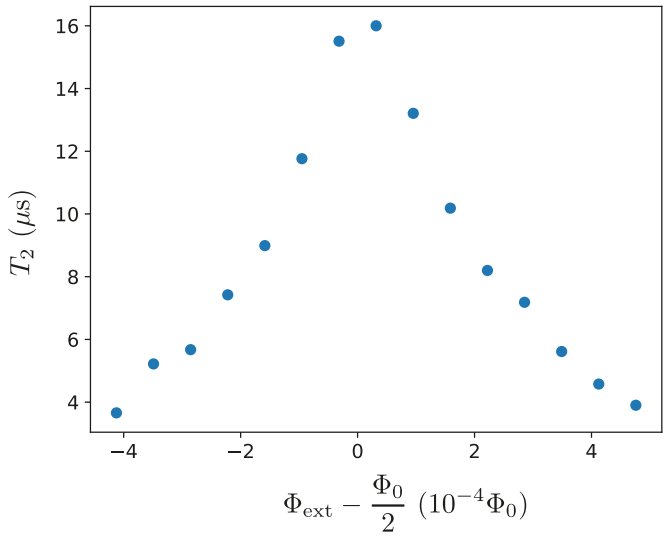

Figure 3.4: Typical measurement of T_2 as a function of flux. Notice how T_2 is enhanced only very close to the sweet spot, within one 10000^{th} of a flux quantum. Such a high sensitivity was also observed in [77, 74, 79].

3.2.2 *Loss mechanisms*

Let's be more specific about Fermi's golden rule. Recall that for a qubit coupled to a bath at temperature T through the interaction $H_{\text{int}} = A\hat{O}\hat{X}$, where $\hat{O}$ is a dimensionless qubit operator and $\hat{X}$ is the operator of the bath, Fermi's golden rule is

$$\Gamma_{1\to 0} = \frac{A^2}{\hbar^2}\left|\langle 0|\hat{O}|1\rangle\right|^2 \cdot S_{XX}(\omega_{01}) \ . \tag{3.22}$$

The spectral noise density $S_{XX}(\omega_{01})$ (see (3.12)) quantifies the ability for the bath to receive energy at the frequency ω_{01} given its temperature T. Note that, in contrast to classical spectral densities, $S_{XX}(\omega) \neq S_{XX}(-\omega)$, meaning that giving and taking energy is not the same for the bath. This is best illustrated at $T = 0$ where the bath can receive energy, but cannot give it [20]. Generally, H_{int} can be found by taking the derivative of the Hamiltonian with respect to an external parameter λ which can be affected by the noise of the bath. Expressedly, if $\delta\lambda$ is the environmental noise around the set parameter λ_0 then

$$\hat{H}(\lambda) \approx \hat{H}(\lambda_0) + \underbrace{\frac{\partial \hat{H}}{\partial \lambda}\delta\lambda}_{H_{\text{int}}} \ . \tag{3.23}$$

$\delta\lambda$ will be expressed by some bath operator. Concretely, in the case of current noise in a coil biasing the Fluxonium at its sweet spot, $\lambda = \Phi_{\text{ext}}$ and $\delta\lambda = M\delta\hat{I}_{\text{coil}}$ where M is the mutual coupling between the coil and the Fluxonium loop. In the following though, we keep the discussion very generic in order to derive some general formulas for the effect of noise on Fluxonium.

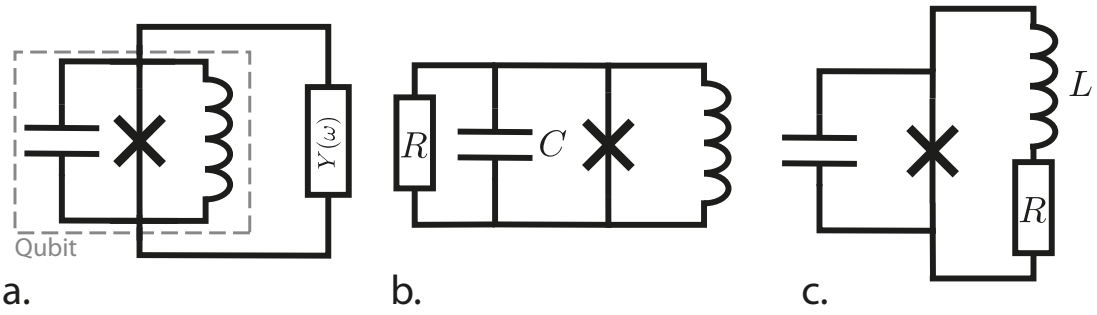

Figure 3.5: a. General circuit model for a linear dissipator. The qubit is shunted by a frequency dependent admittance. b. Circuit model for capacitive type losses. c. Circuit model for inductive type losses.

The operator $\hat{O}$ is often the charge $\hat{n}$ or phase $\hat{\varphi}$ operator. Yet we know that representations in charge and phase contain the same information. A manifestation of this is the relation

$$\langle 1|\hat{n}|0\rangle = i\frac{\omega_{01}}{2\pi} R_Q C \langle 1|\hat{\varphi}|0\rangle \tag{3.24}$$

providing a connection between the charge and phase matrix elements through the total capacitance C of the circuit given by[2] E_C (for a full derivation see [80]). Thus, we can restrict ourselves to considering any loss mechanism as affecting the phase operator $\hat{\varphi}$ only. In this case, it is useful to imagine the lossy bath as an admitance in parallel with the inductance of the Fluxonium [7] (see Fig. 3.5a). The coupling Hamiltonian becomes $H_{\text{int}} = \hat{\Phi}\hat{I}_{\text{admitance}}$ (the integrated power dissipated in the admitance due to the flux across the junction) and we hide the particular properties of the dissipation mechanism in the expression of the admitance $Y(\omega)$ so that [20]

$$S_{II}(\omega_{01}) = \hbar\omega_{01} \operatorname{Re}\left[Y(\omega_{01})\right] \left[\coth\left(\frac{\hbar\omega_{01}}{2k_{\text{B}}T}\right) + 1\right]. \tag{3.25}$$

For specific loss mechanisms we now have to identify the expression for the admitance $Y(\omega_{01})$.

Dielectric losses are one of the main sources of energy loss in superconducting circuits [81]. They correspond to two level systems (TLSs) present in the substrate on which the circuits are patterned which interact with the electric fields of the circuits. This can be modelled by assuming the capacitance possesses a lossy dielectric: the dielectric constant has an imaginary part $\epsilon = \epsilon_0 + i\epsilon_1$. The admittance of a parallel plate capacitor of surface A and distance d is $Y = i\omega\frac{(\epsilon_0+i\epsilon_1)d}{A} = i\omega C - \omega C\tan\delta$. We have introduced the angle δ such that $\tan\delta = \frac{\epsilon_1}{\epsilon_0}$. This is the admittance of a capacitor and (frequency dependent) resistor in parallel (Fig 3.5b.) of which the Q-factor is $Q = \omega RC$ [8] and $R = \frac{1}{\omega C\tan\delta} = 1/\operatorname{Re}\left[Y_{\text{diel}}(\omega)\right]$. Hence

$$\operatorname{Re}\left[Y_{\text{diel}}(\omega_{01})\right] = \frac{\omega_{01}C}{Q_{\text{diel}}}\ , \tag{3.26}$$

2 Equivalently, we can see C as a constant which connects the voltage across the junction to the charge number $\hat{V} = \frac{2e}{C}\hat{n}$

and $Q_{\text{diel}}^{-1} = \tan\delta$ is coventionnally given by the loss tangent of the material (see Tab. 4.3 in Chapter 4).

In full analogy, we can compute inductive losses, the losses due to coupling to the magnetic field, by using a complex permeability for the inductance. The admittance of a coil of inner area A, length l and number of winds N is $Y = (i\omega(\mu_0 + i\mu_1)\frac{N^2 A}{l})^{-1}$. Close to the frequency of interest, we can model this admittance as an inductor and resistor in series $Y = (i\omega L - R)^{-1}$ (Fig 3.5c) where $R = \omega L \tan\delta_\mu$ and $\tan\delta_\mu = \frac{\mu_1}{\mu_0}$ in full analogy with the dielectric case. The Q-factor of such a circuit is given by $Q = \frac{\omega L}{R}$ [8]. Finally, under the approximation that the losses are small ($Q_{\text{ind}} \gg 1$)

$$\text{Re}\left[Y_{\text{ind}}(\omega_{01})\right] = \frac{1}{\omega_{01} L Q_{\text{ind}}} \ , \tag{3.27}$$

with $Q_{\text{ind}}^{-1} = \tan\delta_\mu$. Whereas there generally exist tables of loss tangents for various dielectrics, this is not always the case for magnetic losses. This expression is thus generally used as an estimator for a bound on the quality factor Q_{ind}.

Radiative losses, such as those given by the Purcell rate can equally be calculated using this technique. An expression for the admitance as a function of circuit parameters is given in [80], but is rarely useful because of the lack of knowledge of the circuit parameters involved. We prefer to follow the approach of [73] which relies on finite element simulations. In Sonnet for example, placing a port at the junction position and another at the transmission line input allows the simulation of the admittance as seen by the Josephon junction.

A last source of losses is the one due to quasiparticles tunneling through the junctions in the circuit. Quasiparticles, which should basically not be present at the temperatures at which dilution refrigerators are operated, correspond to electronic excitations above the superconducting gap Δ. In theory, the ratio of the number of quasiparticles to the number of Cooper pairs x_{qp} should be around $\sim 10^{-23}$ at 40 mK, but in practice many measurements find values well above this in the range $10^{-7} - 10^{-5}$ [82, 83, 84, 85, 86, 87, 37]. A thorough treatment of the issue and potential explanations can be found in [88]. Because these losses do not involve a linear interaction Hamiltonian, but the non-linearity of the junction tunneling, the techniques given above combining (3.22) and (3.25) are not valid. The expression for the loss rate from quasiparticles tunneling through the small junction is given as [88]

$$\Gamma_{1\to 0} = \frac{8E_J}{\pi\hbar} x_{\text{qp}} \sqrt{\frac{2\Delta}{\omega_{01}}} \left| \langle 0 | \sin\left(\frac{\hat{\varphi}}{2} - \pi\frac{\Phi_{\text{ext}}}{\Phi_0}\right) | 1\rangle \right|^2 . \tag{3.28}$$

For the losses due to tunneling in the chain, the operator in the matrix element is linearised and E_J is replaced with E_L [89]

$$\Gamma_{1\to 0} = \frac{8E_L}{\pi\hbar} x_{\text{qp}} \sqrt{\frac{2\Delta}{\omega_{01}}} \left| \langle 0 | \frac{\hat{\varphi}}{2} | 1\rangle \right|^2 . \tag{3.29}$$

A summary of the different relaxation rates is given in Table 3.1. Before continuing, it is useful to comment about dielectric and quasiparticle losses in more detail. We can

Loss Type	Expression for $\Gamma_{1\to0}$
Dielectric	$\frac{\hbar\omega_{01}^2 C}{4e^2 Q_{\text{diel}}} \lvert\langle 1\rvert\hat{\varphi}\lvert 0\rangle\rvert^2 \left[\coth\left(\frac{\hbar\omega_{01}}{2k_{\text{B}}T}\right)+1\right]$
Inductive	$\frac{\hbar}{4e^2 L Q_{\text{ind}}} \lvert\langle 1\rvert\hat{\varphi}\lvert 0\rangle\rvert^2 \left[\coth\left(\frac{\hbar\omega_{01}}{2k_{\text{B}}T}\right)+1\right]$
Radiative (including Purcell)	$\frac{\hbar\omega_{01}}{4e^2}\,\text{Re}\left[Y(\omega_{01})\right] \lvert\langle 1\rvert\hat{\varphi}\lvert 0\rangle\rvert^2 \left[\coth\left(\frac{\hbar\omega_{01}}{2k_{\text{B}}T}\right)+1\right]$
Quasiparticles (small junction)	$\frac{8E_J}{\pi\hbar} x_{\text{qp}} \sqrt{\frac{2\Delta}{\omega_{01}}} \left\lvert\langle 0\rvert\sin\left(\frac{\hat{\varphi}}{2}-\pi\frac{\Phi_{\text{ext}}}{\Phi_0}\right)\rvert 1\rangle\right\rvert^2$
Quasiparticles (chain)	$\frac{8E_L}{\pi\hbar} x_{\text{qp}} \sqrt{\frac{2\Delta}{\omega_{01}}} \left\lvert\langle 0\rvert\frac{\hat{\varphi}}{2}\rvert 1\rangle\right\rvert^2$

Table 3.1: Table summarising the different loss mechanisms and their expressions.

see how advantageous it is to reduce the frequency of Fluxoniums with respect to their Transmon counterparts when it comes to the losses. Dielectric losses depend on ω_{01}^2 such that by reducing the frequency by a factor 10, we have gained a factor 100 on the limit given by dieletric loss on qubit lifetimes. This is what enables Fluxonium to be the most coherent quantum circuit to date ($T_2 > 1\,\text{ms}$), despite being limited by delectric losses [79, 33]. Additionally, quasiparticle tunneling through the small junction is supressed at $\Phi_{\text{ext}} = 0.5\Phi_0$ because the matrix element $\langle 0|\sin\left(\frac{\hat{\varphi}}{2}-\pi\frac{\Phi_{\text{ext}}}{\Phi_0}\right)|1\rangle$ vanishes at this point thanks to parity protection [82].

3.2.3 *Single qubit gates*

In the previous section we have seen that by lowering the qubit frequency we can reduce the energy decay rate of the Fluxonium, especially the losses due to dielectrics. In general, the level structure of the Fluxonium has a number of consequences on the availability of gates for controlling the qubit state.

First of all, at the flux symmetry points the matrix elements $\langle j|\hat{\varphi}|k\rangle$ where $j-k$ is even go to 0 exactly. This selection rule can be seen from considerations on the symmetry of the wavefunctions: $\hat{\varphi}$ must couple wavefunctions with opposite phase parity[3]. A direct practical consequence is that the $|0\rangle - |2\rangle$ transition is hard to probe at half flux (even transitions in Fig. 3.6).
Furthermore, in many schemes qubit gates consist of applying microwave tones pulses coupling to the charge degree of freedom. Although inductive coupling schemes in 3D exist as well [74], direct coupling between the field and the charge degree of freedom is standard for 3D Fluxoniums in a cavity in particular (see the antennas in Fig. 3.2 for example). Yet from (3.24) and the low frequency transitions in Fig. 3.6 we see that the "drivability" of the transition, given by the charge matrix element, disappears with

3 A direct proof is to calculate the overlap integral $\int_{-\infty}^{\infty}\psi_j(\varphi)\varphi\psi_k(\varphi)\text{d}\varphi$ where ψ_j and ψ_k have the same symmetry in φ.

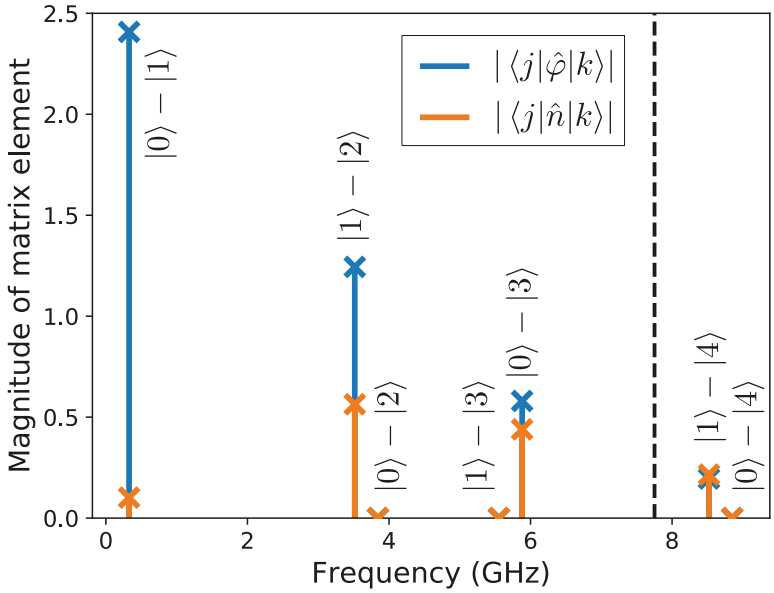

Figure 3.6: Magnitude of the charge (orange) and phase (blue) matrix elements as a function of the transition frequency at $\Phi_{\text{ext}} = \Phi_0/2$. The cavity frequency 7.752 GHz is given by the black dashed line. The qubit parameters are $E_C = 0.97\,\text{GHz}$, $E_L = 0.69\,\text{GHz}$, $E_J = 4\,\text{GHz}$ (same as in Fig. 3.3). Note how the even matrix elements are strictly 0 and how the values of $|\langle l|\hat{n}|k\rangle|$ are supressed with respect to those of $|\langle l|\hat{\varphi}|k\rangle|$ at low frequency.

the qubit frequency ω_{01}, posing a potential issue for fast operations. By decreasing the magnitude of the charge matrix element we increased coherence, but does this come at the cost of slower gates? Indeed, with the perspective of using superconducting qubits for quantum computation, we should strive to keep increasing $\frac{T_2}{T_{\text{gate}}}$ (or at least keep it constant for increasing T_2). In practice though, it is sufficient to increase the drive power to compensate the smaller matrix elements, and obtain Rabi frequencies equivalent to those seen in Transmons without being prone to leakage outside of the computational subspace thanks to the large anharmonicity. In fact 80 ns microwave activated gates on a low frequency Fluxonium are currently the highest fidelidy gates acheived in superconducting circuits [33], with 20 ns gates reaching fidelities above 99.9% [90]. At very low frequencies however, the suppression of the charge matrix element does become a problem and gates are engineered thanks to the phase matrix element $\langle 1|\hat{\varphi}|0\rangle$ as was demonstrated in [77]. There, they exploited the Landau-Zener transition due to the level repulsion of the states in either phase potential wells at half flux to generate an effective $\hat{\sigma}^x$ Hamiltonian with small flux displacements.

3.2.4 *Fluxonium Readout*

Before discussing two qubit gates, we focus on the readout of Fluxonium qubits because some of the principles will be the same. As discussed in Sec. 2.4.3, the qubit and cavity

are coupled through the term $\hat{H}_{\text{int}} = \hbar g \hat{n}(\hat{a} + \hat{a}^\dagger)$. We put ourselves in the dispersive limit, meaning that

$$\left| \frac{E_l - E_k}{\hbar} - \omega_R \right| \gg g |\langle l|\hat{n}|k\rangle| \ , \tag{3.30}$$

where E_l and E_k are the eigenenergies of the Fluxonium state $|l\rangle$ and $|k\rangle$ respectively[4] [91]. In this limit, it is useful to consider the coupling term of the Hamiltonian as a small correction and apply perturbation theory to the uncoupled eigenstates of the system. Labeling the uncoupled states $|\mu, m\rangle = |\mu\rangle \otimes |m\rangle$ (we use Greek letters for the qubit, the Roman alphabet for the cavity), the first two perturbative terms[5] for the energy correction due to the qubit-cavity coupling are given as

$$E^{(1)}_{\mu,m} = \hbar g \langle \mu|\hat{n}|\mu\rangle \langle m|\hat{a} + \hat{a}^\dagger|m\rangle \ , \tag{3.31}$$

$$E^{(2)}_{\mu,m} = \hbar^2 g^2 \sum_{\nu\neq\mu,\ l\neq m} \frac{|\langle \mu|\hat{n}|\nu\rangle|^2 \cdot \left|\langle m|\hat{a} + \hat{a}^\dagger|l\rangle\right|^2}{E_{\mu,m} - E_{\nu,l}} \ . \tag{3.32}$$

The first order term disappears at all fluxes, not because of the $\langle\mu|\hat{n}|\mu\rangle$ term which only vanishes at half flux, but because of the cavity matrix element which vanishes at any flux. The second order term is simplified as $\hat{a} + \hat{a}^\dagger$ only couples to consecutive cavity states

$$E^{(2)}_{\mu,m} = \hbar^2 g^2 \sum_{\nu\neq\mu} |\langle \mu|\hat{n}|\nu\rangle|^2 \left(\frac{m+1}{E_\mu - E_\nu - \hbar\omega_R} + \frac{m}{E_\mu - E_\nu + \hbar\omega_R} \right) \ . \tag{3.33}$$

Thus, the shift imposed by the qubit in state $|\mu\rangle$ on the cavity frequency is

$$\begin{aligned} E^{(2)}_{\mu,m} - E^{(2)}_{\mu,m-1} &= \hbar^2 g^2 \sum_{\nu\neq\mu} |\langle \mu|\hat{n}|\nu\rangle|^2 \left(\frac{1}{E_\mu - E_\nu - \hbar\omega_R} + \frac{1}{E_\mu - E_\nu + \hbar\omega_R} \right) \\ &= \hbar^2 g^2 \sum_{\nu\neq\mu} |\langle \mu|\hat{n}|\nu\rangle|^2 \frac{2(E_\mu - E_\nu)}{(E_\mu - E_\nu)^2 - \hbar^2\omega_R^2} \\ &= \hbar g^2 \sum_{\nu\neq\mu} \frac{2\omega_{\mu\nu} |\langle \mu|\hat{n}|\nu\rangle|^2}{\omega_{\mu\nu}^2 - \omega_R^2} = \hbar\chi_\mu \ , \end{aligned} \tag{3.34}$$

where we have defined the transition frequency $\omega_{\mu\nu} = \frac{E_\mu - E_\nu}{\hbar}$. If the qubit and cavity are coupled through the phase $\hat{H}_{\text{int}} = \hbar g \hat{n}(\hat{a}^\dagger - \hat{a})$, we have to recalculate the second order perturbation theory. This is straightforward and we obtain

$$\hbar\chi_\mu = \hbar g^2 \sum_{\nu\neq\mu} \frac{2\omega_R |\langle \mu|\hat{\varphi}|\nu\rangle|^2}{\omega_{\mu\nu}^2 - \omega_R^2} \ . \tag{3.35}$$

Experimentally, use usually measure the dispersive shift $\chi_\mu - \chi_\nu$ of the cavity frequency when the qubit changes from $|\nu\rangle$ to $|\mu\rangle$, as this does not require knowledge of the bare

4 There is some simplification here with respect to the most general dispersive limit, as we only consider a single mode cavity.

5 Fourth order corrections are in fact visible in experiments [91], but the main features are already captured by the second order terms.

cavity frequency ω_R which is generally inaccessible[6].

It is useful to understand (3.34) in some detail before going further. At $\Phi_{\text{ext}} = \Phi_0/2$ the charge matrix element only couples to even transitions, so when dealing with the dispersive shift of the ground state for example, the only relevant terms in the series correspond to ν being odd. In practice, $\omega_R \approx 7.5\,\text{GHz}$ in most of the devices in this thesis which is not a coincidence. With the knowledge that in general $\omega_{10} \sim 500\,\text{MHz}$ and $\omega_{30} \sim 7\,\text{GHz}$, notice that the term $\beta = 3$ dominates the infinite sum for χ_0 because the denominator is very small. The SNR of the qubit readout is given by $\frac{|\chi_0 - \chi_1|}{\kappa}$ with κ the linewidth of the cavity. No term in the sum for χ_1 is as large though because $\langle 1|\hat{n}|3\rangle = 0$, and $\omega_{14} - \omega_R$ will change sign compared to $\omega_{03} - \omega_R$ thanks to the large anharmonicity thus contributing constructively to the dispersive shift. These considerations are clearly visible in Fig. 3.6. It is thus the proximity of transitions outside the computational subspace with the cavity frequency that defines the magnitude of the dispersive shift of the $0-1$ transition.
This is in stark contrast to the Transmon. While (3.34) is still valid for Transmon qubits, it is the terms involving ω_{01} and $\omega_{12} = \omega_{01} - \alpha$ which are dominant. Because the anharmonicity α is small, there is no decoupling between the cavity frequency and the dispersive shift. The qubit frequency must be close to the cavity frequency if we want the readout to be effective. Moreover, in Transmons the dispersive shift $\chi_1 - \chi_0$ is almost always negative except for the special case of the stradling regime[7]. That is to say that the cavity frequency when the qubit is in $|1\rangle$ is invariably lower than when it is in state $|0\rangle$. This is not the case for Fluxonium, where the dispersive shift routinely changes sign as a function of flux.
In Fig. 3.7 we show a Fluxonium qubit spectrum measured using two tone spectroscopy. In this measurement a first tone at ω_d close to ω_R is used to monitor the cavity frequency. If the qubit state changes, so will the cavity frequency and thus the phase and amplitude of the drive transmitted through the readout cavity (see Chapter 2 for details). The second tone's role is to excite the various qubit transitions. To do this, its frequency ω_p is swept over a wide range at fixed amplitude. When ω_p gets close to one of the Fluxonium's transition frequencies $\omega_{\mu\nu}$, the qubit's state begins to change, leaving a signature on the phase and amplitude of the transmitted cavity drive visible in In Fig. 3.7. Finally, to monitor the Fluxonium's flux dependence, we also sweep the external flux Φ_{ext}. Colored lines, showing deviations of the cavity response from its response with thermal qubit occupation, indicate that the probe tone is at resonance with a qubit transition. The color represents the phase of the cavity response, encoding the sign and magnitude of the dispersive shift due to the qubit. Notice how throughout the spectrum, the lines become more or less thick, indicating the varying susceptibility of the transition to the drive, as expected from the flux dependence of the magnitude of

6 The cavity frequency without the qubit and the cavity frequency with the qubit inside are not the same. We showed this in (2.39), where the cavity frequency is dressed by the qubit and cavity coupling. Even if we effectively eliminate the coupling between qubit and cavity (like here [92]) the cavity frequency is still modified by the presence of the dielectric from the silicon chip on which the qubit is patterned. A measurement of the cavity frequency with no silicon chip inside would not yield the same result as a removal of the coupling between cavity and qubit.

7 The stradling regime is defined as $\omega_R < \omega_{01} < \omega_R + \alpha$

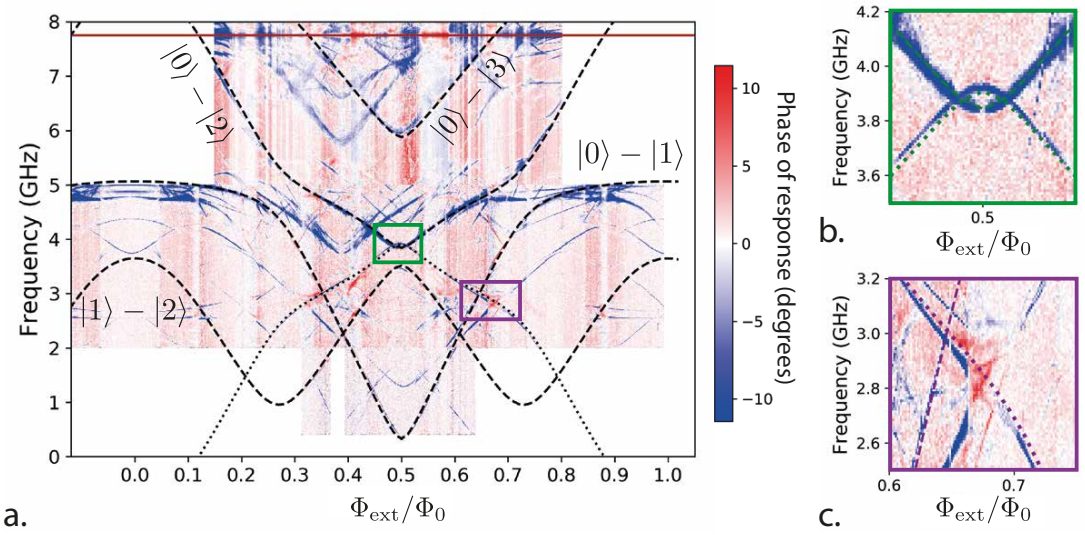

Figure 3.7: Measurement of a 3D Fluxonium spectrum by two tone spectroscopy. The colorscale (blue - white - red) corresponds to the phase of the cavity response with respect to its value away from any qubit transitions. Dashed lines are fits to the Fluxonium Hamiltonian eigenenergies with parameters $E_C = 0.97\,\text{GHz}$, $E_L = 0.69\,\text{GHz}$, $E_J = 4\,\text{GHz}$. The brown line at the top of panel a. is the cavity frequency and the dotted line corresponds to the value of $\omega_R - \omega_{02}$. b. Zoom around the frequency of the $|0\rangle - |2\rangle$ transition at half flux. c. Zoom around 3 GHz at the flux point where the $|0\rangle - |3\rangle$ crosses the cavity frequency. Notice that some of the transitions visible in the spectrum, around 4 GHz at $\Phi_{ext} = 0.4\Phi_0$ for example, are due to the presence of a second Fluxonium on the same chip that is coupled to the same cavity.

the charge matrix element $\langle\mu|\hat{n}|\nu\rangle$. In particular, in the top right inset, we can clearly see how the matrix element of the $|0\rangle - |2\rangle$ transition disappears at half flux because of the selection rule. The cavity mediated $|0\rangle - |2\rangle$ transition is also visible in the inset (upside down hyperbola). In practice this is the frequency $\omega_R - \omega_{02}$ corresponding to the conversion of 2 qubit excitations into a single cavity excitation and vice versa $|\alpha = 0, m = 1\rangle - |\alpha = 2, m = 0\rangle$ (more on this in Chapter 5). As a confirmation of the theory, this transition is not parity protected thanks to the involvement of the cavity and is thus visible at the sweet spot $\Phi_0/2$. In the bottom right inset, we see how the dispersive shift of a transition can change abruptly with flux. See how the visible transitions go from blue to red to blue as we increase the flux. In perfect accord with the discussion above, the flux point where this happens is exactly where the $|0\rangle - |3\rangle$ transition crosses the cavity frequency.

3.2.5 *Diagonalising the Fluxonium Hamiltonian*

Alone, the Transmon qubit can be diagonalised exactly [18]. No analytical solution to the problem of a the transmon coupled to a cavity exists though and we must turn to numerics. A number of open source projects have been developped [93, 94, 95], relying for the most part on the technique of Black Box Quantisation [96]. This relies on the

weak anharmonicity of the Transmon to initialy linearise the circuit, expanding the $\cos(\hat{\varphi})$ to second order, finding the normal modes and then diagonalising the Hamiltonian in the normal mode basis with the cosine expansion truncated to low (4^{th}) order. This technique cannot be used for Fluxoniums, simply because they are not weakly anharmonic and the higher order cosine terms contribute strongly to the spectrum [97].

The Hamiltonian of a Fluxonium qubit coupled to a cavity can be decomposed into 3 terms

$$\hat{H} = \hat{H}_{\text{Fluxonium}} + \hat{H}_{\text{Cavity}} + \hat{H}_{\text{Coupling}} \ , \tag{3.36}$$

where

$$\hat{H}_{\text{Fluxonium}} = 4E_C\hat{n}^2 + \frac{1}{2}E_L\hat{\varphi}^2 - E_J\cos\left(\hat{\varphi} - 2\pi\frac{\Phi_{ext}}{\Phi_0}\right) \ , \tag{3.37}$$

$$\hat{H}_{\text{Cavity}} = \hbar\omega_R\hat{a}_c^\dagger\hat{a}_c \ , \tag{3.38}$$

$$\hat{H}_{\text{Coupling}} = -\hbar g\hat{n}(\hat{a}_c^\dagger + \hat{a}_c) \ . \tag{3.39}$$

When the coupling g is weak, as is defined by the dispersive limit of (3.30), we want to calculate the corrections to the eigenenergies of the qubit and cavity due to the coupling between the two. Here we expose in detail three different methods for doing this.

3.2.5.1 *Perturbation Theory*

The simplest technique is to use the results of second order perturbation theory, as were described in Sec. 3.2.4. For this, we can diagonalise the qubit Hamiltonian (3.37) alone using Qutip [98, 99] by expressing $\hat{n}$ and $\hat{\varphi}$ in terms of the harmonic oscillator operators $\hat{a}_q^\dagger$ and $\hat{a}_q$ [32]

$$\hat{n} = in_{\text{ZPF}}(\hat{a}_q^\dagger - \hat{a}_q) \ , \ n_{\text{ZPF}} = \left(\frac{32E_C}{E_L}\right)^{-1/4} \tag{3.40}$$

$$\hat{\varphi} = \varphi_{\text{ZPF}}(\hat{a}_q^\dagger + \hat{a}_q) \ , \ \varphi_{\text{ZPF}} = \left(\frac{2E_C}{E_L}\right)^{1/4} . \tag{3.41}$$

The linear term $4E_C\hat{n}^2 + \frac{1}{2}E_L\hat{\varphi}^2$ becomes $\hbar\omega_p\hat{a}_q^\dagger\hat{a}_q$ where $\omega_p = \sqrt{8E_CE_L}/\hbar$. The cosine term $\cos\left(\hat{\varphi} - 2\pi\frac{\Phi_{ext}}{\Phi_0}\right)$ can be calculated using the numerical matrix cosine implemented in Qutip. Numerical diagonalisation of the resulting Hamiltonian matrix yields the eigenenergies and eigenstates of the Fluxonium which can be used to fit spectra as in Fig. 3.7. Calculating the dispersive shift is done by fixing a qubit state independent cavity frequency ω_R and using (3.34).

3.2.5.2 *Harmonic modes*

The second technique is to diagonalise the full bipartite Hamiltonian $\hat{H}$ using the harmonic modes defined in (3.41) and (3.40) again. The choice of the dimensions d_q and d_{cav} of at which $\mathcal{H}_q$ and $\mathcal{H}_{\text{cav}}$ are respectively truncated is important to obtain sufficient precision on the transition frequencies and the dispersive shifts without unnecessarily

slowing down the numerics. Numerical diagonalisation of the Hamiltonian matrix yields the eigenenergies E_l and eigenstates $|\psi_l\rangle$ in order of increasing energy. We proceed to label each of the states with two quantum numbers μ and m corresponding to the most likely number of excitations in state for the qubit and cavity mode respectively. For this we follow a technique developped in [100] and calculate the matrix elements of the dipole operator

$$d_{lm} = \langle\psi_l|\hat{a}_c^\dagger + \hat{a}_c|\psi_m\rangle \ . \tag{3.42}$$

d_{lm} is large when the transition $|\psi_l\rangle - |\psi_m\rangle$ corresponds to a single cavity exictation. This yields ladders of states where the qubit number μ is fixed and the photon number is incremented as we move up the ladder. We can thus label $|\psi_l\rangle$ as $|\nu, m\rangle$ where m is the photon number in the resonator. Assigning the quantum number μ to the states $|\nu, m\rangle$ is done by comparing $|\nu, 0\rangle$ with the product states $|\mu\rangle \otimes |0\rangle$ obtained by direct diagonalisation of the Fluxonium Hamiltonian (3.37). In practice we calculate the overlap

$$|\langle\nu, 0|\left(|\mu\rangle \otimes |0\rangle\right)| \ . \tag{3.43}$$

3.2.5.3 *Normal modes*

The third method diagonalises the full coupled Hamiltonian using the normal modes as suggested in [97]. The basis is obtained by defining the operators $\tilde{a}_c$ and $\tilde{a}_q$ which diagonalise the linear part of the Hamiltonian

$$\hat{H}_{\text{lin}} = \hbar\omega_R\hat{a}_c^\dagger\hat{a}_c + 4E_C\hat{n}^2 + \frac{1}{2}E_L\hat{\varphi}^2 - \hbar g\hat{n}(\hat{a}_c^\dagger + \hat{a}_c) = \hbar\tilde{\omega}_R\tilde{a}_c^\dagger\tilde{a}_c + \hbar\tilde{\omega}_Q\tilde{a}_q^\dagger\tilde{a}_q \ . \tag{3.44}$$

Details on how to find identify the operators $\tilde{a}_c$ and $\tilde{a}_q$ is given in [101] and in Appendix B. Once the operators have been defined we proceed as in the harmonic mode case.

A comparison of the different diagonalisation techniques is given in Fig. 3.8. Quite generally, at $\Phi_{\text{ext}} = \Phi_0/2$, all three simulations agree on the frequency and dispersive shift of the $|0\rangle - |1\rangle$ transition as well as the frequency of the cavity to within less than a percent when the dimension of the qubit Hilbert space becomes large. Specifically, the values calculated using perturbation theory and those using the harmonic modes give almost exactly the same results for all d_q as is visible by the almost perfect overlap between the orange and blue curves in the first column. The real difference between the methods is visible in the second column where we quantify the speed of convergence of the simulated values towards the 'true' values obtained in a simulation with $d_q = 50$. For both the cavity and qubit frequency ω_{01} the diagonalisation using the normal modes converges faster, a fact which motivated this method in [97]. Finally, note that if we want a good estimation of the dispersive shift, the Hilbert space dimension needs to be large: $d_q > 15$. This is a manifestation of the sensitivity of the series in (3.34) to the value of the denominators.

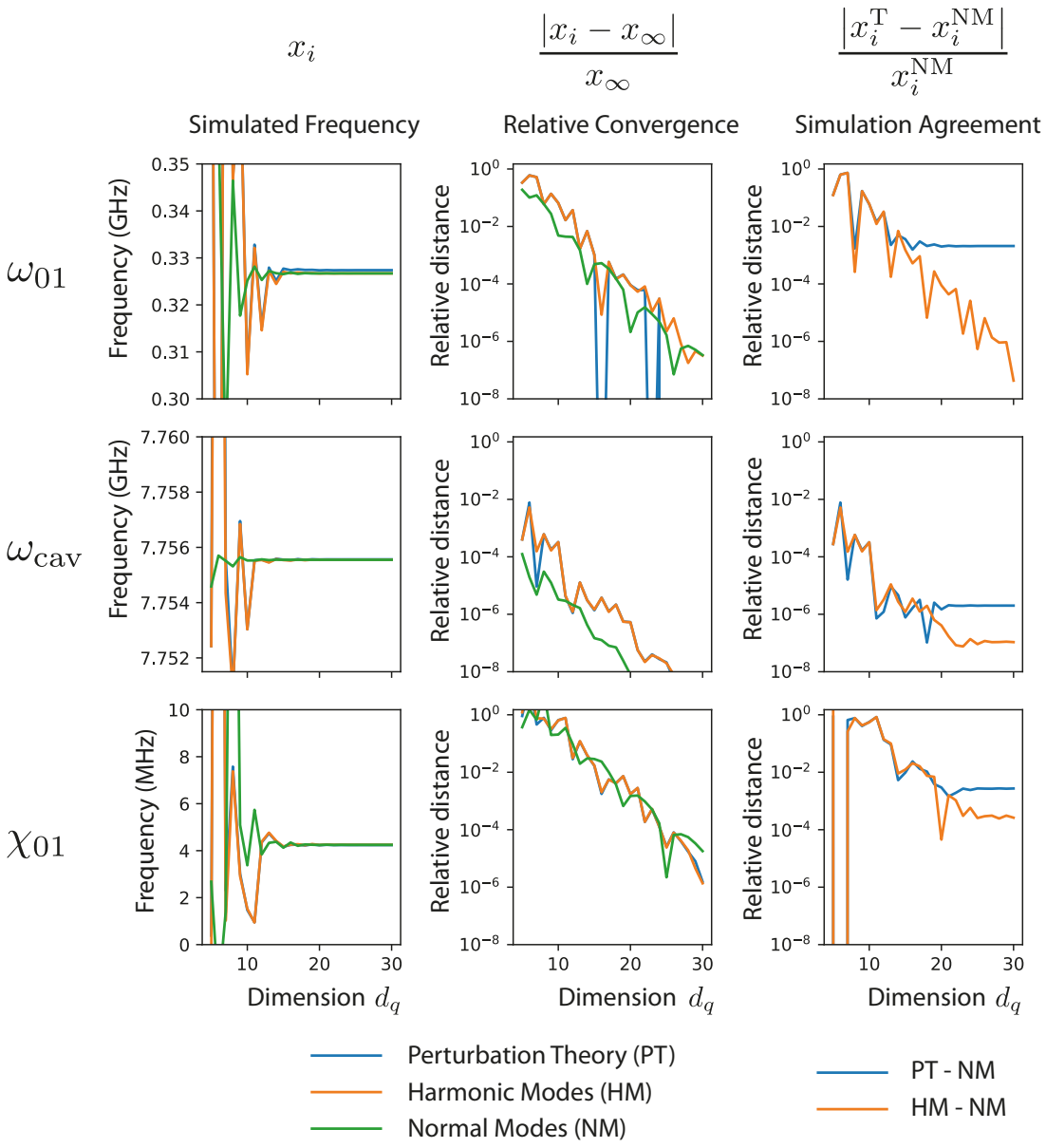

Figure 3.8: Comparison of different numerical techniques to calculate the qubit and cavity transition frequencies as well as the dispersive shift χ_{01} from the Hamiltonian (3.36) as a function of the dimension of the qubit Hilbert space d_q. The three different techniques we use are perturbation theory (PT, blue in the first two columns), the harmonic modes (HM, orange) and the normal modes (NM, green) as described in the text. Data in each row (from top to bottom): frequency of $|0\rangle - |1\rangle$ transition, cavity frequency, dispersive shift of $|0\rangle - |1\rangle$ transition. Data in each column (from left to right): Simulated value of each frequency x_i (i indexes the dimension), relative convergence of x_i to its value x_∞ (for $d_q = 50$), relative distance between different simulations x_i^T (T is the simulation technique) compared to the value of the normal mode simulation. All simulations used the parameters: $E_C = 0.97\,\mathrm{GHz}$, $E_L = 0.69\,\mathrm{GHz}$, $E_J = 4\,\mathrm{GHz}$, $\omega_R = 7.752\,\mathrm{GHz}$, $g = 0.2\,\mathrm{GHz}$, $\Phi_{\mathrm{ext}} = 0.5\Phi_0$. For the HM and NM simulations, the dimension of the cavity Hilbert space was 5.

3.2.6 *Two qubit Gates*

Two qubit gates with Fluxonium are still relatively recent and are not the topic of this thesis, but we provide a brief overview here for the sake of completeness and to illustrate the advantages of the anharmonic spectrum. Quite generally, to obtain a 2 qubit gate you need to find a way of engineering an interaction term $\hat{n}_A\hat{n}_B$ between two qubits A and B. In Transmons this can be done permanently, by coupling the two qubits capacitively in a permanent manner, or temporarily by tuning the qubit frequencies with a magnetic field or by applying a microwave pulse at a well chosen frequency for instance [102, 11, 103, 104]. In practice though, the low anharmonicity and the fact that the frequency of transitions in qubit A depend on the state of qubit B (the transitions $00-10$ and $01-11$ for example) is detrimental to the gate fidelities. Successful workarounds always increase circuit complexity or need additional resources. A significant advantage of Fluxoniums is that coupling within the computational subspace can be mediated by high level transitions as is the case for the dispersive readout. This fact has been exploited in the 2 qubit gate attempts at the university of Maryland [38, 105]. The other approach consists in using the flux tunability, to bring the $0-1$ transitions of both qubits into resonance, implementing a 2 qubit gate whilst remaining in the computational subspace [90].

3.2.7 *Limitations of the Fluxonium qubit*

Despite the numerous advantages and successes of Fluxonium over their Transmon counterparts, they do exhibit some limitations. From a fabrication perspective first of all, Fluxonium devices require fine control over a 3$^{\text{rd}}$ parameter E_L, controlled by the superinductance. Whilst not impossible[8], chains of Josephson junctions do pose a certain fabrication challenge, requiring good control and calibration of e-beam lithography techniques. Furthermore, the additional degree of freedom enabled through Φ_{ext} adds complexity to the measurement setup and can be the source of additional noise. For the experimentalist, it adds another global parameter (one on which everything else depends) to the already highly dimensional parameter space of superconducting experiements. With these engineering challenges come two important physical challenges which are yet to be resolved and are the subject of much of the work in this thesis. The first is the large thermal population of the 1$^{\text{st}}$ excited state at $\Phi_{\text{ext}} = 0.5\Phi_0$. At a temperature of 40 mK the populations of the $|0\rangle$, $|1\rangle$ and $|2\rangle$ states are respectively: 60%, 39%, 1% for a qubit with parameters $E_C = 0.97\,\text{GHz}$, $E_L = 0.69\,\text{GHz}$, $E_J = 4\,\text{GHz}$ such that the $|0\rangle - |1\rangle$ transition has frequency 378 MHz at the sweet spot. This is a big problem for quantum algorithms which expect as input a qubit in a pure state. Initialisation of Fluxoniums to a pure state (usually $|0\rangle$) is a subject of current research and will be discussed in detail in Chapter 5. The second big challenge is Fluxonium readout. Again, Fluxonium may be the most coherent quantum circuit, but this is not of practical importance if the state of the qubit at the end of the algorithm cannot be

8 "Really easy to fabricate", V. Manucharyan, Quantum Information Machines - Les Houches Summer School 2019.

successful determined. Controllably designing a QND dispersive readout for Fluxonium is still a subject of current research and will be the subject of Chapter 6.

3.3 PROTECTED QUBITS

We have discussed in detail the mechanisms which govern error rates in Fluxoniums and in Transmon qubits. The objective of this section will be to sum up some of these considerations and give an overview of how to design even more coherent qubits.

3.3.1 *The laws of error protection*

Environmental noise on quantum degrees of freedom is both ubiquitous and unavoidable and is one of the main sources of errors for quantum systems. Mitigating the effect of noise can be done in three different ways.

1. We can act at the source and reduce the magnitude of the noise affecting our systems. This can be done by filtering the control lines used to address the qubit for example, or by increasing the shielding and thermalisation of our experiments. We should be aware that these efforts can never be perfect, because there will always be a noise source which we will not have considered. We will go into more detail about this topic in Chapters 4 and 5.

2. We can design quantum systems which are as resilient to noise as possible, systems whose fundamental properties make them insensitive to the noise sources we are trying to control. This is the concept of "hardware protection" which we will detail shortly. Of course, even if by design we are able to think of systems insusceptible to noise, this ideal will be confronted to the imperfections of reality where exact control, over fabrication parameters for example is impossible, to achieve.

3. There lies the role of Quantum Error Correction (QEC) whose objective is to detect and correct the residual errors. Error correction presents its own challenges, both from an engineering and physics perspective. Thus, although QEC will be inevitable to have a functioning fault tolerant quantum computer, we should design its building blocks to be as robust as possible to errors, reducing the complexity of the error correction required.

Why can we not rely on error correction techniques? Quite generally, error correction consists increasing the number of error prone systems over which the quantum information is spread in the hope that increased redundency will at some point counter-balance the error rates of each individual subsystem. The subsystem error rate at which point it becomes interesting to implement some kind of QEC is called the "threshold" for that kind of QEC. When the error rate is below the threshold, increasing the number of error prone subsystems can reduce the overall error rate. Moreover, for a constant number of subsystems the overall error rate decreases with the error rate of the individual subsystems or, conversely, when the subsystem error rate is improved the number of required subsystems to achieve an equivalent overall error rate is decreased. These observations mean two things: we need to reduce error rates to a certain point before even being

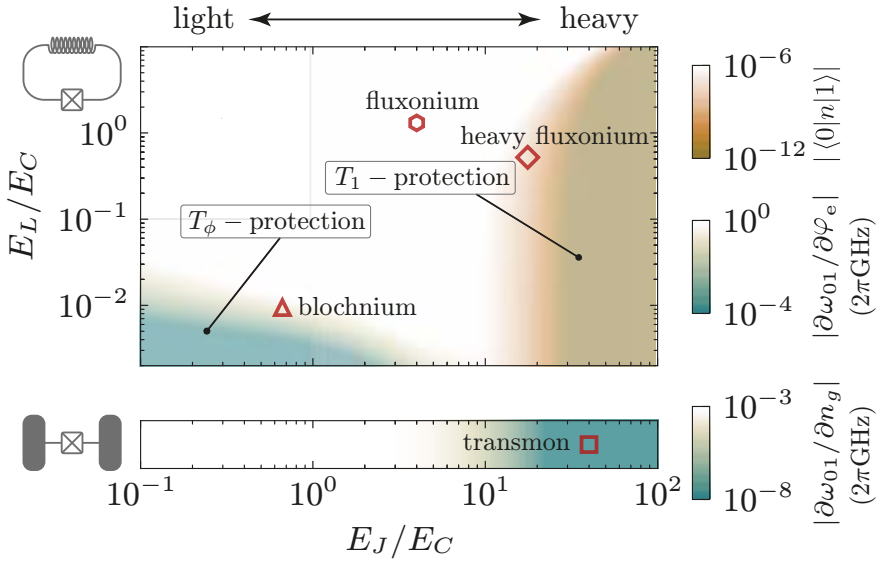

Figure 3.9: Landscape of inductively and capacitively shunted qubits as a function of the E_L/E_C and E_J/E_C ratios. The different markers correspond to the devices described in [18, 67, 109, 79]. The colorscales represent protection against phase-flips (blue) quantified by the dependence of qubit frequency on external parameters $\varphi_e = 2\pi\frac{\Phi_{\text{ext}}}{\Phi_0}$ and n_g ($\Phi_{\text{ext}} = 0.25\Phi_0$ and $n_g = 0.25$), and the protection against bit-flips (brown) is quantified by the charge matrix element $|\langle 0|\hat{n}|1\rangle|$ ($E_C = 1\,\text{GHz}$ and $\Phi_{\text{ext}} = 0.45\Phi_0$). Modes are called light and heavy with respect to the value of the capacitance C which plays the role of the mass in the qubit Hamiltonians. Figure adapted from [59].

able to start with QEC; reducing error rates even further can only be advantageous. As an illustration, the very popular Surface Code [106] needs a large number of physical qubits to obtain a single error tolerant logical qubit at current error rates (on the order of 1000 to 10000[9][107]). Using a hardware efficient approach, involving storing information in the states of a harmonic oscillator, bosonic codes can have exponentially lower bit flip rates than standard transmons [30], potentially allowing us to reduce the hardware overhead dramatically to only a few tens of qubits [108]. The protection afforded by Cat or GKP qubits [29] does not come for free though, with the protection only being guaranteed by the intervention of external pumps to protect the quantum state. Ideally, this external input would not be necessary. Hence the motivation to develop hardware efficient qubits, which by design of their internal degrees of freedom are able to suppress certain error channels.

3.3.2 *The landscape of inductively and capacitively shunted qubits*

Fig. 3.9 provides a good overview of the tradeoffs we have to deal with when designing inductively and capacitively shunted single mode qubits. The main message is that we

9 Note that many thousands of logical qubits are required for computation and that certain qubit gates in the surface code require magic state distillation, increasing the number of required qubits further. At current estimates, 10^8 physical qubits would be required to factor a 2000 bit number using Shor's algorithm.

cannot both have protection against bit-flips and phase-flips, as is visible by the lack of overlap between the brown and blue colored zones in the top panel. The reason for this is the incompatibility between the necessity to have low wavefunction overlap between $|0\rangle$ and $|1\rangle$ for bit-flip protection and the distribution of the wavefunction over many basis states (typically $|n\rangle$ or $|\varphi\rangle$) for phase-flip protection. Blochnium (light Fluxonium) and heavy Fluxonium are exactly opposite in this respect. Ideally, for inductively shunted qubits, you want E_L as small as possible so that the inductor only plays the role of shunting the superconducting islands at zero frequency, removing charge noise but not contributing much to shunting the junction at RF frequencies. This condition is embedded in $E_L/E_J \ll 1$. Then the ratio E_J/E_C determines whether bit-flips or phase-flips are protected. For the Blochnium and heavy Fluxonium points in red, $E_L/E_J \sim 0.015$ and $E_L/E_J \sim 0.036$ respectively, so the large inductance condition is fulfilled. On the y-axis $E_L/E_C = \frac{2}{\pi^2}\left(\frac{R_Q}{Z}\right)^2$ expresses how strongly the high impedance condition must be met: $E_L/E_C < 10^{-2}$ requires $Z > 4.5R_Q$.

The wavefunctions of heavy Fluxonium and Blochnium qubits are shown in Fig. 3.10a&b. The difference in wavefunction localisation in phase space is extremely marked. Even the higher energy levels of heavy fluxonium are very strongly bounded by the potential wells formed by the cosine (leading to exceptionnally long T_1s above 10 ms [109, 110]), whereas in the Blochnium qubit the wavefunctions are delocalised over four wells even for the lowest energy states away from the sweet spot. In comparison, the Fluxonium wavefunctions of Fig. 3.3 lie in some kind of middle ground. As a further illustration of the opposite protection of both qubits, we show the matrix elements $|\langle 0|\hat{\varphi}|1\rangle|$ and $|\langle 0|\hat{n}|1\rangle|$ as well as the derivative of the frequency $\left|\frac{\partial\omega_{01}}{\partial\Phi_{\text{ext}}}\right|$ as a function of the external flux in Fig.3.10c,d&e. In panel d., the lower the value, the higher the protection again energy decay. Notice how the phase matrix element is strongly peaked around $\Phi_{\text{ext}} = 0.5\Phi_0$ for the heavy and normal Fluxonium because only at that flux do the $|0\rangle$ and $|1\rangle$ states hybridise. Blochnium is comparitively unaffected by this as the wavefunctions are already strongly distributed. Heavy Fluxonium shows charge matrix elements orders of magnitude lower than Blochnium at all fluxes because the peak in charge is compensated by an extremely low qubit frequency according to (3.24). Looking at panel e., Blochnium's frequency only depends slightly on flux compared to heavy Fluxonium, except at the sweet spot where the derivatives for all qubits cancel exactly. Note that as the qubit states away from half flux become more and more delocalised in phase space, the qubit becomes more and more tolerant towards deviations from the sweetspot. This is visible in the inset of 3.10 where you can see the Fluxonium qubit's derivative rise much more slowly than for its heavy counterpart and even more slowly for Blochnium. Quite generally, these plots illustrate how standard low frequency Fluxoniums [79] offer some compromise between the extremes of the light and heavy versions.

The reason for the extra bottom panel in Fig. 3.9 is that inductively shunted qubits with $E_L \to 0$ are topologically not equivalent to qubits without the inductive shunt because of the already mentioned offset charge. This perhaps moderates the statement that Blochnium is the dual of the Transmon and heavy Fluxonium is the dual of the Cooper Pair Box. More specifically, a circuit element whose energy is periodic in charge

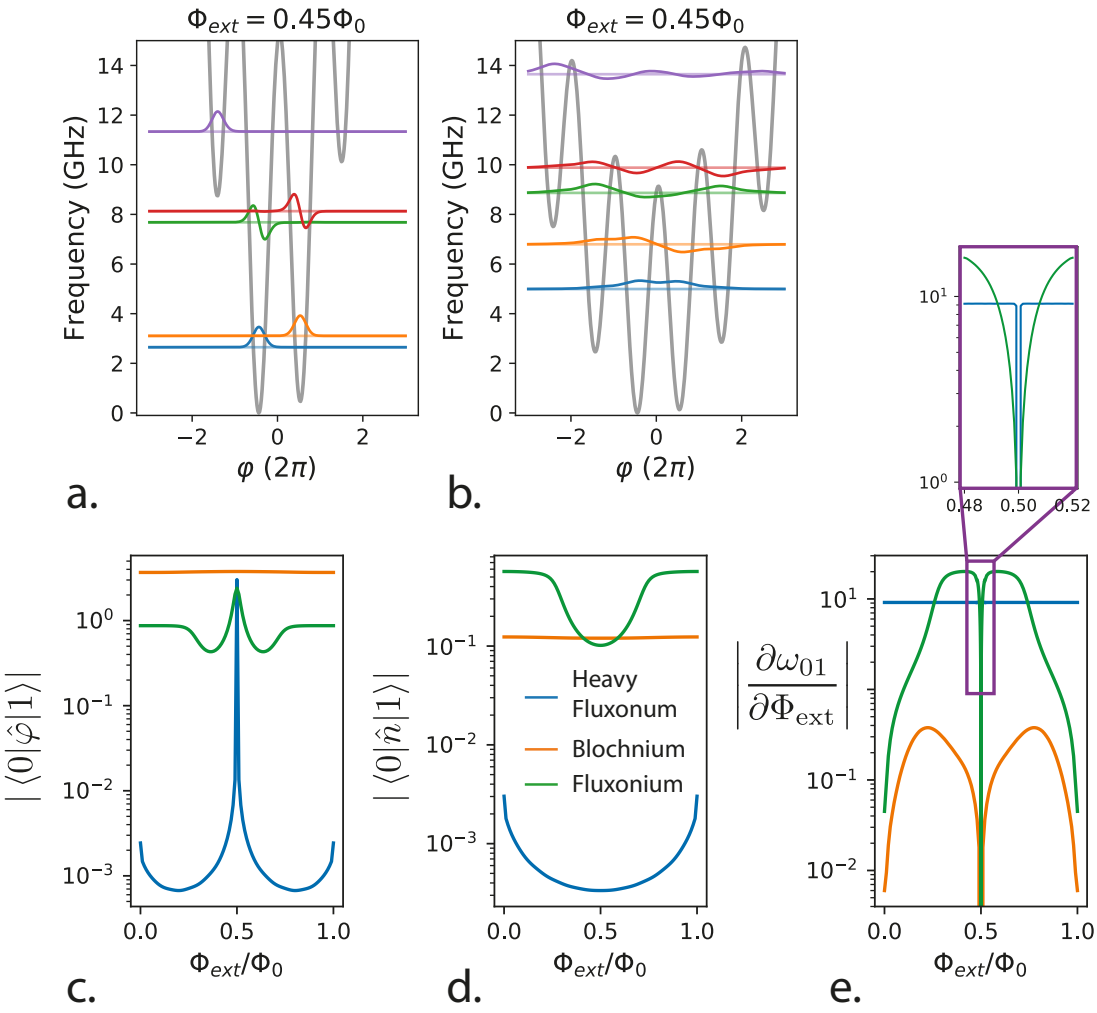

Figure 3.10: Comparison of the properties of the heavy fluxonium in [109] and Blochnium in [67] with the Fluxonium with parameters $E_C = 0.97\,\text{GHz}$, $E_L = 0.69\,\text{GHz}$, $E_J = 4\,\text{GHz}$ we have studied in all figures so far. The wavefunctions of the first 5 energy levels of both qubits (a. heavy fluxonium, b. Blochnium) at $\Phi_{\text{ext}} = 0.45\Phi_0$ are plotted with solid coloured lines, offset by corresponding energies given in GHz (pale coloured lines). In gray we show the potential given by $\frac{1}{2}E_L\varphi^2 - E_J\cos\left(\varphi - 2\pi\frac{\Phi_{\text{ext}}}{\Phi_0}\right)$. c.&d. Comparison of the absolute value of the phase & charge matrix element between states $|0\rangle$ and $|1\rangle$ for all three qubits. e. Comparison of the absolute value of the derivative of ω_{01} with respect to external flux.

is not available, something that would allow localisation of the charge in it's own well, separated by an energy barrier.

Blochnium and heavy Fluxonium do offer interesting properties, but as always, this is not without tradeoffs. Small charge matrix elements and the low frequencies of heavy fluxoniums mean that microwave activated gates are much slower, which can mean work arounds using flux gates [77] or virtual transitions outside the (protected) computational subspace [111]. Low frequencies also require mitigating the thermal population of $|1\rangle$ at dilution fridge temperatures. As an example, the excited state population for a transition at 14 MHz was 49.6% for a base plate temperature of 15 mK in [77]. Furthermore, whilst Blochnium has a "sweet spot everywhere" property, virtually protecting it from flux noise everywhere in the circuit, it does this at the price of reduced anharmonicity for the lower energy levels [67]. Finally, creating an inductance that large is a real fabrication challenge. Some of these issues, notably protecting against energy decay and dephasing simultaneously could potentially be resolved by using multimode circuits.

3.3.3 *The "$0-\pi$" qubit - Beyond single mode circuits*

One of the best characterised multimode noise insensitive qubits is the "$0-\pi$" qubit[112]. Whilst there are others, the bifluxon qubit [113] for example, the "$0-\pi$" presents the advantage of sort of being the assembly of a Transmon and Fluxonium circuit simultaneously, such that many of the arguments discussed previously in this chapter will also be valid here. For a very detailed discussion of "$0-\pi$", Di Paolo's thesis [114] is a good reference and many of the arguments presented here are taken from that work.

The circuit model for the "$0-\pi$" qubit is given in Fig. 3.11a. A circuit theory quantisation leads to the Hamiltonian [111]

$$\hat{H}_{0-\pi} = 4E_C^{\theta}(\hat{n}_\theta - n_g^{\theta})^2 + 4E_C^{\phi}\hat{n}_\phi^2 + E_L\hat{\phi}^2 - 2E_J\cos\hat{\theta}\cos\left(\hat{\phi} - \pi\frac{\Phi_{ext}}{\Phi_0}\right) \quad . \quad (3.45)$$

n_θ and n_ϕ are the conjugate charge numbers to the phases $\theta = \frac{2\pi}{\Phi_0}(-\Phi_1 + \Phi_2 + \Phi_3 - \Phi_4)$ and $\phi = \frac{2\pi}{\Phi_0}(\Phi_1 - \Phi_2 + \Phi_3 - \Phi_4)$ respectively, where Φ_i is the generalised flux at node i. These phase variables define the Transmon like mode (θ) involving the two junctions and the two shunting capacitances, and the Fluxonium like mode (ϕ) involving the two junctions and the two shunting inductances (Fig. 3.11b.). The offset charge n_g^{θ} is present because in the θ mode the superconducting islands either side of the junctions are disconnected. Φ_{ext} is the flux threading the loop created by the two junctions and inductances in the ϕ mode. Importantly, for these modes to be truly Transmon- and Fluxonium-like, E_L should be reduced as far as possible and $E_J/E_C^{\theta} \gg E_J/E_C^{\phi}$. In terms of impedance, we are looking for a low impedance θ mode, such that its wavefunctions are localised in θ, and a high impedance ϕ mode, so that the wavefunctions are delocalised over ϕ. This is possible, given $C_\theta \propto 2(C_J + C)$, $C_\phi \propto 2C_J$, $E_J = E_J^{\text{junction}}/2$ and $E_L = E_L^{\text{inductor}}/2$ following standard combination of parallel capacitors and series inductors, if the shunting capacitance is much larger than the junction capacitance and

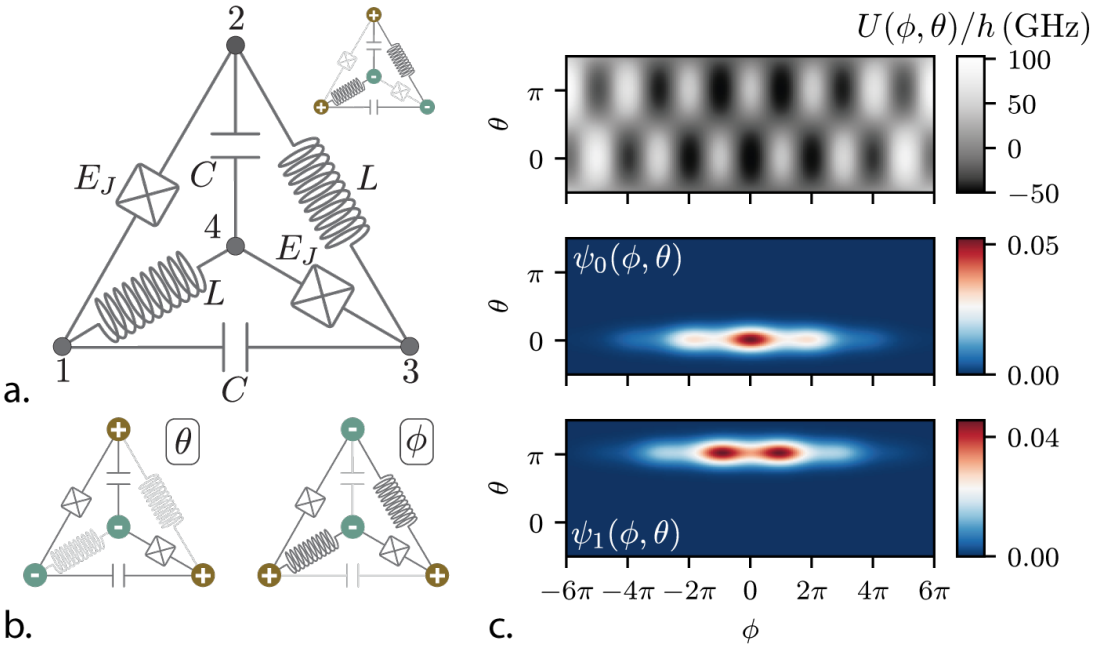

Figure 3.11: Circuit model and wavefunctions of the "$0-\pi$" qubit. a. Full circuit model. With two identical pairs of junctions, capacitances and inductors. The junction capacitance is C_J. The circuit elements participating in the main eigenmodes θ and ϕ of the circuit are represented in b. The harmonic mode of the device is shown above and right of the full circuit. c. Potential and wavefunctions of the "$0-\pi$" Hamiltonian with parameters $E_C^\theta = 0.026\,\text{GHz}$, $E_C^\phi = 56.7\,\text{GHz}$, $E_J = 24.75\,\text{GHz}$ and $E_L = 0.15\,\text{GHz}$. (Top) Potential energy $U(\phi,\theta) = E_L\phi^2 - 2E_J\cos\theta\cos\left(\phi - \pi\frac{\Phi_{ext}}{\Phi_0}\right)$. (Middle and bottom) Ground and first excited eigenstates of the Hamiltonian represented in $\theta-\phi$ space. Subfigures a.&b. are adapted from [111] and subfigure c. from [114].

the shunting inductance much larger than the Josephson inductance. Also worthy of note, because the external flux is spread around a loop containing two junctions, two flux quanta are required to retrieve the periodicity of the ϕ cosine term.

To further our understanding, let's set $\Phi_{\text{ext}} = 0$ and consider the Transmon-like mode θ. Unlike Hamiltonian 3.6, the cosine term $-2E_J \cos\theta$ has a parameter dependent prefactor $\cos\phi$ such that the energy of the mode is minimised not only at $\theta = 0$ (when $\phi = 0$), but also at $\theta = \pi$ (when $\phi = \pi$). Now flipping perspectives, at $\theta = 0$, the ϕ mode describes a Fluxonium Hamiltonian with $\Phi_{\text{ext}} = 0$. At $\theta = \pi$ this is equivalent to Fluxonium at[10] $\Phi_{\text{ext}} = 0.5\Phi_0$. Fig. 3.11c. showing the lowest energy wavefunctions in each potential well along θ illustrates this fact. It is these two states which will form the logical subspace of our qubit. Note that only when E_L is the smallest energy scale in our system are these two states, separated by[11] $\sim E_L\pi^2$, also the lowest energy eigenstates of (3.45). This was not the case in the only "$0-\pi$" experiment to date [111]. How does the qubit defined by these two energy levels fulfill the promise of full protection? Let's start with phase-flips. By working in the Transmon regime, E_J/E_C^θ, the θ degree of freedom is protected from fluctuations in n_g as was explained in Sec. 3.1.1. Flux noise is irrelevant for this mode because there is no loop. The ϕ degree of freedom is protected from flux noise when the parameters E_C^ϕ, E_L and E_J combine in a Blochnium configuration. This configuration being difficult to achieve experimentally, a compromise can be the first order sensitivity afforded at the sweet spot. Finally, the ϕ mode is insensitive to charge noise because of the inductive shunt. How about bit flips? As is evident in Fig. 3.11c., the wavefunction supports of the computational states have negligeable overlap thanks to the large tunneling energy E_J which strongly localises θ. By increasing the system complexity, by using a two mode circuit, we have simultaneously protected against phase and bit-flips.

So should we all be using "$0-\pi$" qubits? No. At least not yet. As always, the mantra that there is no free lunch holds true and "$0-\pi$" is devilishly tricky to fabricate in real life. Reducing cross-capacitances between modes is essential to guarantee $E_C^\phi \gg E_C^\theta$. This was also one of the challenges of Blochnium, a circuit which is only reliably fabricated in a single group worldwide. Also related to fabrication, the description (3.45) of a two mode circuit is only valid if the two capacitors, two inductors and both junctions are identical. This is clearly never true and we are left with an unprotected third mode (top right of Fig. 3.11a.), comprising large capacitances and inductances such that the frequency is low, which is coupled to the θ and ϕ modes. Photon shot noise from this mode can be a limiting factor in the coherence times. What was true for previous devices is also true for "$0-\pi$" qubits and small matrix elements offering bit-flip protection can also impede the realisation of fast protected gates within the computational subspace. The same techniques as used for Fluxonium can be used to resolve these issues. Other, more complex issues regarding readout techniques are also of concern [114]. Concretely, the first experimental realisation of this qubit, whilst

10 This is with respect to the periodicity of Φ_{ext} for Fluxonium, not the $2\Phi_0$ of (3.45).

11 To see this, replace θ and ϕ in the "$0-\pi$" Hamiltonian by their 2^{nd} moments in either potential well: the pairs $(0,0)$ and $(\pi, \sim\pi)$.

impressive, ran into all of these limitations [111]. Gate speeds were slow (800 ns π-pulse) and outside of the computational subspace; the qubit was only insensitive to flux noise at the sweet spot; and whilst $T_1 = 1.56\,\text{ms}$ was state of the art, $T_2 = 8.5\,\mu\text{s}$ would be what is expected of a Transmon without particular optimisation. Resolving these issues is a subject of continuing research [114].

3.4 CONCLUSION

In this chapter we have explored the ingredients which make a good qubit. From the reinterpretation of the Transmon's charge noise insensitivity to the "$0-\pi$" qubit's two modes, delocalising or, on the contrary, localising qubit eigenstates can be a resource for protection against errors. We have also seen that thinking about circuits in terms of their impedance can be useful in identifying which of the two conjugate variables n and φ will fluctuate the most. These considerations help understand in detail the Fluxonium qubit whose first order flux noise insensitivity and low frequency have lead it to be the most coherent superconducting circuit. We also spent some time on the non-trivial numerics of Fluxonium which will come in useful in Chapter 6. So far though, our discussion has being focused on all these qubits in isolation. Yet, like any quantum system they constantly interact with their environment, as we've already exposed when discussing loss mechanisms. Thankfully, this interaction is not completely out of our control. In the following chapter we explore how to choose the right materials for superconducting circuits and how to design the specific interactions we need to protect and control quantum devices.

4

DESIGNING AND FABRICATING SUPERCONDUCTING CIRCUITS

In the previous chapter we focused on qubits with hardware protection to noise. The properties of these devices meant that under certain conditions they were protected from bit-flip and phase-flip errors. The rates at which bit-flips occur are given by Fermi's golden rule (3.22) which we have studied previously. Protected qubits are designed to minimise the matrix element $\left|\langle 0|\hat{O}|1\rangle\right|^2$, ideally bringing it to zero. Additionnally it is desirable to reduce the noise spectral density $S_{XX}(\omega_{01})$ to decrease Γ_1. The phase-flip rate Γ_ϕ can also be described as a function of S_{XX}. The magnitude of the coherences (off diagonal elements) of the density matrix of a two level system decay according to [45]

$$|\rho_{01}(t)| \propto \exp\left[-2\cdot\left|\frac{\partial\omega_{01}}{\partial X}\right|^2\int_{-\infty}^{\infty}\frac{\sin^2\left(\frac{\omega t}{2}\right)}{\omega^2}S_{XX}(\omega)\mathrm{d}\omega\right] \ , \tag{4.1}$$

such that in the case of white noise $S_{XX}(\omega) = S_{XX}^{\text{white}}$ we retrieve the expression

$$|\rho_{01}(t)| \propto \exp\left[-\frac{1}{2}\left|\frac{\partial\omega_{01}}{\partial X}\right|^2 S_{XX}^{\text{white}}t\right] = \exp\left[-\Gamma_\phi t\right] \ , \tag{4.2}$$

corresponding to an exponential decay of the coherences[1]. In this chapter we explain how material, fabrication and design choices can help reduce the magnitude of $S_{XX}(\omega)$ and improve the total coherence times T_2 of superconducting qubits.

4.1 CHOOSING MATERIALS FOR CIRCUIT QED

4.1.1 *Reviewing the properties of superconducting materials*

A number of considerations come into play when deciding which materials to use for superconducting circuits. Clearly, they ought to be superconducting at dilution refrigerator temperatures below 100 mK, though the higher the transition temperature to a normal metal is, the better. This is perhaps best evidenced by the loss-rate due to quasiparticles (3.28) which is proportional to the square-root of the superconducting gap Δ, itself related to the critical temperature T_c

$$\Delta = 1.764 k_B T_c \ . \tag{4.3}$$

Converting the critical temperature of aluminium 1.2 K to a frequency Δ/h we obtain 44 GHz, usually above the energies at play in superconducting circuits. The chosen

1 Often the noise spectrum is not white but depends on inverse of the frequency. This leads to a Gaussian type decay $e^{-\Gamma_\phi^2 t^2}$ [115].

superconductors should also be easy to pattern, using chemical and plasma etching or liftoff techniques for example, and easy to deposit on the substrate: sputtering and evaporation are standard techniques. This facilitates the iteration of samples, hopefully simplifying the production of complex geometries. The combination of substrate and superconductor should be low loss. Indeed, as we discussed in chapter 3, dielectrics are one of the main sources of uncontrolled loss in superconducting circuits.

With these criteria in mind, the superconducting circuits community has converged towards a relatively short list of materials for making devices. For the non-conductive substrate, high resistivity silicon and pure sapphire are the go to materials. For the Josephson junctions, aluminium is standard. Attempts with other materials such as niobium exist [116], although they are notoriously more difficult to fabricate and have not achieved high coherence times. For the superconducting junction pads, or CPW resonators and transmission lines, the (non-exhaustive) list is longer: aluminium (Al), niobium (Nb), titanium nitride (TiN), niobium titanium nitride (NbTiN) and recently tantalum (Ta) have been used. If a high kinetic inductance is specifically required, TiN, NbTiN or niobium nitride (NbN) are interesting candidates or granular aluminium (GraAl) which successfully replaced the junction chain in a Fluxonium [74] and the single junction of a Transmon device [117]. Tungsten (W) nanowires [118], boron doped silicon (Si:B) [119] have also been used, as have materials with a high kinetic inductance like niobium silicate (NbSi) [120] or rhenium (Re) [121].

In the tables 4.1, 4.2, 4.3 we give an overview of the properties of these materials at the time of writing (May 2021). The first two show experiments giving useful benchmarks of the losses of each material by looking at the quality factors of CPW resonators and qubit coherences respectively. Importantly, to correctly quantify the dominant losses in superconducting circuits, experiments which work at the level of single excitations, measuring the Q-factor should be done using the smallest number of circulating photons in the resonator as possible. This means measuring at low enough power and at low enough temperature so that the thermal occupation of the resonator is low. Indeed, the quality factors of superconducting resonators often increase with photon number, as two level systems (TLS) at the interfaces become saturated by the energy exchange with the photons [126]. We thus show the internal quality factor Q_i for both $\bar{n} \sim 1$ and $\bar{n} \sim 10^6$. The third table, presents a summary of the known best achieved material properties for superconducting circuits. We can use the information assembled here to guide the choice of materials for cQED experiments.

Focusing first on the choice between crystalline silicon and sapphire as a substrate, note that both materials exhibit loss tangents $\tan\delta < 10^{-6}$ in the microwave domain although sapphire may be slightly less lossy [148]. The quality factors of CPW resonators are not substantially different between the two though, with single photon values generally in the range $1-2\times10^6$. Currently the best achieved coherences, both in Transmons and Fluxoniums, are found on sapphire substrates. To add perspective though, the lifetime of Fluxonium on sapphire was only improved by a factor 2, with respect to its

Exp	Metal	Substrate	Deposition	Substrate cleaning before deposition	Etch	$\omega_R/2\pi$ (GHz)	Q_i (10^4) $\bar{n} \sim 1$	Q_i (10^4) $\bar{n} \sim 10^6$	Remarks
[122]	Al	Sapphire	MBE	200°C anneal in vac 850°C anneal in O2	BCl_3/Cl_2	6.1	170	850	-
[123]	Al	Si (111)	Evaporation	?	Dry	5	70	400	Magnetic shielding cryoperm + tin
[124]	NbTiN	Si (100)	Sputtering	HF + HMDS	SF_6 then C_4F_8	6.41	110	200	Trenching
[125]	NbTiN	Sapphire	Sputtering	-	SF_6/O_2	4.95	?	> 10	$Q_i(\bar{n} \approx 1) > 10^5$ for $B_\parallel < 6\,\mathrm{T}$ & $B_\perp < 20\,\mathrm{mT}$
[126]	TiN	Si (001) $> 3500\,\Omega\,\mathrm{cm}$	Sputtering	-	BCl_3/Cl_2	5-6	200	1000	Trenching
[127]	TiN	Si (001) $> 10^4\,\Omega\,\mathrm{cm}$	Sputtering	HF	Cl_2 then SF_6	3 - 6	500	2000	-
[128]	TiN	Si (111) $> 10^4\,\Omega\,\mathrm{cm}$	ALD	HF	BCl_3/Cl_2	7.27	100	240	-
[123]	TiN	Si (111)	Sputtering	anneal 1200°C	Wet	5	100	1000	No improvement with magnetic shielding
[129]	GrAl	Sapphire	Evaporation	-	Liftoff	4.55	120	2000	3D geometry, not CPW
[130]	Nb	Si $> 10^4\,\Omega\,\mathrm{cm}$	PVD	BOE + HMDS BOE after etch	SF_6	5.2 - 5.6	110	-	-
[131]	Nb	Si $> 3000\,\Omega\,\mathrm{cm}$	PVD	HF HF after etch	Cl_2	3 - 6	700	1100	Lumped element resonators
[132]	Nb	Si (100) $> 8000\,\Omega\,\mathrm{cm}$	Sputtering	piranha 120°C + HF BOE after etch	BCl_3/Cl_2	6.25 - 7	600	1250	-
[133]	NbN	Si $1 - 15\,\Omega\,\mathrm{cm}$	Sputtering	-	SF_6/O_2	5.22	2	100	$Q_i(\bar{n} \approx 100) > 10^4$ for $B_\parallel < 6\,\mathrm{T}$ & $B_\perp < 300\,\mathrm{mT}$
[134]	NbN	Sapphire	Sputtering	-	NF_3	4.4	15	35	$Q_i > 10^5$ for $B_\parallel < 400\,\mathrm{mT}$
[119]	Si:B	Si (100) $> 3\,\mathrm{k}\Omega$	Epitaxy	-	SF_6	1.48	0.392	-	Al leads and ground plane
[118]	W	Si	Helium beam assisted deposition	-	SF_6	4.5	0.399	-	W nanowires embedded in Nb resonators
[120]	NbSi	Si	Evaporation	-	Liftoff	6.7	1.6		$\bar{n}$ not given
[121]	Re	Sapphire	Epitaxy	anneal 1100°C	SF_6	6	1.4		$\bar{n}$ not given

Table 4.1: Overview of some recent experiments (before May 2021) measuring Q-factors of microwave resonators on different substrates. Sapphire substrates all have (0001) orientation. MBE: Molecular Beam Epitaxy; ALD: Atomic Layer Deposition; PVD: Physical Vapour Deposition; HF: Hydrofluoric acid; HMDS: hexamethyldisilazane; BOE: Buffered Oxide Etchant. In the etch column we detail the gasses used for reactive ion etching, Dry corresponds to the case where no details are given, Wet is a chemical etch and Liftoff means no etch is needed. We use a question mark ? to denote an absence of information. Q_i is the internal quality factor, $\bar{n}$ is the average photon number in the resonator.

Exp	Metal	Substrate	Deposition	Substrate cleaning before deposition	Qubit	$\omega_Q/2\pi$ (GHz)	T_1 (µs)	T_2 (µs)	$Q = T_1\omega_Q$ (10^6)	Remarks
[135]	Ta	Sapphire	Sputtering α phase, 500°C	piranha + O2 plasma piranha before spin piranha + TAMI after etch	2D	3.1	362	105	7.1	Wet etch
[62]	Ta	Sapphire	Sputtering α phase	?	2D	3.9	503	463 (E)	11.6	Dry etch
[130]	Nb	Si $>10^4\,\Omega\,$cm	PVD	BOE + HMDS BOE after etch	2D	3.8 - 4.2	114	-	2.7 - 3.0	-
[136]	-	Sapphire	Evaporation	-	3D	4.1	70	92	1.8	-
[137]	-	Sapphire	Evaporation	-	3D	4.75	110	220 (E)	3.3	Custom filtering
[138]	-	Sapphire	Evaportation	base piranha	3D	?	151	-	?	-
[79]	-	Silicon	Evaporation	-	3D Fluxo	0.395	500	510	1.2	-
[33]	-	Sapphire	Evaporation	-	3D Fluxo	0.163	1200	1160	1.2	-
[139]	Al	Sapphire	MBE	200°C anneal in vac 850°C anneal in O2	2D Squid	5.408	44	15	1.5	-
[140]	Al	Sapphire	Evaporation	-	2D	6.457	22	30	0.9	-
[141]	Al	Silicon	Evaporation	-	2D	4.4 & 3.8	49	95	1.3	-

Table 4.2: Overview of some recent experiments (before May 2021) measuring qubit coherence times on different substrates. Sapphire substrates all have (0001) orientation. MBE: Molecular Beam Epitaxy; PVD: Physical Vapour Deposition; BOE: Buffered Oxide Etch; HMDS: hexamethyldisilazane; TAMI: sequential cleaning in toluene, acetone, methanol and isopropanol for 2 minutes. A '-' in the first column means there is no ground plane metal, as in the case of 3D Transmons for example. We use a question mark ? to denote an absence of information. In the T_2 column, all results are given for Ramsey experiments, except those with (E) which denoted a spin echo measurement. T_1 and T_2 are the maximum achieved values for each experiment (not necessarily the same chip).

Metal	Q_i (10^4) $\bar{n} \sim 1$	T_1 (µs)	Silicon $\tan\delta$ (10^{-4})	Sapphire $\tan\delta$ (10^{-4})	L_K nH/□	T_C (K)
Al	170 [122]	49 [141]	MS: 1.3 (3.2) SA: 35 (29) MA: 327 (294) [142]	26 [137]	-	1.2 [51]
Nb	700 [131]	114 [130]	MS: 3.5 [131]	-	-	9.1 - 9.2 [143, 131]
TiN	500 [127]	-	MS: 4.6 (2.7) SA: 17 (12) MA: 33 (35) [142]	-	0.1 [73]	2 - 4 [127]
NbTiN	110 [124]	-	-	-	0.1 [73]	-
NbN	2 [133]	-	-	-	0.1 - 0.2 [73, 133]	7.4 [133]
Ta	120 [144]	503 [62]	-	-	-	4.2-4.38 [135, 62]
GrAl	120 [129]	-	-	24 - 40 [145, 129]	2 [145]	1.9 - 2.2 [146]
Si:B [119]	0.392	-	-	-	0.05 - 0.5	0.7
W [118]	0.399	-	-	-	0.015	4 - 6
NbSi [120]	1.6	-	-	-	0.83	0.85
Re [121]	1.4	-	-	-	0.002	1.9

Table 4.3: Review of the best parameters for superconducting circuits achieved using different electrode materials some with Al/AlO_X/Al Josephson junctions as of May 2021. T_1 and Q_i are the maximum achieved values available for Transmons and CPW (or lumped element) resonators respectively available in the litterature. The values in the $\tan\delta$ columns are given for the interface loss. When available, the loss tangents for each interface are given (MS: Metal - Substrate; SA: Substrate - Air; MA: Metal - Air). Loss tangents of the bulk are $\tan\delta = 1.3 - 2.8 \times 10^{-7}$ for silicon [142, 147, 148] and $\tan\delta = 2 \times 10^{-8}$ for c-plane sapphire [149]. We cite the loss tangents of the interfaces after HF treatment in parentheses. For an even more complete treatment of the interface dielectric losses see the supplementary material of [126].

silicon counterpart, despite its frequency being halved[2]. Had the dielectric losses been the limiting factor we would have expected a four fold increase according to 3.1. For the Transmon experiments [135, 62], the effect of using a sapphire substrate cannot be separated from the novel use of tantalum, such that we are unable to conclude about the contribution of the dielectric to this result. It has been hypothesised though, that the higher band-gap of sapphire compared to silicon would make sapphire based devices less sensitive to cosmic ray induced charge noise [150]. It thus appears that, at present, the loss from the bulk substrate should not be an overriding factor in the choice of substrate. Indeed, in many geometries, the quality factors of superconducting CPW resonators and qubit are limited by the losses at the metal - substrate (MS), substrate - air (SA) and metal - air (MA) interfaces [147, 142, 151]. Precise knowledge of the losses of each of these interfaces combined with detailed electromagnetic simulations would allow us to design devices with the highest quality factors possible. Yet, quantifying the loss tangents of the interfaces is difficult and has only been achieved by a single group so far for aluminium and TiN on silicon [147] [3]. Nevertheless, surface preparation before metal deposition or liftoff appears critical. A number of groups are now using hydrofluoric acid (or a derivative) to remove oxides at the MS interface with silicon, and this has consistently lead to higher Q-factors and coherences [124, 130, 135, 142, 148, 62]. High temperature annealing in a controlled atmosphere has also proven successful [122, 123], while ion milling was shown to have negative effects on quality factors [130]. Another strategy to reduce losses can be trenching for example [126], but this makes a good contact between the aluminium junctions and the surrounding superconductor difficult to obtain. In the end, practical considerations around fabrication - sapphire is transparent, difficult to etch and non-conductive[4]; the quality of silicon wafer batches can be unpredictable[5] and crystalline orientation is important - can tip the balance in favour of one or the other.

The choice of material for the superconductor depends strongly on the properties wanted for the final circuit. NbTiN [124], Al [122], TiN [126, 127, 128] and Nb [130, 132, 131] co-planar waveguide resonators have been demonstrated to have internal quality factors above $Q_i = 10^6$, and Transmon qubits contacted to Al [139], Nb [130] and Ta [135, 62] have some of the longest coherences ever reported[6]. Another criterium is the response of materials under external magnetic fields. TiN, NbTiN, NbN and GrAl

2 Experiments [79] and [33] also used a very similar fabrication process.

3 The difficulty lies in controllably varying the participations of each interface in the total loss so as to invert the matrix relating the measured quality factors to the loss tangents. Some works have tried to modify the geometry of 3D Transmon devices to be more or less sensitive to different interfaces, but were only able to extract a weighted sum of the interface loss tangents [137], or had too large of a spread in the losses from different devices to be conclusive [138]. The authors of [147] put their success down to the number of devices measured, the novel isotropic etch process used to vary the 3D geometry of their resonators, and the cross-sectional imaging of each device using an SEM, allowing precise electromagnetic simulations.

4 Transparency makes figuring out which side the metal is on tricky, and the fact that it is an electrical insulator means SEM images are impossible without a conductive discharging layer.

5 Some groups have got into the habit of ordering multiple batches of wafers, testing resonators made one a single wafer from each batch and only keeping the batch which works best [148].

6 In a blog post from their quantum computing division dated 4$^{\text{th}}$ March 2019, IBM showed a measurement on a Transmon with $T_1 = 500\,\mu s$, surpassing both of the previously mentioned devices [152]. IBM

resonators in particular have been shown to be insensitive to these with quality factors above $Q_i = 10^5$ for in plane magnetic fields of the order of 1 T and out of plane fields in the mT range for GrAl [154] and NbTiN [125], and for fields on the order of the earth's magnetic field $\sim 200\,\mu$T for TiN [123]. This property is particularly interesting for circuits integrating devices like Fluxonium which need to use an external magnetic field to obtain the correct flux working point. When high kinetic inductance is necessary, kinetic inductance detectors (KID) for example, fields close to superconducting circuits, the materials considerations change once again. GrAl and NbN nanowire resonators have demonstrated Q-factors above 10^5 [154, 155], showing that long photon lifetimes and high impedance are compatible. Finally NbTiN and GrAl have been integrated into Fluxonium devices [74, 156] as a replacement for the junction chain for example.

A major issue with strategies for studying materials for superconducting circuits is the difficulty of comparability between results. A number of factors can influence the quality factors and coherences of superconducting qubits, choice of materials but also electromagnetic packaging [157], radiation shielding [35], microwave line filtering [137, 158]. Evolutions in hygrometry throughout the year and variations in background noise during the day due to human activities can also impact junction fabrication and experimental results respectively. Thus, detailing exactly what material properties are desirable for quantum circuits remains an open problem in general and is a topic of current research.

4.1.2 *Optimising the quality factors of TiN CPW resonators*

Given the encouraging results published in the literature regarding TiN CPW resonators (see Tab. 4.1), we decided to fabricate TiN resonators ourselves in the hope of using them in future experiments in the group. In particular, the moderate magnetic field insensitivity of the quality factor is an interesting property for devices using a Fluxonium given the use of external fields to achieve $\Phi_{\text{ext}} = \Phi_0/2$. As a benchmark for the CPW resonators, we used the intrinsic quality factors Q_i. This has an immediate design implication as, for a two port cavity, only measurements of both S_{11} and S_{21} yield enough information to determine all the coupling κ_i, $\kappa_{c,1}$ and $\kappa_{c,2}$ (see Sec. 2.5.4 for the formulas for resonators in reflection and transmission). Whilst we can cable a dilution refrigerator to make this measurement possible, by using circulators on the output port of the cavity for example, this would limit us to measuring a single resonator per input and output line in the fridge (without using microwave switches at base temperature). Faced with this issue, we chose to use a 'hanger' geometry. As can be seen in Fig. 4.1a. we place 5 CPW resonators coupled by a single port to the same transmission line. The resonators are separated in frequency by about $300 - 400\,$MHz

further improved this claim this in a Tweet on the 20$^{\text{th}}$ of May 2021 by showing a $T_1 = 1.1\,$ms [153]. The techniques and materials use to achieve these results are not publicly available.

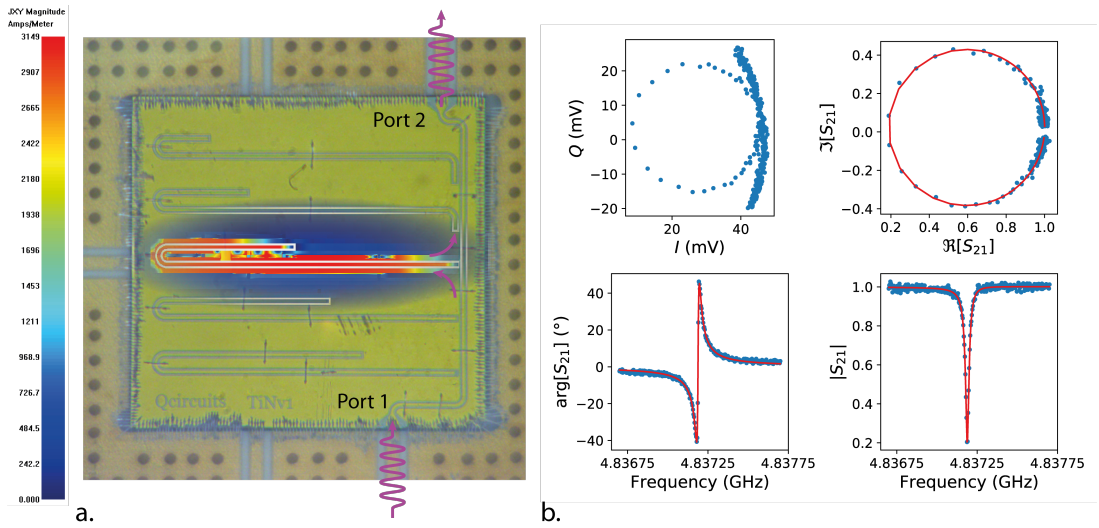

Figure 4.1: a. Hanger resonators fabricated in TiN on a silicon substrate. Purple arrows show the fields propating from port 1, to the resonator and finally to port 2. An overlay from a Sonnet simulation shows how the current density is distributed inside the chip, illustrating how we can address each resonator independently. The chip is wirebonded to a PCB (Printed Circuit Board) visible around the edges. b. Typical response measurement of a resonator using a hanger geometry. We show the raw data in the IQ-plane in the top left subplot and the value of S_{21} after calibration of the phase offset, gain and electrical delay in the others. Red lines are fits to the calibrated data using (4.4). For this resonator the fit parameters are: $\omega_R = 2\pi \times 4.837\,189\,\text{GHz}$, $\omega_0 = \omega_R - 2\pi \times 0.85\,\text{kHz}$, $Q_c = 1.62 \times 10^5$ and $Q_i = 6.95 \times 10^5$.

between 4.5 and 6 GHz so we can address them each separately. For each resonator, a response measurement from port 1 to port 2 of the chip can be described by [159]

$$S_{21}(\omega) = \frac{Q_c + 2iQ_cQ_i\left(\frac{\omega-\omega_R}{\omega_R} + \frac{\omega_R-\omega_0}{\omega_0}\right)}{(Q_i+Q_c) + 2iQ_cQ_i\frac{\omega-\omega_R}{\omega_R}}\,. \tag{4.4}$$

Q_i and Q_c are the quality factors associated with the intrinsic losses of the resonator and the coupling to the transmission line respectively, ω_R is the resonance frequency and ω_0 is the 'bare' resonator frequency. Indeed, this expression takes into account impedance mismatches either side of the transmission line which deform the response function of the resonator. If there are no mismatches, $\omega_R = \omega_0$ and the response function becomes symmetric

$$S_{21}^{\text{sym}}(\omega) = \frac{Q_c + 2iQ_cQ_i\frac{\omega-\omega_R}{\omega_R}}{(Q_i+Q_c) + 2iQ_cQ_i\frac{\omega-\omega_R}{\omega_R}}\,. \tag{4.5}$$

In the symmetric case (4.5), at resonance $S_{21}^{\text{sym}}(\omega_R) = \frac{Q_c}{Q_c+Q_i}$, such that we are most sensitive to the value of Q_i when $Q_i \sim Q_c$. Thus without any a priori knowledge of Q_i we designed our resonators with variable capacitive coupling Q_c to the transmission line, visible in Fig. 4.1a. by the increasing proximity between resonator and transmission line. Going from top to bottom Q_C increases by 3 orders of magnitude from $Q_C \sim 6000$ to $Q_C \sim 10^6$. In reality we never get a direct record of $S_{21}(\omega)$. The experimental setup used

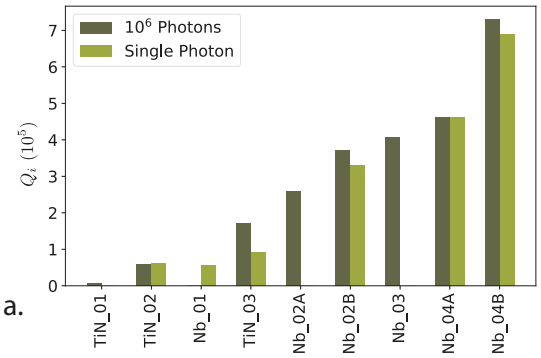

b.

Resonance	Metal	$\omega_Q/2\pi$ (GHz)	Details
TiN_01	TiN	4.5	
TiN_02	TiN	5.4	
Nb_01	Nb	9.3	
TiN_03	TiN	6.3	TiN_02 with HF dip
Nb_02A	Nb	5.3	HF dip before RIE
Nb_02B	Nb	4.8	
Nb_03	Nb	4.5	HF cleaning after RIE
Nb_04A	Nb	5.2	HF dip after RIE + holed PCB
Nb_04B	Nb	4.8	

Figure 4.2: Summary of results from the resonator measurements. a. Quality factors of the different resonators depending on the average number of photons circulating inside. Not all resonators had a hanger geometry, some were used in experiments ongoing in the group at the time of the experimental work. b. Material and fabrication details for each resonator measured in a.

for the measurement introduces a phase offset ϕ, additional gain α and an electrical delay τ. These can be modeled by defining

$$S_{21}^{\text{exp}}(\omega) = \alpha e^{i\phi} e^{i\omega\tau} S_{21}(\omega) \ . \tag{4.6}$$

Because of this, rather than resembling a circle in the complex plane the data is twisted like in the top right panel of Fig. 4.1b and the couplings and resonant frequency cannot be directly determined without further treatment. An algorithm for resolving this issue is given in [160] on which we base ourselves for the fits in this thesis. Detailed discussions are also given in [161, 122].

In Fig 4.2 we show the measured quality factors (a.) for resonators out of TiN and Nb having undergone different treatments (b.). The quality factors measured for TiN are disappointing, given $Q_i = 1.7 \times 10^5$ at the single photon level in regard to the state of the art $Q_i = 5 \times 10^6$ [127]. We put this down to a lack of control of the precise stoichiometry of the TiN films measured thanks to an EDX (Energy Dispersive X-ray) analysis after deposition (see Tab. C.1 in Appendix C for details). Indeed, according to [127] high Q TiN films exhibit a low but non-zero level of oxygen inclusion in the structure, which depends strongly on the deposition parameters used. In our case, the use of a shared sputtering machine with a variety of contaminants and whose chamber was regularly exposed to air (targets were changed weekly) did not allow for ideal deposition conditions. Furthermore, the complicated fabrication workflow spread over three different cleanrooms in Lyon was not conducive to the iterative process needed to develop new recipes. Nevertheless, some progress was made with the surface treatment of metalic films. On both niobium films deposited by colleagues in Paris and with our own TiN samples, HF treatement after the plasma etch increased the measured quality factors. In particular, a TiN sample mesured before and after an HF dip showed an increased quality factor after after the acid treatment. We also observed increased quality factors by using a holed PCB to remove interferences between its box mode and the resonators on our chip and to attenuate the losses of the dieletric below the substrate..

This adds weight to the observation that spurious electromagnetic modes in close proximity to quantum circuits can be detrimental to quality factors [157] and motivated in part the current redesign of our sample holder. Thus, following this study, drilling a hole in the PCB and preparing chips with HF before measurement was generalised to all experiments in the group.

As we have made evident in this part, the choice of materials for superconducting circuits, whilst important, is not always the limiting factor: many other elements play a role in controlling the losses. In particular, a successful initial electromagnetic design can have a large influence on our ability to achieve what we want in cQED experiments as is exemplified by the requirement $Q_c = Q_i$ for hanger resonators. In the next part, we will explore some of the techniques used to design the circuits measured in this thesis.

4.2 CONTROLLING LOSSES IN A 2D FLUXONIUM DEVICE

Designing circuits for cQED experiments is a balancing act between the experiential and the intuitive. Experiential, because a great deal of iteration and trial and error is necessary to converge on the desired parameters. Intuitive, because knowing from where to start the iterative process requires an deep understanding of Maxwell's equations at GHz frequencies possessed by trained physicists and microwave engineers. Yet, circuit design is reaching a sufficient level of maturity that a number of standard tasks can be delegated to computers. Companies like IBM for example have released software which allows a high level of automation in circuit design [162]. In the following sections we give some details into how we can design quantum circuits starting from an idea for an experiment. We will look at some theoretical and software tools used to design the experiments discussed in this thesis. A 3D Transmon experiment will illustrate the use of Black Box Quantisation (BBQ), Energy Participation Ratios (EPR) and the software package pyEPR, and the design of 2D Fluxonium chips will show how we can estimate loss rates at the simulation stage.

4.2.1 *Basics of circuit design*

In Fig. 4.3 we show the different stages necessary to go from an idea to a cQED experiment. We start with an idea, say to make a 2D Fluxonium qubit inductively coupled to a readout resonator. We can formalise this idea, by writing down a Hamiltonian whose dynamics produces the physical effects we would like to measure. For the case of the 2D Fluxonium, the Hamiltonian is given by the expression of Fig. 4.4a. it is then practical to create an ideal electrical circuit model (Fig. 4.4b.) which, when quantised, gives an expression for the parameters of the Hamiltonian as a function of the values of the circuit elements. We gave examples of this in Chapter 2 when deriving the expressions for the dispersive readout or Rabi oscillations. Next, we make a first design of our circuit by using lumped or distributed elements which reproduce the ideal circuit model. This design is heavily constrained. By the Hamiltonian obviously, as the design's objective is to engineer $\hat{H}$, but also by fabrication and experimental constraints. If we make the

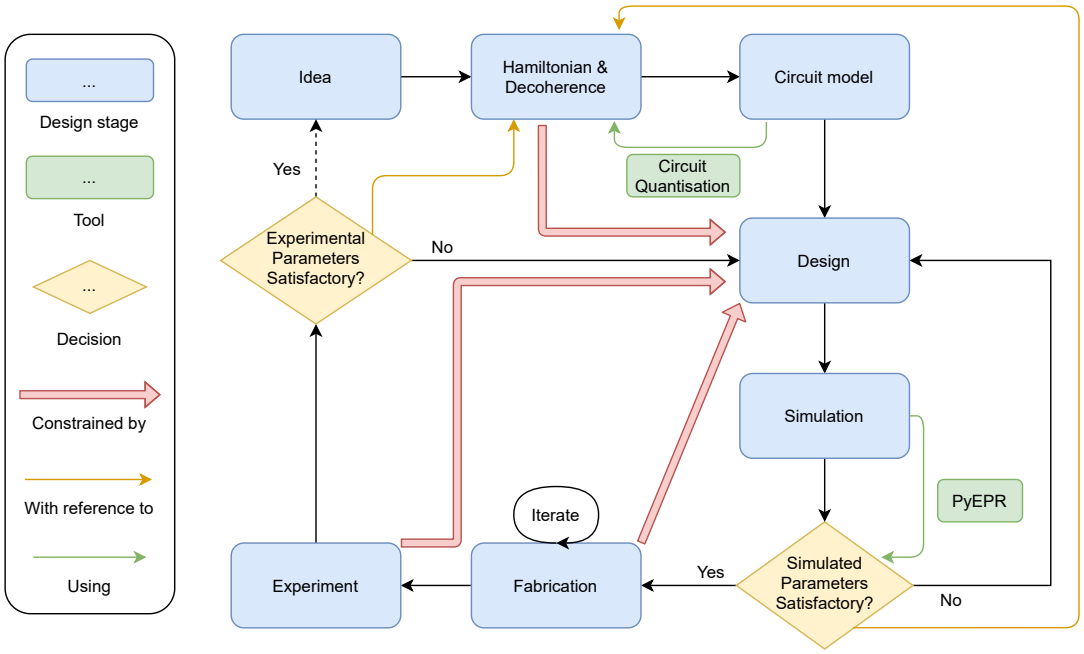

Figure 4.3: Flowchart of circuit QED: from an idea to an experiment.

design too ambitious, for example by using feature sizes under the resolution of the lithography machine, it will be irrealisable. If we make the couplings between the microwave transmission lines and the readout resonator too small for example, we won't have enough power at room temperature to measure the state of the qubit. Usually, we design our circuits directly in a finite-element radio-frequency (RF) electro-magnetic simulation software like Sonnet or HFSS (Fig. 4.4c.). By studying the response function of the circuit or its eigenmodes, we relate variations on the design with changes in quality factors and frequencies themselves connected to the Hamiltonian parameters. Tools like pyEPR can help us make this last step between the classical simulation results and the quantum mechanical parameters of $\hat{H}$. Once we have sufficiently iterated through the design and simulation cycle, comes the fabrication step. This also requires a great deal of iterative work to get the recipes right. Finally, the fabricated chip (Fig. 4.4d.) is measured and we can compare the experimental values to the results expected from the simulation. If the experimental parameters are not satisfactory with respect to the Hamiltonian wished for, we return to the design stage and improve the circuit based on what we have learnt through the measurement.

Let's now look at specific techniques used to design 2D Fluxonium devices during this thesis work and compare the experimental results with those obtained from the simulations.

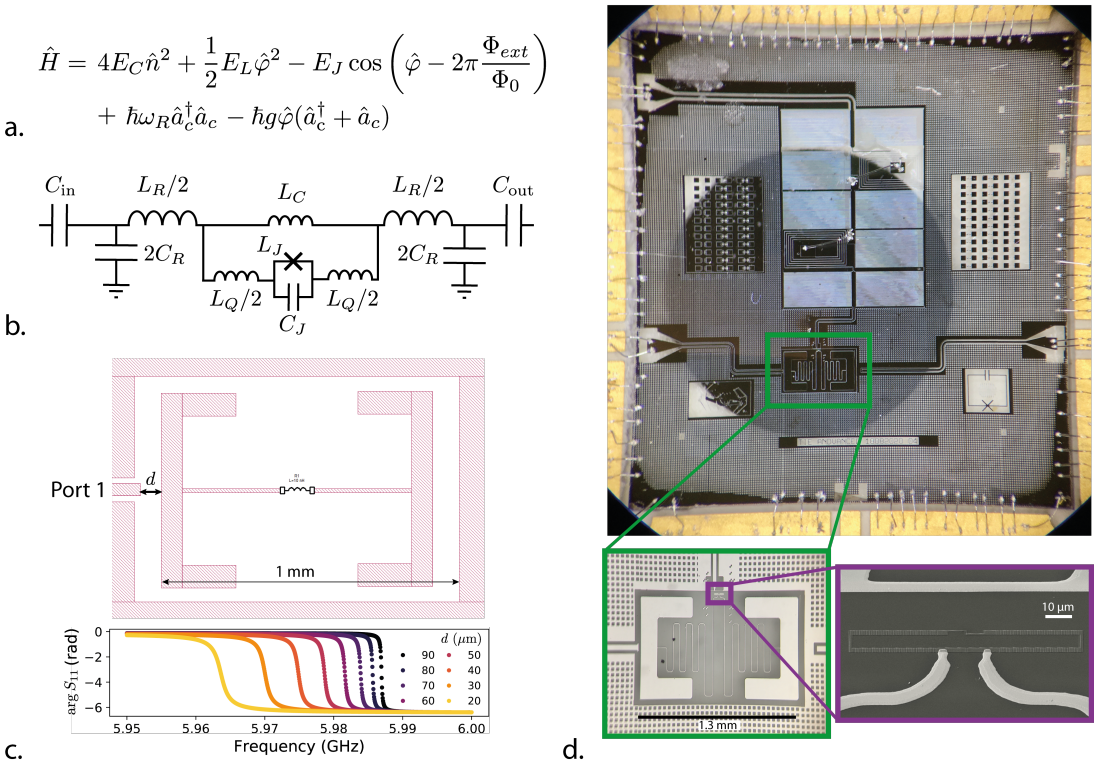

Figure 4.4: The flowchart of Fig. 4.3 illustrated by the different stages of a 2D Fluxonium design process. a. Hamiltonian we want to achieve with our design. b. Circuit model which when quantised leads to the desired Hamiltonian. C_{in}, C_{out}, C_R, L_R, L_C, L_Q, L_J and C_J are all parameters which can be controlled in the design or fabrication stages. c. Illustration of a basic Sonnet simulation of the coupling to the resonator from the transmission line. As the distance between the line on the left and braket shaped resonator is increased, the quality factor of the resonance increases in tandem, as can be seen from the simulated slope of the phase change from 0 to -2π ($\kappa_c = 2\pi \times 1.76\,\text{MHz}$ for the yellow curve, $\kappa_c = 2\pi \times 0.22\,\text{MHz}$ for the black curve). d. Optical and electronic microscope images of the final device. The dark circle visible in the center of the chip is the hole in the PCB visible through the transparent sapphire substrate. C_R is materialised by the large braket shaped capacitors either side of the meander inductor L_R (green zoom - optical microscope). On the purple zoom (SEM image) we see how L_J is given by the small junction inductance, L_Q by the total inductance of the junction chain and L_C by a single large junction between the contacts to the meander.

4.2.2 *From Hamiltonian to circuit model to design*

Following an approach similar to the circuit quantisation of a Fluxonium inductively coupled to a resonator in [73] we can relate the circuit model parameters of Fig. 4.4b. with the Hamiltonian $\hat{H}$.

$$\omega_R = \frac{1}{\sqrt{C_R \tilde{L}_R}} \ , \ Z = \sqrt{\frac{\tilde{L}_R}{C_R}} \ ; \tag{4.7}$$

$$E_C = \frac{e^2}{2C_J} \ , \ E_L = \frac{\Phi_0^2}{4\pi^2 \tilde{L}_Q} \ , \ E_J = \frac{\Phi_0^2}{4\pi^2 L_J} \ ; \tag{4.8}$$

$$g = \frac{\sqrt{\hbar Z/2}\Phi_0}{2\pi} \frac{L_C}{L_Q L_C + L_C L_R + L_Q L_R} \tag{4.9}$$

$$\tilde{L}_R = L_R + L_Q || L_C \ , \ \tilde{L}_Q = L_Q + L_R || L_C \ . \tag{4.10}$$

In the equations above we have used the symbol $||$ to denote the addition of two inductances in parallel. Note that the equations are invertible so that there is a bijection between the requirements on $\hat{H}$ and the circuit elements. The Fluxonium inductance $\tilde{L}_Q$ is only slightly renormalised by the presence of the cavity and coupling inductances, as is the resonator inductance $\tilde{L}_R$ by the Fluxonium and coupling inductances. This is the strong point of this design, L_J, L_Q and L_C are given, up to a small correction, by the inductance of Josephson junctions fabricated in a single e-beam lithography step. Indeed we choose to fabricate L_C using a single large junction identical to those used in the chain for L_Q. Thus, because the inductance of the individual junctions and chain can be calibrated using the normal state junction resistance R_N and the superconducting gap Δ using the Ambegaokar-Baratoff formula [163]

$$E_J = \frac{R_Q \Delta}{2R_N} \ , \tag{4.11}$$

simulating $\tilde{L}_Q$, L_J and L_C is not necessary. Note that in (4.11), Δ is the superconducting gap at $T = 0\,\mathrm{K}$, R_N is the normal state resistance at the critical temperature T_c and $R_Q = \frac{h}{4e^2}$. When using the room temperature resistance, an empirical corrective factor should be used [52], which should be calibrated for each specific fabrication process. At ENS de Lyon this factor approaches 0.85 as of May 2021

$$E_J \approx 0.85 \frac{R_Q \Delta}{2R_N} \ . \tag{4.12}$$

In the green inset of Fig. 4.4d. we show the experimentally realised circuit with the required circuit model. The inductance L_R is essentially given by the meander inductor between the braket shaped pads. This meander inductor is easy to roughly simulate because the theoretical geometric inductance of a line ($1\,\mathrm{nH\,mm^{-1}}$) is only slightly corrected by its mutual inductance with other parts of the meander. Intuitively, if a current flows through the meander, the opposing directions of current in different parts of the inductor have a tendency to cancel each other's magnetic fields because of the principle of superposition. A two port Sonnet simulation, with a port at either end of the inductance, gives a direct estimation of the meander's inductance as a function of frequency. Fig. 4.4d. also highlights the greatest weakness of our design, the difficulty to

estimate the capacitances C_R and particularly C_J. Designing C_R is done by estimating the resonator frequency ω_R. We use a two port simulation and, in a first step, replace the meander inductor and Josephson junctions with an effective lumped element inductor with value $\tilde{L}_R$. It is important to use the same braket pad geometry and ground plane as for the final design to obtain realistic values. The value of frequency at which the transmission $|S_{21}|$ is peaked corresponds to ω_R, yielding C_R by (4.7). The real issue lies with C_J. The circuit model is quite misleading here, as it appears that C_J is solely the intrisic capacitance of the small junction. This is not actually the case, and a large contribution to C_J comes from the capacitance of the junction to the ground plane and to the rest of the junction chain. It is very difficult to calibrate the value of E_C in the simulations, and we will see when we compare with the experimental results that this is a parameter we failed to estimate properly.

4.2.3 *Coupling to the transmission line*

4.2.3.1 *Tuning the coupling*

In the circuit model of Fig. 4.4b. we show two additional capacitances C_{in} and C_{out} which correspond to the couplings κ_{in} and κ_{out} to the transmission lines. Because the metals are lossless in the Sonnet simulation, the resonator linewidth is exclusively given by the coupling to the transmission lines. We thus proceed by simulating a circuit with a single port, whose resonance frequency is tuned close to the target ω_R thanks to a lumped element inductor and whose geometry close to the port is similar to the actual design (Fig. 4.4c.). By fitting the phase of the reflection coefficient using (2.55) we obtain κ_{in} directly. We can tune the coupling by changing the distance between the end of the transmission line and the resonator capacitor pad. An example of how the phase response evolves as a function of this distance is given in the graph of Fig. 4.4c. In practice, we choose κ_{in} and κ_{out} so that $\kappa_{\text{in}} + \kappa_{\text{out}} \approx \chi_{01}$ to maximise the readout signal to noise ratio (SNR) in the case where $\kappa_i = 0$ [164]. Moreover, we need $\kappa_{\text{in}} \ll \kappa_{\text{out}}$ to make sure that the efficiency of the readout in transmission, given by the ratio $\frac{\kappa_{\text{out}}}{\kappa_{\text{in}}+l\kappa_{\text{out}}}$, is high and that information about the qubit state is not lost in the experiment input lines.

4.2.3.2 *Qubit Purcell decay rate*

The input and output couplings affect not only the resonator but also the Fluxonium's lifetime. Because part of the qubit mode is stored in the resonator due to the inductive coupling, one of the decay channels of the Fluxonium is loss of information through the cavity into the transmission line, called the Purcell rate. To estimate the limit of the qubit lifetime due to Purcell decay we follow the treatment presented in [77]. For a cavity with annihilation operator $\hat{a}_c$ and port coupling κ_c we can write, using Fermi's

Golden rule, the transition rate $\Gamma_{i\to j,\downarrow}$ from the eigenstate $|\psi_i\rangle$ to eigenstate $|\psi_j\rangle$ of the coupled cavity-qubit system[7]

$$\Gamma_{i\to j,\downarrow} = \kappa_c |\langle\psi_j|\hat{a}_c|\psi_i\rangle|^2 (n_{\mathrm{BE}}(|\omega_{ij}|)+1) \ . \tag{4.13}$$

Here $n_{\mathrm{BE}}(\omega) = \left(e^{\hbar\omega/k_BT}-1\right)^{-1}$ is the Bose-Einstein distribution and ω_{ij} is the transition frequency between $|\psi_i\rangle$ and $|\psi_j\rangle$. Note that we assume that the energy E_i of $|\psi_i\rangle$ is greater than the energy E_j of $|\psi_j\rangle$. This formula can be interpreted as the rate at which the loss of photons in the resonator to the transmission line induces a transition between the eigenstates $|\psi_i\rangle$ and $|\psi_j\rangle$. We can equally define the upwards transition rate, where energy is taken from the transmission line and this time $E_j > E_i$

$$\Gamma_{i\to j,\uparrow} = \kappa_c \left|\langle\psi_j|\hat{a}_c^\dagger|\psi_i\rangle\right|^2 n_{\mathrm{BE}}(|\omega_{ij}|) \ . \tag{4.14}$$

Its insightful to pause and consider where exactly the coupling κ_c comes from. In general the coupling κ_c should depend on frequency, because according to [20] $\kappa_c(\omega) \propto \rho(\omega)$, where $\rho(\omega)$ is the density of the states of bath constituted by the transmission line. By saying that κ_c is independent of frequency we are implicitely assuming that we are dealing with perfectly 1D 50 Ω transmission lines. In that case $\rho = \frac{2}{\pi c} = \text{const.}$, corresponding to a perfectly ohmic bath. Of course, usually the transmission line is filtered in some way, either voluntarily or not, and ρ then depends on frequency again. Linking the microscopic density of states $\rho(\omega)$ to the classical microwave RF admittance $Y(\omega)$ can be done using the Caldeira-Legett model [165]. The fact that ρ is basically a constant is also a significant difference between the field of cQED and cavity QED (CQED) who work with 3D densities of states. In that case $\rho(\omega) = \frac{\omega^2}{\pi c^3}$ which has fundamental consequences on the couplings between atoms and fields.

Continuing from our intermezzo, we can now recenter the discussion about the decay rates around the Fluxonium qubit itself by labeling the eigenstates of the coupled system with the quantum numbers of the qubit and cavity $|\psi_i\rangle = |\mu, m\rangle$ using the weak coupling argument we detailed in Sec. 3.2.5. For the transtion rate between qubit states we get

$$\Gamma_{\mu\to\nu,\downarrow} = \sum_{m,n} P(m)\kappa_c |\langle\nu,n|\hat{a}_c|\mu,m\rangle|^2 (n_{\mathrm{BE}}(\omega_{\mu,m}-\omega_{\nu,m})+1) \ , \tag{4.15}$$

$$\Gamma_{\mu\to\nu,\uparrow} = \sum_{m,n} P(m)\kappa_c \left|\langle\nu,n|\hat{a}_c^\dagger|\mu,m\rangle\right|^2 n_{\mathrm{BE}}(\omega_{\nu,n}-\omega_{\mu,m}) \ . \tag{4.16}$$

$\omega_{\mu,m} = E_{\mu,m}/\hbar$ is the energy of eigenstate $|\mu,m\rangle$ measured in frequency and $P(m)$ is the probability of having m photons in the resonator. At thermal equilibrium $P(m) = \frac{e^{-m\hbar\omega_R/k_BT}}{1-e^{-\hbar\omega_R/k_BT}}$. The rate $\Gamma_{\mu\to\nu}$ is calculated by summing up the two contributions ↑ and ↓. Note that this estimation requires complete knowledge of the Fluxonium's spectrum obtained by numerical diagonalisation.

7 In general the coupling κ_c depends on frequency. According to [20] $\kappa_c(\omega) \propto \rho(\omega)$, where $\rho(\omega)$ is the density of the states of bath constituted by the transmission line. Because we are working with 1D microwave transmission lines $\rho(\omega) = \text{const.}$ and κ_c is frequency independent.

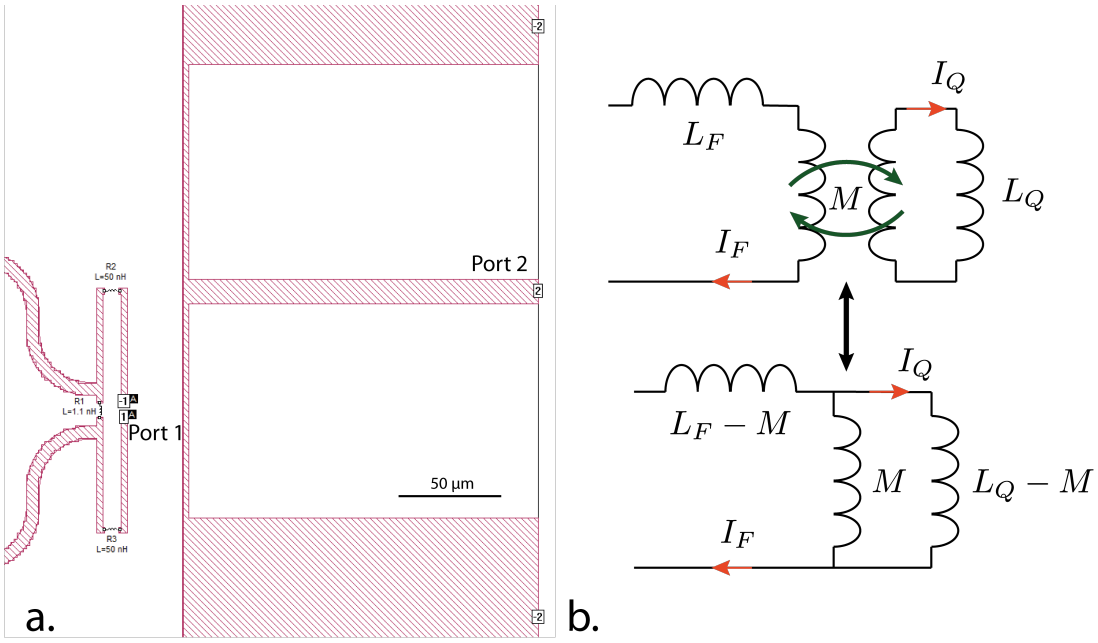

Figure 4.5: Estimating the mutual coupling between the Fluxonium loop and a flux line. a. Sonnet simulation designed to extract M. A port is placed within the Fluxonium loop with lumped element inductances, and a second at the end of the flux line. b. Equivalent circuit for the mutual coupling. Both circuits are equivalent representations of the mutual inductance, something which can be shown using Kirchoff's circuit laws.

4.2.4 *Designing the flux line*

4.2.4.1 *Finding the value of M*

We can bias a single 2D Fluxonium device at the sweet spot by using a global magnetic field produced by a coil around the sample holder for example. Using this field for flux gates is not ideal though because of the lengthy response time of a macroscopic coil $\tau = \frac{L}{Z_0}$ ($Z_0 = 50\,\Omega$, L is the coil inductance). Furthermore, if we are to use multiple Fluxoniums on the same device, we want individual flux control unattainable with a global field. This motivates the development of fast flux lines like those of [139] or [77]. In Fig. 4.4d. we can see the experimental realisation of this flux line, coming from a port at the top of the chip and descending through an on chip filter to a thin line close to the Fluxonium loop visible in the SEM image. We will come back to the filter in Sec. 4.2.6. The physical parameter which defines the characteristics of the flux line is the mutual inductance M between the current line and the Fluxonium loop. In a Sonnet simulation we check the value of M by placing a port on the loop and simulating the parameter Z_{21} of the complex impedance matrix Z between port 1 and a port placed at the end of the flux line (Fig. 4.5a.). Z_{21} is directly related to M [8]

$$\mathrm{Im}\, Z_{21}(\omega) = \omega M \ . \tag{4.17}$$

The value of M will have an incidence on the speed at which we apply flux gates and the power used thereby, as well as the rate at which the qubit relaxes into the flux line.

4.2.4.2 *Maximum gate speed*

The maximum speed of the flux gate is limited by the total inductance L_T seen by the flux line. We see from Fig. 4.5b. that this is given by

$$L_T = L_F - M + \left(\frac{1}{M} - \frac{1}{L_Q - M}\right)^{-1} . \tag{4.18}$$

The gate speed is limited by the reaction time of the RL constituted by the $Z_0 = 50\,\Omega$ transmission line impedance and the inductance L_T of the seen from the flux line

$$T_{\text{gate}} \geq \frac{L_T}{Z_0} . \tag{4.19}$$

Because $L_Q \sim 100\,\text{nH} \gg M \sim 1\,\text{pH}$, $L_T \approx L_F \sim 100\,\text{pH}$ and $T_{\text{gate}} \geq 2\,\text{ps}$, we conclude that this is not a limiting factor for flux gates with Fluxonium.

4.2.4.3 *Dissipated power*

The mutual inductance also impacts the current needed at the 20 mK stage to bias the Fluxonium's flux. The external flux induced by a current in the flux line is $\Phi_{\text{ext}} = MI_F$. If we want to realise a gate which requires changes in flux of the order of the flux quantum, we need to make sure that $I_F = \Phi_0/M$ is not an unrealistic current at the base plate of a dilution refrigerator. For a mutual inductance $M = 2\,\text{nH}$ we obtain $I_F = 1\,\mu\text{A}$. The power dissipated through a $50\,\Omega$ resistor by this current is $P = Z_0 I_F^2 = 5 \times 10^{-11}\,\mu\text{W}$, well within the cooling power specficiations of a standard dilution refrigerator ($\sim 14\,\mu\text{W}$ at 10 mK [166]).

4.2.4.4 *Direct decay into flux line*

The qubit can also decay into the flux line through the mutual inductance. To calculate the rate at which this happens, we follow the treatment in [18]. Returning to the expression 3.22 we identify the qubit operator as $\hat{O} = \hat{\varphi}$, the constant $A = E_L \frac{2\pi}{\Phi_0}$ and the noise operator as $X = \Phi_{\text{ext}} = MI_F$. The current spectral density is given by [20]

$$S_{I_F I_F}(\omega) = \frac{2\hbar|\omega|}{Z_0}\left[n_{\text{BE}}(|\omega|)\theta(-\omega) + (n_{\text{BE}}(|\omega|) + 1)\theta(\omega)\right] , \tag{4.20}$$

where $\theta(\omega)$ is the Heaviside function. Because this expression should be evaluated at the qubit eigenmode frequency, and the calculation of the loss rates depends on the qubit matrix elements, its evaluation can only be done using a numerical diagonalisation of the qubit Hamiltonian.

4.2.5 *Coupling between qubit and resonator*

While for the inductively coupled Fluxonium of Fig. 4.4 the coupling parameter g was given primarily by the design of the Josephson junctions in the chain, this is not the case for capacitively coupled systems. In that case the coupling Hamiltonian reads

$$H_{\text{coupling}} = -\hbar g \hat{n}(\hat{a}_c^\dagger + \hat{a}_c) . \tag{4.21}$$

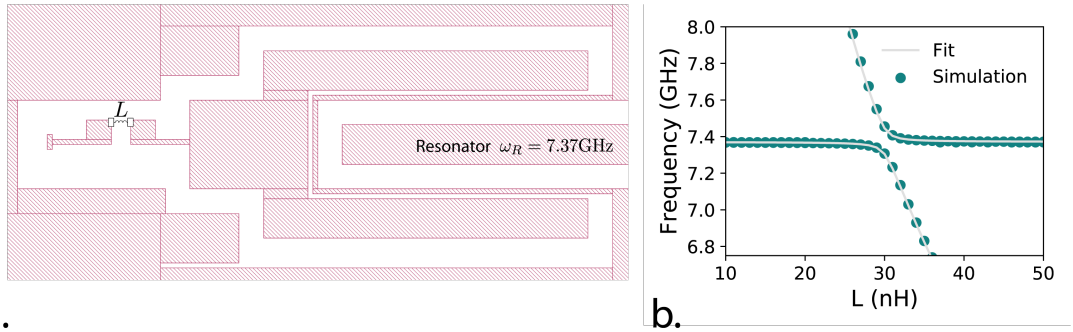

Figure 4.6: Estimating the capacitive coupling g between cavity and Fluxonium. a. A resonator at frequency $\omega_R = 2\pi \times 7.37\,\text{GHz}$ is probed through a single port in reflection (off screen) and is capacitively coupled to a lumped element resonator with the same geometry as a future Fluxonium qubit. The ideal inductor's value L can be swept in the simulation. b. Simulated resonances as a function of the value of L. We fit the simulated data using (4.22) to extract the coupling parameter $g = 70\,\text{MHz}$. The simulation reveals a constant resonator frequency and a qubit frequency which follows the law $\omega_Q = (LC)^{-1/2}$ where $C = 15.5\,\text{fF}$ is a fit parameter.

Determining the coupling parameter g then requires an electromagnetic simulation of the capacitance between Fluxonium and resonator. We base the principle of the simulation on the frequency anti-crossing formula

$$\omega_\pm = \frac{\omega_R + \omega_Q}{2} \pm \sqrt{(\omega_R - \omega_Q)^2 + 4g^2}\ . \tag{4.22}$$

In Fig 4.6 we show the simulation setup with a resonator probed in reflection and a lumped element resonator with the same geometry as a future Fluxonium qubit. By sweeping the value of the ideal inductance and tracking the different resonant frequencies in the simulation we are able to extract g.

4.2.6 *Comparison with experimental results*

Now we have described the techniques used to design the 2D Fluxonium device, we give a comparison between the parameter values expected from the simulations and those obtained experimentally in Tab. 4.4. E_C, E_L, E_J and g were obtained by fitting a two tone spectroscopy measurement like in Fig. 3.7 and a measurement of the cavity frequency as a function of Φ_{ext}. The cavity linewidth κ was obtained by fitting the transmitted signal through the readout cavity with the analytical expression (2.56) for S_{21}. T_1 and T_2 were obtained by using a qubit relaxation and Ramsey pulse sequence respectively. The double exponential expression developped in [82] was a better match to the qubit relaxation data, a result we attribute to quasiparticles (see 5). Finally, we extracted the mutual inductance M from a calculation of the current at 20 mK needed to bias the Fluxonium with a single flux quantum given the knowledge of the current applied into the flux line at room temperature.

As highlighted earlier in this section, the main difficulty of this experiment was the lack of knowledge of E_C before measuring the actual device. While the achieved E_L

Parameter	Simulation	Experiment
$E_C/2\pi\hbar$ (GHz)	-	5.65
$E_L/2\pi\hbar$ (GHz)	0.8	1.5
$E_J/2\pi\hbar$ (GHz)	8	8
$\omega_R/2\pi$ (GHz)	5.5	6.458
$g/2\pi$ (MHz)	30	50
$\kappa_{\text{in}}/2\pi$ (MHz)	0.01	1.84 (κ)
$\kappa_{\text{out}}/2\pi$ (MHz)	1.1	
M (pH)	1.1	1.4
$T_1^{\text{Purcell}}(\Phi_{\text{ext}} = \frac{1}{2}\Phi_0)$ (µs)	1.4×10^3	SE: 1.4 (T_1)
$T_1^{\text{Flux}}(\Phi_{\text{ext}} = \frac{1}{2}\Phi_0)$ (µs)	1.08×10^3	DE: 2.3 (T_{qp}) & 16.4 (T_r)
$T_2(\Phi_{\text{ext}} = \frac{1}{2}\Phi_0)$ (µs)	-	1.5

Table 4.4: Comparison of the simulated and experimentally achieved parameters for the 2D Fluxonium circuit presented in Fig. 4.4. SE: Single Exponential fit to the T_1 relaxation; DE: Double Exponential fit [82]. κ_{in} and κ_{out} were experimentally inaccessible with our experimental setup at the time (cavity transmission measurement) so we only give the value of the total linewidth κ.

and E_J were reasonable for a Fluxonium device, the large value of E_C meant that the $|0\rangle - |1\rangle$ transition was very high: $\omega_{01} = 3.78\,\text{GHz}$. This had various consequences, foremostly that the measured energy relaxation times were disappointing with $T_1 \approx 2\,\mu\text{s}$. Nevertheless, discounting the effect of quasiparticles on our device, the residual relaxation time $T_r = 16.4\mu\text{s}$ is encouraging as it promises, if we are currently limited by dielectric loss, T_1 of the order of 100 µs when qubit frequencies drop below 500 MHz. Another consequence of the large E_C was that the magnitude of the dispersive shift allowing the qubit readout was dominated by the anti-crossing between the cavity transition and the $|1\rangle - |2\rangle$ and $|0\rangle - |1\rangle$ transitions as opposed to $|0\rangle - |3\rangle$ and $|1\rangle - |4\rangle$ in low frequency Fluxoniums (see Sec. 3.2.4). The values of E_L, E_J and g were satisfactory with respect to their targets, but not perfect. This highlights the difficulty to correctly calibrate the resin thickness, oxidation and lithography step which affect junction parameters as these dominate the values of E_L, E_J and g in turn controlling the qubit parameters. Furthermore, the use of a single junction for the inductive qubit cavity coupling lead to unwanted non-linearity in the readout resonator even at low photon numbers. Because of these observations, in the long run it is thus perhaps more advisable to aim for a capacitive coupling between qubit and cavity. Indeed, once the right capacitance is found there is almost no variability, as it depends on the geometry alone. We were quite successful at predicting κ_{out} if we consider the cavity losses to be dominated by the coupling to the transmission line. Our prediction for M was also good and its value is clearly not currently a limiting factor for the qubit lifetimes in our experiment. In fact, this was something we only understood once the device had been fabricated. As can be seen in Fig. 4.4d., we placed a lowpass filter along the flux line with a cutoff at 500 GHz. The idea was to have the filter stop the qubit decaying into the flux line but still allow us to have fast gates: a cutoff at 500 MHz allows gate durations down to 2 ns. In fact, when M is chosen reasonably, the filter is not necessary

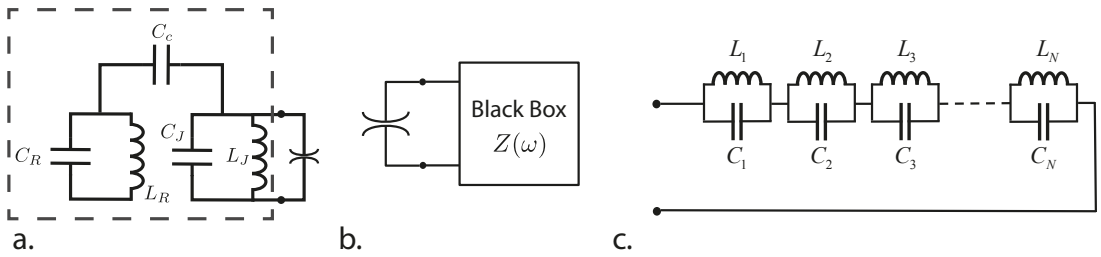

Figure 4.7: a. Circuit model for a Transmon coupled to a resonator similar to Fig. 2.6b. We have decomposed the qubit's junction into a linear inductor L_J and a non-linear element (spider symbol) b. Arbitrary impedance $Z(\omega)$ representing the rest of the circuit considered a black-box seen by the non-linear element. c. Foster decomposition of an arbitrary complex impedance into a series of LC circuits. This part of the figure was taken from [43].

as is evidenced by the value of $T_1^{\text{flux}} = 1.08\,\text{ms}$. The filter will be removed in future iterations.

4.3 3D DESIGN USING ENERGY PARTICIPATION RATIOS

In the previous section we designed a Fluxonium device with full knowledge of the underlying Hamiltonian. The frequency and dispersive shifts of the qubit can then be calculated by the full diagonalisation of the coupled cavity-qubit Hamiltonian. Importantly, each individual constant present in the Hamiltonian was simulated separately: knowledge of the cavity frequency ω_R and the coupling g required two different simulations for example. In this section we present two techniques - Black Box Quantisation (BBQ) and the Energy Participation Ratio (EPR) - which can be used to determine the Hamiltonian of a weakly anharmonic circuit using global simulations of the full device only. We stress that the circuits must be weakly anharmonic for these tehcniques to be valid. In other words the perturbation to the frequencies of the eigenmodes of circuit from the non-linearities should be much smaller than the eigenfrequencies of the bare circuit without non-linearity. This means that while the following techniques can be used to design Transmon qubits and could forseeably be used to design Fluxoniums at $\Phi_{\text{ext}} = 0$, they cannot be used to predict the frequency of Fluxoniums at $\Phi_{\text{ext}} = \frac{1}{2}\Phi_0$. Following the historical approach, treating BBQ before EPR, appears the most pedagogical. Finally we will talk about the design of a 3D Transmon in a cavity used for the experiment of Chapter 7.

4.3.1 *Black Box Quantisation (BBQ)*

We will follow closely the paper by Nigg et al. [96]. For a more introductory presentation, S. Girvin's lecture notes from Les Houches 2011 [43] are a good choice. For more advanced loss models see [167, 168], In chapter 2 Sec. 2.4.3 we derived the Hamiltonian for a Transmon qubit capacitively coupled to a cavity as represented by the circuit model in Fig. 2.6b. We showed that the cavity and qubit frequencies were renormalised by the coupling and that the cavity mode inherited part of the non-linearity of the

Josephson junction of the Transmon. To do this, recall that we separated the linear part of the Hamiltonian from the non-linear terms

$$\hat{H} = \underbrace{\hbar\omega_R \hat{a}_c^\dagger \hat{a}_c + 4E_C\hat{n}^2 + \frac{1}{2}E_J\hat{\varphi}^2 + \hbar g\hat{n}(\hat{a}_c + \hat{a}_c^\dagger)}_{\text{linear}} \underbrace{-E_J\cos(\hat{\varphi}) - \frac{1}{2}E_J\hat{\varphi}^2}_{\text{non-linear}} . \quad (4.23)$$

and then we diagonalised the linear part of the Hamitonian[8]. This idea is the basis of BBQ and is represented in Fig. 4.7a. We have separated the contributions to the energy from the linear part of the Josephson junction $\hat{H}_J^{\text{linear}} = \frac{1}{2}E_J\hat{\varphi}^2$ and the non-linear part $\hat{H}_J^{\text{non-linear}} = -E_J\cos(\hat{\varphi}) - \frac{1}{2}E_J\hat{\varphi}^2$. Separating these two parts of the circuit is a key conceptual step because the response of a linear circuit is completely defined by its impedance matrix Z which relates the voltages $\vec{V}$ and currents $\vec{I}$ at each of the circuit nodes and branches [7]

$$\vec{V} = Z\vec{I} . \quad (4.24)$$

In the case of the cavity-qubit circuit, this allows us to consider the linear part of the circuit as a black-box with a single port to which the non-linear element is connected (Fig. 4.7b.). The impedance of this black-box can be decomposed into its Foster equivalent circuit [169], represented by the circuit in Fig. 4.7c. in the general case. In this representation

$$Z(\omega) = \sum_{p=1}^{N}\left(i\omega C_p + \frac{1}{i\omega L_p}\right)^{-1} \quad (4.25)$$

such that the frequencies $\omega_p = 1/\sqrt{L_pC_p}$ at which the impedance has a pole (or the admittance $Y(\omega) = Z^{-1}(\omega)$ has a zero) correspond to the resonant eigenmodes of the circuit. These eigenmodes (and their eigenfrequencies ω_p) already take into account coupling terms like $\hbar g\hat{n}(\hat{a}_c + \hat{a}_c^\dagger)$, such that the two frequencies $\tilde{\omega}_R$ and $\tilde{\omega}_Q$ at which the admittance of the circuit enclosed in gray dashed lines in Fig. 4.7a. becomes zero are identical to those in the rewritten Hamiltonian

$$\hat{H} = \hbar\tilde{\omega}_R\hat{a}_c^\dagger\hat{a}_c + \hbar\tilde{\omega}_Q\hat{a}_q^\dagger\hat{a}_q - E_J\cos(\hat{\varphi}) - \frac{1}{2}E_J\hat{\varphi}^2 . \quad (4.26)$$

Conveniently, the derivative of the admittance with respect to frequency $Y'(\omega)$ contains information about the impedance of each eigenmode p

$$Z_p = \frac{2}{\omega_p \operatorname{Im} Y'(\omega_p)} , \quad (4.27)$$

allowing us to rewrite the flux corresponding to each mode p as

$$\hat{\Phi}_p = \sqrt{\frac{\hbar Z_p}{2}}(\hat{a}_p^\dagger + \hat{a}_p) . \quad (4.28)$$

The flux across the port of the Foster decomposition of Fig. 4.7c. must be equal to the sum of the fluxes of each of the N LC-circuits by an application of Kirchhoff's laws. Because this flux is also the flux across the non-linear element we get

$$\hat{\varphi} = \frac{2\pi}{\Phi_0}\sum_{p=1}^{N}\hat{\Phi}_p = \frac{2\pi}{\Phi_0}\sum_{p=1}^{N}\sqrt{\frac{\hbar Z_p}{2}}(\hat{a}_p^\dagger + \hat{a}_p) . \quad (4.29)$$

8 It is important to realise that $E_C = \frac{e^2}{2C_\Sigma}$ with $C_\Sigma \neq C_J$ the total capacitance shunting the Transmon's junction. This detail will be important later.

If we limit ourselves to the analysis of the non-linear term up to 4^{th} order, using the formula above we obtain

$$\hat{H} = \hbar \sum_{p=1}^{N} \omega_p \hat{a}_p^\dagger \hat{a}_p \underbrace{- \frac{e^2}{2L_J} \sum_{p=1}^{N} \left[Z_p \left(\sum_{q=1}^{N} Z_q \right) - \frac{Z_p^2}{2} \right] \hat{a}_p^\dagger \hat{a}_p}_{\text{Lamb-shifts}} \underbrace{- \frac{e^2}{2L_J} \sum_{p,r=1}^{N} Z_p Z_r \hat{a}_p^\dagger \hat{a}_p \hat{a}_r^\dagger \hat{a}_r}_{\substack{\text{self-Kerr } (p=r) \\ \text{cross-Kerr } (p \neq \text{r})}} . \tag{4.30}$$

This equation is essentially a generalisation to an arbitrary number of modes of the expressions for the Lamb-shift (E_C), self-Kerr (K_R and K_Q) and cross-Kerr (χ_{RQ}) terms given in Sec. 2.4.3. It is important to realise that aside from the junction inductance L_J, once the electro-magnetic geometry of the device and analytical expression for the non-linearity are specified there are no free parameters in this expression. From a design point of view, this is extremely useful: we can draw a circuit containing a Josephson junction; replace the junction by an ideal inductor L_J in parallel with a microwave port in a finite-element simulation software; simulate the response of the circuit at this port giving us the admittance $Y(\omega)$; find the zeros ω_p of Y and the derivative Y' evaluated at ω_p; and obtain the full quantum mechanical Hamiltonian $\hat{H}$ of the circuit. L_J just needs to be chosen using (4.12) in a way which makes the junction easy to fabricate.

This method was shown to agree with experiments within 10% for the Kerr terms, and within less than a percent for the mode frequencies [96]. It can also be generalised to circuits with more than one junction and to cases with dissipation [96]. If this technique was not used during this thesis it is because of two reasons. The first is that calculating $Y(\omega)$ for many frequencies around the ω_p necessary to obtain $Y'(\omega)$ is computationally expensive. The EPR technique we will turn to now, solves this issue. The second reason is one of convenience, the pyEPR package [170], which provides a big step in streamlining the design workflow, was developped in the middle of the thesis work technique and was immediately used in our research group.

4.3.2 *The Energy Participation Ratio (EPR)*

The theoretical details behind EPR quantisation of superconducting circuits we are about to explicit can be found in the publication by Z. Minev et al [93]. The starting point for the EPR analysis of superconducting circuits is the black-box point of view of Fig. 4.7b. corresponding to the Hamiltonian

$$\hat{H} = \underbrace{\hbar \sum_{p=1}^{N} \omega_p \hat{a}_p^\dagger \hat{a}_p}_{\hat{H}_{\text{lin}}} - E_J \cos(\hat{\varphi}) - \frac{1}{2} E_J \hat{\varphi}^2 , \tag{4.31}$$

where the black-box (linear) part of the circuit is already diagonal, but the non-linear part still needs to be treated. The frequencies ω_p can be obtained from an eigenmode

simulation in Ansys HFSS for example. The crux of the problem can be summed up as finding the coefficients φ_p such that

$$\hat{\varphi} = \sum_{p=1}^{N} \varphi_p (\hat{a}_p^\dagger + \hat{a}_p) \ . \tag{4.32}$$

Recall that these coefficients were given by $\varphi_p = \frac{2\pi}{\Phi_0}\sqrt{\frac{\hbar Z_p}{2}}$ in the previous section. To calculate this, we consider the participation ratio $\wp_p$ defined as the fraction of the inductive energy of mode p which is stored in the Josephson junction. It can be calculated quantum mechanically using the following formula

$$\wp_p = \frac{\overline{\left\langle \frac{1}{2} E_J \varphi^2 \right\rangle}_{\psi_p} - \overline{\left\langle \frac{1}{2} E_J \varphi^2 \right\rangle}_{\psi_p^0}}{\frac{1}{2}\left\langle \hat{H}_{\text{lin}} \right\rangle_{\psi_p}} \ , \tag{4.33}$$

where the overbar $\bar{\cdot}$ denotes the time average and $|\psi_p\rangle$ is a state in which only mode p is excited above its ground state $|\psi_p^0\rangle$. A further comment about the time average is required. In a classical LC circuit, the energy is stored in turn in the capacitive elements (electric field) and then in the inductive elements (magnetic field) of the circuit following a sinusoidal oscillation. In that case, the time averaged inductive energy is equal to half the total mode energy given by $\left\langle \hat{H}_{\text{lin}} \right\rangle_{\psi_p}$, hence the denominator of (4.33). We also consider only the deviations from the ground state energy, such that the participation ratio measures the distribution of the additional energy due to the excitation. For a coherent state $|\alpha\rangle$ in mode p (all other modes in the vacuum state $|0\rangle$)

$$\begin{aligned} \overline{\left\langle \tfrac{1}{2} E_J \varphi^2 \right\rangle}_{\psi_p} - \overline{\left\langle \tfrac{1}{2} E_J \varphi^2 \right\rangle}_{\psi_p^0} &= \overline{\langle \alpha(t) | \tfrac{1}{2} E_J \varphi_p^2 (\hat{a}_p^\dagger + \hat{a}_p) | \alpha(t) \rangle} - \overline{\langle 0 | \tfrac{1}{2} E_J \varphi_p^2 (\hat{a}_p^\dagger + \hat{a}_p) | 0 \rangle} \\ &= \frac{1}{2} E_J \varphi_p^2 (\overline{\alpha^*(t)^2 + \alpha(t)^2 + 2|\alpha(t)|^2}) \\ &= E_J \varphi_p^2 |\alpha|^2 \ , \end{aligned} \tag{4.34}$$

because for a time evolution $\alpha(t) = \alpha(0) e^{-i\omega_p t}$, $\overline{\alpha^*(t)^2} = \overline{\alpha(t)^2} = 0$. Furthermore,

$$\frac{1}{2}\left\langle \hat{H}_{\text{lin}} \right\rangle_{\psi_p} = \frac{1}{2}\hbar\omega_p |\alpha|^2 \ , \tag{4.35}$$

so that we finally obtain

$$\wp_p = \frac{2 E_J \varphi_p^2}{\hbar \omega_p} \ , \tag{4.36}$$

relating the participation ratio to the coefficient φ_p. We chose to calculate (4.36) for a coherent state because this is what is simulated in a classical electromagnetic simulation, but we can obtain the same result for a Fock state. By relating the mode impedance to the participation ratio

$$Z_p = \frac{\omega_p \Phi_0^2}{4\pi^2 E_J} \wp_p \ , \tag{4.37}$$

we can use equation (4.30) to calculate the anharmonicities and cross Kerr rates to 4^{th} order.

The participation ratio $\wp_p$ can be determined in an electromagnetic simulation by determining the ratio of energy stored in a lumped element inductor which takes the place of the junction, to the total magnetic energy stored in the electromagnetic mode[9]. The magnetic energy E_{mag} in the simulation is then given by the sum of two terms: the inductive energy E_{ind}, corresponding to the energy stored in the lumped element inductor, and the field energy $E_{\text{H-field}}$ stored inside the magnetic field of the eigenmode

$$E_{\text{mag}} = E_{\text{ind}} + E_{\text{H-field}} \ . \tag{4.38}$$

The electric energy of the eigenmode E_{elec} on the other hand is stored both in any lumped element capacitances in the simulation E_{cap} and in the electric fields $E_{\text{E-field}}$

$$E_{\text{elec}} = E_{\text{cap}} + E_{\text{E-field}} \ . \tag{4.39}$$

Generally, we do not use any lumped element capacitances in the simulation, such that $E_{\text{cap}} = 0$. Finally, because of detailed balance, $E_{\text{mag}} = E_{\text{elec}}$. These relations lead to an expression for the participation ratio

$$\wp_p = \frac{E_{\text{ind}}}{E_{\text{mag}}} = \frac{E_{\text{E-field}} - E_{\text{H-field}}}{E_{\text{E-field}}} \ . \tag{4.40}$$

The energies in each of the fields is obtained by integrating over the entire simulation volume taking into account the different dielectric regions.

4.3.3 *Designing the Purcell rate of a Transmon in a cavity*

We used the EPR method to design the 3D Transmon device used for the experiment of Chapter 7. The electromagnetic eigenmode simulations were done using HFSS, the results for the field and current distributions of each eigenmode were then used by pyEPR to calculate the participation ratios of each mode and return the anharmonicities and cross-Kerr rates. In Fig. 4.8a. we show the design layout used in HFSS to calculate the different eigenmodes and their coupling to the output port. The large quasi-rectangular volume represents the aluminium cavity and carries perfect E boundary conditions, meaning that the electric field must be perpendicular to the surface. In the centre, we represent the qubit chip by a rectangular dielectric with the losses and dielectric constant of sapphire. The Transmon pads are visible as 2D sheets (the thickness of aluminium is negligeable) with perfect E boundary conditions. Between the two, as is visible in Fig. 4.8b., we place another sheet whose width is equivalent to the width of the leads going to the Transmon's junction (slightly pink rectangle) Fig. 4.8d. This sheet carries a lumped element RLC boundary condition, with an inductance equal to the targeted junction inductance L_J. We also define a current line (black line) through the middle of the junction sheet connecting the Transmon pads. This line is not necessary for the HFSS simulation, but is used by pyEPR to define the direction of current in the junction. The cavity port is defined by a metallic rod entering the cavity through a cylinder with perfect E boundary conditions, representing the tube whose

9 Here we change the denominations compared to the pyEPR paper [93].

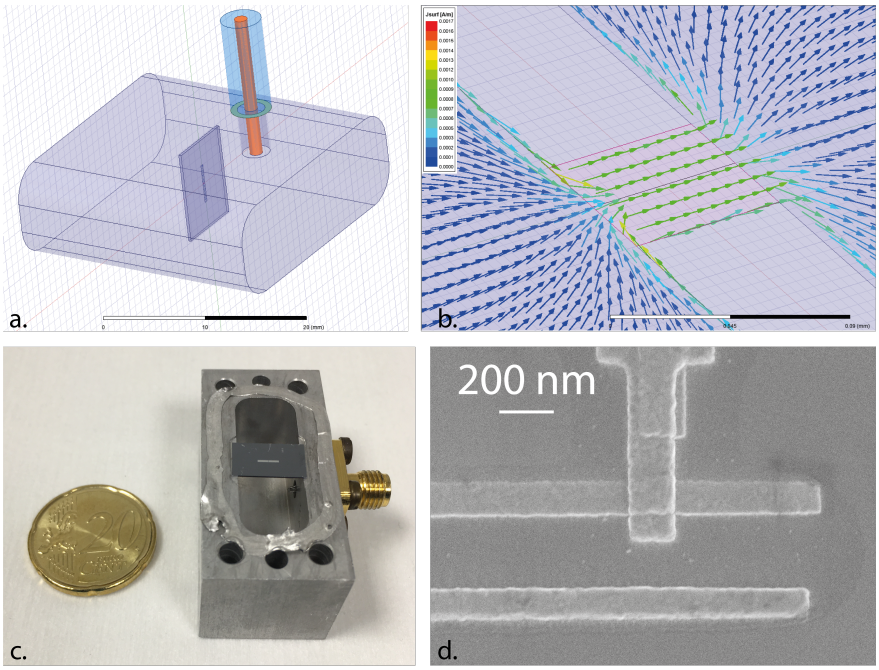

Figure 4.8: a. HFSS design layout for the 3D Transmon in a cavity shown in the c. panel. Note how the port opening with the antenna is visible behind the silicon chip in c. and represented by the orange material in the simulation. b. Current field for the frequency corresponding to the qubit eigenmode at the position of the rectangle with inductive boundary conditions (pink). These boundary conditions represent the inductance of the junction in the acutal device, shown in d.

length corresponds to the cavity thickness through which the coupling pin is threaded. The blue cylinder above the cavity in the simulation corresponds to the dielectric of the SMA connector seen in gold plated stainless steel in Fig. 4.8c. To realistically simulate the electromagnetic environment seen by the cavity through the pin, we terminate the SMA connector dielectric by a lumped element $50\,\Omega$ boundary condition. Although the cavity has two ports because we measure the cavity response in transmission (the other side of the cavity is not visible in Fig. 4.8c.), because the coupling is asymmetrical ($\kappa_{\text{in}} \ll \kappa_{\text{out}}$), we only model a single one in HFSS to reduce the simulation completion time.

Our objective in this experiment was to measure the fluorescence of the Transmon and post-select the results on a subsequent projective measurement of the qubit. This objective introduced a number of criteria on the qubit parameters. Firstly, we wanted the readout SNR of the qubit to be high, so we target $\kappa_{\text{out}} = \chi_{01}$ (see Sec. 4.2.3). Because we readout by probing the cavity in transmission, we require $\kappa_{\text{out}} \approx \kappa$ to make the output port dominate the information extraction. Secondly, to maximise the SNR of the fluorescence signal coming out of the cavity, we want to make sure the decay rate of the qubit is limited by its Purcell decay rate into the transmission line $T_1 \lesssim T_1^{\text{Purcell}}$, so that the majority of information about the qubit contained in the fluorescence field can be registered by the experimentalist. Finally, it was also necessary to have a sufficiently long T_1 compared to the duration of the readout $T_1 \gg T_{\text{RO}}$ so that the fidelity

Parameter	V1 (Timur)		V2 (Kuno)		V3 (Kuno)	
	Target	Measured	Target	Measured	Target	Measured
$\kappa/2\pi$ (MHz)	1	1.3	1	1.41	12	12.38
$\omega_{01}/2\pi$ (GHz)	4.27	3.59	4.32	4.87	4.32	4.81
L_J (nH)	5.84	-	9	-	9	-
$\chi_{01}/2\pi$ (MHz)	0.88	3.5	4.56	6	4.56	4.55
$E_C/2\pi\hbar$ (MHz)	84.8	?	127	152	127	152
T_1^{Purcell} (µs)	-	-	-	19.6	7.5	8.83
$\frac{2E_C}{\hbar\chi_{01}\kappa}$ (µs)	30.7	?	6.8	5.7	0.7	0.9
T_1 (µs)	-	13	-	10 (T_r) 4.6 (T_{qp})	-	6.4

Table 4.5: Table comparing the simulated and measured device parameters for three iterations of the experiment. The name of the fabricated qubit is given in parentheses. The target parameters are determined by simulation except for κ which is controlled at room temperature by lengthening or shortening the pins inside the cavity belonging to the SMA connectors. For a good rule of thumb for how much you need to cut the pin by see Chapter 2 of [58]. In the second iteration, we saw double exponential T_1 curves so we give T_r and T_{qp} for this case.

of the readout would be high.

In Tab. 4.5 we show how the targeted values of parameters and their measured values compare as we iterated through different devices. In the very first iteration (V1) we were optimistic about our fabrication capabilities and aimed for Purcell rate of around 100 µs. This was calculated using the approximate formula for a two level system dispersively coupled to a single mode cavity

$$\frac{1}{T_{\text{Purcell}}^{\text{approx}}} = \Gamma_{\text{Purcell}}^{\text{approx}} = \kappa \left(\frac{g}{\Delta}\right)^2 = \frac{\chi\kappa}{2E_C/\hbar} \,. \tag{4.41}$$

We can understand this formula intuitively by reminding ourselves that $\left(\frac{g}{\Delta}\right)^2$ is the proportion of the qubit mode which lives inside the physical cavity (see Chapter 2 equation (2.40)). Thus the proportion of the cavity losses that the qubit sees is $\left(\frac{g}{\Delta}\right)^2$ leading to (4.41). With the actual T_1 being much lower than expected and χ_{01} completely different from the targeted value, we decided to fabricate another sample.

In V2, the measured parameters agree with the simulations using HFSS and pyEPR to within $\sim 10\%$. The main issue lies in the discrepancy between the measured $T_1 \sim 5 - 10\,\mu\text{s}$ and the measured Purcell time $T_1^{\text{Purcell}} = 19.6\,\mu\text{s}$ despite having good agreement between T_1 and the predicted Purcell limit $T_{\text{Purcell}}^{\text{approx}} = 5.7\,\mu\text{s}$. This discrepancy has been studied in detail in [63]. The main issue is that the cavity does not behave as a single mode resonator, but allows a number of harmonics to couple to the Transmon qubit. The break down of the single mode approximation can explain the deviation of the true Purcell rate away from the one predicted by (4.41). To simulate the true Purcell rate we fall back on the quality factor of the eigenmode corresponding to the qubit transition. Assuming the losses in the simulation are dominated by the coupling

to the port, the quality factor of the qubit eigenmode is a direct mesure of the Purcell limit.

The improvements achieved thanks to this approach are visible in the 3$^{\text{rd}}$ column of Tab. 4.5. We made the cavity output port pin much longer, leading to a linewidth of $\kappa = 12.4\,\text{MHz}$. Consequentially, the Purcell limit of the qubit went down and appears to significantly limit the T_1 time of the Transmon. Note that the predictions of the approximate Purcell rate formula are far removed from the experimental results. Overall, the results of this experiment validate the EPR method for the design of 3D Transmons in our group.

4.4 CONCLUSION

A good choice of material and a thought-out design are essential to obtaining the properties we are looking for in quantum circuits. A number of materials have been used to effectively fabricate circuits whose long lifetimes with respect to current operation speeds are promising for sophisticated gate sequences. The level of control is such that we are able to tune certain material properties, like kinetic inductance, for specific uses in our devices. We also have a remarkable level of control on the Hamiltonian of our devices and the exploration of the design techniques in this chapter justifies the term "Hamiltonian engineering". The subject has matured sufficiently for there to be ready-to-use techniques (BBQ & EPR) embedded in user friendly software (pyEPR, Metal) to help design superconducting circuits. An understanding of how the Hamiltonian parameters can be designed manually though, can provide significant physical insight into the electrodynamic mechanisms at work. The experiments on Transmons and Fluxoniums studied in this chapter reinforce the quantitative agreement between simulation and measurement. Yet, as was already mentioned in the materials section, external factors (substrate cleaning, radiation shielding...) significantly affect the performances of superconducting quantum devices. In the following chapter, we go through some experiments which illustrate how to mitigate some of this effects.

5

THE FLUXONIUM QUBIT AND ITS ENVIRONMENT

In this chapter we continue on our quest to better control the environment of our qubits. For low frequency Fluxoniums this is particularly important, because of their high thermal occupation and susceptibility to flux noise, two effects not present in Transmons. This chapter will be constructed as follows. First we will give details on the predicted and observed effect of certain only partially controlled environmental factors on superconducting devices. In particular, we will see how temperature and external radiation can disturb the ideal conditions needed for quantum circuits. This should motivate our own work on environmental mitigation strategies over multiple Fluxonium device measurements, leading to close to state of the art energy decay times $T_1 \sim 100\,\mu s$. In the last part of the chapter, we will focus specifically on the different techniques used to reset low frequency Fluxonium qubits to their ground-state, many of which were benchmarked during this thesis.

5.1 THE EFFECT OF THE ENVIRONMENT ON LOW FREQUENCY QUBITS

To motivate the experimental work realised during this thesis on mitigating the effect of environmental noise, we first give some theoretical background and orders of magnitude to understand the origins of the noise we are trying to reduce.

5.1.1 *Temperature dependence of T_1*

Temperature has a direct effect on the energy decay times of two-level systems. To see this, consider a qubit interacting with a bath such that the populations of the qubit states are governed by the detailed balance equations

$$\frac{\mathrm{d}p_0}{\mathrm{d}t} = \Gamma_\downarrow p_1 - \Gamma_\uparrow p_0 \ , \tag{5.1}$$

$$\frac{\mathrm{d}p_1}{\mathrm{d}t} = \Gamma_\uparrow p_0 - \Gamma_\downarrow p_1 \ , \tag{5.2}$$

where $\Gamma_\uparrow$ and $\Gamma_\downarrow$ are the qubit excitation and deexcitation rates and p_0 and p_1 are the respective populations of each of the qubit states $|0\rangle$ and $|1\rangle$. Formally, p_0 and p_1 are the diagonal elements of the qubit density matrix ρ in the $\{|0\rangle, |1\rangle\}$ basis. As we saw in the previous chapter, the rates $\Gamma_\uparrow$ and $\Gamma_\downarrow$ are related to the spectral noise density of the bath, itself dependent on the Bose-Einstein distribution $n_{\mathrm{BE}}(\omega)$

$$\Gamma_\uparrow = \mathcal{N} \left| \langle 1|\hat{\sigma}^+|0\rangle \right|^2 n_{\mathrm{BE}}(\omega_{01}) \ , \tag{5.3}$$

$$\Gamma_\downarrow = \mathcal{N} \left| \langle 0|\hat{\sigma}^-|1\rangle \right|^2 (n_{\mathrm{BE}}(\omega_{01}) + 1) \ . \tag{5.4}$$

In the above equations, $\mathcal{N}$ is a proportionality factor which scales with the qubit-bath coupling as was shown in Chapter 4. Importantly, these equations are only valid

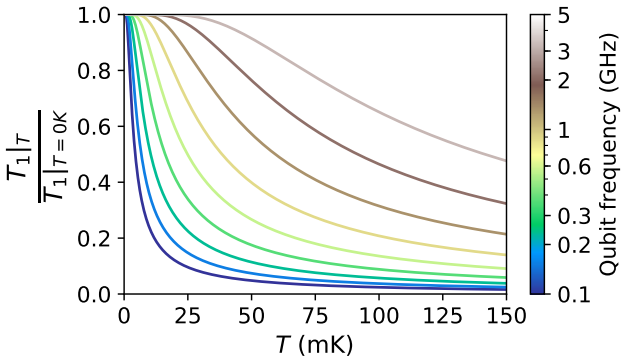

Figure 5.1: T_1 as function of the effective bath temperature with respect to its value at $T = 0$ following (5.6).

when the coupling between the bath and the qubit is linear, so they do not hold for quasiparticle relaxation for example. To determine the temperature dependence of T_1, we consider the steady-state of (5.1) and (5.2) and use the fact that $|\langle 1|\hat{\sigma}^+|0\rangle|^2 = |\langle 0|\hat{\sigma}^-|1\rangle|^2$ in (5.3) and (5.4) which leads to the detailed balance equation

$$\frac{p_1}{p_0} = \frac{\Gamma_\uparrow}{\Gamma_\downarrow} = \frac{n_{\mathrm{BE}}(\omega_{01})}{n_{\mathrm{BE}}(\omega_{01}) + 1} = e^{\frac{-\hbar\omega_{01}}{k_B T}} \ . \tag{5.5}$$

To obtain the final exponential, we have used $n_{\mathrm{BE}}(\omega) = \left(e^{\hbar\omega_{01}/k_B T} - 1\right)^{-1}$. Recalling the definition $\Gamma_1 = \Gamma_\uparrow + \Gamma_\downarrow$ (see 2) we can derive

$$\Gamma_1 = \Gamma_\downarrow \left(1 + e^{-\hbar\omega_{01}/k_B T}\right) = \Gamma_1|_{T=0} \coth\left(\frac{\hbar\omega_{01}}{2k_B T}\right) \Leftrightarrow T_1 = T_1|_{T=0} \tanh\left(\frac{\hbar\omega_{01}}{2k_B T}\right) , \tag{5.6}$$

given that at zero temperature $\Gamma_1 = \Gamma_\downarrow$ and reusing (5.4). In Fig. 5.1 we show how the hyperbolic tangent affects the qubit relaxation time. As the temperature is increased T_1 remains almost constant as long as $\hbar\omega \gg k_B T$. For large temperatures $\hbar\omega \ll k_B T$, T_1 decreases as $1/T$. Thus, to maximise coherence times, we would like to make sure that $\hbar\omega_{01} \gg k_B T$. This clearly is not always the case in Fluxonium qubits as, with a temperature to frequency conversion factor of $\frac{k_B}{h} \approx 21\,\mathrm{GHz\,K^{-1}}$, dilution refrigerator temperatures of 20 mK are already equivalent to a qubit frequency of $\omega_{01} = 2\pi \times 420\,\mathrm{MHz}$, such that T_1 is already diminished compared to its value at zero temperature. The importance of keeping the temperature as low as possible will become clear in the experiments of Sec. 5.2

5.1.2 *Thermal occupation of the qubit states*

As is evident from (5.5), the temperature of the bath also impacts the thermal population of qubits. This is particularily problematic for quantum circuits using Fluxoniums, again because of their low frequency. For $\omega_{01} = 2\pi \times 500\,\mathrm{MHz}$ the population ratio between the excited and ground states is 0.3 for a bath at 20 mK. At 100 MHz the ratio becomes $\frac{p_1}{p_0} = 0.79$. Many quantum algorithms assume a qubit initialised in a pure

starting state, such that Fluxoniums must be reset to the ground-state before being used for operations. This is not the case for Transmon qubits, whose excited state population is usually measured at the percent level. This is already well above the expected $p_1 \sim 10^{-4}\%$ for a 5 GHz qubit at 20 mK. In practice, effective bath temperatures are in fact determined by this ratio between the excited and ground state populations, and are usually measured somewhere in the range 50 - 140 mK [87, 137].

5.1.3 *Thermal photon induced dephasing*

This unexpectedly high bath temperature also has an impact on coherence because of the qubit's coupling to a thermally populated readout cavity. Intuitively, photons circulating in the readout cavity are constantly gaining information about the quantum state through their interaction with the qubit, leading to a decay of the off-diagonal elements of the density matrix as the two systems become entangled. Decoherence induced by uncontrolled degrees of freedom gaining information about the qubit is called measurement induced dephasing [171, 172]. We can be quantitative about the dephasing rate Γ_ϕ induced by the average number of thermal photons $\bar{n}_{\text{th}}$ in the cavity. Because the cavity mode is bosonic, $\bar{n}_{\text{th}}$ is directly related is directly related to the Bose-Einstein distribution

$$\bar{n}_{\text{th}} = n_{\text{BE}}(\omega_R) \ . \tag{5.7}$$

At 20 mK we expect $\bar{n}_{\text{th}} \sim 10^{-8}$ according to this formula, yet experiments report values between 6×10^{-4} to 0.15, orders of magnitude above the theoretical prediction [137]. The formula for the dephasing rate induced by the $\bar{n}_{\text{th}}$ photons is

$$\Gamma_\phi = \frac{\bar{n}_{\text{th}} \kappa \chi_{01}^2}{\kappa^2 + \chi_{01}^2} \ , \tag{5.8}$$

where κ is the cavity linewidth and χ_{01} is the dispersive shift of the qubit's $|0\rangle - |1\rangle$ transition.

The discrepancy between the experimentally observed $\bar{n}_{\text{th}}$ and qubit population ratios $\frac{p_1}{p_0}$ and their theoretical prediction is a subject of on-going research. Unthermalised photons from the microwave lines coupling into the cavity are one possible source and have motivated research into new types of filters, designed specifically for superconducting circuit applications[1]. In one experiment, using these filters right in front of the readout entry port increased the qubit coherence time to its limit with no pure dephasing $T_2 = 2T_1$ [137]. A second possible source of thermal photons is stray radiation from the ≥ 4 K stages of the dilution refrigerator and radiation from outside the crogenic unit. To mitigate the effect of this radiation, comprehensive radiation shielding is used, often composed of copper, lead or aluminium cans sometimes coated with stycast, carbon black or eccosorb [137, 173, 174].

1 A number of groups have designed and fabricated their own homemade filters and attenuators (University of Maryland (Manucharyan group), University of Chicago (Cleland group), UCSB - Google, Néel Institute...), but as these components are often critical for device performance, the designs are rarely published for fear of relinquishing a competitive advantage.

5.1.4 *Quasiparticles*

Another advantage of making sure stray radiation does not reach the superconducting device is the reduction of the number of quasi-particles. We already mentioned in Chapter 3 that the expected number of quasiparticles at dilution fridge temperatures of 40 mK were 16 orders of magnitude lower than the observed number. This impressive discrepancy has been theorised to originate from out of equilibrium quasiparticles excited by highly energetic photons $\hbar\omega \geq 2\Delta$ arriving on the superconducting junction. Theories taking into account this effect, that the density of quasiparticles can be separated into two contributions: one temperature independent (non-equilibrium) and one temperature dependent (equilibrium) [175, 89]; have been successful in explaining experiments where qubit transitions are correlated with the charge parity either side of a single Josephson junction [176, 83], and the temperature dependence of T_1 [177]. Furthermore, reducing infrared radiation coming from inside the dilution refrigerator by using absorbing shields was shown to increase lifetimes by reducing the quasiparticle number[173, 174]. The presence of lead bricks around the dilution refrigerator also had significant effects on the lifetime of resonators and qubits [35, 36].

Experimentally, the quasiparticle density x_{qp}, defined as the ratio of the number of quasiparticles to the number of Cooper pairs in the superconductor, can be determined by a time averaged T_1 measurement. Because the quasiparticle loss rate Γ_{qp} is proportional to x_{qp} (see 3 (3.28)) which in turn is proportional to the number of quasiparticles n_{qp} in the superconducting islands either side of the junction, we can define a loss rate $\tilde{\Gamma}_{\text{qp}}$ associated with the loss due to a single quasiparticle in the islands [82]. The total quasiparticle rate then becomes

$$\Gamma_{\text{qp}} = n_{\text{qp}}\tilde{\Gamma}_{\text{qp}} \ . \tag{5.9}$$

The qubit lifetime is given by the sum of all relaxation rates, such that, assuming no thermal population at equilibrium, the population P of the qubit prepared in $|e\rangle$ as a function of time is

$$P(t) = e^{-n_{\text{qp}}\tilde{\Gamma}_{\text{qp}}t - \Gamma_r t} \ , \tag{5.10}$$

where Γ_r is the qubit relaxation rate due to mechanisms other than quasiparticles. To go further, we assume that the number of quasiparticles n at a given moment is distributed according to a Poisson law $p_\lambda(n)$ with average λ

$$p_\lambda(n) = \frac{\lambda^n e^{-\lambda}}{n!} \ . \tag{5.11}$$

If we make a series of T_1 measurements such that the measurement sequence is much shorter than the time it takes for the number of quasiparticles to change, the average relaxation trace will be given by a 'double-exponential'

$$\langle P(t)\rangle = e^{\lambda\left(\exp\left(-\tilde{\Gamma}_{\text{qp}}t\right)-1\right)}e^{-\Gamma_r t} \ . \tag{5.12}$$

A typical example of such a double exponential decay curve is given in Fig. 5.2, where we can clearly see the difference at long times between the two fits. Using a logarithmic scale can be useful to make out the difference, as an exponential decay follows a straight line in a graph with a logarithmic y-axis.

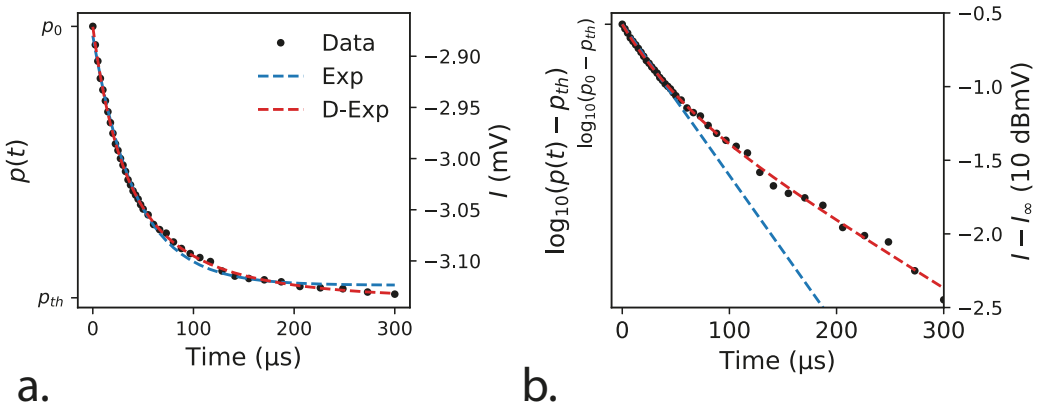

Figure 5.2: Qubit excitation p as a function of time after a π-pulse exhibiting a double exponential decay. In panel a. the qubit population $p(t)$ is shown on a linear y scale, in b. we use a logarithmic scale after substracting the thermal equilibrium excitation p_{th} obtained from the fit. Blue and red dashed lines denote fits to an exponential $P(t) = e^{-t/T_1}$ and to the double exponential (5.12) respectively. In this case, the extracted decay rates were, $T_1 = 42\,\mu s$ for the exponential fit and $T_{qp} = 1/\tilde{\Gamma}_{qp} = 58\,\mu s$ and $T_r = 1/\Gamma_r = 96\,\mu s$ with $\lambda = 1.0$ for the double exponential fit.

5.1.5 *Summary*

Qubit loss rates depend on the bath with which they interact. This bath is often characteristed by an effective frequency dependent temperature which encompasses the net effect of the environment on the qubit. This effective temperature can have a direct effect on the qubit lifetimes and qubit population. In certain cases, this can be explained microscopically as dephasing due to photons in the cavity or the decay due to quasiparticles excited by incumbent high energy photons. If we are to achieve qubits with long lifetimes, the goal should be to reduce this effective temperature and stray radiation. In the next section, we see which strategies we can implement to achieve this goal.

5.2 ENVIRONMENTAL MITIGATION STRATEGIES IN FLUXONIUM EXPERIMENTS

About a year of this thesis work, between the summer of 2018 and the summer of 2019, was spent trying to achieve the same high coherences with Fluxonium qubits as those reported in [79]. Indeed, through a collaboration with the Manucharyan group, we had access to samples we knew had been measured with $T_1,\ T_2 > 100\,\mu s$ at the University of Maryland. An essential part of the scientific project at the time, was to demonstrate that these lifetimes could be achieved in other laboratories and in particular at the ENS in Lyon. In this section we detail some of the iterative work necessary to achieve state of the art, including failed experiments, and highlight some of the group's current best practices for Fluxonium experiments. The purpose is mainly to expose some things which could be tried to improve coherence times in future experiments and which have proven their worth in the literature or in our group. During the work of this thesis, many

of these techniques did not affect our qubits either negatively or positively, leading us to believe that in one of our dilution refrigerators, the Cryoconcept, there is some still unknown noise source which is extremely detrimental to qubit lifetimes.

The subsections will follow the work of the first year of Fluxonium experiments chronologically, with the titles of the different subsections underlining a particular technique or improvement explored during that period. Occasionally, improvements from later on in the thesis will also be discussed. In Table 5.1 and Fig. 5.3 we summarise the main changes to the experiment during the one year period.

5.2.1 *Fluxonium from scratch: optimising the readout and finding the spectrum*

We recieved our first Fluxonium device over the summer of 2018 from the University of Maryland. The setup consisted of a single Fluxonium device, patterned in aluminium on a silicon chip inside a 3D copper cavity. Although the fabrication technology was identical to that reported in [79], the Manucharyan team had not reported long lifetimes ($T_1 < 100\,\mu s$) for this sample and we were to use it to test our setup before receiving another device with longer lifetimes later on. In 2018, the group had just moved from Paris with two dilution refrigerators, one made by Bluefors reaching $\sim 24\,mK$ at base temperature[2], and the other made by Cryoconcept reaching $\sim 35\,mK$. With two other experiments running in the Bluefors fridge, our experiment was setup in the Cryoconcept. The first step was to identify the cavity frequency, which we achieved using a spectrum analyser in transmission on the setup input and output lines. The Maryland group had sent us a spectrum of the qubit measured on their setup, which we immediately tried to reproduce using a two tone spectroscopy measurement as is explained in Sec. 3.2.4. This was a mistake. Indeed, the parameter space which controls the visibility (SNR), frequency and linewidth of the resonances in a two tone spectroscopy measurement is very large. The matrix elements, readout power and integration time and the probe drive power influence the visibility of the transition, the flux point changes its frequency and the drive power and matrix elements affect the linewidth. This is too many parameters for an initial measurement where the ideal values of these parameters are all unknown. Moreover, in an attempt to optimise T_2, the group in College Park had designed the Fluxonium so that the dispersive shift χ was much smaller than the cavity linewidth κ. This made finding the qubit spectrum even more difficult.

From experience it is best to start by optimising the readout, something which was greatly simplified when we received a Traveling Wave Parametric Amplifier (TWPA) [178] from Lincoln Labs (see Run 4 in Table 5.1). The idea is to increase the readout pulse input amplitude until observing the non-linearity inherited from the qubit. The non-linearity is evident in Fig. 5.4a., where we show an example of the cavity transmission as a function of frequency. When the amplitude of the readout tone becomes high enough, the cavity drifts to lower frequencies and the resonance shape is deformed. Using an amplitude just below the visible onset of the non-linearity is usually a good

2 After refilling the helium lines with ^{3}He, this fridge now achieves $\sim 15\,mK$ fully cabled.

Run	Cabling	Qubit	$\kappa_{in}/2\pi$ (MHz)	$\kappa_{out}/2\pi$ (MHz)	T_1 µs	T_2 µs	Changes from previous run	Problems encountered	Why warmup?
1-3		1	$\kappa/2\pi = 9$ MHz		-	-	-	Low RO SNR Qubit 0-1 transition invisible	Arrival of TWPA
4	A	1	$\kappa/2\pi = 9$ MHz		17-25	4-6	TWPA added on output	Qubit pulses heat fridge	Setup changes
6	B	1	0.13	1.5	-	-	Readout in reflection Thermalisation improved Heat sinks at 4K on input DC line thermalisation improved	Qubit pulses heat fridge	Fridge heating
7	C	1	1.25	2	9	5-6	Open input coupling Switch directional coupler and attenuator on input	Unplanned power cut stops progress	Power cut
8	C	2	1.7	2.5	22	2-3	New qubit (UMaryland $T_1 = 100$ µs, $T_2 = 200$ µs)	-	Setup changes
9	D	2	1.7	2.5	20-30	7-15	10 dB → 20 dB at 20 mK	-	Setup changes
10	E	2	1.7	2.5	27	-	Readout in transmission Eccosorb inside cryoperm	-	Setup changes
11	F	2	1.7	2.5	-	-	Etched cavity Qubit cleaned with acetone/IPA Eccosorb in different cryoperm than cavity	Chip broke inside cavity when it was closed	No qubit
12	F	2	1.7	2.5	6-8	-	Remove 10 dB @ 4K	-	Setup changes
13	F	2	1	1	-	-	-	Magnetic field hysteresis	Flux issues
14	F	2	1	1	10	5	Removed some aluminium around sample Changed DC line conversion box	Helium lines get blocked	Fridge blocked
15	F	2	1	1	8	5	-	-	Nitrogen trap blocked
16	G	2	1	1	-	2-4	Remove cryoperm around eccosorb	-	-
17	G	2	1	1	6	-	-	Helium lines get blocked	Fridge blockage
18	G	2	1	1	3	-	Filled stray holes in stage platforms Fridge pump maintenance Copper plates with stycast and eccosorb at 20 mK	-	-

Table 5.1: Table summarising the different experimental runs (full refrigerator cycling to room temperature) and the different setup details when using the Cryoconcept dilution refrigerator. These different runs span just over a year between July 2018 and September 2019. Run 5 is not listed as the cabling was very different, and the results inconclusive.

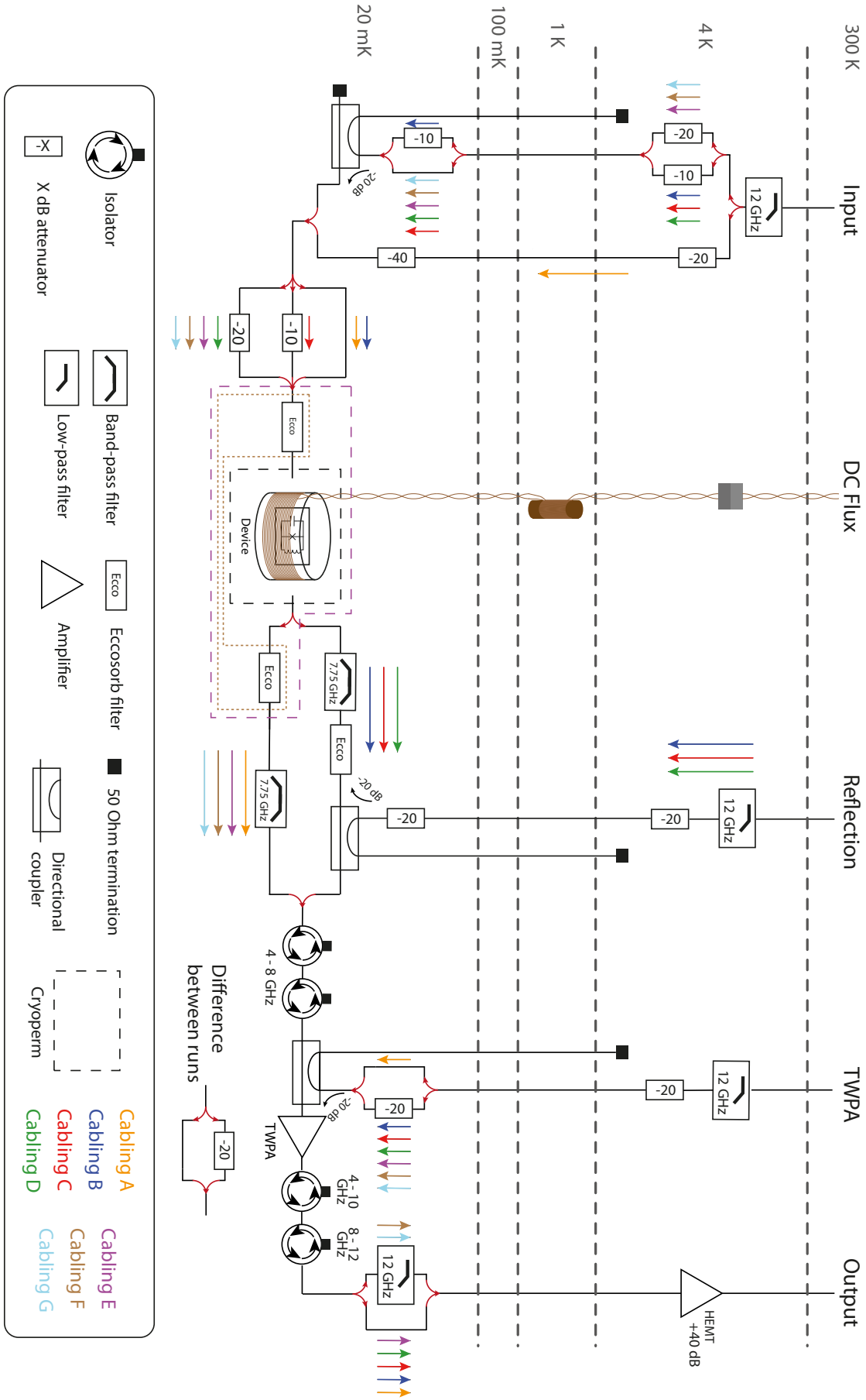

Figure 5.3: Summary of the different cabling schemes used in successive experimental runs in the Cryoconcept dilution refrigerator.

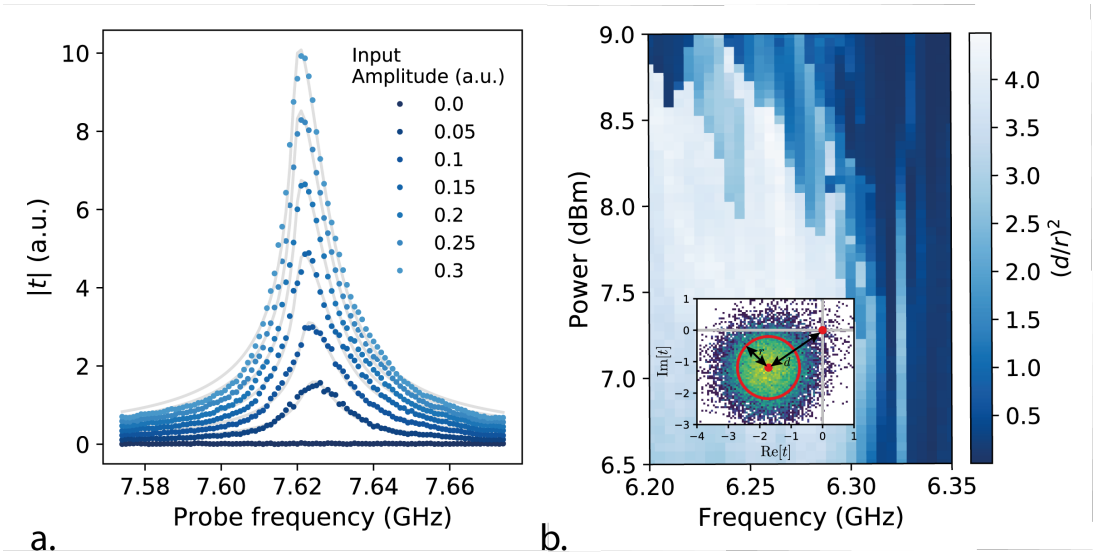

Figure 5.4: Optimising the readout. The data in a. comes from a Fluxonium experiment not discussed in this section, and the data in b. comes from a 3D Transmon experiment. a. Absolute value of the cavity transmission ($t = \bar{I}_{\text{out}} + i\bar{Q}_{\text{out}}$) as a function of the readout amplitude. Grey lines are fits to a Duffing oscillator equation. b. SNR of the readout signal as a function of the TWPA pump parameters: pump power and frequency. The SNR is defined as the ratio $(d/r)^2$ shown in the inset for a typical readout histogram. The SNR decreases dramatically if we pump too hard or move the pump frequency into the dispersive feature. Note that the point at which the SNR is highest is not necessary the point with the highest gain.

choice. Then, keeping the readout power and integration time constant, we sweep the power and frequency of the TWPA drive around the values specified in the specification sheet to optimise the readout SNR in the complex plane. This is measured by the ratio $(d/r)^2$ of the distance of the gaussian distribution from the origin to its standard deviation (see inset of Fig. 5.4b.). A typical 'TWPA map' is shown in Fig. 5.4b., where we can clearly see the increase in SNR at certain parameter combinations as well as the dispersive feature above 6.3 GHz.

Once the readout parameters are set, it is useful to know at which flux point we are working at. To do this, the simplest is to probe the cavity at fixed frequency and measure its response as a function of external flux, controlled by the voltage or current in the flux line. This is a direct measurement of the dispersive shift of the qubit on the cavity, depending on the thermal equilibrium of the qubit levels at each flux point. A typical result of this measurement is shown in Fig. 5.5, where we can distinguish two axes of symmetry as a function of flux. These axes correspond to the symmetries of the qubit spectrum around the flux points $\Phi_{\text{ext}} = k\Phi_0$ and $\Phi_{\text{ext}} = (k + \frac{1}{2})\Phi_0$ ($k \in \mathbb{Z}$). Without a priori knowledge of the qubit spectrum, it is not possible to determine which of the two points of symmetry correspond to which flux points, but this limits the search for the $|0\rangle - |1\rangle$ transition at $\Phi_{\text{ext}} = \frac{1}{2}\Phi_0$ to two possibilities. It is generally easiest to look for qubit transitions above 1 GHz, because at those frequencies the charge matrix elements are larger. A map like Fig. 5.5 and a few well identified transitions are sufficient to find

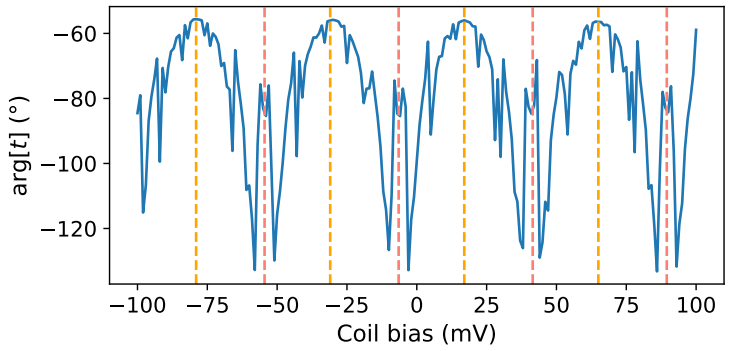

Figure 5.5: Typical phase response ($t = \bar{I}_{\text{out}} + i\bar{Q}_{\text{out}}$) of the cavity at fixed frequency as a function of the external flux (coil voltage). The symmetry axes corresponding to fluxes $\Phi_{\text{ext}} = k\Phi_0$ and $\Phi_{\text{ext}} = (k + \frac{1}{2})\Phi_0$ ($k \in \mathbb{Z}$) are given by orange and pink dashed lines respectively.

the parameters E_C, E_J, E_L through a fit of the Fluxonium Hamiltonian. Once these parameters are known, the frequencies of all the other transitions as a function of flux as well as their matrix elements can be infered. Unlike Transmons, Fluxonium devices in this thesis seemed to be much more sensitive to drives at high power when doing two tone spectroscopy. If a transition is not visible, sometimes it is necessary to reduce the drive power rather than increase it. In particular, because the spectrum of a Fluxonium is much more complicated than a Transmon, increasing the drive power can make higher order transitions appear which complicates the identification of direct qubit transitions.

Searching for the qubit spectrum on the first generation of devices lead us to realise the importance of making sure the cavity linewidth κ was of the same order of magnitude as the qubit's dispersive shift χ. This was a major change between the Runs 4 and 6 (Table 5.1), where we closed the input and output ports of the cavity to be more in line with the expected $\chi < 1\,\text{MHz}$ of the $|0\rangle - |1\rangle$ transition at $\Phi_{\text{ext}} = \frac{1}{2}\Phi_0$ communicated by the Maryland group. It was during Run 4 that we obtained the highest T_1 measured for this sample, fluctuating around $\sim 20\,\mu\text{s}$.

5.2.2 *Thermalising RF and DC control lines*

One of the immediate consequences of working with lower frequencies is the need for more power in the qubit drives. Following the discussion of chapter 3, we know that if the frequency drops by an order of magnitude (from 5 GHz to 500 MHz for instance), the charge matrix element $|\langle 1|\hat{n}|0\rangle|$, which is directly proportional the Rabi frequency $\Omega \propto |\langle 1|\hat{n}|0\rangle|$, is reduced by two orders of magnitude. This boils down to the realisation that to obtain the same gate speed for Fluxonium qubits as for Transmon qubits (all other things being equal), we need to increase the drive power by 20 dB. This potentially poses a problem, because attenuators at the 20 mK stage, at which cooling power is limited, will also dissipate 100 times more power. To remedy this, we replaced a $-40\,\text{dB}$ attenuator on the input line with a directional coupler and an attenuator in Run 7 (see cabling A versus all other cablings after C in Fig. 5.3). This presents

the advantage that, by routing the uncoupled signal to the isolated port terminated by a 50 Ω at 4 K, 99% (in the case of a −20 dB input coupling) of the input signal is dissipated at a stage where cooling power is not an issue. Importantly, the attenuator must come after the directional coupler for this to work. This was the error of Run 6, as in that case 90% of the power was still dissipated at 20 mK. There is also no noise level increase by dissipating at 4 K because signals from the isolated port are attenuated by −40 dB into the coupled port[3]. Aside from the specific case of the mixing chamber stage, attenuation along the lines is calculated following the standard techniques and considerations about noise temperature explicited in [179]. Finally, fridge heating also motivated the reopening of the cavity input port between Runs 6 and 7 to increase the proportion of the incoming field reaching the qubit.

Once the attenuation has been designed properly it is important to make sure that all attenuators are properly thermalised to avoid hot spots in the fridge. It is also important to reduce the thermal leakage from higher temperature stages inside the dilution refrigerator. Between Runs 4 and 6 we spent some time improving the thermalisations within the fridge. Attenuators at 4 K were thermalised using Apiezon vacuum grease whilst at lower temperatures we used unoxidised copper strips tightly screwed to both the component and fridge (Fig. 5.6a.). This follows the recommendations of the book by Ekin [51] on low temperature measurements. Futher efforts were put in to reduce the thermal conduction between levels due to the RF and DC cabling. Before starting to use the refrigerator we ordered new stainless steel microwave cables for the input lines which have low thermal conductivity at low temperatures [179]. In the same vein, but with the additionnal consideration of quantum efficiency, superconducting NbTi cables were used for the output lines. Considerable work was also done on the twisted pairs used for the flux control. To bias the Fluxonium devices we used a homemade coil with $\sim$ 1500 turns wound around a brass (copper in subsequent iterations[4]) support thermalised to the 20 mK stage (Fig. 5.6e.). The leads of the coil were routed as a twisted pair up to the 4 K stage and soldered to a connector whose electronic temperature was thermalised to 4 K (Fig. 5.6f.). Importantly, to stop the direct galvanic contact between the 4 K and 20 mK stage due to the twisted pair, we thermalised the DC lines at the 1 K stage using a copper post (pictured in 5.6c.) and left a long length of cable between the 1 K and 20 mK stages (5.6d.), to make sure there were no thermal shorts between stages. Later on, between Runs 17 and 18 we also made sure there were no holes in the platforms above 20 mK by sealing them with stycast (5.6b.).

Unfortunately, none of these experimental efforts helped with the improvement of our coherence times whose maximum values were recorded as $T_1 = 25\,\mu s$ and $T_2 = 6\,\mu s$

3 Recent measurements done on 3D Transmons in the group, with the isolated port terminated at 20 mK, have shown that this setup can also improve T_1 in certain cases, something which we attribute to the thermal decoupling between the input and coupled lines.

4 In a later Fluxonium experiment in the Bluefors fridge, we made a coil support out of leftover brass from the laboratory workshop. This brass was slightly ferromagnetic, which was not the case of the brass support we used initially which came from the Maryland group. Using a magnetic material to bias a flux sensitive device turned out to be a bad idea and we saw flux jumps at a rate of around 1 per minute during that cooldown. In all future experiments we used copper coil supports.

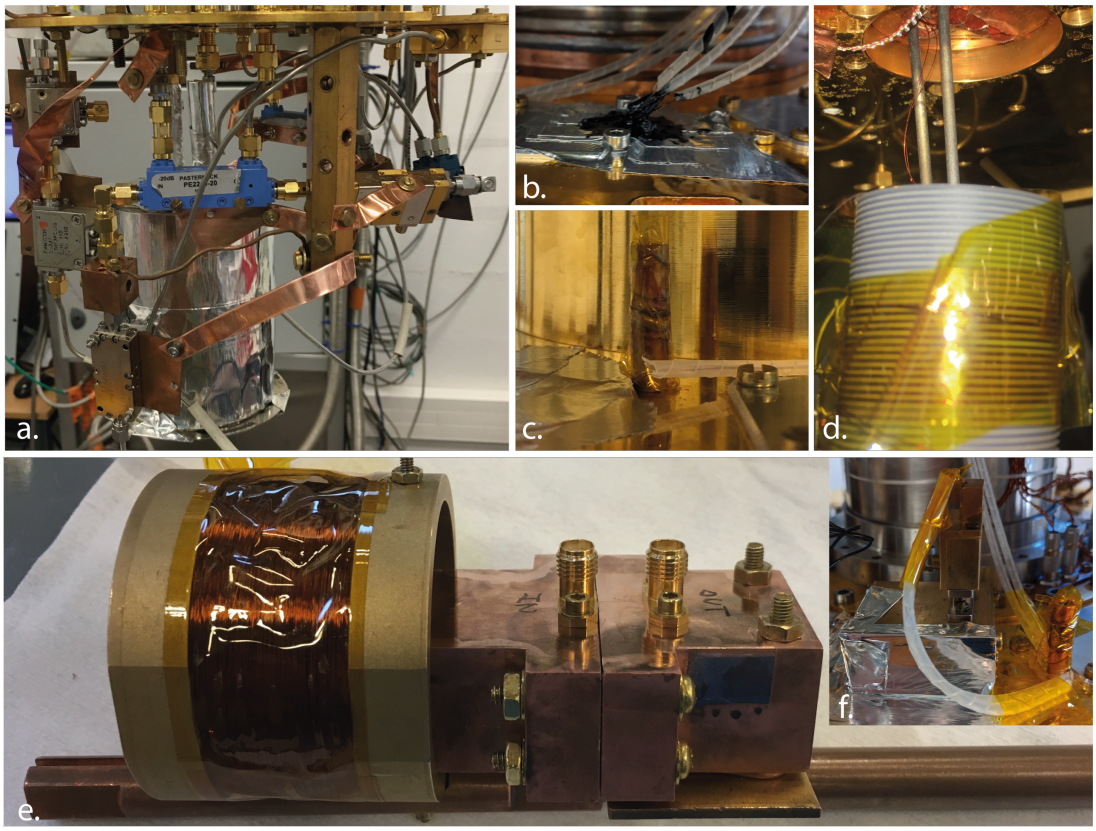

Figure 5.6: Examples of the thermalisation work done on the Fluxonium experiments during this thesis. a. Copper bands were used to thermalise the components to the dilution refrigerator. The cryoperm shield containing the coil and cavity can be seen in the background. b. Plugging the holes in the fridge using stycast prevents radiation leakage from the hot to the cold stages. c. Twisted pair wrapped around a copper post at the 1 K stage. The wire is maintained in thermal contact with the post using Apiezon vacuum grease or GE varnish and capton tape. d. When possible we used a spirally grooved tube of PCB around which we wrapped the DC wiring at the 100 mK stage. This allows a long length to avoird thermal shorts between stages, without taking up too much space. In the cryoconcept, with the 100 mK stage unusable we left a long length of wire wrapped around the fridge at the 1 K stage. e. Cavity and coil taken out of the cryoperm shielding. Both coil and cavity were solidly screwed onto a copper post, itself screwed into the base plate of the dilution refrigerator. f. 15 pin D-sub connector at 4 K to which the coil leads were soldered. The copper post thermalises the wires coming from the 70 K stage to 4 K.

at $\Phi_{\text{ext}} = \frac{1}{2}\Phi_0$ for this qubit with $E_C = h \times 0.84\,\text{GHz}$, $E_L = h \times 0.56\,\text{GHz}$ and $E_J = h \times 2.41\,\text{GHz}$.

5.2.3 *Using another qubit as a sanity check*

Because so far the coherence of the last sample had been disappointing despite our efforts regarding the fridge cabling, we concluded that the issue was perhaps with the sample sent from the University of Maryland. The Manucharyan group obliged our request for a new sample (at that time we did not have the equipement - an evaporator -

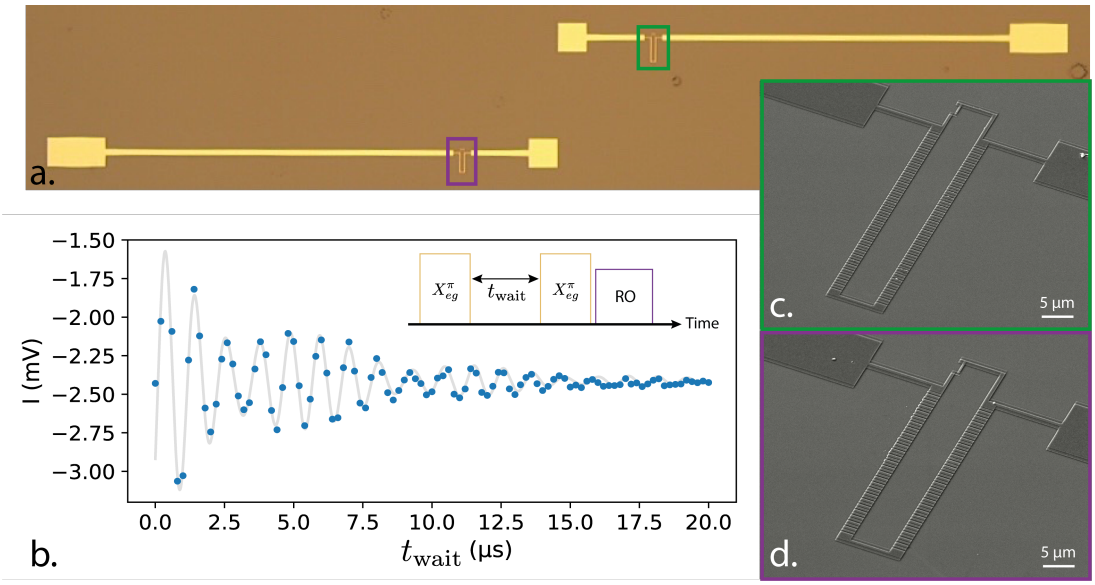

Figure 5.7: Two Fluxonium device. a. Optical image of two aluminium Fluxoniums patterned on a silicon substrate (image credit goes to the University of Maryland). The loops of each Fluxonium do not have the same area, as is revealed in the SEM images of subfigures c. and d., so the flux periodicity of each qubit is different. The Hamiltonian parameters are $E_C = h \times 0.99\,\text{GHz}$, $E_L = h \times 0.61\,\text{GHz}$, $E_J = h \times 3.89\,\text{GHz}$ (measured at the University of Maryland) for the qubit on the right and $E_C = h \times 0.97\,\text{GHz}$, $E_L = h \times 0.69\,\text{GHz}$, $E_J = h \times 4.0\,\text{GHz}$ (measured at ENS de Lyon) for the qubit on the left. b. Average result of the readout after the Ramsey sequence shown above the graph for Φ_{ext} close to the sweet spot of the qubit on the left. We fit the model (5.13) to the data. Because of the capacitive coupling between the two Fluxoniums we can make out two frequencies separated by $\sim 165\,\text{kHz}$ and a decay time of $T_2 = 5.3\,\mu\text{s}$.

to make Fluxoniums ourselves) which they had previously measured to have $T_1 = 200\,\mu\text{s}$ and $T_2 = 100\,\mu\text{s}$ at $\Phi_{\text{ext}} = \frac{1}{2}\Phi_0$ for both qubits on the sample. Indeed, as part of their research on 2 qubit gates, they had designed samples with two Fluxoniums capacitively coupled to each other as is visible on Fig. 5.7a. The spectrum for this device is shown in Chapter 3 Fig. 3.7. We decided to focus on only one of the two Fluxoniums (the device on the left in 5.7a.), to simplify the benchmarking of T_1 and T_2. Throughout Runs 8 to 10 we consistently measured T_1 between 20 and 30 µs, independent of any changes to the fridge cabling and experimental setup. T_2 on the other hand was difficult to benchmark, as its value depends much more strongly on Φ_{ext} than T_1 (see Fig. 3.4 in Chapter 3). The highest measured T_2 was between 10 and 20 µs in Runs 8 to 10 and we recurrently saw beating oscillations in later runs when the readout had been further improved. In Fig. 5.7b. we show the results of a Ramsey measurement on our qubit. We can adjust the parameters of the functional

$$f(t) = Ae^{-t/T_2}\left(\cos(\omega_1 t + \phi) + \epsilon\cos(\omega_2 t + \phi) + b\right) \ , \tag{5.13}$$

to fit the data in Fig. 5.7b. We interpret ω_1 and ω_2 to be the frequencies of the qubit we were measuring, dependent on the state of the second qubit on the chip. The capacitive coupling between the Fluxoniums could have been a limiting factor to the T_2 given

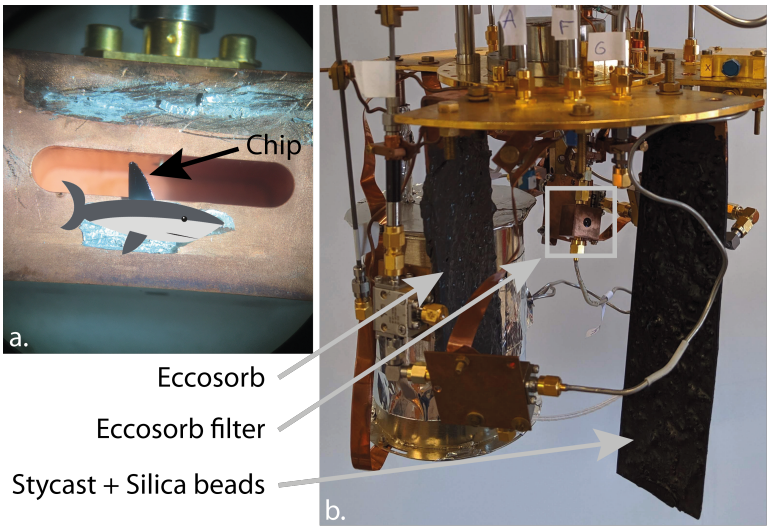

Figure 5.8: a. Residual shard of the Fluxonium device after breakage, mounted inside the copper cavity. Its physical resemblence to a shark fin is striking. b. Photograph of the base plate of the cryoconcept fridge showing the two copper panels coated with absorbing materials. We can also identify the homemade eccosorb filters placed at the cavity input and output ports.

that the sweet spot for the qubit we were measuring did not correspond to the sweet spot of the the second qubit because of the unequal loop sizes (Fig. 5.7c. and d.). This effect would have been observed in the Manucharyan group though, and they claimed to have observed much higher T_2.

With the newly arrived chip not having resolved the issue with our coherence times, we decided to try etching the copper readout cavity and clean the qubit chip. Unfortunately, upon closing the cavity again, the chip broke, something which became clear in Run 11 during which we could not measure any sign of the qubit. Opening the cavity again after warming up, revealed a small fragment of the chip on which both Fluxoniums appeared to be intact. The reason for the breakage was the important thickness of the indium wire which we had used to maintain the chip inside the cavity. Subsequently, all chips were secured using much thinner indium foil. By mounting the still apparently functional shard inside the cavity we were able to resume experiments in Run 12 (Fig. 5.8a.).

5.2.4 *Eccosorb and stycast as absorbers*

Throughout all the experimental runs care was taken to correctly filter out stray radiation coming down the microwave lines. High frequency filtering can be done using multiple techniques, typically using commercial low pass K&L filters or homemade copper powder [180] or eccosorb [181] filters. We use homemade Eccosorb filters (Fig. 5.8b.) on the input and output ports of the readout cavity in all experiments (Fig 5.3). In more recent iterations of the cabling inside the Bluefors fridge, we also place K&L filters just before (after) the eccosorb filters on the input (output) ports to increase the filtering

further. During the experimental work in the Cryoconcept, a publication by Serniak et al. [182], showed that placing the eccosorb filters close the the cavity inside a cryoperm and aluminium shield reduced the number of quasiparticles x_{qp} in their Transmon qubit. Between Runs 10 and 15, we tried to place the eccosorb filters within the same cryoperm box as the cavity or within their own cryoperm, consistently wrapping them with aluminium foil as an equivalent to the aluminium shield. These attempts lead to no significant change in T_1 or T_2 and the eccosorb filters were subsequently taken out of the cryoperm and aluminium shielding for pratical reasons. It is likely that at this point we were limited by something other than quasiparticles, potentially to do with the breakage of the qubit chip.

In a last test of high frequency absorbers, we placed two thick copper sheets ($\sim$ 1 mm) respectively coated with stycast and eccosorb at the base plate on the dilution refrigerator. These copper sheets can be seen in Fig. 5.8b. For the stycast and silica beads mixture we followed the recipe proposed in [173] with the omission of carbon power which was not available. For the eccosorb coating we used type CR 110 and followed the recipe provided by the manufacturer. Again here, no difference between before and after was observed, despite results from other groups suggesting otherwise [173, 174]. The results of this experiment are not conclusive however, because of the small surface area of the absorbing material and the likelihood that factors outside of those controlled by high frequency absorbers were the source of the short lifetimes.

5.2.5 *Temperature as a critical parameter*

Having exhaused our ideas for improvements on the setup we were left faced with the following observations

- Our T_1 time had been degraded ever since the second Fluxonium device had broken;
- No changes to the setup in the Cryoconcept fridge seemed to have any significant effect on the coherence times even before the chip had broken.

From the first observation it seemed clear that we either needed to go back to the original Fluxonium device used in Runs 1 to 7, or obtain a new device. From the second observation we concluded either one of two things: either the device was getting degraded during transport, possibly from high altitude radiation during the transatlantic flight to Europe; or the Cryoconcept fridge itself was somehow problematic and we should try measuring Fluxoniums in a different dilution refrigerator. Luckily, the transport problem had already been adressed by another group collaborating with the University of Maryland based at the University of Massachusetts Amherst. They were also having issues with reproducing the lifetimes observed by the Manucharyan group with devices shipped by airmail to Amherst. Yet, devices driven from College Park to Amherst did not show any improvement, de facto excluding the issue with airtravel.

From this we devised the following protocol. We would ask for a new device from the University of Maryland which had been previously measured in their fridges to have

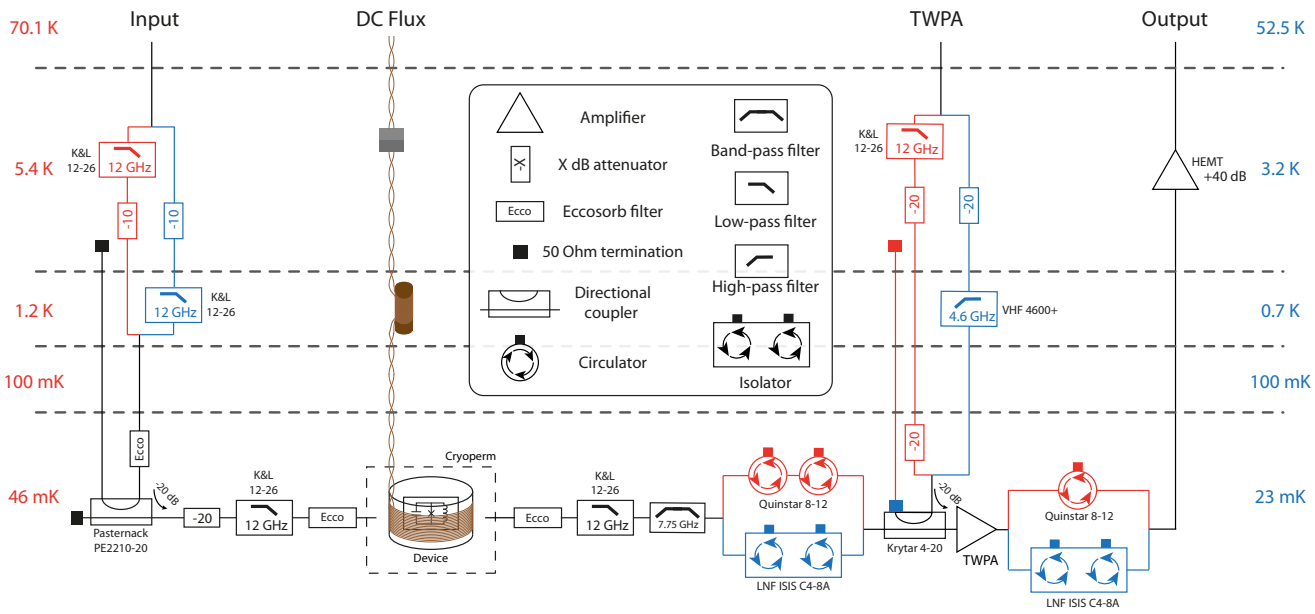

Figure 5.9: Comparison of the wirings in the Cryoconcept and Bluefors fridges. Elements in red were used in the run in the Cryoconcept whereas elements in blue were used in the Bluefors fridge. We show the measured fridge stage temperatures for each fridge in blue and red either side of the cable diagram. There is no temperature measurement on the 100 mK stage.

high coherence, sent to Lyon by plane. We would measure this device with no changes, first in the Bluefors fridge, then in the Cryoconcept, taking care to use as far as possible the same cables and components in both fridges to have some basis for comparison.

The new device we recieved from College Park was another two Fluxonium device which had been measured to have T_1 and T_2 between 70 and 100 µs for both qubits at half flux. Using cablings, shown in Fig. 5.9, similar to those described previously, we measured the Fluxonium qubits' T_1 times in both fridges. Much care was taken, going as far as using the same cables for the wiring at base temperature, to make sure the two setups were comparable. The results shown in Fig. 5.10a. are unequivocal: the energy decay times in the Bluefors fridge are 2 to 3 times longer than in the Cryoconcept and attain the values measured at the University of Maryland. Because the changes to the cabling are relatively minor, without any changes to the input attenuation or filtering, so the discrepancy in T_1 must be attributed to something else. One obvious difference between the two fridges is their difference in temperature at each stage. The Bluefors fridge is consistently colder at the 20 mK stage but also at the still, 4 K and 70 K stages. This suggests that both the actual temperature of the device as well as the level of thermal radiation in the fridge may play a role in reducing qubit lifetimes. To test the first hypothesis, a year later we performed a measurement of T_1 as a function of the base plate temperature in a third Bluefors dilution refrigerator fitted with a heater at the base plate. We waited around 2 h at each temperature set point for the fridge components to thermalise before measurement. The results for both qubits are shown in Fig. 5.10b. As the temperature increases above 40 mK we see a clear decrease in T_1 down to

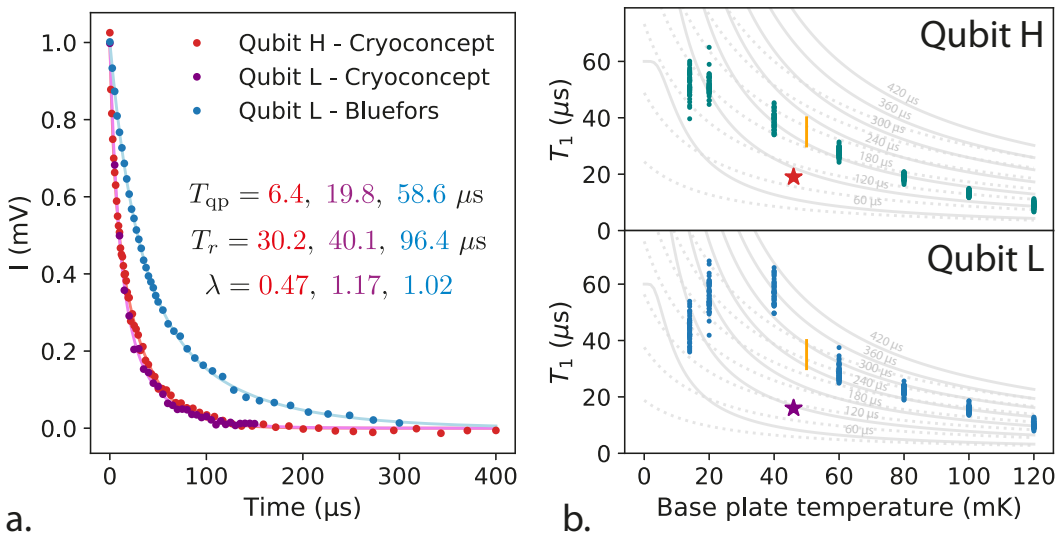

Figure 5.10: The effect of temperature on the qubit T_1. a. Examples of lifetimes of the two qubits in both the Cryoconcept and Bluefors fridges. All the relaxation curves are fitted with double exponentials, whose parameters are visible in the figure. T_1 was measured at $\Phi_{\text{ext}} \approx \frac{1}{2}\Phi_0$ ($\omega_{01}^H = 318\,\text{MHz}$), $\Phi_{\text{ext}} \approx 0.35\Phi_0$ ($\omega_{01}^L = 3.49\,\text{GHz}$) and $\Phi_{\text{ext}} \approx 0.485\Phi_0$ ($\omega_{01}^L = 382\,\text{MHz}$) for the red, purple and blue data respectively. b. Spread of T_1 measurements as a function of the dilution refrigerator mixing chamber stage temperature at $\Phi_{\text{ext}} \approx 0.49\Phi_0$ for both qubits ($\omega_{01}^L \approx 270\,\text{GHz}$ and $\omega_{01}^H \approx 360\,\text{GHz}$). T_1 was obtained by fitting the time decay of the probability of obtaining the qubit in $|0\rangle$ at time t after preparing it in state $|0\rangle$ at a time $t = 0$ with an exponential model. 50 realisations of the experiment are done at each temperature point, showing a certain spread of T_1. For comparison we show the values of an exponential fit to the data in a. with the stars and with yellow bars the range of values reported by the Manucharyan group at 50 mK. The grey lines in the background show the expected temperature dependence for different qubit lifetimes at $T = 0\text{K}$ according to (5.6). Dotted lines are the predictions for qubit temperatures 20 mK above the base plate temperature.

around 10 µs at 120 mK. Corroborating this data was the fact that prior to sending us the sample, the group at the University of Maryland had measured a decrease of both Fluxoniums' T_1 to the 30 to 40 µs range at a fridge temperature of 50 mK (shown as the yellow bars in Fig. 5.10b). Curiously though, the T_1 measurements do not seem to follow the hyperbolic tangent dependence on temperature described in (5.6) shown in Fig. 5.10 by the grey lines. This is the case even when we take into account a possible discrepancy between the temperature of the base plate and the temperature of the qubit. This result is fundamental because it shows that the qubit cannot be thought of as being in contact with the same bosonic bath at all temperatures. Moreover, the measured T_1 seem to saturate at low temperatures, possibly indicating some other limiting factor at low temperatures.

Understanding why the T_1 behaves this way is still an open question, but it is not alone. It would also be interesting to study the dependence of T_1 on the temperature of the other fridge stages. In our measurement, it was necessary to deactivate the

temperature measurement at all but the 20 mK stage to ensure a fast temperature feedback control loop. We were thus unable to monitor the temperature of the 4 K stage for example, while the base plate was above 14 mK. Futhermore, although we fit the data in Fig. 5.10b. with an exponential model, most relaxation curves we observed on this third device exhibited double exponential decays, whether in the Cryoconcept or Bluefors fridge. The reason for this - quasiparticles or an other unknown mechanism - is not yet clear and will be explored in detail in Chapter 6.

5.2.6 *DOs and DO NOTs of Fluxonium experiments*

By successive iteration we converged on an experimental setup which allowed us to measure state of the art lifetimes with Fluxonium qubits fabricated at the University of Maryland. The various experiments presented here and some found in the literature lead us to a list of techniques we know work, some which do not and a number of open questions.

In a Fluxonium experiment **DO**

- Use the coldest dilution refrigerator available;
- Spend time thermalising components thoroughly to avoid hot spots in the fridge;
- Carefully calculate the heat load on the RF and DC lines to prevent fridge heating;
- Protect the device from high frequency noise using filters or shielding;
- Optimise the readout before attempting to find the qubit spectrum when starting from scratch.

In a Fluxonium experiment **DO NOT**

- Use brass as a support for a coil without checking its magnetic properties first;
- Use thick indium wire to secure the chip inside the cavity;
- Leave the voltage source used for the flux bias plugged in during cooldown (not adressed here, but can lead to a lot of flux jumps);
- Necessarily increase the power when a qubit transition is invisible.

OPEN QUESTIONS

- Does putting the eccosorb filters inside a cryoperm shield really matter for T_1 and T_2?
- At what level of T_1 and T_2 do protective shields (lead, eccosorb, stycast) and filtering have an effect?
- Is the temperature of the stages above the base plate critical to qubit coherence?
- Why is fridge temperature such a critical parameter for Fluxonium qubits?

5.3 RESET STRATEGIES FOR LOW FREQUENCY FLUXONIUM QUBITS

We have mentioned multiple times that the relatively low frequency of Fluxonium qubits can be problematic because of the high thermal occupancy of the excited state. It is therefore desirable to develop schemes which purify the quantum state, resetting it to a known starting configuration. In fact, the ability to quickly and effectively prepare the qubit state is an issue also outside the specific sub-field of Fluxonium qubits. Indeed, even for qubits with $\hbar\omega \gg k_B T$ such that the thermal occupation is negligeable, when the T_1 relaxation time is long, waiting for the qubit to decay naturally to the ground-state can be a significant proportion of the run time of a quantum algorithm. Because of this, numerous studies have also been carried out on resetting Transmon qubits to their ground-state. We can draw inspiration from these studies to help the state preparation of Fluxonium devices. For ease of notation, we use letters ($|g\rangle$, $|e\rangle$, $|f\rangle$...) for the qubit states and integers for the cavity Fock states ($|0\rangle$, $|1\rangle$, $|2\rangle$...) in this part of the thesis.

5.3.1 *Overview of qubit reset techniques*

There are many techniques which have been used to reset Transmon and Fluxonium qubits to a known pure state. We can broadly define some categories to classify the different strategies. Perhaps the most naive (but not the least resource intensive) is to reset the device by either heralding the qubit state or by applying some feedback after a readout. The principle of heralding preparation is to start every protocol with a strong measurement of the qubit state and discard those times where the measurement result was not the one desired. The advantage of this technique is its simplicity, and the fact that is is limited only by the readout fidelity, which can be high (99.2% in [183]). For Fluxonium qubits though, because the thermal population is high, close to 50% of realisations must be discarded, leaving a lot of deadtime. Reset by feedback solves this problem, as after the readout, we apply a π-pulse on the qubit conditioned on the result of the measurement (see Fig. 5.11c.). Say we wanted to prepare $|g\rangle$. If the measurement result is $|g\rangle$ we do nothing; if it is $|e\rangle$ we can apply a π-pulse to retrieve the $|g\rangle$ state. Feedback state preparation was used on a Fluxonium qubit in [34] to prepare the $|g\rangle$ ($|e\rangle$) state with 98% (90%) fidelity within 1036 ns. The fidelity of the state preparation is limited here both by the readout as well as the π-pulse fidelity. The time of the preparation is limited by the duration of the readout, the electronic feedback loop and the duration of the π-pulse when necessary.

A broad category of resets are those which exploit the higher levels of the Transmon and Fluxonium artificial atoms and the presence of the coupling to the readout cavity. An established reset technique using this concept is the DDROP protocol which consists of simultaneously driving the $|g,0\rangle - |e,0\rangle$ and $|g,0\rangle - |g,1\rangle$ transitions [184]. The first drive converts the qubit $|e\rangle$ state into the ground-state conditionned on the cavity being empty, whilst the second drive populates the cavity once the qubit is in $|g\rangle$ stopping the first drive from re-exciting the qubit. Another well studied technique is to drive the (not-forbidden) $|f,0\rangle - |g,1\rangle$ transition after applying a π-pulse to transfer any residual population in $|e\rangle$ to $|f\rangle$ (Fig. 5.11a.). This effectively converts two qubit

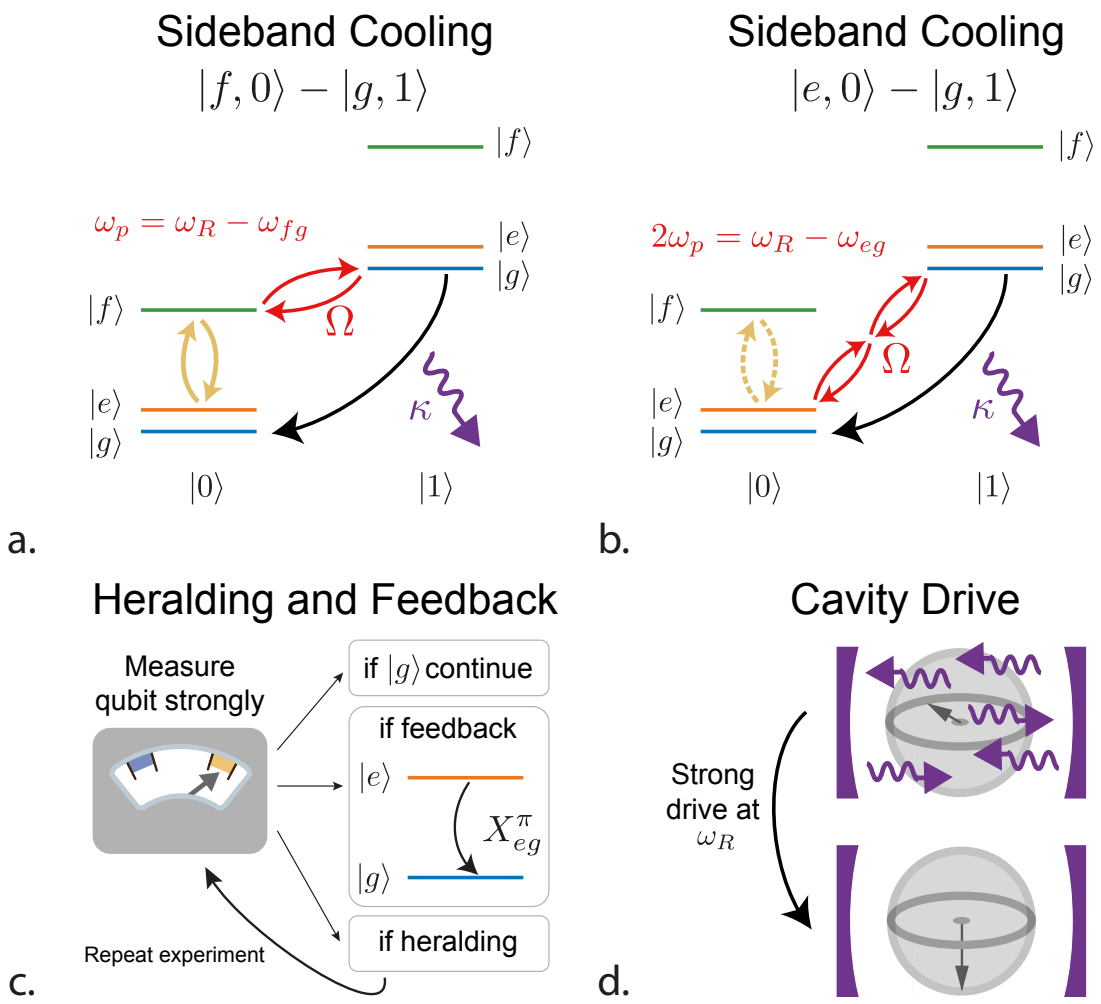

Figure 5.11: Overview of the different qubit reset techniques presented in this thesis. a. Qubit reset by driving the $|f,0\rangle - |g,1\rangle$ transition by using a pump tone at the frequency $\omega_p = \omega_R - \omega_{fg}$. At the same time a Rabi drive on the $|e\rangle - |f\rangle$ transition brings the residual population into the $|f\rangle$ state before conversion into the cavity. The lossy cavity then dissipates the converted energy. For this to work the cavity decay rate must be much greater than the qubit re-excitation rates $\kappa \gg \Gamma_{g\to e}, \Gamma_{e\to f}, \Gamma_{g\to f}$. b. Similar idea but by driving the $|e,0\rangle - |g,1\rangle$ transition by using a pump tone at the frequency $\omega_p = (\omega_R - \omega_{eg})/2$. The Rabi drive on the $|e\rangle - |f\rangle$ transition is not necessarily useful here because the population in $|f\rangle$ is supposed to be low. c. Qubit reset by feedback or heralding. The qubit is first strongly read. Then, in the case of feedback if the result is not the one targeted, an additional unitary is applied to prepare the desired state. In the case of heralding, the measurement is repeated until we obtain the desired state. d. By applying a strong drive at the resonator frequency to populate the cavity, the populations of the qubit states change, hopefully preparing it in a pure state.

excitations into a single cavity excitation mediated by a pump tone, by the means of a 4^{th} order process allowed by the expansion of the cosine non-linearity. As long as the Rabi rate $\Omega_{|f,0\rangle-|g,1\rangle}$ of the qubit to photon conversion is smaller than the cavity decay rate κ, the photon in the cavity will decay, leaving the state $|g,0\rangle$ before the cavity excitation can be swapped back into the qubit $|f\rangle$ state. This protocol was demonstrated on Transmons in [185] with 0.2% residual excitation and within 500 ns. Reset to within 2% was achieved by [186] in 210 ns. Using this transition to generate single photons was demonstrated in [187] a reference which also provides insight into the theoretical description of multilevel qubit drives. Other transitions have also been used, using the 3^{rd} excited state of Fluxonium in [77] for example. Higher qubit transitions can also be used to drive the protected transitions Λ type [110, 109].

Other more specific reset techniques exploit flux tunability, something which is not always available in Transmon devices. In [188], the authors showed how a qubit could be coupled to flux tunable lossy cavity. By bringing the cavity into resonance with the qubit transition, the qubit decay times are shortened. More recently, fast flux gates in a Fluxonium circuit were used to accelerate a reset protocol using the concept of sideband cooling we already described for the $|f,0\rangle - |g,1\rangle$ transition. The Alibaba group showed that it is possible to reset a Fluxonium qubit by directly driving the $|e,0\rangle-|g,1\rangle$ transition away from the $\Phi_{\text{ext}} = \frac{1}{2}\Phi_0$ sweet spot [189]. Indeed, at the sweet spot, this transition is forbidden for parity reasons. Their protocol consisted of a flux gate biasing the qubit away from $\Phi_{\text{ext}} = \frac{1}{2}\Phi_0$, a drive on the $|e,0\rangle - |g,1\rangle$, dissipating the qubit excitation in the cavity, before bringing the flux back to $\Phi_{\text{ext}} = \frac{1}{2}\Phi_0$. They claimed a reset fidelity of 98% in 200 - 500 ns depending on the flux point to which the qubit was taken during the excursion. In this thesis we show that it is in fact possible to drive this transition at the sweet spot as long as the available pump power is high enough (Fig. 5.11b.). This is because the 4^{th} order process at the base of this mechanism needs to 2 pump photons to convert the qubit excitation into a cavity excitation.

We can end this discussion with a simple method for preparing Fluxonium qubits, but one which has yet to be understood at a theoretical level. There have been many reports that a strong drive at the readout cavity frequency (but not only) has a purifying effect on the qubit state (Fig 5.11d.). Some of these reports are informal (from the Devoret group at Yale [66], or the Pop group in Karlsruhe) but this technique has also been mentioned in publications by the Manucharyan group for example [38, 33]. In both these works, a large drive at the cavity frequency had a tendency to prepare the qubit in the $|e\rangle$ state. The preparation time is slow, around $T_1/5$ in both cases and the residual population in $|g\rangle$ is on the order of 10 to 20%. Quantifying the rate at which the qubit populations are affected by this drive at different amplitudes and fluxes is the subject of Chapter 6.

In the next subsections we present some of our results concerning the reset of Fluxonium qubits.

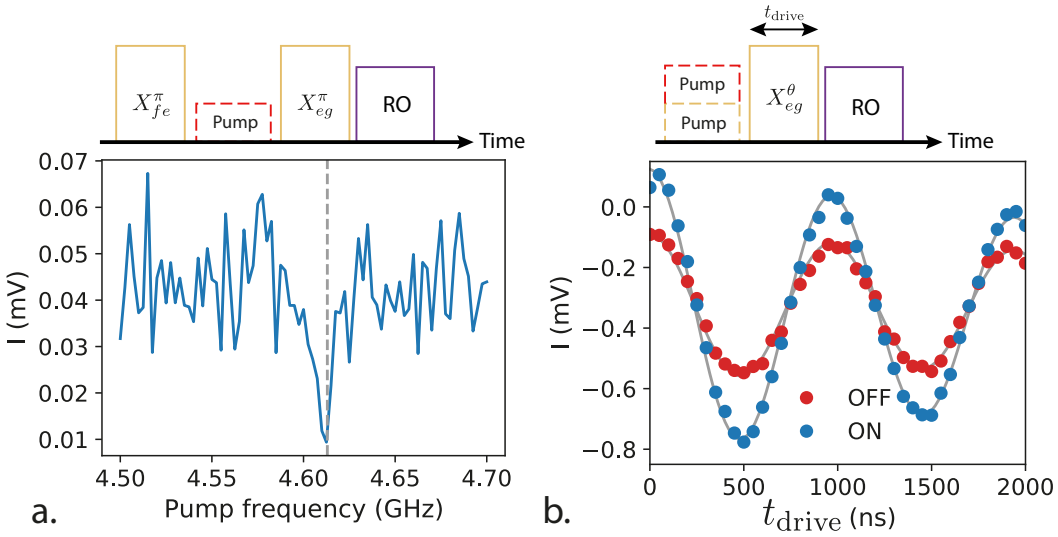

Figure 5.12: Effect of the cooling pump at $\wp = \omega_R - \omega_{02}$ on the qubit. a. Real part of the cavity response as the frequency of pump ω_p is swept. The full measurement sequence is shown above the graph. The durations of the π-pulses on $|g\rangle - |e\rangle$ and $|e\rangle - |f\rangle$ are fixed to 500 and 420 ns respectively. The pump duration is 2000 ns. The gray line shows the frequency chosen for the cooling pump in this experiment: $\omega_p = 2\pi \times 4.612$ GHz. b. Rabi oscillations of the $|g\rangle - |e\rangle$ transition with (ON) and without (OFF) cooling applied before the qubit rotation. Here the simultaneous drives at ω_p and ω_{fe} are both active for 20 µs when the cooling is applied. Grey lines correspond to an exponentially decaying cosine model.

5.3.2 *Driving the $|f,0\rangle - |g,1\rangle$ transition*

In this section we will consider the Fluxonium qubit ($E_C = 2\pi\hbar \times 0.84$ GHz, $E_J = 2\pi\hbar \times 2.41$ GHz, $E_L = 2\pi\hbar \times 0.56$ GHz) of runs 1 to 7 in Table 5.1. The qubit is coupled dispersively to a readout cavity and the qubit transitions can be driven by external fields coupling to the Fluxonium's charge operator $\hat{n}$. At $\Phi_{\mathrm{ext}} = \frac{1}{2}\Phi_0$, $\omega_{eg} = 2\pi \times 540$ MHz and $\omega_{fe} = 2\pi \times 2.41$ GHz; the cavity frequency is $\omega_R = 2\pi \times 7.563$ GHz and its linewidth is $\kappa = 2\pi \times 9.4$ MHz.

With these qubit parameters we expect the populations $p_g = 64\%$, $p_e = 34\%$ and $p_f = 2\%$ of the $|g\rangle$, $|e\rangle$ and $|f\rangle$ states respectively for a bath at 40 mK. Because p_f is so low, we can neglect the populations of the other qubit states in the following and consider only the qutrit made of $|g\rangle$, $|e\rangle$ and $|f\rangle$. We also see that we have a lot to gain by preparing the qubit in the $|g\rangle$ state, as $p_e = 34\%$ is far from negligeable. In Fig. 5.12a. we show the spectroscopy used to find the pump frequency ω_p. The pulse sequence used, shown above the graph in Fig. 5.12a., is designed to maximise the contrast in cavity response between the case where the pump is on resonance with the cooling transition and when it is not. Experimentally we set $\omega_p = 2\pi \times 4.612$ GHz, almost exactly the theoretically predicted frequency $\omega_R - \omega_{02} = 2\pi \times 4.613$ GHz. To verify that this is indeed the cooling transition we measure Rabi oscillations on the $|g\rangle - |e\rangle$ transition

with and without preparing the qubit state using the protocol described in Fig. 5.11a. The results are shown in Fig. 5.12b. and by fitting a decaying cosine model given by

$$f(x) = Ae^{-t/T_R}\cos(\Omega t) + b \ , \tag{5.14}$$

where A, T_R, Ω and b are free parameters, to the measured Rabi oscillations (grey lines), we deduce that the contrast of the Rabi oscillations is increased by a factor 1.95 when preparing the qubit state with the cooling mechanism. Whilst this already gives some information about the efficiency of the cooling protocol, we need to determine the qubit populations to be more quantitative. This is typically done by using a gaussian model to extract the populations of each qubit pointer state in histograms of the qubit readout, but here such a high readout fidelity was unattainable. We devised a technique using only the phase of the cavity response and different gates to perform a tomography of the qubit.

Let us define χ_g, χ_e and χ_f the dispersive shifts of states $|g\rangle$, $|e\rangle$ and $|f\rangle$ on the cavity frequency. The frequency of the cavity for any population of the three qubit levels is

$$\omega_R = \omega_R^{\text{bare}} + p_g\chi_g + p_e\chi_e + p_f\chi_f \ , \tag{5.15}$$

where ω_R^{bare} is the frequency of the cavity uncoupled from the qubit (inaccessible, see the discussion in Chapter 3). Theoretically, the phase of the cavity response in transmission is given by

$$\arg\left[S_{21}(\omega)\right] = -\arctan\left(\frac{2(\omega-\omega_R)}{\kappa}\right) \ . \tag{5.16}$$

We can also fix the frequency of the cavity probe. We choose $\omega_R^{\text{th}} = \omega_R^{\text{bare}} + p_g^{\text{th}}\chi_g + p_e^{\text{th}}\chi_e + p_f^{\text{th}}\chi_f$, the frequency of the cavity when the qubit is in thermal equilibrium with its environment, such that

$$\arg[t] = -\arctan\left(\frac{(p_g^{\text{th}}-p_g)\chi_g + (p_e^{\text{th}}-p_e)\chi_e + (p_f^{\text{th}}-p_f)\chi_f)}{\kappa/2}\right) \ . \tag{5.17}$$

We also knew from exchanges with the Manucharyan group that all the dispersive shifts were much smaller that the cavity linewidth (we did not know the qubit/cavity coupling). To give a sense of scale, for a charge coupling between qubit and cavity with coupling constant $g = 2\pi \times 100\,\text{MHz}$, $\chi_g = 2\pi \times 290\,\text{kHz}$, $\chi_e = 2\pi \times 620\,\text{kHz}$ and $\chi_f = 2\pi \times 340\,\text{kHz}$. The arctan can therefore be approximated as a linear function so that

$$\arg[t] = -\frac{(p_g^{\text{th}}-p_g)\chi_g + (p_e^{\text{th}}-p_e)\chi_e + (p_f^{\text{th}}-p_f)\chi_f}{\kappa/2} \ . \tag{5.18}$$

Finally, although we do not know g, we do know that the dispersive shifts are proportional to g^2 at second order (see Chapter 3). We can define $\chi_x^0 = \chi_x/g^2$, $x \in \{g, e, f\}$ and include g^2 in a multiplicative unknown in our equation. Indeed, we can calculate the χ_x^0 through a numerical simulation of the Fluxonium without needing any knowledge of g. The thermal populations p_x^{th} are also unknown and they can be included in an additional phase offset ϕ. Thus

$$\arg[t] = \phi - \frac{2g^2}{\kappa}\left(p_g\chi_g^0 + p_e\chi_e^0 + p_f\chi_f^0\right) \ . \tag{5.19}$$

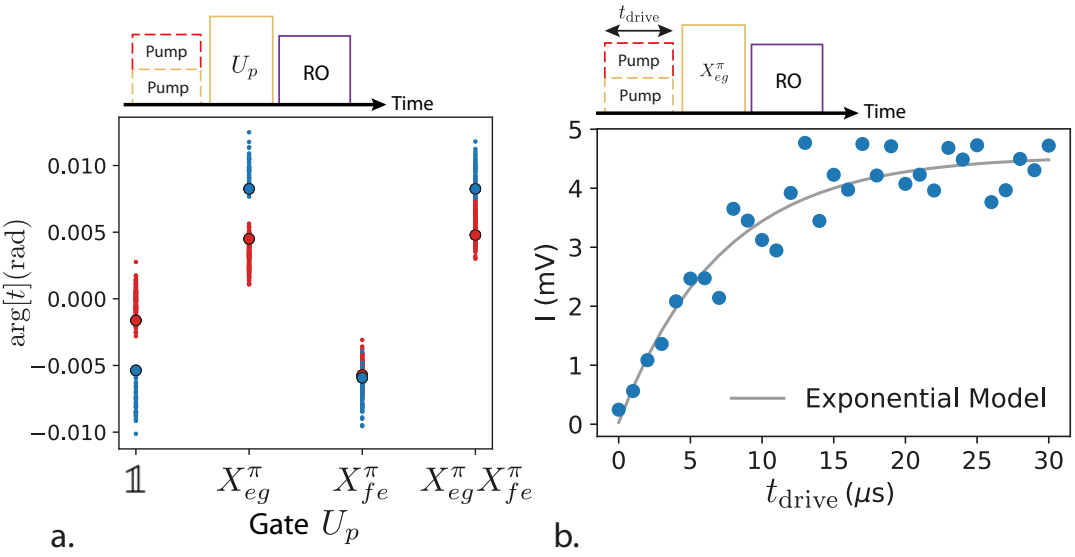

Figure 5.13: Benchmarking the cooling process using the $|f,0\rangle - |g,1\rangle$ transition. a. Phase of the cavity response after each qubit gate with (blue) and without (red) the cooling procedure for a 141 repetitions of the measurement. Fitting the model defined by (5.20) in both cases gives predicted values to arg[t] shown by the larger markers circled in black. From the model given by (5.20) we obtain $p_g^{\text{th}} = 71\%$, $p_e^{\text{th}} = 29\%$ and $p_f^{\text{th}} \sim 0\%$ for the qubit in the thermal state and $p_g^{\text{cool}} = 95\%$, $p_e^{\text{cool}} = 4\%$ and $p_f^{\text{cool}} \sim 1\%$ after we have prepared the qubit state by cooling. When on, the cooling sequence is applied for 20 µs b. Real part of the cavity response as the duration of the two simultaneous tones at ω_p and ω_{fe} is swept in the measurement sequence above the graph. Adjusting the characteristic time of an exponential relaxation model to the data gives a cooling rate of 7.1 µs.

ϕ also contains the dependence of the measurement result on the electrical delay and impedance mismatches in the experimental setup. In the above equation, there are 5 unknowns: the phase offset ϕ, the multiplicative factor $\frac{2g^2}{\kappa}$ and the qubit populations. This is where the qubit gates come in. For each qubit state we want to know the populations of, we can apply the gates $\mathbb{1}$, X^π_{eg} (π-pulse on $|g\rangle - |e\rangle$), X^π_{fe} (π-pulse on $|e\rangle - |f\rangle$) and $X^\pi_{eg}X^\pi_{fe}$ (two successive π-pulses, first on $|e\rangle - |f\rangle$ then on $|g\rangle - |e\rangle$), before reading out the qubit state. Assuming the gates have 100% fidelity, we obtain a set of 5 equations with 5 unknowns which can be solved simultaneously to find the populations.

$$\begin{cases} \arg[t]_{\mathbb{1}} & = \phi - \frac{2g^2}{\kappa}\left(p_g\chi_g^0 + p_e\chi_e^0 + p_f\chi_f^0\right) , \\ \arg[t]_{X^\pi_{eg}} & = \phi - \frac{2g^2}{\kappa}\left(p_e\chi_g^0 + p_g\chi_e^0 + p_f\chi_f^0\right) , \\ \arg[t]_{X^\pi_{fe}} & = \phi - \frac{2g^2}{\kappa}\left(p_g\chi_g^0 + p_f\chi_e^0 + p_e\chi_f^0\right) , \\ \arg[t]_{X^\pi_{eg}X^\pi_{fe}} & = \phi - \frac{2g^2}{\kappa}\left(p_f\chi_g^0 + p_g\chi_e^0 + p_e\chi_f^0\right) , \\ 1 & = p_g + p_e + p_f \ . \end{cases} \tag{5.20}$$

We use this technique to benchmark the effectiveness of our cooling procedure. In Fig. 5.13a. we show the phase of the transmitted signal as a function of the gate after cooling or with the qubit in the thermal state. After cooling the population of the

ground state increases from 71% to 95% and the population of $|e\rangle$ is reduced from 29% to 4%, corresponding to a reduction of the effective temperature from 29 mK to 8 mK. These values make intuitive sense with respect to the results shown in Fig. 5.13a. as $\arg[t]_{X^{\pi}_{eg}} \approx \arg[t]_{X^{\pi}_{eg}X^{\pi}_{fe}}$ and $\arg[t]_{\mathbb{1}} \approx \arg[t]_{X^{\pi}_{fe}}$ if $p_g \approx 1$ in (5.20). Additionally, we can explain the fact that $\arg[t]_{X^{\pi}_{fe}}$ is close to insensitive to the p_e/p_g ratio by noting that $\chi_g/\chi_f \approx 1$. Finally, the ratio of the difference in populations $\frac{p_g^{\text{cool}}-p_e^{\text{cool}}}{p_g^{\text{th}}-p_e^{\text{th}}} = 2.2$ is commensurable with the factor 2 contrast increase of the Rabi oscillations in Fig. 5.12b. Factoring in pulse fidelities estimated to be above 90% does not change the results significantly.

Because the speed at which we can reset the qubit is also important, in Fig. 5.13b. we sweep the length of the cooling pulses, montoring the quadrature of the readout signal to measure the effect of increasing the cooling duration. The results follow an exponential saturation with time constant $T_{\text{cool}} = 7.1\,\mu\text{s}$, 5 times shorter than the measured T_1. Whilst this is a longer than a typical qubit gate, it suggests that it is still worthwhile using the cooling sequence to reset the qubit rather than simply waiting for the spontaneous qubit decay.

5.3.3 *Driving the $|e,0\rangle - |g,1\rangle$ transition*

The second type of cooling we used during the experiments in this thesis, is the reset of the qubit using the $|e,0\rangle - |g,1\rangle$ transition shown in Fig. 5.11b. We will show the results for this technique using the two Fluxonium sample measured in runs 14 and 15 (see Tab. 5.1). The Fluxonium in question had $E_C/h = 0.97\,\text{GHz}$, $E_L/h = 0.69\,\text{GHz}$ and $E_J/h = 4\,\text{GHz}$ so that at $\Phi_{\text{ext}} = \frac{1}{2}\Phi_0$, $\omega_{eg} = 2\pi \times 375\,\text{MHz}$ and $\omega_{fe} = 2\pi \times 3.495\,\text{GHz}$. The cavity frequency was $\omega_R = 2\pi \times 7.752\,\text{GHz}$ and its linewidth was $\kappa = 2\pi \times 2.9\,\text{MHz}$.

We start by looking for the pump frequency and power using the measurement sequence shown in Fig. 5.14a. First we apply a cooling tone for a fixed duration of 10 µs before: either immediately reading out the qubit state, or first applying a π-pulse on the $|e\rangle - |g\rangle$ transition before reading out. By monitoring the distance $\left|\bar{Z}^{\mathbb{1}}_{\text{out}} - \bar{Z}^{X^{\pi}_{eg}}_{\text{out}}\right|$ between the average readout signal of these two cases in the IQ-plane, we can find the power and frequency at which the cooling pump is most effective (shown in Fig. 5.14a.). Interestingly, the optimal frequency depends linearly on the drive power, which is commensurate with an AC-stark shift of the qubit as the power is increased. At low powers we retrieve the predicted pump frequency $\omega_p = \frac{\omega_R - \omega_{eg}}{2} = 2\pi \times 3.689\,\text{GHz}$. Furthermore, it is not necessarily the highest pump powers which lead to the highest contrast. When the power was too high, we saw a saturation and then a decrease in the contrast as high order terms from the cosine non-linearity became important.

The effect of the cooling tone on the average readout signal can be seen in the Rabi oscillations of Fig. 5.14b. The increase in contrast is here 12 fold, which seems incompatible with the measurement of Fig. 5.12b. Indeed, for the measurement contrast to increase by such a large factor, the ratio of qubit populations in the thermal state

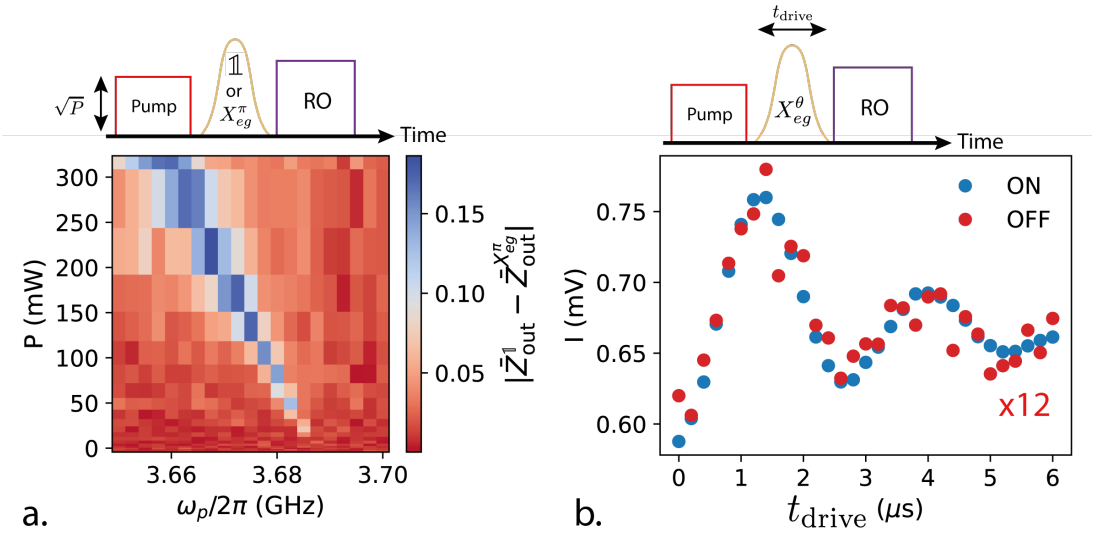

Figure 5.14: Effect of the cooling pump at $\omega_p = \frac{\omega_R - \omega_{eg}}{2}$ on the qubit. a. Distance between average measurement results in the IQ-plane after the measurement sequence shown above. The pump power referred to the source and frequency are varied while its duration 10 µs is kept fixed. The π-pulse on the $|e\rangle - |g\rangle$ transition lasts 350 ns and has a hyperbolic secant shape. b. Rabi oscillations with (blue) and without (red) using the cooling pump for 10 µs. For better visibility the case without cooling has been magnified 12 times and offset vertically for better comparison.

should close to unity $\frac{p_1^{\text{th}}}{p_0^{\text{th}}} \approx 1$. Yet for a qubit at 540 MHz at the same nominal temperature we predicted $\frac{p_1^{\text{th}}}{p_0^{\text{th}}} = 0.53$ and measured 0.41 (see Fig. 5.13), far away from 1 even when taking into account the lower frequency of the qubit this time around. It was only after the experiment was over that we realised that explaning this requires taking into account the presence of the second Fluxonium on the same chip. Everytime we measure the qubit, we are in fact measuring the computational subspace of the two qubit system containing four states: $|g,g\rangle$, $|e,g\rangle$, $|g,e\rangle$ and $|e,e\rangle$. Because the charge coupling between the two qubits only mediates a small hybridisation of the states (a few hundreds of kHz according to the beats in the Ramsey measurement of Fig. 5.7b.), these four states are very close to the product states $|g\rangle \otimes |g\rangle$, $|e\rangle \otimes |g\rangle$, $|g\rangle \otimes |e\rangle$ and $|e\rangle \otimes |e\rangle$ of the uncoupled qubits. In the following we will use the convention that the first letter denotes the state of the qubit whose parameters were given above. In the IQ-plane, these four states are materialised by the 4 gaussian distributions whose projection on the real quadrature I when the qubit is in the thermal state is given by the red points in the left panel of Fig. 5.15a. The histogram can be decomposed into a single gaussian on the right and the overlap of three gaussians on the left. From various other measurements we deduce that the gaussian peak on the right corresponds to the $|g,g\rangle$ state, whereas the other three states cannot really by identified in the distribution on the left. As is evident by comparing the cases with and without a π-pulse on $|e\rangle - |g\rangle$ (the red histograms in the right and left panels respectively), the expected contrast of Rabi oscillations is low. This is not due to the infidelity of the π-pulse, for which we measured a fidelity of around 99%. When the cooling pump is applied, the distributions (blue) become more polarised, leading to a large increase in the contrast

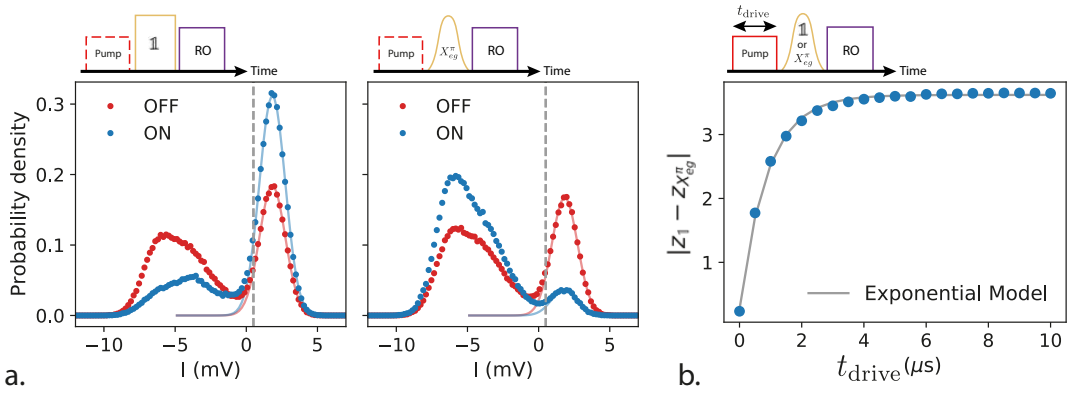

Figure 5.15: Benchmarking the cooling process using the $|e,0\rangle - |g,1\rangle$ transition. a. Real part of the readout histograms for 200000 iterations of each of the different experiments show in the pulse sequences above the graphs. Points in red are taken when the cooling is off, points in blue show the results when the measurement sequence started with the cooling pump. Fits to the gaussian part of the distribution on the right of the gray dashed line are shown with solid lines. The pump was applied for 10 µs when the cooling was on. b. Distance between average measurement results in the IQ-plane as a function of the pump duration in the measurement sequence shown above. The gray line is the fit an exponential saturation with time constant 890 ns.

of Rabi oscillations.

By studying these histograms we can determine the effectiveness of the cooling procedure. Because the gaussian distributions of the $|e,g\rangle$, $|g,e\rangle$ and $|e,e\rangle$ states cannot be identified, we focus on measuring the population p_{gg} in the $|g,g\rangle$ state. This is determined by fitting the model

$$f(x) = p_{gg} \cdot \frac{1}{\sqrt{2\pi}\sigma} e^{-\frac{(x-\mu)^2}{2\sigma^2}} \quad , \tag{5.21}$$

a weighted normalised gaussian with mean μ and standard deviation σ, to the points on the right of the gray dashed line in Fig. 5.15a. μ and σ are kept fix for all the distributions and the results of the fit are shown by the red and blue solid lines. The information about p_{gg} in each situation, and the knowledge that the π-pulse on $|e\rangle - |g\rangle$ almost exactly inverts the populations p_g and p_e, is enough to deduce the cooling effectiveness[5]. We can start with the following assumptions

$$1 = p_{gg} + p_{eg} + p_{ge} + p_{ee} \text{ and } \frac{p_{gg}}{p_{eg}} = \frac{p_{ge}}{p_{ee}} \quad . \tag{5.22}$$

The first neglects the presence of the higher energy levels of both Fluxoniums. The second is a consequence of detailed balance. From this we deduce

$$1 = p_{gg} + p_{eg} + p_{ge} + \frac{p_{eg}}{p_{gg}} p_{ge} \quad . \tag{5.23}$$

5 The π-pulse is not selective because its duration (100 ns) is much smaller than the inverse of the frequency splitting between the transitions $|gg\rangle - |eg\rangle$ and $|ge\rangle - |ee\rangle$ (165 kHz). It switches p_{gg} with p_{eg} as effectively as p_{ge} with p_{ee}.

Solving for p_{ge} leads to

$$p_{ge} = \frac{1 - p_{gg} - p_{eg}}{1 + \frac{p_{eg}}{p_{gg}}} \ . \tag{5.24}$$

We have direct access to p_{gg} and p_{eg} both with and without cooling, thanks to the fitting technique explained above and the high fidelity π-pulse. We can thus deduce $p_{gg}^{\text{th}} = 42\%$, $p_{eg}^{\text{th}} = 38\%$, $p_{ge}^{\text{th}} = 10\%$ and $p_{ee}^{\text{th}} = 10\%$; $p_{gg}^{\text{cool}} = 71\%$, $p_{eg}^{\text{cool}} = 8\%$, $p_{ge}^{\text{cool}} = 19\%$ and $p_{ee}^{\text{cool}} = 2\%$; such that for the qubit we are interested in $p_g^{\text{th}} = 52\%$, $p_e^{\text{th}} = 48\%$ and $p_g^{\text{cool}} = 90\%$, $p_e^{\text{cool}} = 10\%$. These populations represent effective temperatures of 225^{+225}_{-75} mK and 8.2 ± 0.4 mK. Finally, to measure the time it takes to achieve the qubit reset, we monitor the contrast $\left|\bar{Z}^{\mathbb{1}}_{\text{out}} - \bar{Z}^{X^{\pi}_{eg}}_{\text{out}}\right|$ as a function of the pump duration in Fig. 5.15b. A fit of an exponential model to the saturation curve gives $T_{\text{cool}} = 890\,\text{ns}$, much shorter than the $T_1 = 10\,\mu\text{s}$. With this value for T_{cool}, sideband cooling of the $|e,0\rangle - |g,1\rangle$ transition appears to be more effective than using the $|f,0\rangle - |g,1\rangle$ transition in the previous section, although in the latter case we had not swept the pump power to opimise the cooling rate. Combined with the use of a different qubit with different T_1, this makes comparisons delicate.

As a final note, we mention that it is also possible to pump the upper sideband of the same transition. By applying a pump at $\omega_p = \frac{\omega_R + \omega_{eg}}{2}$ if is possible to prepare state $|e\rangle$ rather than $|g\rangle$. This involves creating a qubit as well as a cavity excitation by the conversion of two pump photons.

5.3.4 *Reset by strong drive*

To motivate why the qubit state might be affected by a strong drive at the cavity frequency, it is worth taking a moment here to highlight some of the remaining inconsistencies with the results of the two last sections. Consider the effective temperatures of the qubit in the thermal state. In the previous section we found $T_{\text{eff}} = 29\,\text{mK}$ and here $T_{\text{eff}} = 320\,\text{mK}$ despite the qubit frequencies being relatively similar. How can we explain this, when the range expected from the literature is 50 to 140 mK (see Sec. 5.1.2)? While the first case could be explained by the poor readout signal and unknown π-pulse fidelity, the second temperature appears more robust because it is directly extracted from the readout histograms. This leads us to question the fidelity of our readout pulses. In Fig. 5.16 we qualitatively illustrate the problem. Although the qubit's thermal population prior to the readout pulse is constant, the population p_{gg} of the ground-state (gaussian distribution at the bottom of the histograms) appears to be depleted as the amplitude of the readout pulse increases. This is a clear sign that the readout pulse is affecting the qubit populations. Whilst this can appear to be something negative which needs to be understood more fully (which will be the case in Chapter 6), it can also be used as a ressource.

To see this we can turn to another Fluxonium device with two qubits. This is the device which is studied in detail in Chapter 6 and whose parameters and properties are

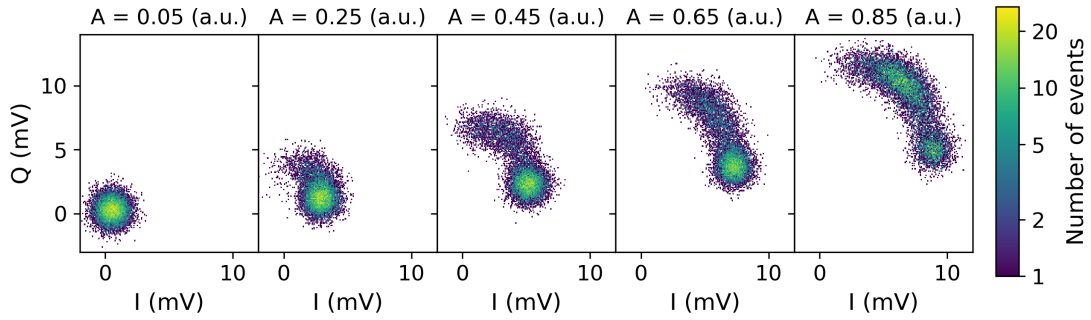

Figure 5.16: Histograms of 10000 (I,Q) quadratures obtained by heterodyne measurement of 800 ns long readout pulses as a function of the pulse amplitude A for the device described in Sec. 5.3.3. The results of that section were obtained with $A = 0.45$.

described there. At the half flux point $\Phi_{\text{ext}} = \frac{1}{2}\Phi_0$, the dispersive shifts of the $|e,g\rangle$ and $|g,e\rangle$ states are the same, which is why there are only three visible pointer states in the readout histogram of Fig. 5.17a. Because the signal to noise ratio of the histograms is sufficient, we can immediately extract the qubit populations by fitting 4 gaussians to the experimental distribution corresponding to the states $|g,g\rangle$, $|e,e\rangle$, $|\text{other}\rangle$ and the overlapping states $|g,e\rangle$ and $|e,g\rangle$. We use the designation of $|\text{other}\rangle$ for the points in the histogram which do not belong to the 3 pointer-states visible in Fig. 5.17a. To efficiently extract the populations, we use the gaussian mixture model available in the python package scikit-learn [190]. We use our ability to extract the qubit populations from the histogram to monitor the effect of a strong cavity pulse in Fig. 5.17b. As the length of the cavity pulse is increased, the $|g,g\rangle$ state is emptied rapidly, bringing the ground-state population down to 2.5% within an exponential decay time of 190 ns. This is around 500 times faster than $T_1 \sim 100\,\mu\text{s}$. Unfortunately, emptying the state $|g,g\rangle$ comes at the price of increasing the population in the $|\text{other}\rangle$ states, outside of the computational subspace. Interestingly, the pulse amplitude necessary to produce this behaviour is only 50% greater than the readout amplitude suggesting that the mechanisms behind it depend sharply on the drive power.

In other measurements done on the same qubit as in Sec. 5.3.3, we were able to increase the Rabi constrast by applying a strong pump at frequencies away from the transitions we discussed above or the cavity frequency. Depending on the frequency, we tended to increase or decrease the population of the ground-state. This suggests that the interaction between the pump and the complicated level structure of Fluxonium devices is important in explaining these measurements fully.

5.3.5 *Heralding and Feedback*

At the basis of qubit reset by heralding, there is the assumption that the qubit readout resitutes the state of the qubit with high fidelity. We can express this as condition on the probability

$$P(|g\rangle\,|\text{“g”}) = 1\ . \tag{5.25}$$

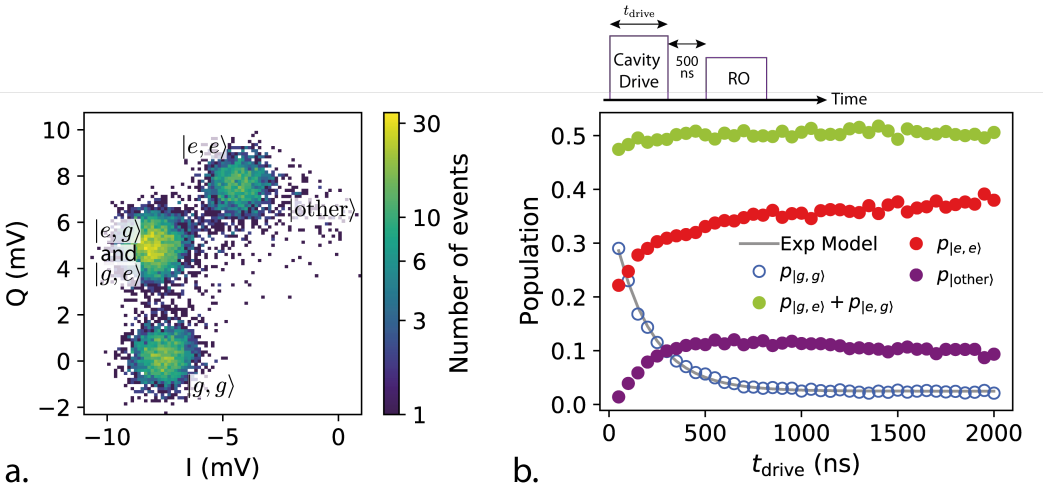

Figure 5.17: a.Histograms of 10000 acquisitions of a 1300 ns readout pulse on the qubit described in Chapter 6. We have identified the different parts of the distribution with their corresponding qubit state. The state $|other\rangle$ corresponds to the points in the histogram which do not belong to states in the computational subspace. b. Populations as determined by a gaussian mixture model in each of the qubit states as a function of the cavity pulse drive time in the sequence above the graph. The ratio of the amplitude of the drive to the amplitude of the readout is 1.6, and the readout duration 1300 ns, identical to a. An exponential model is fit to the decay of $p_{g,g}$ with time a constant of 190 ns.

For a measurement outcome "g" which is up to the experimentalist to define (obtaining readout quadratures within some distance of the centre of the pointer state distribution at the bottom of Fig. 5.16 for example), the likelihood of being in state $|g\rangle$ should be close to 1. Here we are focusing on the state $|g\rangle$ but this idea can be generalised to any target state. Calculating $P(|g\rangle\,|\text{"g"})$ is non-trivial and is presented in detail in Chapter 7 for the case of the readout of a 3D Transmon. Regardless of the exact value of $P(|g\rangle\,|\text{"g"})$, it can be useful to start measurement sequences on low frequency Fluxoniums with a single readout pulse to project the qubit into the energy eigenbasis.

Reseting the qubit by feedback also requires a high fidelity $P(|g\rangle\,|\text{"g"})$. We attempted it on the 2 Fluxonium device, whose readout histogram is shown in Fig. 5.17. The main constraint here is the electronics hardware needed to perform the feedback. Indeed, once the readout has been performed, it is necessary to generate the correct control pulse based on the measurement outcome, before the state of the qubit changes. This can be done using custom FPGA boards for example or with commercial devices, like the control systems provided by the companies Quantum Machines or Zürich Instruments (ZI). We tried to perform feedback using a combination of the ZI HDAWG for pulse generation and ZI UHFQA for acquisition and feedback, but this was unsuccessful because of unresolved communication issues between the two instruments.

5.4 CONCLUSION

Limiting the environmental noise affecting superconducting qubits and Fluxoniums in particular is critical to obtaining long coherence times. At a theoretical level we saw how the temperature of the environment can affect T_1 and T_ϕ by increasing the population of the readout cavity for example. Temperature also poses a problem in terms of the thermal population of the qubit, especially for low frequency devices like Fluxonium. Stray, high energy radiation (radioactivity, infrared...) can create quasi-particles or take superconducting devices out of equilibrium with their environment. These effects can be prevented by various degrees of shielding and filtering, which we tried to put in place in the Cryoconcept fridge. The ineffectiveness of these measures on coherences suggest that we are limited by something still unidentified. Only by changing to the Bluefors dilution refrigerator were we able to retrieve close to state-of-the-art lifetimes and put forwards the strong dependence of Fluxonium qubits on temperature. In the last part of the chapter we reviewed the different methods which can be used to reset Fluxonium devices to a known pure state. We explored optical-pumping type cooling which resets the ground-state population to above 90% in only a fraction of the T_1 time. By exploring the reset through measurement, heralding, feedback and strong cavity drives, we demonstrated that reading out the state of Fluxonium qubits is non-trivial. This motivates the experiment of the following chapter, where we describe quantitatively how the transition rates between the states of Fluxonium qubits are affected by a cavity drive.

6

TRANSITION RATES IN FLUXONIUM

6.1 INTRODUCTION

In some of the last results of the previous chapter we saw that the readout drive could have a significant effect on the state of Fluxonium qubits. This was evident in the readout of our own two qubit system but it has also been observed elsewhere. In the Yale group even a small number of cavity photons (~ 2) were shown to increase the qubit decay rate [37] and variations in the qubit excitation and deexcitation rates $\Gamma_\uparrow$ and $\Gamma_\downarrow$ were observed in a GraAl Fluxonium in the Karlsruhe group [34]. This effect was harnessed as a resource in the Maryland group to purify the state of Fluxonium qubits before measurement [38, 33]. There have also been observations that high photon numbers in the readout cavity impact the qubit state in Transmons [191, 92, 192]. These effects are especially problematic as they reduce the QNDness of the readout, such that we are no longer sure that the qubit is indeed in the state corresponding to the measurement outcome. Some theoretical works have tried to explain these effects by considering non-linearities beyond the standard dispersive limit [193, 194, 195], but there is no consensus yet on an explanation for non-QND phenomena in the fluxonium qubit.

This chapter presents one of the main experimental works of this thesis, about the effect of a cavity drive on the transition rates between levels in a capacitively coupled two Fluxonium system. The objective is to obtain a quantitative analysis of the depletion of the ground state population shown qualitatively in Fig. 5.16. To do this, our goal is to measure the transition rates $\Gamma_{\mu\nu}$ between the states $|\nu\rangle$ and $|\mu\rangle$ of the coupled two Fluxonium system, both as a function of the photon number $\bar{n}$ and of the external flux bias Φ_{ext}.

We start by presenting the experimental setup and some first calibrations of the qubit parameters. We then expose some of the problems we risk facing when trying to measure $\Gamma_{\mu\nu}(\bar{n}, \Phi_{\text{ext}})$, notably the correct definition of $\bar{n}$ and the dependence of the dispersive shifts of the qubit both on $\bar{n}$ and Φ_{ext}. Addressing these issues will bring us to develop a novel pointer-state identification scheme in the IQ-plane and a rigorous self-consistent definition of $\bar{n}$. We are then able to show that the population of each qubit state depends on the amplitude of the field in the readout cavity to which it is coupled. To determine the mechanisms involved at a microscopic level, we then use the information contained in a 104 µs long measurement record to extract the transition rates between qubit states while the cavity is occupied. These transition rates, varying between 1 and 200 kHz, vary strongly both in flux and in photon number. Finally we show how a numerical simulation of the measurement record could reproduce some of the features we observe.

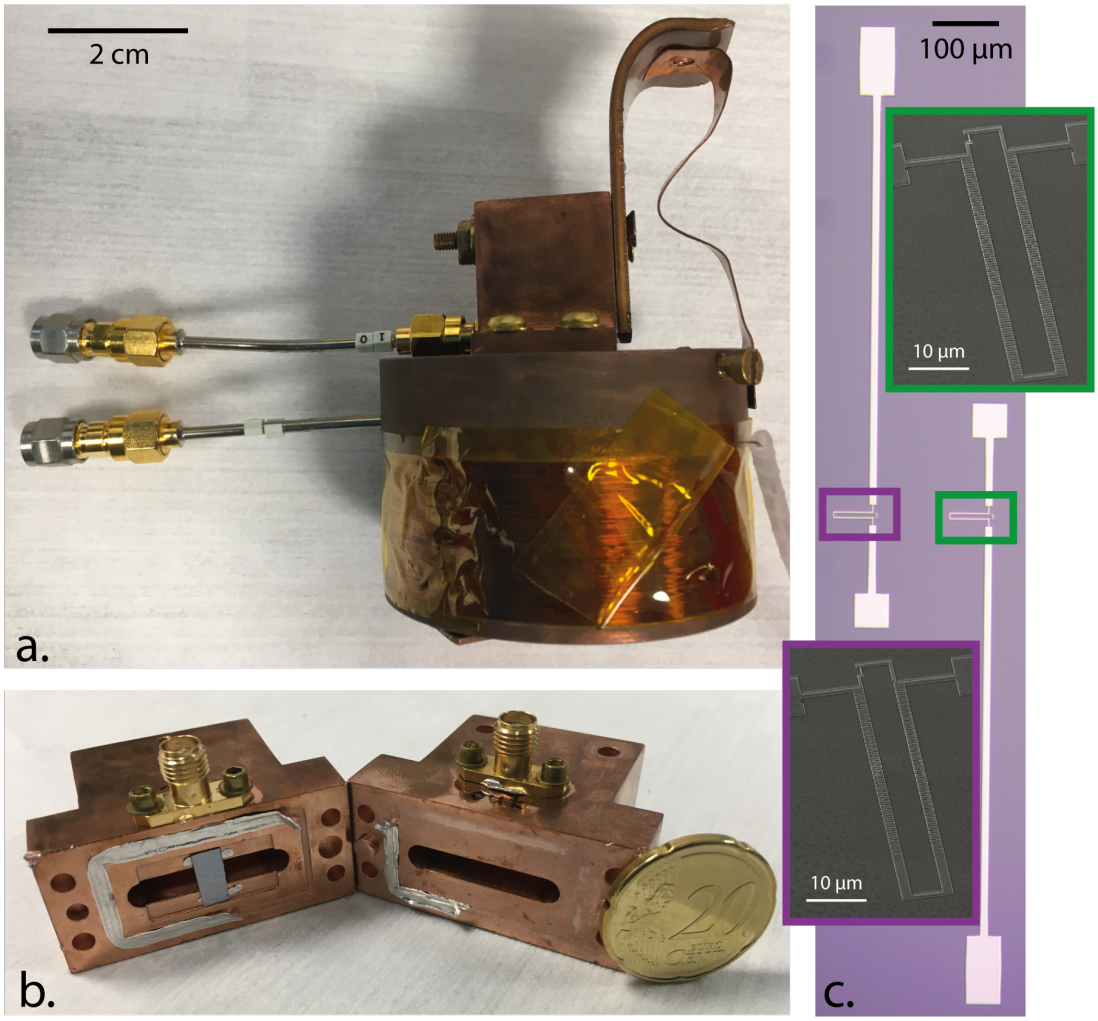

Figure 6.1: Experimental setup and Fluxonium device. a. Side view of the cavity placed within the copper coil wound in house. b. Open copper cavity showing the silicon chip on which the Fluxoniums are patterned on the left hand side. The indium seal of the cavity is still visible around the opening. c. Optical image of the two qubit chip. The qubit-qubit and qubit-cavity couplings are mediated by the Fluxonium antennas. The inset SEM images show the junction chain. Notice how the surface enclosed by chain in the purple frame is the same as the one in the green frame but with less junctions.

6.2 CHARACTERISING THE TWO-FLUXONIUM SYSTEM

6.2.1 *Experimental setup*

The device under test in this chapter is shown in Fig. 6.1. The silicon chip carrying the two patterned Fluxoniums (panel c) is placed inside a copper cavity with two ports (panel b.), one of which (the output port) is much more strongly coupled to the cavity than the other (the input port). The Fluxonium loops, visible in the SEM images of Fig. 6.1, are designed to have the same surface area so that their flux periodicity is the same, despite the number of junctions in each Fluxonium being different. Details about

the fabrication of the devices can be found in [79].

In the experiment, the device is placed inside a cryoperm at the base plate of the Bluefors dilution refrigerator. The DC cabling is thermalised as described in Chapter 5. For the RF pulses, a schematic of the measurement setup is given in Fig. 6.2. Qubit pulses are either generated directly by a Zurich Instruments HDAWG ($\omega < 2\pi \times 600\,\mathrm{MHz}$) or first upconverted by using a Polyphase Microwave single sideband mixer (SSB) and a local oscillator (LO) signal generated by a Rhode & Schwarz SGS100A RF source ($\omega \geq 2\pi \times 600\,\mathrm{MHz}$). Signals at the cavity frequency are generated similarily using an Anapico APSIN12G RF source as the LO. The cavity output signal is first amplified by a Josephson Traveling Wave Parametric Amplifier (TWPA) [178] provided by Lincoln Labs followed by a High Electron Mobility Transistor (HEMT) amplifier from Caltech [196] and finally by a room temperature amplifier. The signal is then downconverted using another Polyphase Microwave single sideband mixer (SSB) with the LO and RF ports reversed to act as an image reject mixer. Finally the now low frequency ($\sim$ MHz) signal is filtered and then amplified one last time by a Femto HVA-500M-20-B amplifier, before being sent to an AlazarTech 9351 acquisition card. Numerical demodulation yields the I and Q quadratures of the readout signal. A full schematic of the room temperature and cryogenic cabling is shown in Fig. 6.2.

6.2.2 *Basic device characterisation*

We start by determining the resonator linewidth, by measuring a cavity ring down close to the resonant frequency. Determining the bare cavity frequency ω_R will come later. In Fig. 6.3a. we show a measurement trace of the Alazar acquisition board as a function of the time after which the card is armed for acquisition when a square pulse is transmitted through the cavity. The oscillations correspond to the 50 MHz modulation of the AWG IF. The acquired voltage amplitude decays at a rate $\kappa/2$ where κ is the cavity linewidth. From this we extract $\kappa = 2\pi \times 10.2\,\mathrm{MHz}$.

The next step is to determine the parameters of both Fluxonium qubits on the silicon chip. To do this we measure the qubit spectrum using a two tone spectroscopy

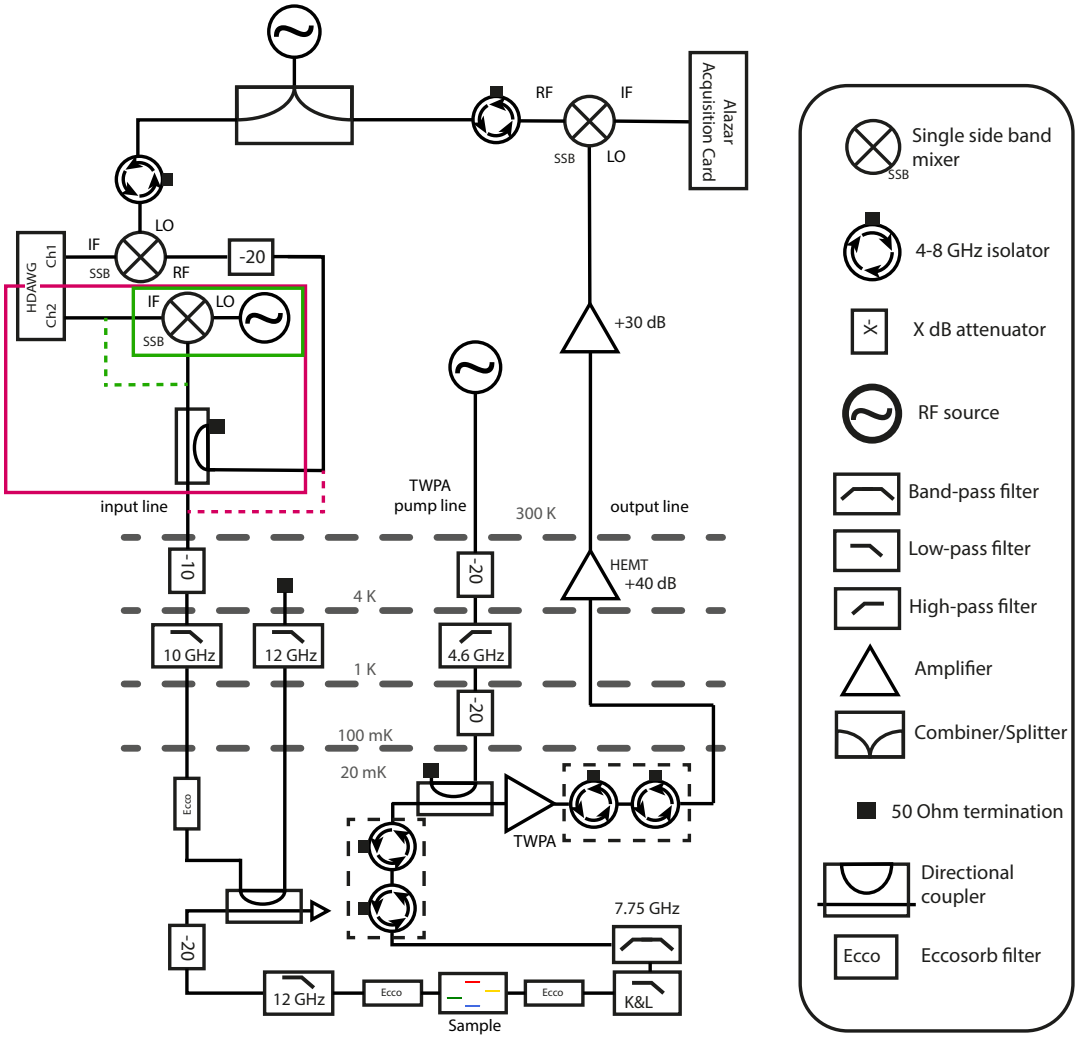

Figure 6.2: Schematic of the measurement setup. In green we mark the part of the measurement setup necessary if $\omega \geq 2\pi \times 600\,\mathrm{MHz}$. If $\omega < 2\pi \times 600\,\mathrm{MHz}$ we drive the qubit directly using the ouput of the AWG (dashed green). We use the components in the pink box exclusively for the initial qubit spectroscopy and device characterisation. None of these components are necessary for quantum jump trajectories shown later in the chapter, for which an equivalent bypass could have been used (dashed pink).

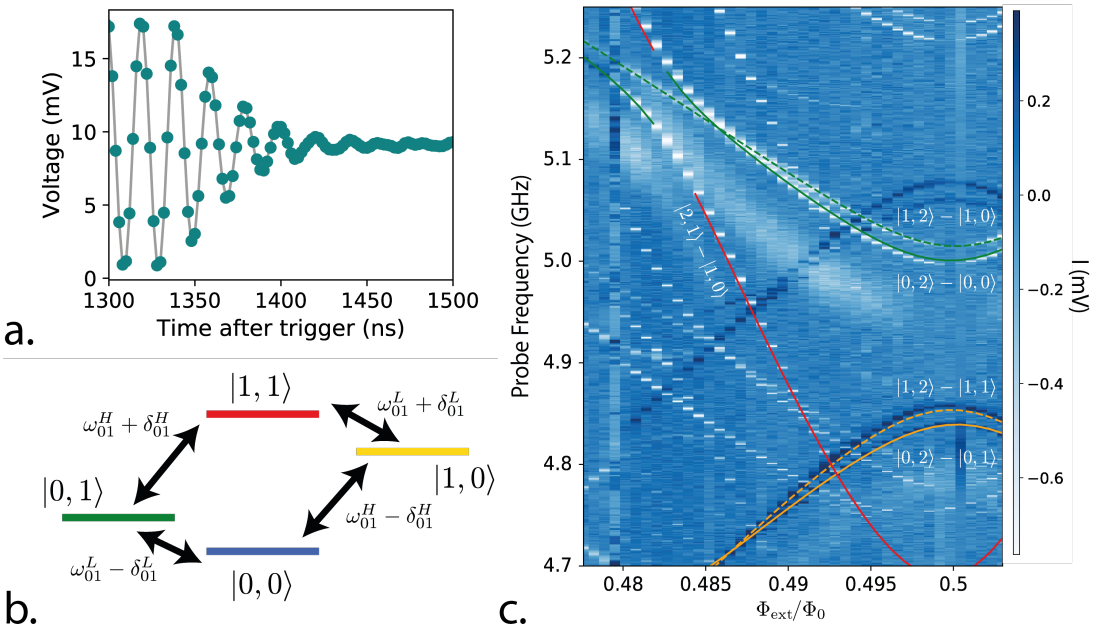

Figure 6.3: Basic characterisation of the device. a. Cavity ring-down mesurement. At time 0 ns a square pulse is sent to the cavity and its transmission recorded by the Alazar acquisition card. The transmitted amplitude falls to 0 at a rate $\kappa/2$ once the readout drive is terminated. b. Level structure of the computational subspace and the four qubit states under study in the experiment. c. Spectroscopy of the qubit as a function of the external flux of qubit L. Colored lines show the predicted transition frequencies obtained by the diagonalisation of the Hamiltonian of (6.1). The non-labeled resonances correspond either to unidentified qubit transitions or to spurious sidebands of the measurement setup. The $|2,1\rangle - |1,0\rangle$ transition's minimum is slightly shifted with respect to the other transitions because of a slight flux imbalance between the two Fluxonium loops of around $\sim \frac{3}{10000}\Phi_0$.

(as defined in Chapter 3) shown in Fig. 6.3c. We model the two coupled qubits and the cavity by the following Hamiltonian

$$\begin{aligned}\hat{H} = &\underbrace{\hbar\omega_R \hat{a}^\dagger \hat{a}}_{\text{cavity}} \\ &\underbrace{+ 4E_C\hat{n}_L^2 + \frac{1}{2}E_L^{(L)}\hat{\Phi}_L^2 - E_J^{(L)}\cos\left(\hat{\Phi}_L - 2\pi\frac{\Phi_{\text{ext}}^{(L)}}{\Phi_0}\right)}_{\text{lower energy qubit}} \\ &\underbrace{+ 4E_C\hat{n}_H^2 + \frac{1}{2}E_L^{(H)}\hat{\Phi}_H^2 - E_J^{(H)}\cos\left(\hat{\Phi}_H - 2\pi\frac{\Phi_{\text{ext}}^{(H)}}{\Phi_0}\right)}_{\text{higher energy qubit}} \\ &\underbrace{-\hbar g_c\hat{n}_L(\hat{a}^\dagger + \hat{a}) - \hbar g_c\hat{n}_H(\hat{a}^\dagger + \hat{a})}_{\text{cavity-qubit coupling}} \underbrace{-\hbar g_{\text{HL}}\hat{n}_L\hat{n}_H}_{\text{qubit-qubit coupling}} .\end{aligned} \tag{6.1}$$

Here $\hat{a}^\dagger$ is the cavity annihilation operator and ω_R the cavity frequency. The operators $\hat{\Phi}_X$ and $\hat{n}_X$ are respectively the phase twist across the inductance and the charge on the capacitor of qubits L (low) and H (high) labeled in reference to the frequency of

their $|0\rangle - |1\rangle$ transition at $\Phi_{\text{ext}}^{(X)} = 0.5\Phi_0$. Finally, E_C, $E_L^{(X)}$ and $E_J^{(X)}$ are the charging energy, inductive energy and Josephson energy of each qubit, and g_c and g_{HL} are the qubit-cavity and qubit-qubit couplings respectively. Because the antenna geometry of both qubits is identical, we consider E_C and g_c to be the same for both qubits. We discuss different diagonalisation methods for $\hat{H}$ in Chapter 3 and Appendix B.

To identify the transitions of Fig. 6.3c. we do not need to include ω_R and g_c as fit parameters, as they only change the frequencies marginally. By fitting the calculated transition frequencies of the diagonalised Hamiltonian to the transitions visible in 6.3c. we obtain a charging energy $E_C = 2\pi\hbar \times 1.00\,\text{GHz}$ for both qubits, Josephson energies $E_J^{(H)}/h = 5.41\,\text{GHz}$ and $E_J^{(L)}/h = 5.95\,\text{GHz}$, inductive energies $E_L^{(H)}/h = 1.09\,\text{GHz}$ and $E_L^{(L)}/h = 0.86\,\text{GHz}$, and the magnitude of the capacitive coupling between the qubits $g_{HL}/h = 252\,\text{MHz}$. From the values of $E_L^{(H,L)}$ we can deduce that the qubit framed in purple in Fig. 6.1 is qubit H (smaller number of junctions so smaller inductance), while the one in green is qubit L. Close to the half flux quantum (we associate values of Φ_{ext} with the flux threading the loop of qubit L), the energy levels of the coupled fluxonium system ressemble a diamond structure shown in Fig. 6.3b. where the $|0\rangle - |1\rangle$ transition frequency of each qubit ($\omega_{01}^L = 2\pi \times 157.1\,\text{MHz}$ and $\omega_{01}^H = 2\pi \times 327.6\,\text{MHz}$) depends only weakly on the state of the second. The splitting between the two transition frequencies δ_{01}^X is of the order of $2\pi \times 100\,\text{kHz}$. In Fig. 6.3b. and c. we note $|i,j\rangle$ the eigenstate[1] with i excitations in qubit H and j excitations in qubit L.

6.3 EXPOSING THE EXPERIMENTAL STRATEGY

Now we have determined some of the basic parameters of the Hamiltonian required to describe the system we are studying, we would like to turn to the effect of the readout on this system. To motivate this we show the histograms of the recorded quadratures of a square readout pulse as a function of the drive amplitude a_{RT} in Fig. 6.4. As we saw previously, as the amplitude of the cavity pulse increases, the populations of the qubit states more and more affected. This is particularly noticable in the lowest gaussian visible in the histograms, which only begins to populate as a_{RT} increases. Furthermore, we see that compared to Fig. 5.16, there is some structure to the distribution at the top right of the histograms, suggesting that there are some transitions between the identifiable four state computational subspace and higher excited states. Removing the contribution of these levels to properly compute the transition rates within the computational subspace will be critical. Moreover, our stated objective was to calculate the transition rates as a function of the average photon number in the cavity $\bar{n}$ and the external flux Φ_{ext}. To do this we will have to related the amplitude a_{RT} to the number of photons $\bar{n}$ in the cavity. This is non-trivial as the number of photons inside the cavity depends on its frequency with respect to the readout drive, which in turn

1 Note that $|i,j\rangle$ is not a separable state in the basis of isolated qubits because the two qubits are coupled. Yet, because the coupling is weak, $|i,j\rangle$ is very close to $|i\rangle \otimes |j\rangle$

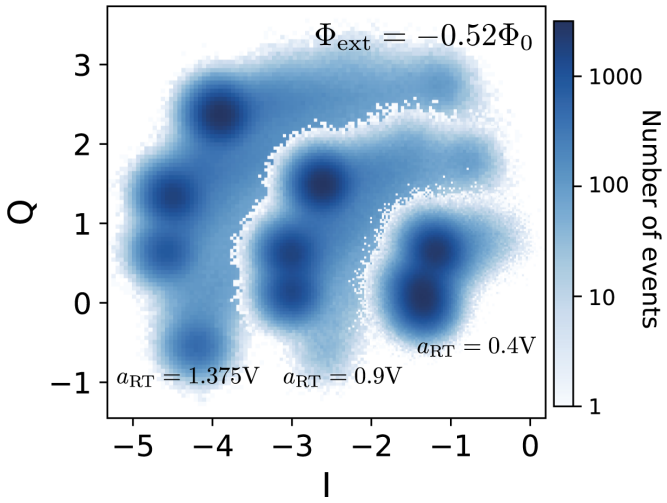

Figure 6.4: Histograms of the I and Q measurement results as a function of the amplitude of the cavity drive a_{RT} at $\Phi_{\mathrm{ext}} = 0.52\Phi_0$. Here the signal coming from the cavity was integrated for 2600 ns, and the axes are calibrated to the number of photons in the cavity.

depends on the state of the qubit. We would be able to simulate the cavity frequency, for each qubit state if we had access to all the parameters of the full Hamiltonian in (6.1). To determine g_c and ω_R we need to know the dispersive shift imposed by each qubit state on the cavity. This is encoded in the position of each pointer-state in the IQ-plane visible in Fig. 6.4 for example. Because the positions of the distributions in the IQ-plane will change with different values of Φ_{ext} (because the dispersive shifts change) we developped a method for detecting an arbitrary number pointer-states in the IQ-plane readout histograms. With the combination of these techniques we will be able to associate a photon number $\bar{n}$ and a qubit state $|i, j\rangle$ with each readout trace of amplitude a_{RT} at flux Φ_{ext}.

Once this technical part has been completed successfully, we can turn to the measurement of $\Gamma_{\mu\nu}(\bar{n}, \Phi_{\mathrm{ext}})$. To do this, we track the number of jumps between qubit states during the cavity drive. The transmitted field is demodulated in steps, each step being associated with a particular qubit state which is estimated using the information contained in the entire measurement record (past and future). This is based on Baysian estimation and the past quantum state formalism [42]. Counting the jumps between states within a set time yields $\Gamma_{\mu\nu}(\bar{n}, \Phi_{\mathrm{ext}})$ directly.

We start by determining g_c and ω_R.

6.4 DETERMINING THE PARAMETERS g_c AND ω_R

6.4.1 *Photon-Number Dependence of Qubit-Cavity Steady-State*

6.4.1.1 *Deriving a self-consistent relation for $\bar{n}$*

We start by clearly defining what is meant by the average photon number $\bar{n}$. As mentioned previously, this task is delicate when the cavity frequency not only depends on the qubit state (cross-Kerr) but also on its own occupation (self-Kerr) to many orders. We define the frequencies $\omega_R(|n\rangle, |i,j\rangle, \Phi_{\text{ext}})$ as the frequency of the cavity when the coupled qubits' state is $|i,j\rangle$, the flux is set to Φ_{ext} and $n \in \mathbb{N}$ is the number of excitations (photons) inside the cavity. In this case, the Hamiltonian of the cavity, having adiabatically eliminated the qubit degrees of freedom is

$$\hat{H}_{\text{cav}}(|i,j\rangle, \Phi_{\text{ext}}) = \hbar \sum_{k} \sum_{l=0}^{k} \omega_R(|l\rangle, |i,j\rangle, \Phi_{\text{ext}}) |k\rangle\langle k| \ . \tag{6.2}$$

This means that the energy difference between two successive cavity Fock states is

$$E_{k+1} - E_k = \hbar\omega_R(|k\rangle, |i,j\rangle, \Phi_{\text{ext}}) \ . \tag{6.3}$$

When a classical field drives the cavity, the steady field inside is a coherent state $\left|\sqrt{\bar{n}}\right\rangle$ with an average of $\bar{n}$ photons. Taking the definition of 6.3 to the continuous limit

$$\omega_R(\bar{n}, |i,j\rangle, \Phi_{\text{ext}}) = \frac{1}{\hbar}\frac{\partial}{\partial \bar{n}} \left\langle \sqrt{\bar{n}} \right| \hat{H}_{\text{cav}}(|i,j\rangle, \Phi_{\text{ext}}) \left| \sqrt{\bar{n}} \right\rangle \ . \tag{6.4}$$

Equivalently, we can consider the total system Hamiltonian without the adiabatic elimination

$$\omega_R(\bar{n}, |i,j\rangle, \Phi_{\text{ext}}) = \frac{1}{\hbar}\frac{\partial}{\partial \bar{n}} \left\langle \sqrt{\bar{n}}, i, j \right| \hat{H}(\Phi_{\text{ext}}) \left| \sqrt{\bar{n}}, i, j \right\rangle \ . \tag{6.5}$$

If $|k,i,j\rangle$ is an eigenstate of $\hat{H}$ indexed by the product state $|k\rangle \otimes |i,j\rangle$ with which it has the greatest overlap (k is the cavity excitation number and $|k,i,j\rangle \approx |k\rangle \otimes |i,j\rangle$ well below n_{crit} the critical photon number of the dispersive regime [197, 91]), then

$$\left|\sqrt{\bar{n}}, i, j\right\rangle = e^{-|\bar{n}|/2} \sum_{k=0}^{\infty} \frac{\bar{n}^{k/2}}{\sqrt{k!}} |k,i,j\rangle \ . \tag{6.6}$$

These definitions equip us for the following calculation where to simplify notation we have omitted Φ_{ext} and defined $E_{k,|i,j\rangle} = \langle k| \otimes \langle i,j| \hat{H} |k\rangle \otimes |i,j\rangle$

$$\begin{aligned}
\sum_{k=0}^{\infty} e^{-\bar{n}} \frac{\bar{n}^k}{k!} \omega_R(|k\rangle, |i,j\rangle) &= \frac{1}{\hbar} \sum_{k=0}^{\infty} e^{-\bar{n}} \frac{\bar{n}^k}{k!} (E_{k+1,|i,j\rangle} - E_{k,|i,j\rangle}) && (6.7)\\
&= \frac{1}{\hbar} \left[\sum_{k=1}^{\infty} e^{-\bar{n}} \frac{\bar{n}^{k-1}}{(k-1)!} E_{k,|i,j\rangle} - \sum_{k=0}^{\infty} e^{-\bar{n}} \frac{\bar{n}^k}{k!} E_{k,|i,j\rangle} \right] && (6.8)\\
&= \frac{1}{\hbar} \frac{\partial}{\partial \bar{n}} \sum_{k=0}^{\infty} e^{-\bar{n}} \frac{\bar{n}^k}{k!} E_{k,|i,j\rangle} && (6.9)\\
&\approx \frac{1}{\hbar} \frac{\partial}{\partial \bar{n}} \sum_{k=0}^{\infty} e^{-\bar{n}} \frac{\bar{n}^k}{k!} \langle k,i,j| \hat{H} |k,i,j\rangle && (6.10)\\
&= \frac{1}{\hbar} \frac{\partial}{\partial \bar{n}} \sum_{k,l=0}^{\infty} e^{-\frac{\bar{n}}{2}} \frac{\bar{n}^{\frac{k}{2}}}{\sqrt{k!}} \langle k,i,j| \hat{H} |l,i,j\rangle e^{-\frac{\bar{n}}{2}} \frac{\bar{n}^{\frac{l}{2}}}{\sqrt{l!}} && (6.11)\\
&= \frac{1}{\hbar} \frac{\partial}{\partial \bar{n}} \left\langle \sqrt{\bar{n}}, i, j \right| \hat{H} \left| \sqrt{\bar{n}}, i, j \right\rangle . && (6.12)
\end{aligned}$$

From (6.10) to (6.11) we used the orthogonality of the energy eigenstates. Defining $P_{\bar{n}}(k) = e^{-\bar{n}} \frac{\bar{n}^k}{k!}$ and using (6.5) we obtain the identity

$$\sum_{k=0}^{\infty} P_{\bar{n}}(k) \times \omega_R(|k\rangle, |i,j\rangle, \Phi_{\text{ext}}) = \omega_R(\bar{n}, |i,j\rangle, \Phi_{\text{ext}}) . \tag{6.13}$$

This is useful because it relates a quantity which can be simulated

$$\omega_R(|k\rangle, |i,j\rangle, \Phi_{\text{ext}}) = \frac{\left(\langle k+1,i,j| \hat{H} |k+1,i,j\rangle - \langle k,i,j| \hat{H} |k,i,j\rangle \right)}{\hbar} , \tag{6.14}$$

to a quantity we measure experimentally $\omega_R(\bar{n}, |i,j\rangle, \Phi_{\text{ext}})$.

For the time being though, $\bar{n}$ remains ill defined for given driving conditions because it also depends on $\omega_R(\bar{n}, |i,j\rangle, \Phi_{\text{ext}})$ as the number of photons inside the cavity depends on the detuning between drive and cavity frequency. To remove this circularity we define $\bar{n}$ self-consistently as the fixed point of the equation [198]

$$\bar{n}_{|i,j\rangle,\Phi_{\text{ext}}}(a_{\text{RT}}) = \frac{|\mu a_{\text{RT}}|^2}{\frac{\kappa^2}{4} + (\omega_{\text{RO}} - \omega_R(\bar{n}, |i,j\rangle, \Phi_{\text{ext}}))^2} , \tag{6.15}$$

where κ is the cavity linewidth, a_{RT} is the amplitude of the cavity drive on the room temperature setup in V and μ is a proportionality coeficient calibrated by a populated Ramsey experiment (see next section), such that μa_{RT} is the amplitude of the coherent field entering the cavity at the dilution refrigerator base plate. This equation can be derived by considering the steady-state of the Langevin equation defining the field inside the cavity in the frame rotating at the cavity frequency

$$\dot{\hat{a}} = -i(\omega_{\text{RO}} - \omega_R(\bar{n}, |i,j\rangle, \Phi_{\text{ext}}))\hat{a} - \frac{\kappa}{2}\hat{a} + \sqrt{\kappa_{c1}}\hat{a}_{\text{in}} . \tag{6.16}$$

Here $\hat{a}_{\text{in}}$ is the input field operator at the frequency ω_{RO}, and κ_{c1} is the input port coupling. With this we can see the equivalence between the room temperature amplitudes and the microscopic description of the cavity coupled to the transmission line

$$\kappa_{c1} \left\langle \hat{a}_{\text{in}}^{\dagger} \hat{a}_{\text{in}} \right\rangle = |\mu a_{\text{RT}}|^2 \ . \tag{6.17}$$

Note that other than g_c and ω_R which come into the calculation of $\omega_R(\bar{n}, |i,j\rangle, \Phi_{\text{ext}})$, and μ which we are about to calibrate, there are no other free parameters in (6.15). This means that $\bar{n}$ is now a simulatable quantity.

6.4.1.2 *Calibrating μ*

We can find the value of μ in (6.15) by performing a populated Ramsey experiment to measure the AC-stark shift and measurement induced dephasing rate at $\Phi_{\text{ext}} = 0.5\Phi_0$ on qubit L. The pulse sequence in question is shown in Fig. 6.5a. Between the $\frac{\pi}{2}$ pulses necessary for a Ramsey sequence, we add a cavity displacement pulse at frequency ω_d whose objective is to populate the cavity with photons. We design the sequence with $t_{\text{ramsey}} \gg 1/\kappa$ so that we can neglect the transients during which the cavity is not in its steady-state. We add a readout pulse at the beginning of the sequence to be able post-select the experiments on the two qubits being initially in state $|0,0\rangle$. This ensures that our $X_{\frac{\pi}{2}}$ pulse only drives the transition between levels $|0,0\rangle$ and $|0,1\rangle$ and not the transition between $|1,0\rangle$ and $|1,1\rangle$, whose transition frequencies are separated only by $\sim 100\,\text{kHz}$. We can determine the decay rate Γ_d and oscillation frequency ω_{AC} of the Ramsey oscillations. They are related to μ, a_{RT}, the detuning of the drive $\Delta = \bar{\omega}_R - \omega_d$ with respect to the average cavity frequency $\bar{\omega}_R = \frac{\omega_R(|0,0\rangle)+\omega_R(|0,1\rangle)}{2}$ and the dispersive shift χ between the two qubit states. It is predicted that [199, 58]

$$\Gamma_d = \chi \,\text{Im}\left\{\alpha^*_{|0,0\rangle}\alpha_{|0,1\rangle}\right\} \ , \ \omega_{\text{AC}} = \chi \,\text{Re}\left\{\alpha^*_{|0,0\rangle}\alpha_{|0,1\rangle}\right\} \ , \tag{6.18}$$

wehre

$$\alpha_{|0,0\rangle} = \frac{\mu a_{\text{RT}}}{i(\Delta - \frac{\chi}{2}) + \frac{\kappa}{2}} \text{ and } \alpha_{|0,1\rangle} = \frac{\mu a_{\text{RT}}}{i(\Delta + \frac{\chi}{2}) + \frac{\kappa}{2}} \tag{6.19}$$

are the steady amplitudes of the cavity for the two qubit states. Note that $\bar{\omega}_R$ is unknown and must be determined experimentally. For the amplitudes considered here, we make the approximation that $\bar{\omega}_R$ is fixed because the cavity occupation is low ($\bar{n} << 1$, n_{crit}). Similarly, while the dispersive shift χ generally depends on the cavity occupation n and by extension on the cavity drive amplitude

$$\chi(n) = \omega_R(n+1, |0,0\rangle) - \omega_R(n, |0,0\rangle) - [\omega_R(n+1, |0,1\rangle) - \omega_R(n, |0,1\rangle)] \ , \tag{6.20}$$

this is negligeable for the amplitudes in this case as they are far below the single photon occupancy of the cavity. Here, the dispersive shift $\chi = 2\pi \times 3.14\,\text{MHz}$ is determined experimentally by using the position of the pointer-states in the IQ-plane[2]

$$\chi = \frac{\kappa}{2}\left(\tan\left(\arg[\bar{Z}_{\text{out}}^{|0,0\rangle}]\right) - \tan\left(\arg[\bar{Z}_{\text{out}}^{|0,1\rangle}]\right)\right) \ . \tag{6.21}$$

The results of the populated Ramsey experiment are shown in Fig. 6.5b. By adjusting the model of (6.18) and (6.19) to reproduce the experimental results at low a_{RT} we obtain $\mu = 17.4\sqrt{\text{photons}}.\text{MHz}\,\text{V}^{-1}$ and $\bar{\omega}_R = 2\pi \times 7.5742\,\text{GHz}$.

2 See Chapter 2 for a definition of $\bar{Z}_{\text{out}}$.

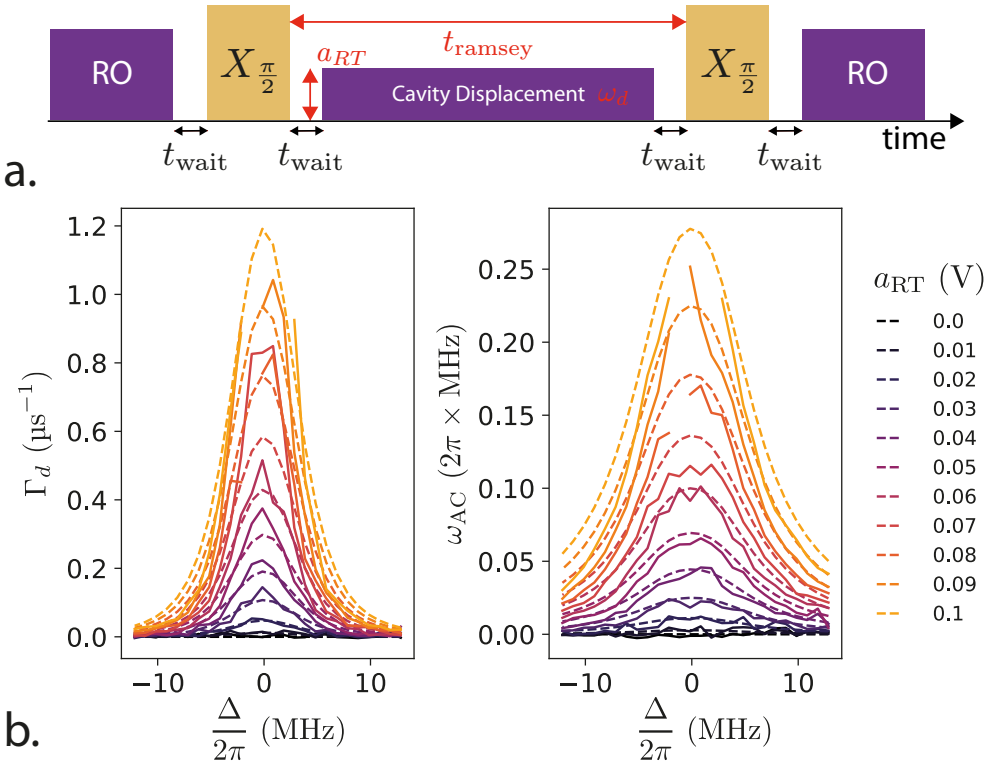

Figure 6.5: a. Measurement sequence of the populated Ramsey experiment. An initial readout pulse is used to herald the initial state $|0,0\rangle$. This is followed by a $\frac{\pi}{2}$ pulse on the $|0,0\rangle - |0,1\rangle$ transition after waiting $t_{\text{wait}} = 100\,\text{ns}$. The cavity is then displaced before a second $\frac{\pi}{2}$ pulse completes the Ramsey sequence. A final readout pulse allows the single-shot determination of the qubit state. a_{RT} the amplitude of the cavity drive, ω_d the frequency of the cavity diplacement pulse and t_{ramsey} are all varied in this experiment. b. Dephasing rate Γ_d and frequency stark-shift ω_{AC} of the $|0,0\rangle - |0,1\rangle$ transition as a function of $\Delta = \omega_R - \omega_d$. These quantities are obtained from the Ramsey oscillations (not shown) with t_{wait} varied. Dashed lines correspond to the model given by the equations (6.18) and (6.19) with the parameters $\mu = 17.4\sqrt{\text{photons}}.\text{MHz}\,\text{V}^{-1}$ and $\bar{\omega}_R = 2\pi \times 7.5742\,\text{GHz}$ adjusted so that the model reproduces the experiment results as faithfully as possible for low a_{RT}.

6.4.2 *Pointer state location in complex plane*

To determine the correct values for ω_R and g_c we need to be able to compare the experimental values of the cavity frequency $\omega_R(\bar{n}, |i,j\rangle, \Phi_{\text{ext}})$ with the numerically calculated $\sum_{k=0}^{\infty} P_{\bar{n}}(k) \times \omega_R(|k\rangle, |i,j\rangle, \Phi_{\text{ext}})$. We can obtain the experimental cavity frequencies by remembering that the position of the pointer states in the IQ plane is determined by the detuning of the qubit state dependent cavity frequency with respect to the cavity probe frequency. Specifically, the transmission of the cavity when the qubit state is stationary is

$$S_{21}(\omega_{\text{RO}}, \bar{n}, |i,j\rangle, \Phi_{\text{ext}}) = \frac{2\sqrt{\kappa_{c1}\kappa_{c2}}}{\kappa - 2i(\omega_{\text{RO}} - \omega_R(\bar{n}, |i,j\rangle, \Phi_{\text{ext}}))}\,, \tag{6.22}$$

where κ_{c2} is the cavity output coupling. Then

$$\frac{\kappa}{2}\tan\arg\left[S_{21}(\omega_{\mathrm{RO}},\bar{n},|i,j\rangle,\Phi_{\mathrm{ext}})\right]=\omega_{\mathrm{RO}}-\omega_R(\bar{n},|i,j\rangle,\Phi_{\mathrm{ext}})\ , \tag{6.23}$$

Determining the correct position of the pointer states in the IQ plane is thus essential to be able to deduce the qubit state dependent cavity frequency at each flux. To determine these positions with no prior knowledge as to how many states might be resolvable at each flux and how they may be positioned along the cavity response circle we developed an novel procedure which uses the information contained in rare events of IQ-plane histograms. This method comprises a series of steps:

1. Define the variance of the distribution of a pointer state in the IQ-plane;
2. Adjust the readout time so that the readout histograms have constant SNR for any set of parameters a_{RT} and Φ_{ext};
3. Rescale the I and Q coordinates into arbitrary units valid for any measurement amplitude;
4. Analyse the curvature of a contour around the base of the histogram and extract the segments where the curvature is greater than we expect (signature of a pointer state);
5. Fit these contour segments with circles whose centres all lie on the same 'resonance circle' passing through the origin of the complex-plane corresponding to the response of a cavity probed in transmission.

6.4.2.1 *On the variance of the pointer-state distributions in the complex plane*

A prerequisite for detecting the position of the pointer-states in the IQ-plane is knowing the variance of the distribution of their (I,Q) coordinates. For a given measurement amplification chain, the variance depends only on the integration time after demodulation. We calibrate the variance by averaging a single read-out of duration 1300 ns and amplitude $a_{\mathrm{RT}}=1\,\mathrm{V}$ at half flux ($\Phi_{\mathrm{ext}}=0.5\Phi_0$). We choose this flux point because we can easily distinguish the qubit pointer states (as is evident from the centre histogram of Fig. 6.7). For a different integration time τ in ns, the variance $\sigma^2_{|\mathrm{pointer}\rangle}(\tau)$ of a pointer-state in the IQ-plane is given by

$$\sigma^2_{|\mathrm{pointer}\rangle}(\tau)=\sigma^2_{|\mathrm{pointer}\rangle}(1300\,\mathrm{ns})\cdot\frac{1300\,\mathrm{ns}}{\tau} \tag{6.24}$$

as a function of the variance $\sigma_{|\mathrm{pointer}\rangle}(1300\,\mathrm{ns})$ of the calibration measurement. In the above we have made the assumption that the qubit does not change during the measurement, or equivalently that the integration time is much shorter than the characteristic time of a qubit transition Γ^{-1}: $\tau\ll\Gamma^{-1}$. The SNR, defined as the ratio of the distance between two pointer states in the IQ-plane to $\sigma^2_{|\mathrm{pointer}\rangle}(\tau)$, depends also on the readout field amplitude. The pointer-states separate with the amplitude of the transmitted readout pulse and their variance decreases with the measurement integration time so that

$$\mathrm{SNR}\propto a_{\mathrm{RT}}\sqrt{\tau}\ . \tag{6.25}$$

6.4.2.2 *Histogram resampling & rescaling*

To obtain a constant SNR for our analysis, we ajusted the length of the readout integration time depending on the amplitude a_{RT} of the input signal according to (6.25). Following this, we create histograms in the IQ-plane with a constant number of bins along each axis. This makes the dimensions of the histograms describing the readout results independent of the amplitude a_{RT}. We have thus defined a measurement parameter independent coordinate set and SNR on which we can run our state detection algorithm (see the difference between the histograms of Fig. 6.6 a and b).

6.4.2.3 *Extracting information from the contour*

The basis for the state detection is a histogram contour at a specific level. For density histograms, the height h at which the contour is drawn is given by

$$h = \frac{1}{\delta^2 N_{\mathrm{exp}}} \ , \tag{6.26}$$

where δ is the bin width in mV along each axis and N_{exp} is the number of repetitions of the experiment. An example of a typical histogram and the corresponding contour is shown in Fig. 6.6b. If there are multiple disconnected contours at this level, we discard all but the longest one. We can now consider the contour as a path in two dimensional space. To remove measurement noise, we apply a gaussian filter on each of the x and y coordinates of the contour. The width of the filter is determined empirically. At each point z_j along the contour we associate an angle $\beta_j = \arg[z_{j+1} - z_j]$ which defines the direction of change of the contour. For any closed contour which does not cross itself, $\sum_j \beta_j = 2\pi$, corresponding to a full rotation in the complex plane. We calculate and filter the gradient of these angles to obtain a measure of the local curvature $\mathcal{C}$ along the contour $\mathcal{C} = \frac{\mathrm{d}\beta_j}{\mathrm{d}j}$. The curvature of our example contour is shown in Fig. 6.6c. As a global rule, points where $\mathcal{C}$ is large and negative, corresponding to turning hard to the right when going around the contour clockwise, signal a possible pointer state. If $\mathcal{C}$ is positive, this signals zones between pointer states. We can classify points along the contour pertaining or not to pointer states by thresholding $\mathcal{C}$ above a certain level. This threshold is determined relative to the maximum curvature of the contour of each histogram specifically. The proportionality coeficient between threshold and peak curvature is fixed for all histograms and is determined empirically. Points whose curvature is below the threshold are arranged into groups. Each group signals a priori the position of a pointer state. These different groups for the example contour are shown in colour in Fig. 6.6c.

6.4.2.4 *Fitting circles on the blocks*

Because the contour goes around the exterior of the histogram and pointer states manifest themselves by a gaussian distribution of possible IQ values, the contour groups are expected to be close to arcs of circles surrounding the base of each pointer state distribution. We call c_ν the circle from which the arc pertaining to pointer state $|\nu\rangle$ is taken. In the next step we fit all the state circle arcs detected in the previous step simultaneously with circles c_ν, under the condition that their centres lie on another

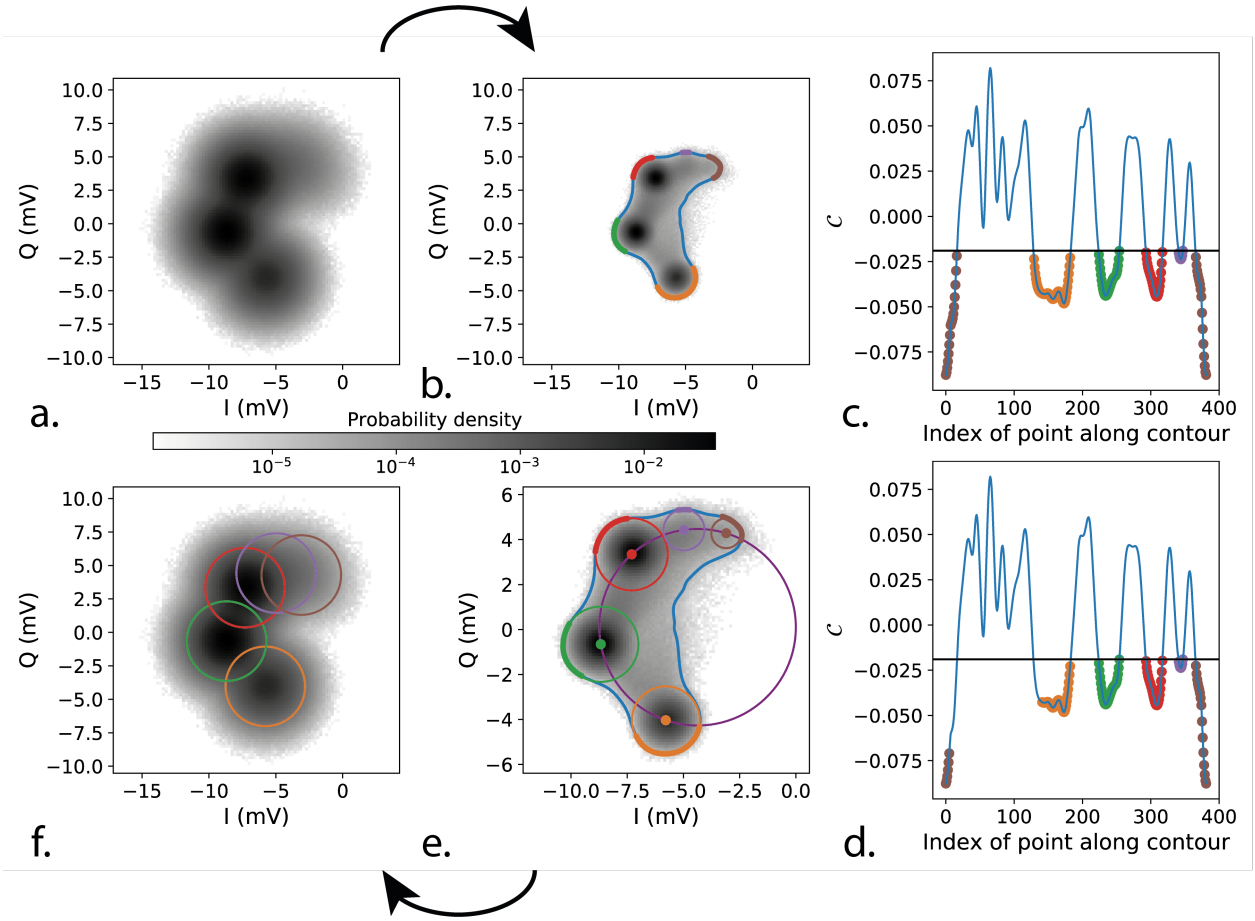

Figure 6.6: Zone detection algorithm on a typical histogram, measured here at $\Phi_{\text{ext}} = 0.5\Phi_0$. a. Histogram of the quadratures $\bar{I}_{\text{out}}$ and $\bar{Q}_{\text{out}}$ for $N_{\text{exp}} = 20\times10^6$ iterations of a 260 ns readout. b. Identical histogram when the integration time is increased by a factor 8 ($\tau_{\text{resampled}} = 2080$ ns) with the rare event contour drawn in in blue. Coloured points along the contour correspond to points where the curvature is below the threshold. c. Curvature $\mathcal{C}$ along the contour. The curvature threshhold under which points are to be considered a signature of a pointer state is shown by the horizontal black line. Point groups below the threshold are highlighted in colour and correspond to the points in colour in panel b. These point groups are reproduced in colour on the histogram to the left. d. Curvature $\mathcal{C}$ along the contour but with the coloured points reduced to those selected by the iterative filtering process. e. Identical histogram to b (axes have been rescaled for clarity) with the final fit of state circles c_ν to the detected state arcs. In purple we have drawn the cavity resonance circle. f. Histogram identical to a. but with circles of radius $2\sigma_{|\text{pointer}\rangle}(260\,\text{ns})$ centred at the positions where pointer states were detected.

'resonance circle' which passes through the origin of the IQ-plane. The resonance circle corresponds to the possible values of I and Q if the transmitted signal is scattered exactly by the scattering formula (6.22). This limits the number of fit parameters to: x_0 and y_0 the centre of the resonance circle (whose radius is $\sqrt{x_0^2 + y_0^2}$); γ_ν the angle around the resonance circle at which to position the centre of the state circle c_ν and r_ν the unphysical radius of c_ν. Knowledge of the angle γ_ν is the critical parameter which

makes the link between experiment and theory given by (6.23).

At this point, the algorithm needs a lot of fine tuning, principally because the fit parameter space is large. We use a variety of techniques to force convergence to a result which makes sense, by forcing the resonance circle to lie somewhere in the centre of our histogram coordinates and by ensuring that state circles are not too large or too small. In particular, once a first estimate for the γ_ν is obtained, we combine curve groups together whose centres are closer than $\sigma_{|\text{pointer}\rangle}(\tau)$. This is equivalent to saying that two gaussians are indiscernable if the distance between their means is smaller than their standard deviation. Furthermore, to determine more accurate groups of points, we discard those which lie inside the resonance circle. Indeed, inside the resonance circle we may see the result of state transitions during the readout integration time, so we cannot guarantee in that case that curvature outliers correspond truely to a pointer state. Finally, the multi-circle fit is iterated until groups are no longer modified. In Fig. 6.6e we show the result of the circle fit and in Fig. 6.6d the groups of points along the contour below the threshold after those points which do not fulfill the criteria above have been removed.

With the positions of the states along the resonance circle now well defined, we can define the theoretic gaussian distributions $P(z|\,|\nu\rangle)$ of width $\sigma_{|\text{pointer}\rangle}(\tau)$ corresponding to the probability of obtaining a measurement results $z = I + iQ$ with the knowledge that the qubit state was $|\nu\rangle$.

$$P(z|\,|\nu\rangle) = \frac{1}{\sqrt{2\pi}\sigma_{|\text{pointer}\rangle}(\tau)} \exp\left[\frac{-(z-z_\nu)^2}{2\sigma_{|\text{pointer}\rangle}(\tau)^2}\right] , \tag{6.27}$$

where $z_\nu = x_0 + iy_0 + \sqrt{x_0^2+y_0^2}e^{i\gamma_\nu}$. The contours at the 2σ level of these distributions are given in Fig. 6.6f.

6.4.3 *Matching experimental and simulated cavity frequencies*

We finally have all the tools at hand to determine the qubit-cavity coupling g_c and the bare cavity frequency ω_R. We start by letting the state location algorithm just described run on IQ-plane histograms over the flux range of interest at fixed $a_{RT} = 1.125\,\text{V}$. This gives us the positions of the qubit pointer-states in the IQ-plane which, up to some offset determined by the bare cavity frequency ω_R, yields the frequency of the cavity in each qubit state $\omega_R(\bar{n}, |i,j\rangle, \Phi_{\text{ext}})$ for the average photon occupation $\bar{n}$. We self consistently calculate $\sum_{k=0}^{\infty} P_{\bar{n}}(k) \times \omega_R(|k\rangle, |i,j\rangle, \Phi_{\text{ext}})$ and $\bar{n}$ numerically using the techniques described in Sec. 6.4.1 and Appendix B. By adjusting the value of ω_R and g_c in the numerical model we can match the experimentally determined cavity frequencies with the calculated ones. The overlap between the numerical model and the frequencies taken from the experiment can be seen in Fig. 6.7. In other results not featured here, the correspondence between theory and experiment is excellent for a wide range of fluxes and amplitudes. We conclude that $\omega_R = 2\pi \times 7.567\,\text{GHz}$ and $g_c = 2\pi/times111\,\text{MHz}$. A full table of all Hamiltonian parameters is given in Tab. 6.1. Note that with a Hamiltonian model with this level of precision we can identify which

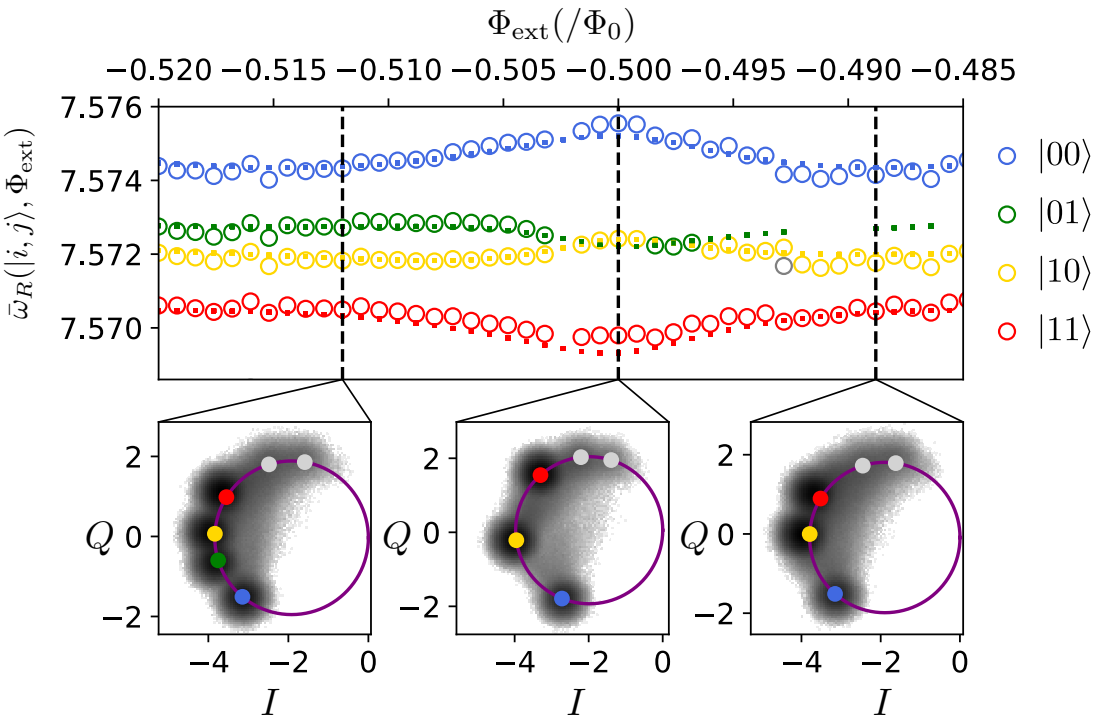

Figure 6.7: (Top) Qubit state dependent cavity frequency as a function of flux at $a_{RT} = 1.125\,\text{V}$. Empty circles correspond to experimentally measured cavity frequencies deduced from equation (6.23). Colored squares correspond to the numerically calculated values of the cavity frequency using equations (6.13) and (6.15). At certain points the numerics fails for state $|0,1\rangle$ explaining the absence of numerical values. (Bottom) Histograms of readout results in the IQ-plane (integration time 1560 ns) at the flux points marked by dashed lines. The axes have been calibrated to the number of photons in the cavity. The purple circles correspond to the cavity response. Colored dots correspond to the positions of the pointer-state circle centres along the resonance circle (see Sec. 6.4.2 for details). Grey points in all plots correspond to states detected by the state detection algorithm, but which we are unable to assign a qubit state to.

Parameter	Value
ω_R	$2\pi \times 7.567\,\text{GHz}$
κ	$2\pi \times 10.2\,\text{MHz}$
E_C	$2\pi\hbar \times 1.00\,\text{GHz}$
$E_J^{(H)}$	$2\pi\hbar \times 5.41\,\text{GHz}$
$E_L^{(H)}$	$2\pi\hbar \times 1.09\,\text{GHz}$
$E_J^{(L)}$	$2\pi\hbar \times 5.95\,\text{GHz}$
$E_L^{(L)}$	$2\pi\hbar \times 0.86\,\text{GHz}$
g_{HL}	$2\pi \times 252\,\text{MHz}$
g_{cav}	$2\pi \times 111\,\text{MHz}$

Table 6.1: Table of all system parameters.

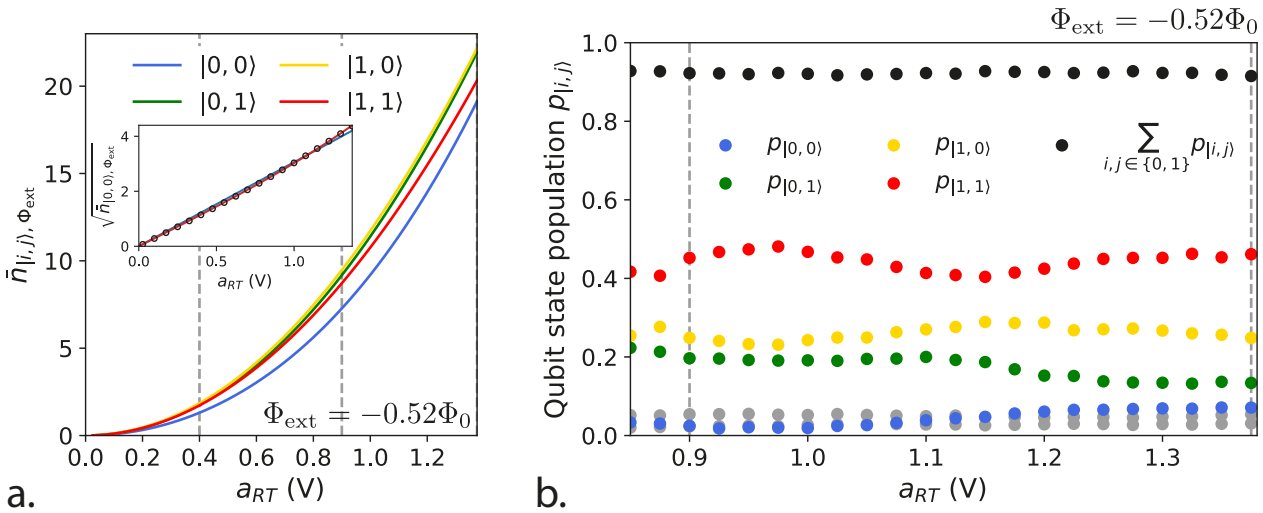

Figure 6.8: a. Qubit state dependent mean photon number inside the cavity at $\Phi_{\text{ext}} = -0.52\Phi_0$. Dashed lines correspond to the amplitudes at which the histograms of Fig. 6.4 are taken. (Inset) Square root of the average photon number when the qubit is in $|0,0\rangle$ as a function of a_{RT}. Gray circles correspond to the calculated $\bar{n}$ and the blue line to a quadratic model $\bar{n} = Ca_{\text{RT}}^2$ where C is an adjustable parameter. The red line corresponds to a model described by $\bar{n} = \frac{Ca_{\text{RT}}^2}{1+(B+Da_{\text{RT}}^2)^2}$ where C, B and D are adjustable parameters. This is the functional form of (6.15) when $\omega_R(\bar{n}, |i,j\rangle, \Phi_{\text{ext}})$ is a quadratic function of a_{RT}. b. Populations of qubit states as a function of cavity drive amplitude at $\Phi_{\text{ext}} = -0.52\Phi_0$. The colored dots correspond to pointer states we can correctly label in the IQ-plane and grey markers are pointer states which we identify but aren't able to assign a qubit state to. Notice that these unknown states are always populated, regardless of drive amplitude. The sum of the occupation probabilities of the coloured dots is given in black. Grey dashed lines correspond to the amplitudes of the histograms in Fig. 6.4.

pointer state corresponds to which qubit state with a single readout experiment and without the necessity for qubit spectroscopy or π-pulses as is traditionally the case.

6.5 QUBIT STATE POPULATIONS AS A FUNCTION OF PHOTON NUMBER

Now we have resolved the theoretical model and the definition of $\bar{n}$ as a function of a_{RT}, we can start to be more quantitative about the effect of the readout drive on the qubit. In Fig. 6.8a. we show the 'Rosetta stone' of the experiment, which translates the controlled fixed amplitude a_{RT} of the drive at $\omega_{RO} = 2\pi \times 7.572\,\text{GHz}$ into the average photon number of the coherent state inside the cavity for each two qubit state. Usually, if the cavity is linear, the number of photons inside the cavity should increase quadratically with the drive amplitude. Here there is a slight deviation from this quadratic behaviour as the non-linearity of the cavity induced by the qubits becomes non-negligeable at higher photon numbers. The dependence of the photon number on the amplitude is accurately captured by a linear dependence of the cavity frequency on photon number, which progressively detunes the cavity from the drive frequency (see the inset of Fig. 6.8a.).

In Fig. 6.8b. we show how the population $p_{|i,j\rangle}$ of state $|i,j\rangle$ evolves with the cavity drive amplitude a_{RT}. The population of each state $|i,j\rangle$ is determined as the fraction of points in each experiment whose (I,Q) coordinate z is such that the probability $P(z|\,|i,j\rangle)$ is larger than any other probability $P(z|\,|k,l\rangle)$, where $(k,l) \neq (i,j)$. For N_{exp} readout traces

$$p_{|i,j\rangle} = \frac{1}{N_{\mathrm{exp}}} \sum_{r=1}^{N_{\mathrm{exp}}} \delta_{|i,j\rangle,\mathrm{argmax}_{|k,l\rangle}\, P(z_r||k,l\rangle)} \ , \tag{6.28}$$

where $\delta_{|i,j\rangle,|k,l\rangle}$ is unity only if $|i,j\rangle$ is the same state as $|k,l\rangle$ and z_r is the coordinate of the readout r in the IQ-plane. Surprisingly, the states with higher energy are consistently more heavily populated that those with lower energy, suggesting that the additional cavity drive brings the qubit out of thermal equilibrium with its environment. Moreover, the dependence of the populations on the drive amplitude is not monotonous even at such low photon number, something that was already observed in [34]. To understand the dynamics of the populations, we turn to the study of the transition rates between each state.

6.6 EXTRACTING THE TRANSITION RATES

6.6.1 *Measurement sequence*

The measurement sequence for extracting the transition rates (Fig. 6.9a.) consists of a single cavity pulse whose transmitted signal is demodulated in successive time bins yielding a trajectory of quantum jumps. During the first part of the pulse, for a time T_{wait}, the transmitted signal is discarded (the reason for which will become clear later) after which it is numerically demodulated during a time T_{traj} and integrated in bins of length t_{bin}. This provides a measurement trace $\{z_k|k \in \{1,2,\ldots,N\}\}$ of positions in the IQ-plane corresponding to times t_k (Fig. 6.9b.) for each cavity pulse. To gather information about different photon numbers and different fluxes, the measurement is repeated $N_{\mathrm{exp}} = 50000$ times for each value of a_{RT} and Φ_{ext}. Initially, we associate to each point of the measurement trace z_k a qubit state $|i,j\rangle$ which maximises the probability $P(z_k|\,|i,j\rangle)$

$$|i,j\rangle = \underset{|k,l\rangle}{\mathrm{argmax}}\, P(z_k|\,|k,l\rangle) \ . \tag{6.29}$$

An example of a quantum jump trajectory given by this assignment is shown in Fig 6.9c. Note that this assignment is made without using the information contained in the entire measurement record outside of the single time bin t_k from which z_k is taken. Knowing the qubit state at each time bin allows us obtain the transition rates between the qubit states.

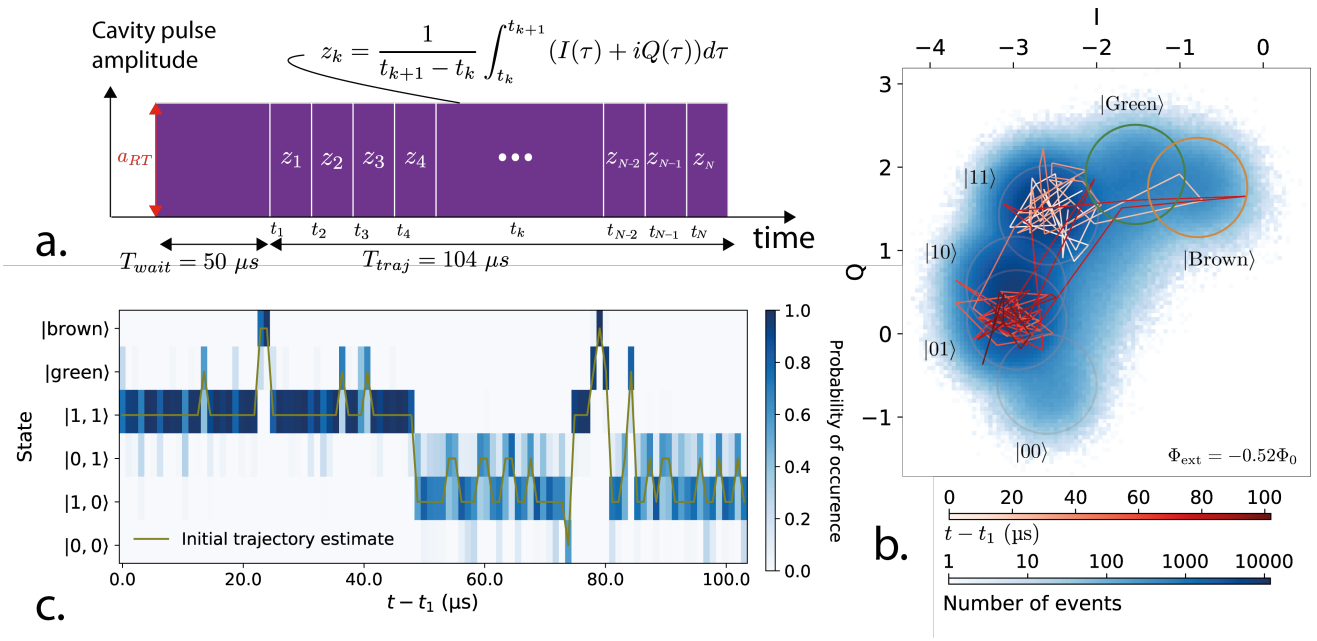

Figure 6.9: a. Pulse sequence of the trajectory measurement. The cavity is driven for a fixed waiting time $T_{\text{wait}} = 50\,\mu$s before the transmitted signal is acquired for $T_{\text{traj}} = 104\,\mu$s. The acquisition is broken down into bins of length $t_{k+1} - t_k = t_{\text{bin}} = 1040$ ns during which the signal is integrated leading to a trajectory $\{z_1, z_2, \ldots, z_N\}$ of positions in the IQ-plane. b. Typical trajectory in the complex plane super imposed on the readout histogram obtained for a 1040 ns integration time and $a_{\text{RT}} = 0.9$ V. Circles correspond to $2\sigma_{|\text{pointer}\rangle}(t_{\text{bin}})$ excursions around the detected pointer state centres in a histogram with longer integration time. The |Green⟩ and |Brown⟩ circles correspond to pointer-states whose qubit state equivalence was not identified. Note how some points find themselves within two circles at the same time. c. Assigned qubit states as a function of time for the trajectory shown in panel b. The probabilities $P(z_k|\,|i,j\rangle)/\sum_{|k,l\rangle} P(z_k|\,|k,l\rangle)$ are shown in by the blue colormap and the most likely trajectory defined by the qubit states assigned at each time is shown in green.

6.6.2 *Defining the transition rates*

The transition rates between the different qubit states are defined as the coefficients of the detailed balance equations describing the time evolution of the state populations $p_{|\nu\rangle}$

$$\frac{\mathrm{d}p_{|\nu\rangle}(t)}{\mathrm{d}t} = \sum_{\mu} \Gamma_{\nu\mu} p_{|\mu\rangle}(t)\ . \tag{6.30}$$

From now on we also use Greek letter indices to denote the multi-index of the state of the two qubits when appropriate notationaly: $|\nu\rangle \Leftrightarrow |i,j\rangle$. To keep the equation compact, we have used a convention where $\Gamma_{\nu\nu} = -\sum_{\mu\neq\nu}\Gamma_{\mu\nu}$. This is also useful when doing numerics on the matrix $(\Gamma)_{\nu\mu} = \Gamma_{\nu\mu}$. Note also that $-\Gamma_{\nu\nu} = \Gamma_{\nu}^{\text{tot}}$ is equal to the total rate at which the system leaves state $|\nu\rangle$. To give some intuition of how the

transition rates relate to the jump probabilities $P^k_{\nu\to\mu}$ defined above, the probability of starting in state $|\nu\rangle$ and not leaving for a time t is given by

$$P_{\text{stay},\nu}(t) = e^{-\Gamma^{\text{tot}}_\nu t} \ . \tag{6.31}$$

Similarly, the probability that the first jump away from $|\nu\rangle$ happened before t and that the state became $|\mu\rangle$ is

$$P_{\nu\to\mu}(t) = \frac{\Gamma_{\mu\nu}}{\Gamma^{\text{tot}}_\nu}(1 - e^{-\Gamma^{\text{tot}}_\nu t}) \ . \tag{6.32}$$

These last two expressions give us a tool for estimating the rates $\Gamma_{\nu\mu}$ from the quantum jump trajectories. If $t_{\text{bin}} \gg 1/\Gamma^{\text{tot}}_\nu$, then Taylor expanding the exponential in (6.32) yields

$$P_{\nu\to\mu}(t_{\text{bin}}) \approx \Gamma_{\mu\nu} t_{\text{bin}} \ . \tag{6.33}$$

We can calculate the probability $P^k_{\nu\to\mu}$ of the qubit state jumping from $|\nu\rangle$ to $|\mu\rangle$ between times t_k and t_{k+1} by counting the number of jumps $N^k_{\nu\to\mu}$ from state $|\nu\rangle$ to $|\mu\rangle$ and dividing by the total number of jumps leaving state $|\nu\rangle$ at t_k, $\sum_\mu N^k_{\nu\to\mu}$. Convieniently, in our experiment, because the cavity drive parameters do not change during our measurement, $P^k_{\nu\to\mu} = P_{\nu\to\mu}$ is independent of the time step. Note that this is true whether or not we are in the steady-state of Eq. (6.30), which is not the case for the $N^k_{\nu\to\mu}$ which explicitly depend on time. Obviously

$$\sum_\mu P_{\nu\to\mu} = 1 \ . \tag{6.34}$$

The transition rates and jump probabilities are thus related in the following way

$$\forall \nu \neq \mu \ , \ \Gamma_{\nu\mu} t_{\text{bin}} = P_{\mu\to\nu} \ ; \tag{6.35}$$

$$\forall \nu \ , \ \Gamma_{\nu\nu} t_{\text{bin}} = -(1 - P_{\nu\to\nu}) \ . \tag{6.36}$$

If we assume that the matrix Γ possesses only a single eigenvalue with value 0 (all others are negative such that all energy eigenstates of the Hamiltonian have non-zero transition rates between each other), then the equilibrium populations of the qubit in the steady state are determined by the eigenvalue equation

$$\Gamma \vec{p}_{\text{th}} = 0 \ . \tag{6.37}$$

Equivalently, regardless of the initial state, at infinite time the qubit's populations should be in the steady-state. This mean Finally, in the steady state, the populations of each qubit state are related to the matrix Γ by

$$\lim_{t\to\infty} e^{\Gamma t} \vec{p}_{\text{init}} = \vec{p}_{\text{th}} \ . \tag{6.38}$$

6.6.3 *Forward-Backward state estimation*

In the previous section we gave a method for estimating the transition rates using the quantum jump trajectory. This relied on the assignment of each z_k to a qubit

state, about which we then defined jump probabilities. Unfortunately, as is clear from Fig. 6.9b. the SNR is too small to assign a qubit state to each z_k with a high probability of being correct. In particular, some points in the IQ-plane could be associated with two different qubit states with similar probability. One way of correcting for this is to consider the information contained in the entire measurement record. For this we use the Past Quantum State (PQS) formalism described in detail in [42] and in Quentin Ficheux's thesis [48]. This formalism helps predict the outcome of a generalised measurement of a quantum system at time t_{meas} based on the quantum trajectory of the quantum state ρ inferred from weak measurements at times $t < t_{\text{meas}}$ and $t > t_{\text{meas}}$, as well as the knowledge of the starting state at $t = 0$ and the result of a strong measurement at $t = t_{\text{final}}$. Some of the main results of this formalism, useful for interpreting the results of this chapter and the next are given in Appendix D. Because the measurement of the qubit at each time step is projective, we do not need to deal with the off-diagonal elements of the density matrix describing the qubit state. In that case, the PQS formalism simplifies to a Forward-Backward Bayesian estimation used for example in [200] to estimate the number of photons in a microwave resonator of a cavity QED experiment.

For a single quantum jump trajectory, we define $P_{\text{F}}(|\nu\rangle, k)$ as the (forwards) probability of the qubit being in state $|\nu\rangle$ in time bin k given all the information on the trajectory prior to time t_k. Equivalently, $P_{\text{B}}(|\nu\rangle, k)$ is the (backwards) probability of the qubit being in state $|\nu\rangle$ in time bin k given all the information on the trajectory after time t_k. We can relate successive time steps to each other through the following equations [201]

$$P_{\text{F}}(|\mu\rangle, k+1) = \sum_{\nu} (e^{\Gamma t_{\text{bin}}})_{\mu\nu} \cdot \frac{P(z_k|\,|\nu\rangle) P_{\text{F}}(|\nu\rangle, k)}{\sum_{\sigma} P(z_k|\,|\sigma\rangle) P_{\text{F}}(|\sigma\rangle, k)} , \tag{6.39}$$

$$P_{\text{B}}(|\mu\rangle, k-1) = \sum_{\nu} (e^{\Gamma^T t_{\text{bin}}})_{\mu\nu} \cdot \frac{P(z_k|\,|\nu\rangle) P_{\text{B}}(|\nu\rangle, k)}{\sum_{\sigma} P(z_k|\,|\sigma\rangle) P_{\text{B}}(|\sigma\rangle, k)} . \tag{6.40}$$

In the above equations, the second term is the Bayesian update, which corrects the probability $P_{\text{F,B}}(|\nu\rangle, k)$ of being in state $|\nu\rangle$ based on the measurement result at time t_k. The denominator is there for normalisation. The first term with the exponential corresponds to the state evolution between times t_k and $t_{k\pm1}$ due to the transition rates captured in the matrix Γ. We take into account both the forward and backward propagating probabilities in $P_{\text{FB}}(|\nu\rangle, k)$ (forward-backward) defined as

$$P_{\text{FB}}(|\nu\rangle, k) = \frac{P_{\text{F}}(|\nu\rangle, k) P_{\text{B}}(|\nu\rangle, k)}{\sum_{\mu} P_{\text{F}}(|\mu\rangle, k) P_{\text{B}}(|\mu\rangle, k)} . \tag{6.41}$$

$P_{\text{FB}}(|\nu\rangle, k)$ consists of our best estimate for the probability of the qubit being in state $|\nu\rangle$ at time t_k given the information contained in the entire measurement record. Importantly, the initial probability $P_{\text{F}}(z_0|\,|\nu\rangle)$ is initialised with the equilibrium populations given by (6.38). The backward probabilities are initialised with the maximally entropic state $P_{\text{B}}(z_{N+1}|\,|\nu\rangle) = \frac{1}{\dim \mathcal{H}}$, where $\dim \mathcal{H}$ is the dimension of the Hilbert space in which we are working. Because $P_{\text{FB}}(|\nu\rangle, k)$ is the best estimate we have for the probabilities, we can assign to each time step the most likely state defined as

$$|\mu\rangle = \underset{|\nu\rangle}{\text{argmax}}\, P_{\text{FB}}(|\nu\rangle, k) , \tag{6.42}$$

in equivalence with (6.29). Note that the forward-backward estimation needs to be done for each of the N_{exp} measurement traces.

A certain circularity now becomes clear, because we need (6.42) to calculate Γ which in turn is needed to obtain $P_{\text{FB}}(|\nu\rangle, k)$ and (6.42). We resolve this by iterating the procedure described above until the entries of the Γ matrix converge.

1. Initialise $\Gamma^{(0)}$ with the transition rates obtained from the jump rates deduced from the probabilities $P(z_k||\nu\rangle)$.
2. Use these transition rates $\Gamma^{(i)}$ to estimate the forward-backward probabilities $P_{\text{FB}}^{(i+1)}(|\nu\rangle, k)$ using (6.39), (6.40) and (6.41).
3. From $P_{\text{FB}}^{(i+1)}(|\nu\rangle, k)$ update the transition rate matrix to $\Gamma^{(i+1)}$.
4. Repeat.

The results of this iterative procedure on the qubit state assignment is shown in Fig. 6.10a. Thanks to the Bayesian update, which takes into account the information either side of time point t_k, we are able to significantly reduce the switching between qubit states in the final iteration of the forward-backward procedure compared to the initial qubit trajectory. We attribute the jumps we saw before using the forward-backward probabilities to the measurement noise. This is especially evident for the states $|0,1\rangle$ and $|1,0\rangle$ which are not well resolve in the IQ-plane. The convergence of this algorithm for finding the transition rates is shown in Fig. 6.10b and c. We see that all the transition rates converge exponentially to stationary values as the number of iterations increase. This is a good sign for the behaviour of the numerics, because calculating $P_{\text{FB}}(|\nu\rangle, k)$ and γ is computationally intensive. Five iterations are sufficient to obtain a relative difference of $\sim 10^{-2}$ on the transition rates estimates between the 4^{th} and 5^{th} iterations of the algorithm. We also note that the transition rates are all below the $1/t_{\text{bin}} = 1040\,\text{ns}^{-1}$ threshold for the rates resolvable with time bins of 1040 ns.

6.6.4 *Flux and Photon-Number Dependent Transition Rates*

By applying the foward-backward algorithm on measurement records of different fluxes and amplitudes, we are able to extract the transition rates $\Gamma_{\nu\mu}(\bar{n}, \Phi_{\text{ext}})$. The results for the fixed amplitude $a_{\text{RT}} = 0.275$ and fixed flux $\Phi_{\text{ext}} = -0.52\Phi_0$ are shown in the left and right panels of Fig. 6.11 respectively. Strikingly, the transition rates are neither constant in flux nor in the mean photon number. In flux the transition rates exhibit order of magnitude variations when Φ_{ext} is varied over a $\frac{1}{100}\Phi_0$ range (around $\Phi_{\text{ext}} = -0.5\Phi_0$) as well as showing factor of two enhancements within $\frac{1}{1000}\Phi_0$ around $\Phi_{\text{ext}} = -0.508\Phi_0$ or $-0.517\Phi_0$ for example. In particular, not all of the transition rates are affected equally e.g. at $\Phi_{\text{ext}} = -0.508\Phi_0$ where the variations in $\Gamma_{|0,1\rangle\to|0,0\rangle}, \Gamma_{|1,1\rangle\to|0,0\rangle}$ and $\Gamma_{|1,1\rangle\to|1,0\rangle}$ are more pronounced than for the other transitions. We also note that the flux dependent transition rates exhibit some symmetry around the point $\Phi_{\text{ext}} = -0.5\Phi_0$, similarly to the two qubit spectrum which is also quasi-symmetric.

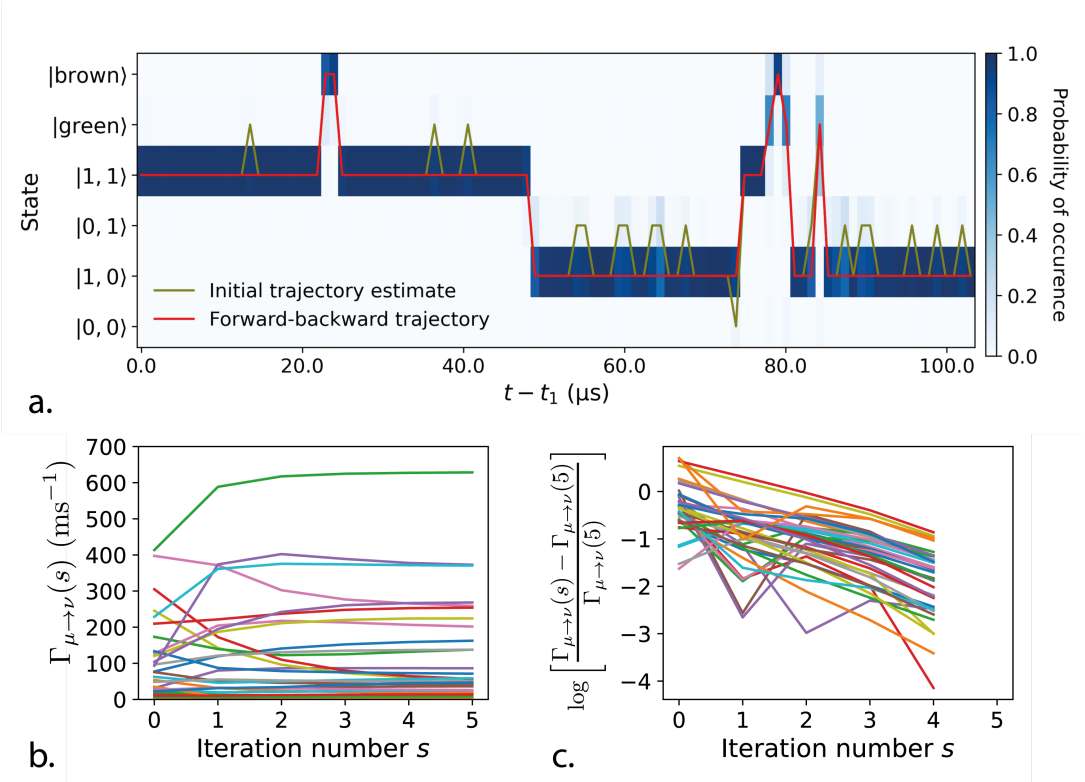

Figure 6.10: Results of the forward-backwards algorithm. a. The assigned qubit states as a function of time for the same trajectory as shown in Fig. 6.9b. but after the forward-backwards procedure are shown in red. For comparison, the initial trajectory is shown again in green. The probabilities $P_{\mathrm{FB}}^{(i+1)}(|\nu\rangle, k)$ are shown in by the blue colormap. b. Values of the transition rates as a function of the forward-backwards iteration number s. We only show the off-diagonal elements of the matrix Γ which is why they are all positive. Each color corresponds to a different rate. c. Relative convergence of the forward-backward estimation of the transition rates compared to the last iteration.

Fig. 6.11 constitutes one of the few quantitative measurements of the transition rates in Fluxonium qubits over a wide range of parameters. Yet, the fact that strong drives away from the qubit frequency may affect the qubit state is not a new problem. For more than a decade already a number of experiments have observed changes in the qubit transition rates as the amplitude of a drive away from the qubit frequency increases, both in Transmons and in Fluxoniums [92, 202, 203, 37, 34, 204]. Interestingly, experiments do not consistently report an increase or decrease in the qubit excitation or deexcitation rates as a function of the average photon number in the drive. This is inline with our own observations, as the transition rates do not evolve monotonically as a function of the average photon number in Fig. 6.11. As the necessity to use strong drives for fast gates in quantum algorithms becomes more and more evident, there has recently been renewed interest in explaining these effects. A number of theoretical efforts, mostly focused on the more prevailent Transmon qubit have attempted to explain some of the experimental results [197, 205, 193], also reproducing in turn the potential increase or descrease of the transition rates, depending on the effects considered. A

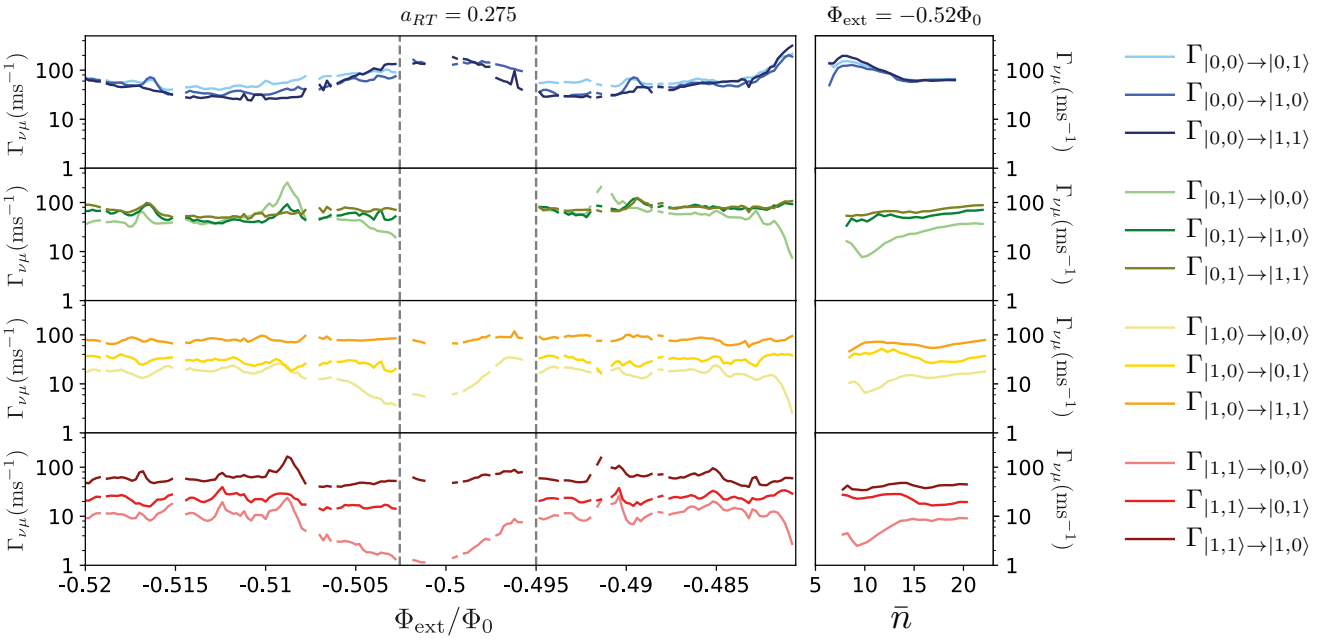

Figure 6.11: Transition rates between levels as a function of flux (left) or as a function of the mean photon number (right). In the region of flux between the gray dashed lines, states $|1,0\rangle$ and $|0,1\rangle$ cannot be differentiated using a dispersive measurement because their dispersive shifts almost exactly coincide. In this region the pointer state labeled $|0,1\rangle$ should be considered a statistical mixture of the two single excitation states $\rho = (|1,0\rangle\langle 1,0| + |0,1\rangle\langle 0,1|)/2$. Photon numbers in the right are given for the state $|\nu\rangle$ which we are leaving through the transition $\Gamma_{\mu\nu}$. Missing points are due to issues with the identification of the pointer-states in the IQ-plane or to poor convergence of the forward-backward analysis.

recent theoretical work [194, 195] was even able to demonstrate some non-monotonous effects by carefully considering how the cosine non-linearity can mix drive and qubit operators, naturally leading to effective qubit transitions. Unfortunately, generalising these theories to the Fluxonium qubit is difficult because it cannot be considered to be weakly non-linear. Looking at the average photon number dependence of the transition rates, in particular the clear peak in the transition rate leaving the coupled qubit ground-state at $\bar{n} \approx 7$ photons, suggests starting with a theory resembling the one developped in [191] which looks for correspondances between the frequency of virtual transitions enabled by the drive and the qubit frequency. This is direction of research is supported by the fact that some features are well defined in flux, resembling coincidences between cavity, drive and qubit levels at specific Φ_{ext}, which lead to enhanced transition rates at certain photon numbers. Coincidentally, the values for $\Gamma_{\nu\mu}$ reported here are also very close to those recently reported in a work by Gusenkova et al., who also saw a non-monotonous evolution of the transition rates as a function of $\bar{n}$, albeit over a much larger range [34]. Given the differences between our device and theirs - different ratios between the terms in the Hamiltonian and the use of granular aluminium for the fluxonium inductance - it appears possible that the mechanisms driving the transitions between levels might be common to all types of Fluxonium atoms. In that case, the fact that they could readout the state of their Fluxonium at very high photon

numbers could be due to a feature of the qubit spectrum at the flux point at which the qubit was measured. Regardless of the mechanisms involved, it appears urgent to find solutions to this readout problem for future experiments with Fluxonium.

6.7 SIMULATING QUANTUM JUMP TRAJECTORIES

6.7.1 *Taking into account non-poissonian statistics*

Implicit in the previous sections was that the distribution of quantum jumps followed poissonian statistics. We assumed this when Taylor expanding $P_{\nu\to\mu}(t)$ in (6.33) so that we could simply count the number of jumps at each time step to determine the transition rates. Yet it is known that energy decays observed in Fluxonium devices often show the so called double exponential behaviour

$$\langle P(t)\rangle = e^{\lambda(\exp(-t/T_{\rm qp})-1)}e^{-t/T_{\rm r}} \tag{6.43}$$

we derived in Chapter 5 which is usually attributed to quasi-particles [82]. Non-poissonian distributions leading to double exponential decay was also observed in Fluxonium quantum jumps both in Yale [37] and in Karlsruhe [34].

In Fig. 6.12 we show a typical example of the ensemble average $\langle P_{{\rm stay},\nu}(t)\rangle$ of the probability of not leaving state $|\nu\rangle$ up until time t. Here the average is taken over all the $N_{\rm exp} = 50000$ experiments at flux $\Phi_{\rm ext} = -0.508\Phi_0$ and drive amplitude $a_{\rm RT} = 1.15\,\mathrm{V}$ for the quantum jump trace before applying the forward-backwards algorithm. At short times we clearly see a departure from the linear time dependence expected when plotting $\langle P_{{\rm stay},\nu}(t)\rangle$ on a logarithmic scale. The non-linear dependence on time is reproduced phenomenologically by a double exponential model adjusted to the experimental results.

This result could pose a real issue for the use of the forward-backward algorithm described in the previous section. Indeed, in that case we assumed the transition rates to be constant over all $N_{\rm exp} = 50000$ experiments. This cannot be the case if the phenomenogically double exponential decay of Fig. 6.12 is explained by quasiparticles. Indeed, in that case (assuming the number of quasiparticles $n_{\rm qp}$ does not change over the duration of the cavity pulse) for each experimental record i the transition rates would be different

$$\Gamma_i = \Gamma_r + \Gamma_{\rm qp} n_{\rm qp}^i \ , \tag{6.44}$$

where Γ_r are the (fixed) transition rates, independent of $n_{\rm qp}$, $\Gamma_{\rm qp}$ are the transition rates induced by quasiparticles and $n_{\rm qp}^i$ is the number of quasiparticles for the specific experiment i. Taking this dependence on $n_{\rm qp}$ into account is possible only if the length of the cavity pulses are sufficiently long to gather statistics about the transition rates with $n_{\rm qp}$ constant which, with pulses of 104 µs and transition rates of the order of 10 kHz to 100 kHz, is not the case here. This problem could also potentially be resolved by using the parameter estimation techniques described in [206], but it is mathematically involved and numerically complex to implement. In fact, as we will show in the following,

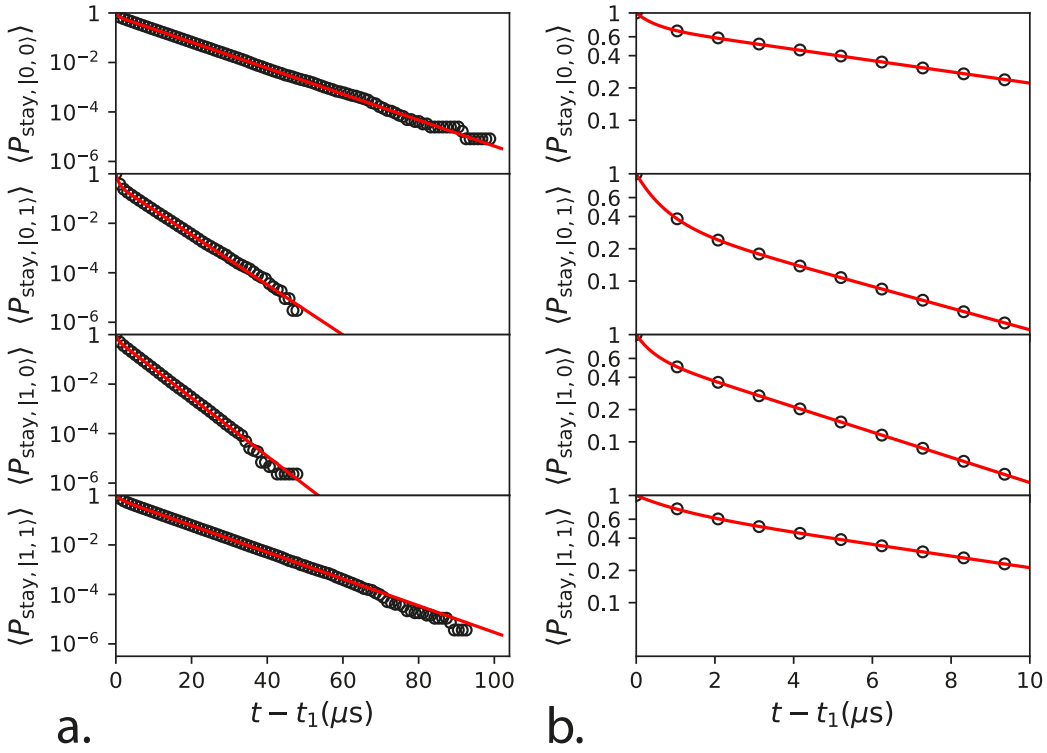

Figure 6.12: Typical dependence of $\langle P_{\text{stay},\nu}(t)\rangle$ on time, shown here for $\Phi_{\text{ext}} = -0.508\Phi_0$ and $a_{\text{RT}} = 1.15\,\text{V}$, before the forward-backward procedure has been applied. The black dots correspond to the experimentally extracted probabilities and the red lines to a double exponential model like (6.43) adjusted to reproduce the experimental results. Note that the model forces a probability of 1 at time 0. Panel b. is a zoom on the short times of panel a. In this case, $t_{\text{bin}} = 260\,\text{ns}$.

the double exponential decay can at least in part be explained by the finite SNR of the readout histograms. To support this and dismiss the presence of quasiparticles, we simulate quantum jump trajectories numerically.

6.7.2 *Simulating quantum jump trajectories*

In the following we consider only the four states within the computational subspace. For each pair Φ_{ext} and a_{RT} the positions of the pointer states in the IQ-plane is known. The following steps are used to simulate N_{exp} noisy trajectories in the IQ-plane. We assume that the transition rates given in the matrix Γ are known.

1. Initialise the trajectory probabilistically with one of the 4 positions $z_{|\nu\rangle}$. The probability of initialising the trajectory with state $|\nu\rangle$ is given by $\left[\lim_{t\to\infty} e^{\Gamma t}\right]_{\nu 0}$.

2. For each step k in the trajectory, generate the state of the qubit at time $k+1$ following the probabilities $p_{\nu\to\mu}(T) = [e^{\Gamma T}]_{\mu\nu}$ depending on the state of the qubit in step i. T is the length of the time step of the trajectory we want to simulate. This is done by drawing a uniformly distributed random number between 0 and

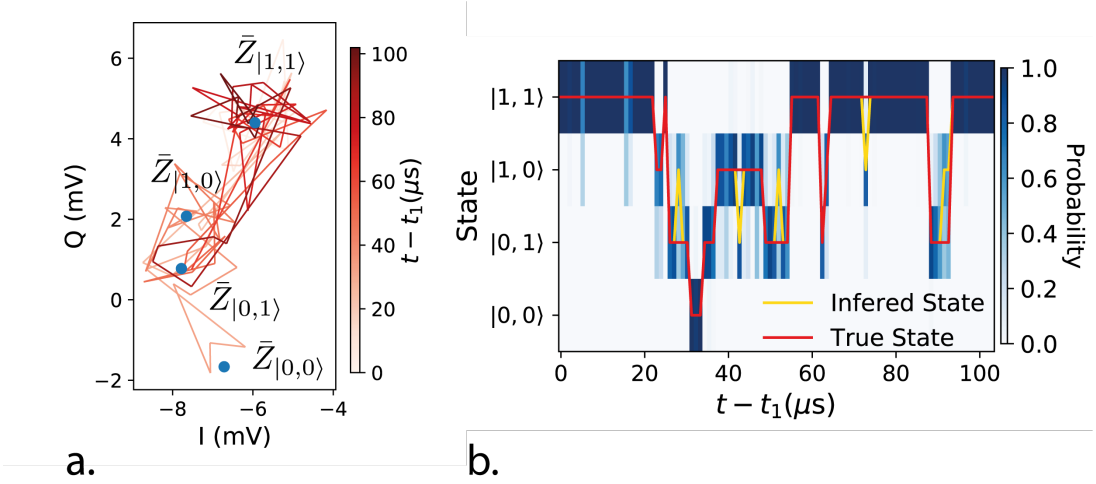

Figure 6.13: Typical simulated noisy quantum jump trajectory for 4 qubit states. a. The noisy trajectory is shown in the IQ-plane with blue markers denoting the experimentally determined centre of each pointer state. The transition rates used to simulate the trajectory were taken from the results of the forward-backwards algorithm applied to the measurement records for $\Phi_{\text{ext}} = -0.508\Phi_0$ and $a_{\text{RT}} = 0.925\,\text{V}$. b. Effect of the noise on the qubit state assignment. In red we show the qubit state generated by the simulation before noise is added to the trace, and in yellow the state which maximises $P(z_k||\nu\rangle)$ for the simulated measurement record. These probabilities are calculated according to a gaussian probability distribution with the same standard deviation σ_{IQ} as the added noise. The colormap shows the probabilities $P(z_k||\nu\rangle)/\sum_{|\mu\rangle} P(z_k||\mu\rangle)$ for each state.

1 and comparing it with the jump probabilities for each state. Do this for the N time steps of the trajectory to simulate.

3. Add noise to the trajectory by generating N normally distributed complex random numbers with variance σ_{IQ}^2 and adding it to the position of each state. With this we have reproduced the 2D measurement trace.

4. For each value in the trajectory assign the state with the highest probability of occurence according to the same probability distribution as the noise. This is equivalent to (6.29). By doing this we have simulated misinterpreted jumps in the trajectory.

An example of a trajectory generated in such a manner is given in Fig 6.13a. The added gaussian noise leads to mistakes in the states infered from the trajectory and the true qubit states which are known perfectly from the simulation. The differences between the two are shown in Fig. 6.13b.

6.7.3 *Reproducing double exponential decay with gaussian noise*

With the above simulation, we can redo the same analysis of Fig. 6.12 for the simulated trajectories. In Fig. 6.14 we show the probabilities $\langle P_{\text{stay},\nu}(t)\rangle$ extracted from 40000 simulated measurement traces. To underline the non-exponential time depen-

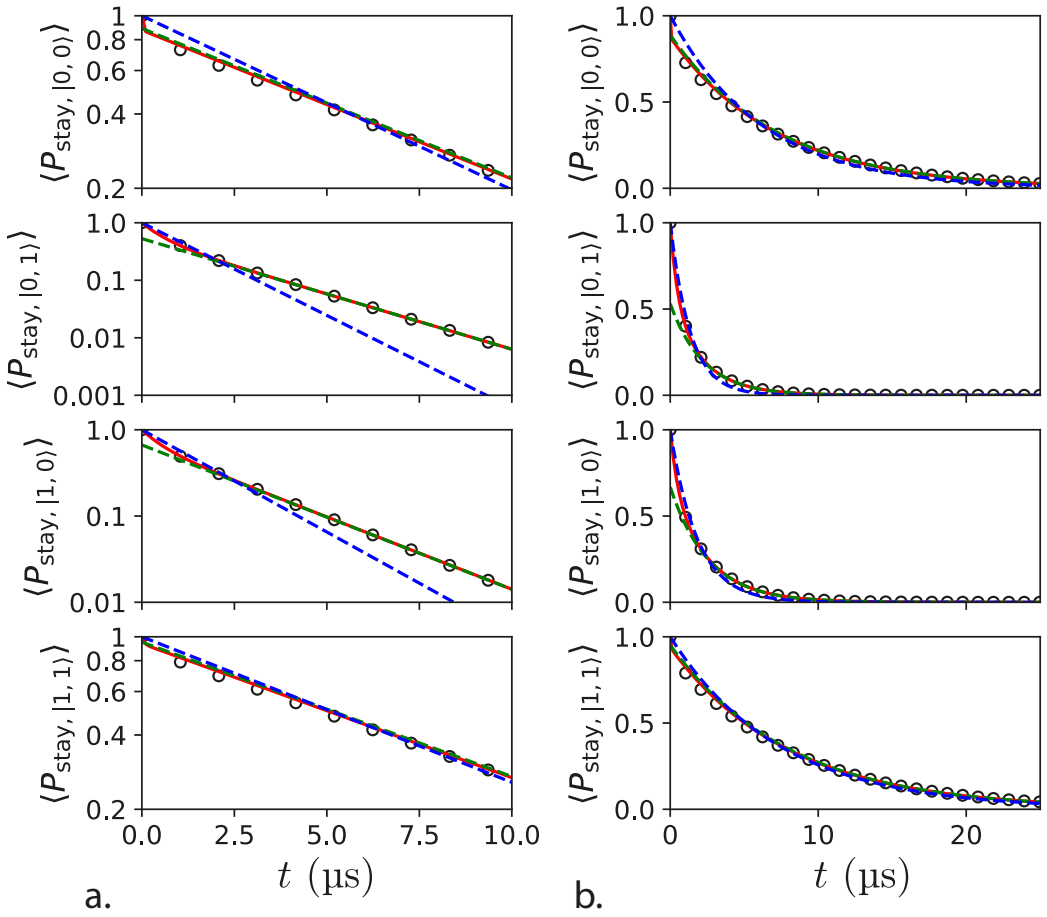

Figure 6.14: Simulated dependence of $\langle P_{\text{stay},\nu}(t)\rangle$ on time, shown here for $\Phi_{\text{ext}} = -0.508\Phi_0$ and $a_{\text{RT}} = 0.925\,\text{V}$. Compared to Fig. 6.9 we have set $t_1 = 0$. a. and b. show the same information on different scales. Black circles correspond to the probabilities extracted from the simulation, with a single point with coordinates (0,1) is added by hand to respect the unit probability condition at time 0 (the point is barely visible because of the plot boundaries). The solid red line is generated from a double exponential model like (6.43) (model A), the blue dashed line corresponds to a functional $f(t) = e^{-t/T}$ with T as an adjustable parameter (model B) and the green dashed line to $f(t) = Ae^{-t/T}$ with T and A as adjustable parameters (model C).

dence we compare different models: a double exponential model like (6.43) which must go through $(0, 1)$ (model A - red); an exponential model which must go through $(0, 1)$ (model B - blue); an exponential fit which is not contrained on its y-intersect (model C - green). Imposing a y-intersect of 1 can be interpreted as a physical boundary condition: at time 0^+, the likelihood of still being in the state in which we were in at $t = 0^-$ must be 1. Only the double exponential model is able to reproduce the simulated results over the full range of values and take into account the boundary condition. By observing the quality of the overlap between model C and the simulated probabilities at long times, we deduce that beyond the first few time bins, $\langle P_{\text{stay},\nu}(t)\rangle$ follows an exponential law. This result suggests that non-exponential decay seen in Fig. 6.12 could at least be in part due to the noise in the measurement, and invites us to be cautious when claiming

the role of quasiparticles on transition rates when dealing with quantum jump statistics.

To check how far our simulations are able to reproduce quantitatively the double exponential decay rates observed in the experiment, we first generated simulated quantum jump trajectories using the corrected transition rates extracted from the forward-backwards algorithm for measurements taken at $\Phi_{\text{ext}} = -0.508\Phi_0$ (see illustration of Fig. 6.15a.). Then, we compare the parameters of a double exponential model adjusted to $\langle P_{\text{stay},\nu}(t)\rangle$ taken from the raw, forward-backwards and simulated quantum jump trajectories for varying cavity drive amplitudes (Fig. 6.15). Our first observation is that the value of the parameters T_r, T_{qp} and λ tend to converge in most cases for large a_{RT}. This is no coincidence, because as the drive amplitude increases, so does the SNR of our measurement (see (6.25)). Thus as a_{RT} increases, the forward-backwards procedure corrects less and less the transition rates extracted from the raw quantum jump trajectories. We also see that the parameters extracted from the simulation statistics qualitatively match the dependence on drive amplitude of those taken from the raw trajectories. In particular, the values of the model adjusted to the raw and simulated statistics are often quite similar, especially for T_r. This is a sign that it may be possible to reproduce the same statistics of the measured raw trajectories simply by adding gaussian noise to an ideal quantum jump trajectory. There are discrepancies though between the simulations and measurement statistics; like the fact that the adjusted parameter λ has consistently lower values for the simulations compared to the raw trajectories. In the future, to improve the correspondence in the statistics between the raw and simulated trajectories, our simulation model should take into account the finite integration time of the readout and the presence of additional excited states which contribute to the transition rates.

Following this comparison, it appears that simulations taking into account the gaussian noise of the measurement can, a least in part, reproduce the double exponential statistics of the quantum jump traces of our Fluxonium device. This adds weight to the argument that we did not make an error in using the forward-backwards algorithm on the datasets from the measurement. Indeed, if the double exponential decay was due to quasiparticles, using the forward-backwards algorithm would have yielded the wrong results for the transition rates. For $a_{\text{RT}} \gtrsim 0.8\,\text{V}$, the statistics from the simulated, raw and forward-backward quantum jumps tend to converge, indicating that either the quasiparticles manifesting themselves as non-poissonian trajectory statistics disappear at strong drives, or the double exponential is partially explained by the noise of the measurement. Thus, although we cannot completely exclude the effect of quasiparticles, we can increase our confidence in the results of Fig. 6.11, especially at high amplitude, where the SNR of the trajectories is large.

6.8 CONCLUSION

We have extracted the cavity photon induced transition rates in a coupled fluxonium qubit system thanks to a rigorous analysis of cavity measurement traces and a comprehensive theoretical understanding of our system Hamiltonian. We were able to show

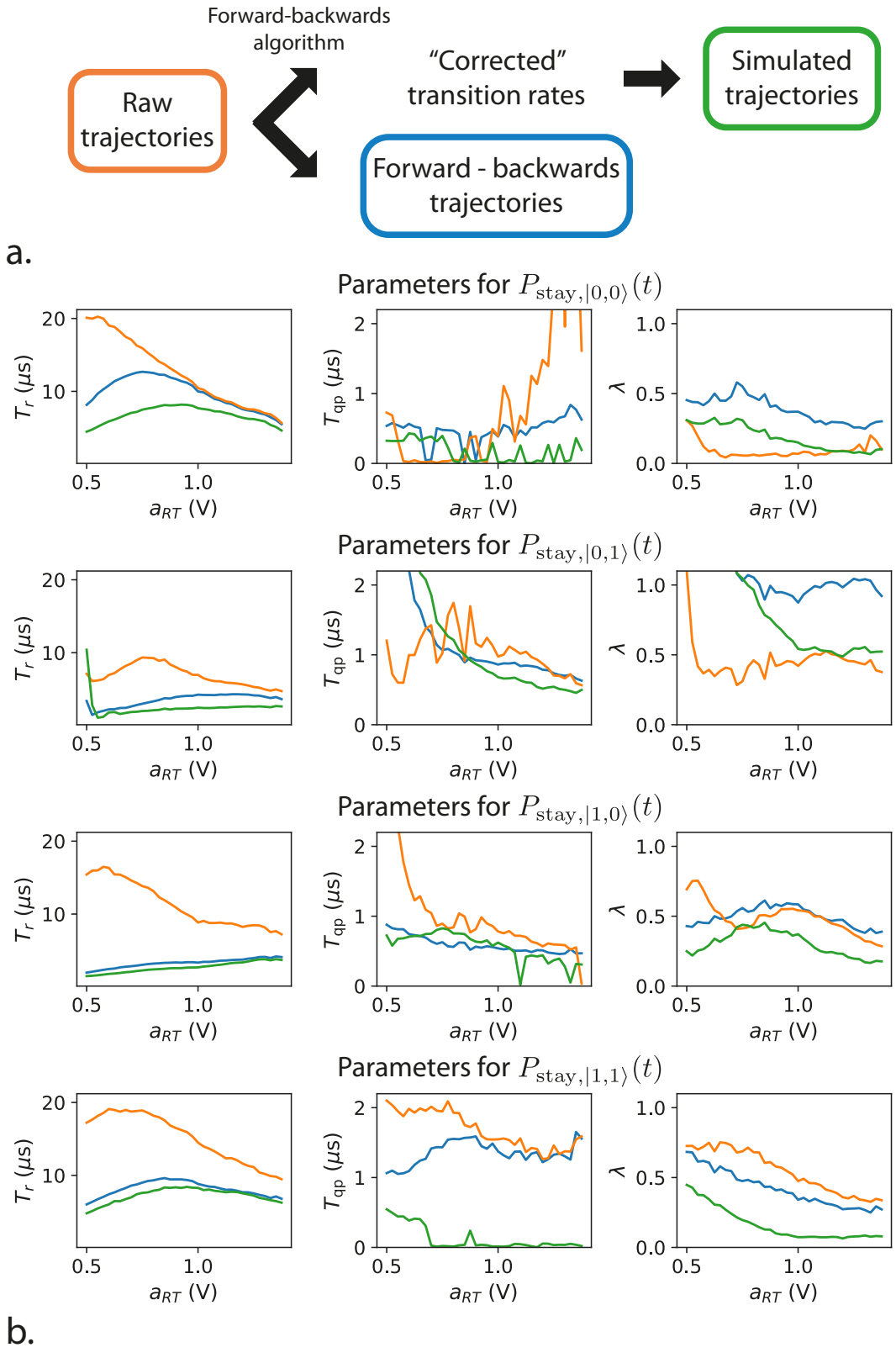

Figure 6.15: Comparison of the experimental (raw and forward-backwards) quantum jump statistics with the simulated ones. a. We apply the forward-backwards algorithm on the raw trajectories, yielding "corrected" transition rates and the statistics of the forward-backwards trajectories. We use the corrected transition rates as the basis for our simulated trajectories. b. Comparison of the adjustable parameters of (6.43) which best reproduce the time dependence of the probabilities $\langle P_{\mathrm{stay},\nu}(t)\rangle$ extracted from the raw quantum jumps, those remaining after the forward-backwards procedure and a quantum jump simulation ($t_{\mathrm{bin}} = 1040\,\mathrm{ns}$). Each row corresponds to a different state and the colored lines correspond to the amplitude dependence of each model parameter.

that these rates evolve as a function of cavity photon number and external flux. With this work, we have brought a timely contribution to the resolution of the extensively documented issues with superconducting circuit readout. Our quantitative measurement is interesting because it provides hints as to the possible directions of research to explain the dependence of transition rates on photon number. Both the rates we found and the value at which photon number affects the transition rates are within the range of values observed in the literature [34, 37, 66, 38] and we hypothesise that the mechanisms governing the transition rates dependence on a_{RT} and Φ_{ext} could be common to all Fluxoniums. The smallest resonant features in the transition rates arise within 1000^{th} of a flux quantum in flux, and when the cavity occupation is changed on the order of a single photon. This indicates that elements of explanation could be resonant crossings between qubit and cavity levels in a manner close to those reported in [191], possibly due to matrix elements allowed by the cosine non-linearity and the strong drive [195]. Understanding the transition rates in Fluxonium qubits would certainly be a large step in resolving long standing issues with Fluxonium qubit readout, and could be essential to the design of future multi-Fluxonium devices. We also explored the effect of gaussian noise on the statistics of our quantum jump trajectories, highlighting that care must be taken with interpreting double exponential decay qubit decay obtained from quantum jump trajectories as the definitive sign of the presence of quasiparticles.

7

THERMODYNAMICS OF A QUBIT GATE

This chapter stands apart in this thesis for multiple reasons. We have, up until now, been focused mainly on the Fluxonium qubit, which plays no part in the results of this chapter. Second, the project presented here only really started at the beginning of the last year of the thesis work, well after most of the results obtained with the Fluxonium qubit. Finally, while the motivations for the experiments up until now have been quite practical in nature, especially in the context of quantum computing (better qubit readout, error protection, design), this chapter appears more fundamental in the question it seeks to answer: "What is the energy balance of a qubit measurement?" Although not connected by design to the rest of this thesis, it is not hard to see parallels between the fundamental energetics of quantum measurements, the qubit transition rates during readout explored in Chapter 6 and the loss of information on the qubit state due to energy and information exchange between a qubit and its environment (Chapters 3 and 4). As an illustration of how many of these concepts are in fact interrelated, a different flavour of the past quantum state formalism as the one used in Chapter 6 will find its place here.

The chapter is structured as follows. First we provide a short introduction to quantum thermodynamics, focusing on the concept of quantum heat. In the next parts we present the results of an experiment designed to shed light on the microscopic energy exchanges at play during a qubit gate. We will show that these exchanges can be interpreted as the result of the backaction of a weak measurement of the field used to prepare the qubit state.

7.1 A SHORT HISTORY OF QUANTUM HEAT

At its origins, thermodynamics served as a formalism to design more efficient machines during the second industrial revolution, harnessing the laws of heat exchange to extract work. The highly practical motivations for the development of this theory are visible in the very name of the discipline, which suggests using temperature ('thermo') to produce movement ('dynamics'). From a modern point of view, the difference made between work and heat can be characterised by the reversibility of the process. The exchange of work between two systems can be done reversibly (think of Newton's pendulum), whereas heat exchanges cannot: once your warm water is at room temperature, there is no way of extracting the heat from the air back into the cup. Another point of view, rephrasing the Clausius inequality, is to say that while work can be fully converted into heat, the converse is not true. For the 21st century physicist, the concept of irreversibility appears deeply connected to the information about the microscopic state of the systems studied. The statistical physics approach to thermodynamics is to consider its laws as emerging from microscopic interactions when the system size

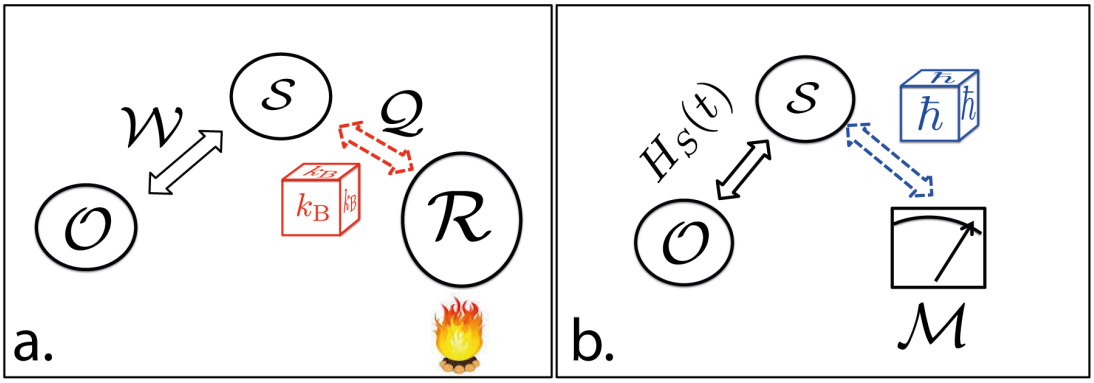

Figure 7.1: Classical versus quantum thermodynamics (taken from [41]). a. A system $\mathcal{S}$ exchanges work with a controller $\mathcal{O}$ and heat with a thermal reservoir $\mathcal{R}$. The random action of the reservoir on the system is illustrated by the die k_B. b. In the quantum case, the measurement apparatus is the source of quantum randomness illustrated by the die $\hbar$. Reversible interactions with the controller are described by the time dependent Hamiltonian $H_S(t)$.

becomes large [207, 208]. In that case, irreversibility is just the manifestation that it is difficult to keep track of the exact state of $\gtrsim 10^{23}$ degrees of freedom. This hypothetical ability is the basis of the Maxwell's demon thought experiment [209]. Can an omniscient being (the demon) extract work for free from a heat bath by knowing exactly all of the microscopic degrees of freedom? The resolution of the paradox, involving the erasure of the demon's memory, intimately relates information to energy and to this day gives a lower bound on the amount of energy needed to run a classical computer [210, 211]. Finally, the lack of information about a system can also be the origin of perceived randomness. For a small enough system interacting with a heat bath, the state of the system will undergo apparently random fluctuations due to the presence of the bath. A prime example of such stochastic dynamics is Brownian motion [212]. The idea of this microscopic interpretation of heat is shown in Fig. 7.1a. taken from the lecture notes of Alexia Auffèves [41]. The difference between the reversible property of work exchange and the stochastic effects of the heat bath on the system is symbolised by a die with the conversion factor between temperature and energy k_B. The presence of the Boltzmann factor also underlines that at zero temperature, the thermal reservoir can have no effect on the system, as there are no fluctuations.

Presenting classical thermodynamics in this way allows us to effectively introduce analogies with quantum systems. Elouard et al. propose a formal treatment of one way to connect quantum mechanics to stochastic thermodynamics and its interpretation in [40] from which parts of the following are taken. We can identify work with the action of an external perturbation on the quantum system, formalised by the time dependent Hamiltonian $\hat{H}_S(t)$ in Fig. 7.1b. and the unitary time evolution operator $\hat{U}(t) = \exp\left(-\frac{i}{\hbar}\int_0^t \hat{H}_S(\tau)\mathrm{d}\tau\right)$ derived from it. A typical example of such a Hamiltonian in the context of circuit QED could be

$$\hat{H}_S(t) \propto \epsilon(t)\hat{a}\hat{\sigma}^+ + \epsilon^*(t)\hat{a}^\dagger\hat{\sigma}^- \ , \tag{7.1}$$

which describes the exchange of excitations between a photon field ($\hat{a}$, $\hat{a}^\dagger$ operators) and a qubit ($\hat{\sigma}^-$, $\hat{\sigma}^+$ operators). It is visible from the hermiticity of $\hat{H}_S(t)$ that both the conversion of a photon into a qubit excitation and the opposite are possible, highlighting the reversibility of the process. This is true of any physical Hamiltonian as the Schrödinger equation is time symmetric. The ability to extract excitations from the qubit gives access a usable energy which can be transformed into mechanical motion (think radiation pressure for example), coming back to the original 19^{th} century definition of work. Irreversibility can arise in two ways. The first is dissipation in the case of an open system, but that can be interpreted as an inability to track the leakage of information into a bath through a number of unitary channels. In that case, there is no conceptual difference with the irreversibility of the classical case. The second is quantum measurement. In the textbook case of a Von Neumann projective measurement, if the state of the system is not in an eigenstate of the measurement operator, then the unknown state before the measurement is lost. Because the outcome of the measurement is random, it is symbolised by the die labeled $\hbar$ in Fig. 7.1b. A major feature of this random outcome is that it can be generated on pure states - states with zero entropy - and at zero temperature.

The realisation that quantum measurement can be interpreted thermodynamically has motivated a number of works trying to understand and harness the consequences thereof. Recent experimental work on quantum Maxwell's demons [213, 214, 215] and measurement driven engines [216, 217] are examples of this. Progress has also been made on the theory side in understanding the thermodynamic consequences of entanglement, coherence and control [218, 219, 220, 221], devising generalised fluctuation theorems [222, 223] and relating thermodynamic quantities to quantum observables for example [224, 225]. Numerous concepts are still debated, notably the concept of "quantum heat" defined in [40]. It is enlightening to consider a simple example to illustrate the concept. Consider a two level system with Hamiltonian $\hat{H} = \frac{\hbar\omega_Q}{2}\hat{\sigma}^z$. We can prepare the qubit in the state $|+X\rangle = \frac{1}{\sqrt{2}}(|g\rangle + |e\rangle)$ and subsequently projectively measure the $\hat{\sigma}^z$ component. The measurement has two outcomes of equal probability: "g" for which the state of the qubit immediately after the measurement is $|g\rangle$, and "e" for $|e\rangle$. Because the measurement operator and the Hamiltonian commute, the possible pointer-states of the measurement are eigenstates of the Hamiltonian with energies $-\frac{\hbar\omega_Q}{2}$ and $\frac{\hbar\omega_Q}{2}$ for "g" and "e" respectively. Yet the initial expectation value of the energy was $\left\langle \hat{H} \right\rangle_{|+X\rangle} = 0$. This change in the internal energy of the qubit, defined as the expectation value of $\hat{H}$ for a given qubit state, is called the "quantum heat" Q_q

$$Q_q = \left\langle \hat{H} \right\rangle_{|\text{before measurement}\rangle} - \left\langle \hat{H} \right\rangle_{|\text{after measurement}\rangle} . \tag{7.2}$$

Note that here, because the qubit's internal energy can change positively or negatively with equal magnitude and probability, and more generally because the measurement operator and $\hat{H}$ commute, over many iterations of the same experiment the average quantum heat $\langle Q_q \rangle$ is zero. This need not be true when the measurement operator and Hamiltonian do not commute. Take for example the qubit prepared in $|g\rangle$ and measured along $\hat{\sigma}^x$. In that case, $\langle Q_q \rangle = \frac{\hbar\omega_Q}{2}$ such that the act of measuring provides energy to

the system. This observation is at the basis of a theoretical proposal for a measurement based engine [226].

The two examples exposed in the previous paragraph are not so different. We obtain the same measurement result statistics measuring $|g\rangle$ along $\hat{\sigma}^x$ as measuring $|+X\rangle$ along $\hat{\sigma}^z$. What about the difference in $\langle Q_q \rangle$? At zero temperature, preparing state $|+X\rangle$ itself must cost energy. $E_{\text{preparation}} = \frac{\hbar\omega_Q}{2}$ on average to be exact. Thus, measuring the qubit along an axis rotated by an angle θ to the one defined by the energy of the system and accepting that the measurement transfers some average heat to the system appears equivalent to preparing the qubit in a state along the θ axis of the Bloch sphere at the cost of some unitary exchange of energy (work), and then having zero energy transfer on average between measurement apparatus and qubit.

It is always possible to decompose a measurement apparatus into two systems, an ancilla and the probe. The ancilla acts in a unitary manner on the system to be measured by applying work. By doing this, the system becomes entangled with the ancilla, such that the probe can project the state of the entangled ancilla/system ensemble without any energetic cost. In a sense, coming back to our qubit example, the change of the qubit state's energy after measurement in a basis not colinear to the energy operator, just reveals the unitary energy exchange done by some state preparation that has not been accounted for. Collapse of the wavefunction comes for free.

We can use this reasoning once more to explain the single shot energy differences $-\frac{\hbar\omega_Q}{2}$ and $\frac{\hbar\omega_Q}{2}$ for the measurement of $|+X\rangle$ in the $\hat{\sigma}^z$ basis. This is the idea of the experiment of this chapter.

7.2 PRINCIPLE OF THE EXPERIMENT

Compared to the previous section, although we consider a qubit interacting with a resonant drive, we do not limit ourselves to a $\frac{\pi}{2}$-pulse preparing $|+X\rangle$, but we are dealing with any arbitrary rotation of the qubit around the $\hat{\sigma}^y$ axis on the Bloch sphere. We assume the qubit starts in the ground state $|g\rangle$, and is driven by a coherent field $|\psi_{\text{in}}\rangle$. Initially, the qubit and the propagating drive mode a are in the separable state $|\psi_{\text{initial}}\rangle = |\psi_{\text{in}}\rangle \otimes |g\rangle$ (Fig. 7.2a.). Owing to the light-matter coupling between the drive mode and the qubit, they evolve into the entangled state [227, 228]

$$|\psi_{\text{final}}\rangle = \lambda_g |\psi_g\rangle \otimes |g\rangle + \lambda_e |\psi_e\rangle \otimes |e\rangle \tag{7.3}$$

where λ_g and λ_e are the probability amplitudes for each state in the superposition, and $|\psi_{g,e}\rangle$ designate the outgoing states of the drive mode after interaction with the qubit. Note that these parameters and states depend on $|\psi_{\text{in}}\rangle$ implicitly, and that $\langle\psi_g|\psi_e\rangle \neq 0$ in general. The number of excitations $\hat{a}^\dagger\hat{a} + |e\rangle\langle e|$ before and after the interaction must be conserved, which leads to the equality

$$\langle \hat{a}^\dagger\hat{a} \rangle_{|\psi_{\text{in}}\rangle} = |\lambda_g|^2 \langle \hat{a}^\dagger\hat{a} \rangle_{|\psi_g\rangle} + |\lambda_e|^2 \left[\langle \hat{a}^\dagger\hat{a} \rangle_{|\psi_e\rangle} + 1 \right]. \tag{7.4}$$

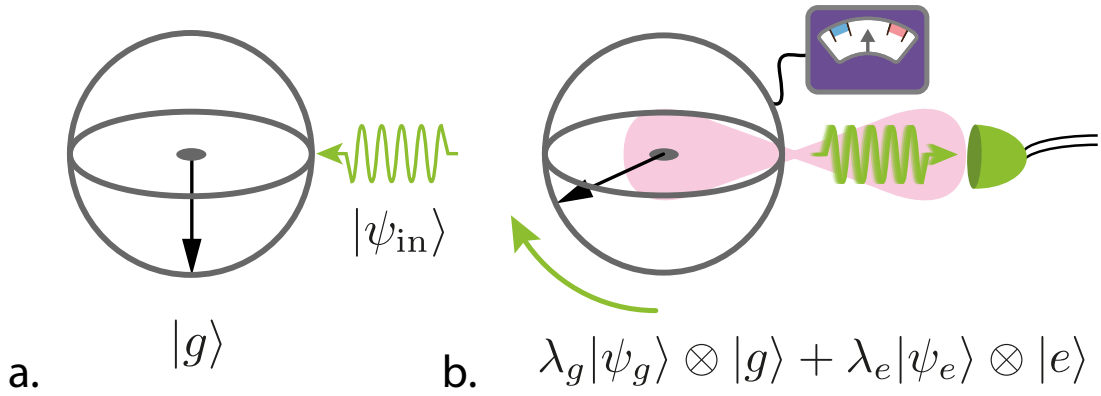

Figure 7.2: Principle of the experiment. a. A coherent wavepacket at the frequency ω_Q is sent to interact with a qubit initially prepared in $|g\rangle$. b. After the interaction, the qubit and wavepacket states are entangled. The outgoing wavepacket is recorded and the qubit is measured strongly along $\hat{\sigma}^z$. Tracing over the field degrees of freedom reveals a rotation of the qubit around the y-axis of the Bloch sphere, such that the qubit state has energy $\hbar\omega_Q|\lambda_e|^2$.

This can be rewritten as

$$\text{tr}\left[\hat{a}^\dagger\hat{a}\rho_F^{\text{initial}}\right] - \text{tr}\left[\hat{a}^\dagger\hat{a}\rho_F^{\text{final}}\right] = \text{tr}\left[|e\rangle\langle e|\,\rho_Q^{\text{final}}\right] - \text{tr}\left[|e\rangle\langle e|\,\rho_Q^{\text{initial}}\right] \ , \tag{7.5}$$

where ρ_F and ρ_Q are the density matrices of the propagating field and qubit respectively, calculated by taking the partial trace of the total density matrix ρ. This last equality (7.5) corresponds to the physical intuition that an energy $\hbar\omega_Q|\lambda_e|^2$ must have been transfered from the pulse to the qubit state during state preparation. It is then unsurprising that (7.4) holds for the case where $\langle\hat{a}^\dagger\hat{a}\rangle_{|\psi_g\rangle} - \langle\hat{a}^\dagger\hat{a}\rangle_{|\psi_e\rangle} = 1$, i.e. there can be a single photon difference in energy between the outgoing qubit pulse when the qubit is measured in $|e\rangle$ or $|g\rangle$ after the interaction. Much less intuitive is that this does not need to be the case. Indeed $\langle\hat{a}^\dagger\hat{a}\rangle_{|\psi_g\rangle} \neq \langle\hat{a}^\dagger\hat{a}\rangle_{|\psi_{\text{in}}\rangle}$ in general, which gives extra freedom to the energy expectation values of the outgoing fields. In our experiment we propose to measure these energy expectation values, by recording the outgoing pulses and post-selecting the results on the outcome of a strong qubit measurement. This is illustrated in Fig. 7.2b. By doing this, we hope to shed light on some of the energy transfer mechanisms between pulse and qubit during a quantum gate and conversely on the effect of the backaction of the qubit measurement on the outgoing drive mode.

As an important sidenote, one can legitimately ask the question as to the fidelity limitations of qubit gates due to the entanglement of (7.3). Indeed the the purity of the qubit density matrix reads

$$\text{tr}\left[(\rho_Q^{\text{final}})^2\right] = 1 - 2|\lambda_g\lambda_e|^2\left(1 - |\langle\psi_e|\psi_g\rangle|^2\right). \tag{7.6}$$

Luckily, the overlap between $|\psi_g\rangle$ and $|\psi_e\rangle$ tends to 1 as the drive amplitude increases [229, 230]. The lack of purity also determines how much information can be extracted about the drive mode when measuring the qubit state. Indeed, if the state is pure, this suggests that the system density matrix is separable, and measuring the

qubit gives no information about the drive mode. From a thermodynamics point of view, when the qubit is measured in its energy basis, the measurement backaction prepares the drive mode in states of different energies.

7.3 CALIBRATION OF THE EXPERIMENTAL SETUP

7.3.1 *Experimental setup*

The experiment described in the previous section can conveniently be realised in a circuit QED setup. We place the 3D Transmon qubit designed in Chapter 4 of frequency $\omega_Q = 2\pi \times 4.81\,\text{GHz}$ inside an aluminium cavity of frequency $\omega_R = 2\pi \times 7.69\,\text{GHz}$ at the base plate of a dilution refrigerator at 20 mK (see Fig. 7.3). The cavity has two ports, one weakly coupled through which we send the readout drive and a second more stongly coupled port through which we apply qubit pulses. The microwave pulses for the qubit and readout are generated in two independent channels in a Tabor WX1284C AWG at 100 MHz and 125 MHz respectively. These frequencies are upconverted by single sideband mixers (Polyphase) by mixing with continuous microwave tones generated by an Anapico APSIN12G for the qubit and a WindFreak SynthHD for the readout. The local oscillators are split before mixing to keep a static phase reference during downconversion.

Outgoing fields leave the cavity through the well coupled port and are then amplified at the 20 mK stage by a Travelling Wave Parametric Amplifier (TWPA) [178] provided by Lincoln Labs before further amplification by a High Electron Mobility Transistor amplifier (HEMT) made by Low Noise Factory at the 4 K stage. At room temperature, the output channel is split, and downconverted using the two continuous wave local oscillators. The signals are then digitized using an Alazar acquisition board. Numerical heterodyning (see Chapter 2) yields both quadratures of the fields at both the qubit and readout frequency. The TWPA itself needs to be driven by a continuous microwave tone for which we use an Anapico APSIN20G.

7.3.2 *Measuring fluorescence*

7.3.2.1 *Calibrating the Purcell rate*

Because our experiment requires knowing the number of photons in the outgoing drive mode, we start by measuring the fluorescence of the qubit into the transmission line. In the limit where the cavity input port coupling is much smaller than the output port coupling, the field exiting the cavity at the qubit frequency is given by [71]

$$\hat{a}_{\text{out}} = \hat{a}_{\text{in}} - \sqrt{\Gamma_a}\hat{\sigma}^-, \tag{7.7}$$

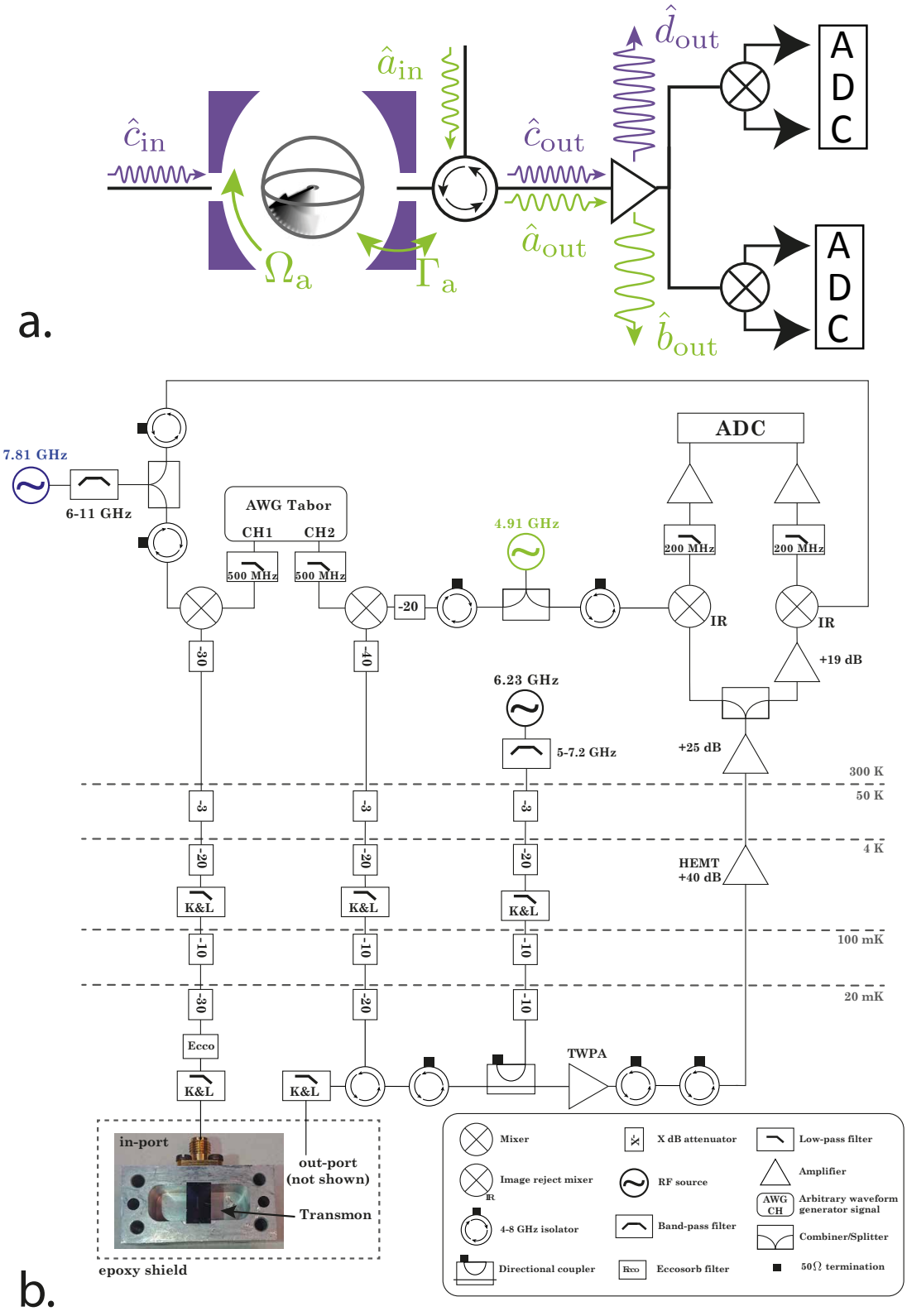

Figure 7.3: Experimental setup. a. Implementation of the protocol shown in Fig. 7.2 in a circuit QED setup. A Transmon qubit is placed inside a microwave cavity and is addressed through a well coupled output port on the right. The input port on the left serves for the readout in transmission. A circulator directs the outgoing field into the amplification and acquisition chain. b. Full cryogenic and room temperature measurement setup.

where Γ_a is the Purcell decay rate of the qubit into the transmission line. The expectation value $\langle \hat{a}_{\text{out}} \rangle (t)$ is directly related to the measured quadratures of the outgoing qubit field

$$\langle \hat{a}_{\text{out}} \rangle = \frac{\langle I_{\text{out}} \rangle + i \langle Q_{\text{out}} \rangle}{\sqrt{G}} \tag{7.8}$$

where I_{out} and Q_{out} are defined like in (2.63) and (2.64) (the expectation value are averages over many measurements) and G is the power gain of the measurement chain. Before directly measuring the time dependence of $\langle \hat{a}_{\text{out}} \rangle$ it is useful to calibrate Γ_a. To do this, we define the reflection coefficient

$$r = \frac{\langle \hat{a}_{\text{out}} \rangle}{\langle \hat{a}_{\text{in}} \rangle} = 1 - \frac{\sqrt{\Gamma_a} \langle \hat{\sigma}^- \rangle}{\langle \hat{a}_{\text{in}} \rangle} \ . \tag{7.9}$$

The expectation value of the lowering operator is given by the steady-state solution of the Bloch equations (see Appendix A)

$$\langle \hat{\sigma}^- \rangle = -z_{\text{th}} \frac{\Omega_a \Gamma_1 (\Gamma_2 - i\delta)}{2 \left[\Gamma_1 (\Gamma_2^2 + \delta^2) + \Gamma_2 \Omega_a^2 \right]} \ , \tag{7.10}$$

and we can relate the Rabi frequency Ω_a of the qubit to the amplitude of the input coherent field using

$$\langle \hat{a}_{\text{in}} \rangle = \alpha_{\text{in}} = \frac{\Omega_a}{2\sqrt{\Gamma_a}} \ . \tag{7.11}$$

The detuning between the drive frequency and the qubit frequency is $\delta = \omega_Q - \omega_d$, $1/\Gamma_1 = T_1 = 5.5 \pm 0.3\,\mu\text{s}$ and $\Gamma_2 = \Gamma_\phi + \frac{\Gamma_1}{2}$ with $1/\Gamma_\phi = T_\phi = 2.4\,\mu\text{s}$ are measured independently using the depolarisation and Ramsey sequences discussed ealier in this thesis. $z_{\text{th}} = -1 + 2p_e^{\text{th}}$ is obtained by a direct fit of the thermal population observed in the qubit readout histograms (see Sec. 7.4.3.1). Replacing the expressions for $\langle \hat{\sigma}^- \rangle$ and $\langle \hat{a}_{\text{in}} \rangle$ in (7.9) and taking into account the gain of the amplification chain we obtain the reflection coefficient measured by the experimentalist in a single tone qubit spectroscopy

$$r_{\text{exp}} = \sqrt{G} r = \sqrt{G} \left(1 + z_{\text{th}} \frac{\Gamma_a \Gamma_1 (\Gamma_2 - i\delta)}{\left[\Gamma_1 (\Gamma_2^2 + \delta^2) + \Gamma_2 \Omega_a^2 \right]} \right) \ . \tag{7.12}$$

The scaling factor $\sqrt{G}$ can be determined simply by measuring the reflection off the qubit away from the resonance frequency $|\delta| \to \infty$. Then, the only residual parameters are the Purcell rate Γ_a and the Rabi frequency Ω_a. We can adjust these two parameters following the model of (7.12) to match the measurement of r shown in Fig. 7.4. From this we obtain $\Gamma_a = 2\pi \times 20\,\text{kHz}$.

7.3.2.2 *Time dependent fluorescence field*

The results of Fig. 7.4 were obtained with the qubit in the steady-state of the Bloch equations. It is also possible to measure the dynamics of the expectation value of the outgoing mode amplitude

$$\langle \hat{a}_{\text{out}} \rangle (t) = \alpha_{\text{in}} - \sqrt{\Gamma_a} \langle \hat{\sigma}^- \rangle (t) \ . \tag{7.13}$$

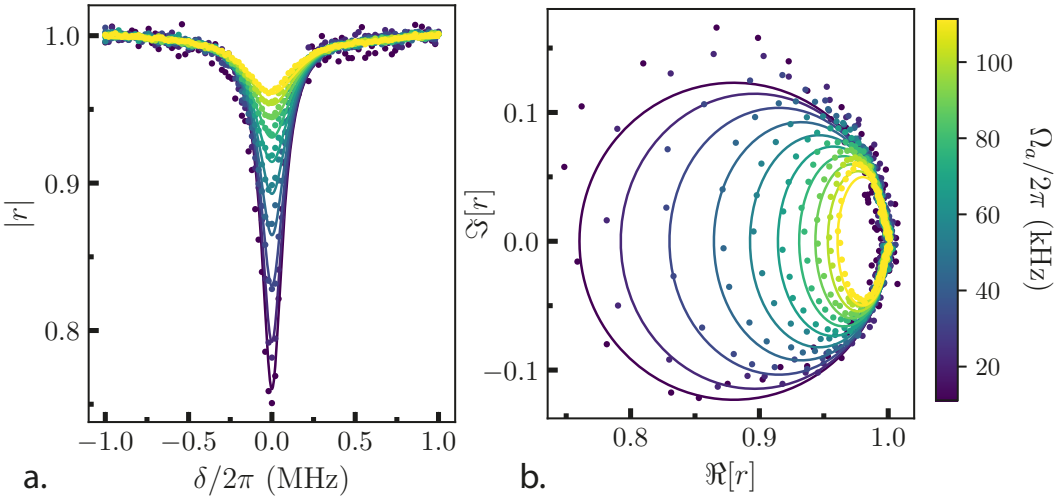

Figure 7.4: Measuring the qubit Purcell rate. a. Absolute value of the reflection off the qubit as a function of the detuning δ. A colorscale encodes the Rabi frequency of each experiment extracted from the model (7.12) which is adjusted to the complex values of r shown in panel b. The reflection coefficient is obtained by measuring the quadratures of a 10 µs drive at the qubit frequency ω_Q.

This was already done multiple times in our research group and the reader is encouraged to look at the theses of Nathanaël Cottet or Quentin Ficheux for details [71, 48]. We concentrate here on the dynamics of the expectation value of the outgoing photon rate $\overline{\dot{n}_\mathrm{m}}^\rho$ which will be used to calculate the total number of outgoing photons in the drive mode. Multiplying (7.7) with its adjoint yields [7, 20, 71]

$$\overline{\dot{n}_\mathrm{m}}^\rho = |\alpha_\mathrm{in}|^2 + \Gamma_a \frac{1 + \langle\hat{\sigma}^z\rangle_\rho}{2} - \frac{\Omega_a}{2}\langle\hat{\sigma}^x\rangle_\rho \ . \tag{7.14}$$

We have each time made explicit over which state ρ the expectation values are taken. This will become useful later, when the averages will be taken depending on the measured state of the qubit. The three terms on the right can be interpreted physically. The first is simply the photon flux due to the incoming field. Because the cavity port couplings are so asymmetric, almost all the incoming photon flux in the qubit drive is reflected instead of being transmitted. The second term is the spontaneous emission of the qubit into the transmission line. If $\rho = |g\rangle\langle g|$, then the second term is zero. The last term is the stimulated emission due to the Rabi cycling of the qubit under the drive. In Fig. 7.5 we show the oscillations of $\langle I_\mathrm{out}(t)^2\rangle + \langle Q_\mathrm{out}(t)^2\rangle$ as a function of time t as recorded on our acquisition card whilst applying a qubit drive with varying amplitude. Here the expectation values are taken over all 100000 iterations of the experiment and the amplitude of the drive is proportional to the Rabi frequency Ω_a extracted from the oscillations. This measurement is the temporal version of the Mollow triplet and was already measured in several experiments [231, 232, 233, 234]. As expected from (7.14), the amplitude and frequency of the oscillations increase with the amplitude of the drive due to the $\frac{\Omega_a}{2}\langle\hat{\sigma}^x\rangle_\rho$ term. Yet, as Ω_a goes to zero, we expect the power in the acquisition card to vanish equally. This is clearly not the case in Fig. 7.5, which is expected since the noise of the amplifier chain comprises a large part of the power

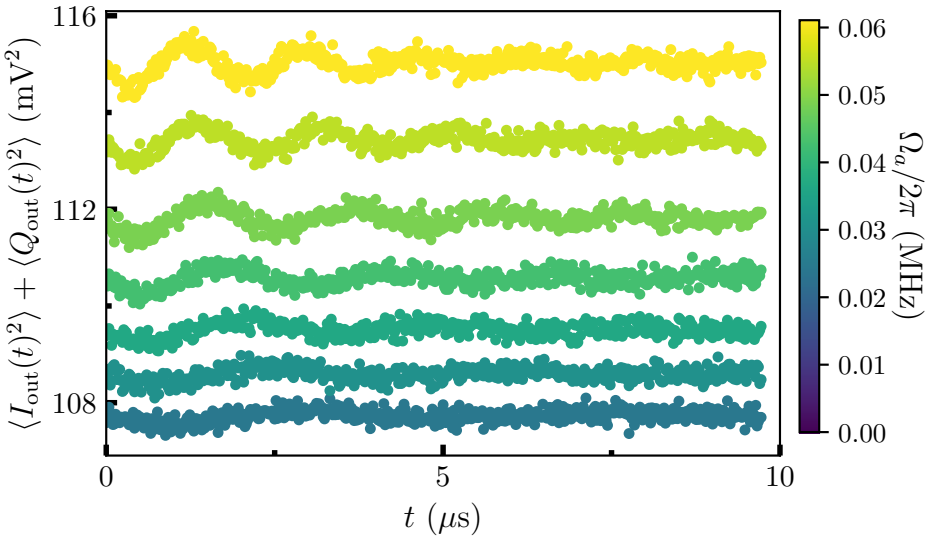

Figure 7.5: Average power measured by the acquisition card as a function of time t after the start of a drive at ω_Q. The Rabi frequencies are determined from an independent Rabi oscillation measurement (drive then readout of $\hat{\sigma}^z$, not shown).

coming from the experimental setup. The qualitative agreement is satisfying though and suggests a correctly functioning experimental setup. In the following we describe how we calibrate $\overline{\dot{n}_{\rm m}}^{\rho}$ from the power acquired by the ADC.

7.4 WEAK VALUES OF THE PHOTON NUMBER

7.4.1 *Calibrating the noise of the amplification chain*

While the amplitude measurements (see (7.8)) do not suffer from the added noise of the amplification chain because the amplitude of the noise averages to 0, this is not the case for the noise power. We can relate the field operator after amplification $\hat{b}_{\rm out}$ to the outgoing cavity field $\hat{a}_{\rm out}$ by [20]

$$\hat{b}_{\rm out} = \sqrt{G}\hat{a}_{\rm out} + \sqrt{G-1}\hat{N}^{\dagger}_{\rm vac} \,. \tag{7.15}$$

In general, $\left\langle \hat{N}^{\dagger}_{\rm vac}\hat{N}_{\rm vac}\right\rangle \neq 0$ which should be taken into account when measuring the outgoing power

$$\langle I^2_{\rm out}\rangle + \langle Q^2_{\rm out}\rangle = \left\langle \hat{b}^{\dagger}_{\rm out}\hat{b}_{\rm out}\right\rangle = G\overline{\dot{n}_{\rm m}} + G\left\langle \hat{N}_{\rm vac}\hat{N}^{\dagger}_{\rm vac}\right\rangle . \tag{7.16}$$

This added noise offsets the traces in Fig. 7.5 by about 100 mV^2. To remove this offset, we measure the reflection of a tone at ω_Q whilst simultaneously applying a continuous drive at the cavity frequency ω_R, AC-Stark shifting the qubit frequency away from ω_Q. The sequence used to do this is shown in the inset of Fig. 7.6. To prove that the Stark-shift pulse is indeed effective, we do a two tone spectroscopy of the qubit (as defined in Chapter 3), obtained while a continous drive is applied at ω_R (Fig. 7.6). As the strength of the cavity drive increases, the qubit shifts to lower frequencies. Thus,

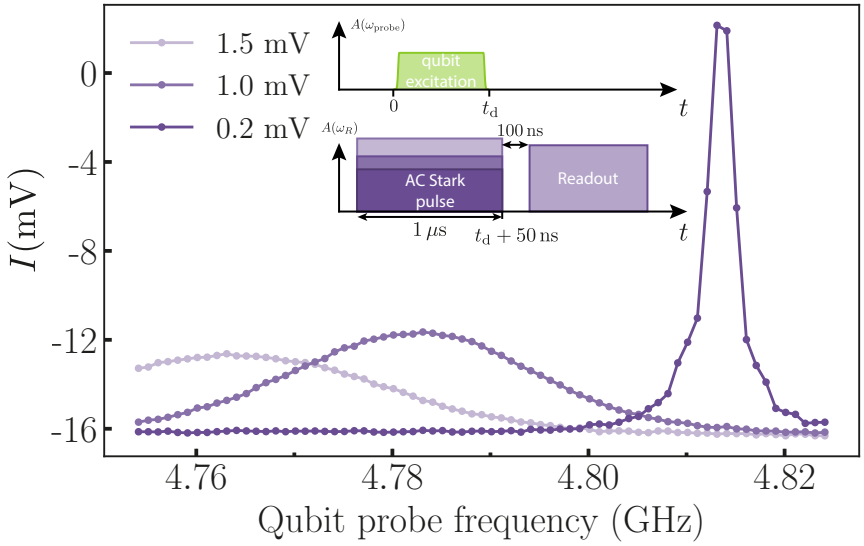

Figure 7.6: Calibration of the AC-Stark shift. Using the pulse sequence shown in the inset, we realize a qubit spectroscopy by sending a weak microwave pulse near the qubit frequency, followed by a readout pulse sent on the cavity whose measured transmission is used to infer the qubit excitation (quadrature shown on the y-axis). The experiment is repeated for varying cavity drive amplitudes (colors), showing that as the cavity population increases the qubit frequency decreases as expected for a negative AC-Stark shift. When the cavity drive is sufficiently strong, we observe the qubit detuned from its bare frequency by much more than its linewidth.

applying a drive at ω_Q while the cavity is populated acts as a reference for the amplifier chain where $\langle\hat{\sigma}^x\rangle = \frac{1+\langle\hat{\sigma}^z\rangle}{2} = 0$ because the tone at ω_Q is no longer resonant with the qubit transition. Thus the power acquired at the qubit frequency whilst the cavity drive is switched on is

$$\left\langle \hat{b}_{\rm out}^{\dagger \rm ref}\hat{b}_{\rm out}^{\rm ref}\right\rangle = G\left\langle \hat{a}_{\rm in}^{\dagger}\hat{a}_{\rm in}\right\rangle + (G-1)\left\langle \hat{N}_{\rm vac}\hat{N}_{\rm vac}^{\dagger}\right\rangle + \left\langle \hat{N}_c^{\dagger}\hat{N}_c\right\rangle \ . \tag{7.17}$$

We include a contribution $\left\langle \hat{N}_c^{\dagger}\hat{N}_c\right\rangle$ to account for cross-talk in our aquisition card when the cavity drive is on. We can access the added contribution to the noise due to cross-talk by acquiring the noise spectrum at ω_Q when the cavity drive is on but the qubit drive is switched off. The expectation value of the power entering the acquisition card is then given by

$$\left\langle \hat{b}_{\rm out}^{\dagger \rm c}\hat{b}_{\rm out}^{\rm c}\right\rangle = (G-1)\left\langle \hat{N}_{\rm vac}\hat{N}_{\rm vac}^{\dagger}\right\rangle + \left\langle \hat{N}_c^{\dagger}\hat{N}_c\right\rangle \ . \tag{7.18}$$

$(G-1)\left\langle \hat{N}_{\rm vac}\hat{N}_{\rm vac}^{\dagger}\right\rangle$ is determined by switching off all inputs into the measurement chain and measuring the power spectrum in our aquisition card at ω_Q again. Finally we can relate the outgoing photon flux to all of these measurable quantities through

$$\overline{\dot{n}_{\rm m}} = \frac{\Omega_a^2}{4\Gamma_a}\frac{\left\langle \hat{b}_{\rm out}^{\dagger}\hat{b}_{\rm out}\right\rangle - (G-1)\overline{\left\langle \hat{N}_{\rm vac}\hat{N}_{\rm vac}^{\dagger}\right\rangle}}{\overline{\left\langle \hat{b}_{\rm out}^{\dagger \rm ref}\hat{b}_{\rm out}^{\rm ref}\right\rangle} - \overline{\left\langle \hat{b}_{\rm out}^{\dagger \rm c}\hat{b}_{\rm out}^{\rm c}\right\rangle}} \ , \tag{7.19}$$

where the bar $\bar{\cdot}$ over the expectation values denotes the time average and we have used the fact that $\left\langle \hat{a}_{\rm in}^{\dagger}\hat{a}_{\rm in}\right\rangle = |\alpha_{\rm in}|^2 = \frac{\Omega_a^2}{4\Gamma_a}$.

7.4.2 *Post-selected outgoing photon flux - part 1*

The pulse sequence used to measure $\overline{\dot{n}_{\mathrm{m}}}$ as a function of time is shown in Fig. 7.7a. First, a pulse of amplitude $\alpha_{\mathrm{in}} > 0$ drives the qubit at frequency ω_Q for a duration $t_{\mathrm{d}} = 400\,\mathrm{ns}$. The reflected pulse is recorded by the ADC to yield the instantaneous power including noise $\left\langle \hat{b}^{\dagger}_{\mathrm{out}} \hat{b}_{\mathrm{out}} \right\rangle$. We chose Gaussian edged pulses Fig. 7.7a. following the functional

$$f(t) = \begin{cases} A \exp\left(-\frac{(t-2w)^2}{\frac{2w^2}{8\ln 2}} \right), & \text{for } t \leq 2w\ ; \\ A \exp\left(-\frac{(t-t_{\mathrm{d}}+2w)^2}{\frac{2w^2}{8\ln 2}} \right), & \text{for } t_{\mathrm{d}} - t \leq 2w\ ; \\ A, & \text{else}\ , \end{cases} \tag{7.20}$$

where $w = 10\,\mathrm{ns}$ and A is the pulse amplitude, to limit spectral leakage during the pulse rise time. The qubit is measured dispersively 20 ns later using a pulse of duration $t_{\mathrm{RO}} = 704\,\mathrm{ns}$ allowing us to post-select the qubit pulse records on the result of this measurement. After waiting 5 µs a second readout pulse is applied which is used as a protection against drifts of T_1 over time (more on this in Sec. 7.4.4). At the end of the sequence, we determine $\left\langle \hat{b}^{\dagger \mathrm{ref}}_{\mathrm{out}} \hat{b}^{\mathrm{ref}}_{\mathrm{out}} \right\rangle$ and $\left\langle \hat{b}^{\dagger \mathrm{c}}_{\mathrm{out}} \hat{b}^{\mathrm{c}}_{\mathrm{out}} \right\rangle$ using the part of the sequence during which the Stark shift pulse at the cavity frequency is switched on.

In Fig. 7.7b. we show the measured photon flux $\overline{\dot{n}_{\mathrm{m}}}^{\rho}$ as a function of time for three 400 ns Gaussian edged qubit pulses with different drive amplitudes (grey points). The rotation angles $\theta = \pi$, 1.8π and 2.6π of the Bloch vector after time t_{d} were calibrated including the effect of the Gaussian edged shape by measuring Rabi oscillations as a function of the drive amplitude in an independent measurement (not shown). Initially we aimed to measure the outgoing power as a function of the qubit state after measurement (see Fig. 7.2). To do this we average the instantaneous power arriving at the acquisition card conditioned on the measurement outcome of the first readout pulse of Fig. 7.7a. Using the same calibration as for the unpost-selected averages, we show $\overline{\dot{n}_{\mathrm{m}}}^{\rho}$ conditioned on the measurement outcome "g" (blue) and "e" (red) in Fig. 7.7b. The measurement outcome "g" ("e") is defined as a measured value $\bar{Z}_{\mathrm{out}}$ in the IQ-plane within a distance $1.5\sigma_{\mathrm{IQ}}$ of the centre Z_g (Z_e) of the Gaussian distribution corresponding to the pointer-states of $|g\rangle$ ($|e\rangle$). The circles within which the outcome is either "g" or "e" are shown in Fig. 7.8a. σ_{IQ} is the standard deviation of the Gaussian distribution of a single pointer state in the IQ-plane. To high fidelity, these measurement outcomes coincide with the qubit being projected to the pure states $|g\rangle$ and $|e\rangle$ for "g" and "e" respectively (see Sec. 7.4.3.2). We observe a clear deviation from the unconditional average power, thus revealing the correlation between qubit and drive mode.

It is possible to capture the dependence of the drive power on the qubit measurement outcome using the past quantum state formalism we already introduced in Chapter 6 [39, 235, 42]. A full description of the drive mode at each moment in time can be given by considering both the initial starting condition via the density matrix of the qubit $\rho(t)$ and the final measurement result through the effect matrix of the qubit $E(t)$ (see Appendix D). The density matrix obeys the standard Lindblad equation

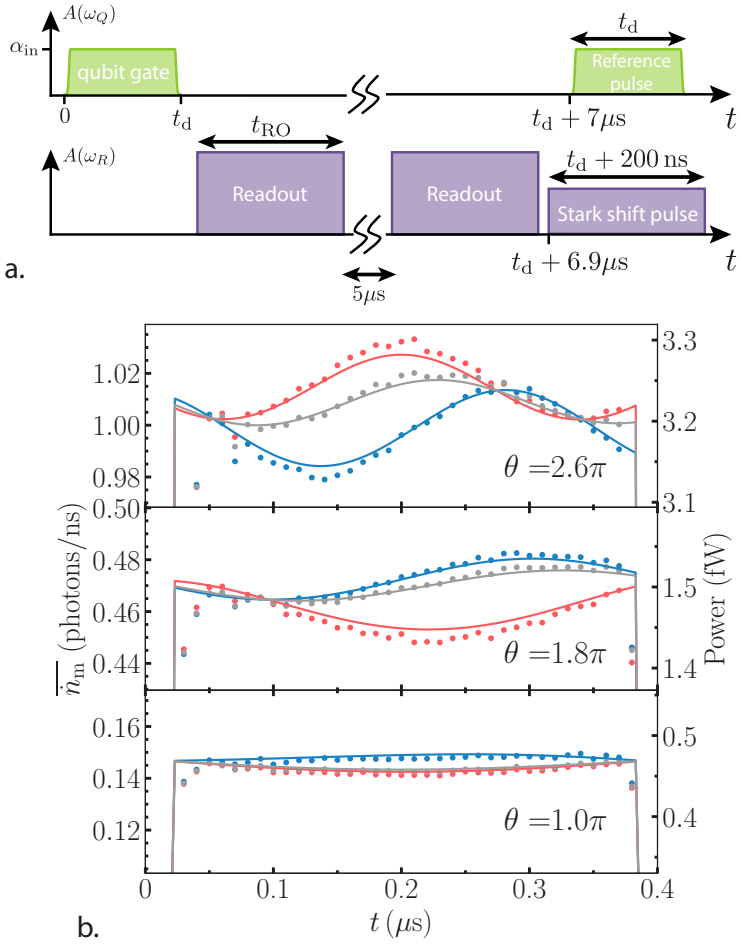

Figure 7.7: a. Complete measurement pulse sequence. The qubit gate and readout serve the basic objectives of the experiment, determining the backaction of the qubit measurement on the driving mode. The second readout allows an in situ measurement of T_1 to control any possible drifts. The reference pulse and Stark shift pulse are used to calibrate the noise of the experimental setup. b. Measured average outgoing photon flux $\overline{\dot{n}_{\rm m}}$ as a function of time t for three drive powers resulting in rotation angles $\theta = \pi$, 1.8π and 2.6π going from bottom to top (grey: no post-selection, blue/red: readout outcome "g"/"e"). Corresponding output powers are shown on the right axis. Lines: expected power from Eq. (7.21) using the past quantum state formalism and parameters detailed in the text. The time delay between the experimental and numerical data has been adjusted by hand.

while the effect matrix is constrained by its value at the final measurement time and is back propagated using the adjoint of the Lindblad equation. One can show that the post-selected expectation value of the outgoing photon rate is given by [236]

$$\overline{\dot{n}_{\mathrm{m}}}^{E,\rho} = |\alpha_{\mathrm{in}}|^2 - \Omega_a \mathrm{Re}_E\langle\hat{\sigma}^-\rangle_\rho + \Gamma_a \mathcal{I}(E,\rho) \ , \tag{7.21}$$

where $\mathcal{I}(E,\rho) = \frac{\mathrm{Tr}[E\hat{\sigma}^-\rho\hat{\sigma}^+]}{\mathrm{Tr}[E\rho]}$ can be understood as the weak value of a photo-detection rate and ${}_E\langle\hat{\sigma}^-\rangle_\rho = \frac{\mathrm{Tr}[E\hat{\sigma}^-\rho]}{\mathrm{Tr}[E\rho]}$ is the weak value of the $\hat{\sigma}^-$ operator. In our case, ρ is initialized at time $t = 0$ in a thermal state

$$\rho(0) = p_g^{\mathrm{th}} |g\rangle\langle g| + p_e^{\mathrm{th}} |e\rangle\langle e| \ . \tag{7.22}$$

The effect matrix E is defined at measurement time $t = t_{\mathrm{d}}$ conditioned on the post-selected readout outcome. For example, if the outcome was "g", then

$$E(t_{\mathrm{d}}) = \mathbf{P}(|g\rangle\,|\text{“g”})\,|g\rangle\langle g| + \mathbf{P}(|e\rangle\,|\text{“g”})\,|e\rangle\langle e| \ , \tag{7.23}$$

where $\mathbf{P}(|g\rangle\,|\text{“g”})$ is defined as the probability of indeed being in state $|g\rangle$ at the beginning of the readout pulse, given that the measurement record integrated over the readout time yields the outcome "g". If we are to reproduce the measurement results theoretically, we thus need to have access to the thermal populations and the probabilities $\mathbf{P}(|x\rangle\,|\text{“y”})$, $x, y \in \{g, e\}$.

7.4.3 *Analysing the qubit readout*

7.4.3.1 *Readout histograms*

A histogram of the recorded quadratures for 40000 readout pulses is shown in Fig. 7.8a. By using a gaussian mixture model (GMM) [190] on the distribution of points in the complex plane, we can identify the qubit state which most likely yielded each quadrature pair. The resulting segmentation of the recorded points in the complex plane is shown by the blue, red and grey shadings in the histogram overlay. The GMM algorithm directly gives the weights of the Gaussian probability mixture with the highest likelihood of reproducing the histograms obtained from the readout quadratures. We identify these weights as the qubit populations of each state immediately before the readout. In other words, the proportion of points within the blue shading of Fig. 7.8b. corresponds to our best guess for the population p_g of the qubit state $|g\rangle$. To make sure an increase in the readout amplitude does not affect the measured qubit populations, we monitor the qubit p_g, p_e and p_f as a function of the room temperature readout pulse amplitude in Fig. 7.8c. At low amplitude, the measurement is very imprecise, as the pointer states of the readout are not yet fully separated, explaining the change in population below an amplitude of 0.5Vpp. At higher amplitudes, the populations do not change with the readout amplitude, indicating that the amplitude of the readout pulse has no effect on the observed qubit populations. On this scale, the pulse amplitude used in the post-selection readout is 2Vpp and we saw no variation of the thermal population between 1.5Vpp and this value. For the rest of the work the thermal populations are set to $p_g^{\mathrm{th}} = 0.892 \pm 0.002$ and $p_e^{\mathrm{th}} = 0.088 \pm 0.002$ obtained from 30 measurements of p^{th} over

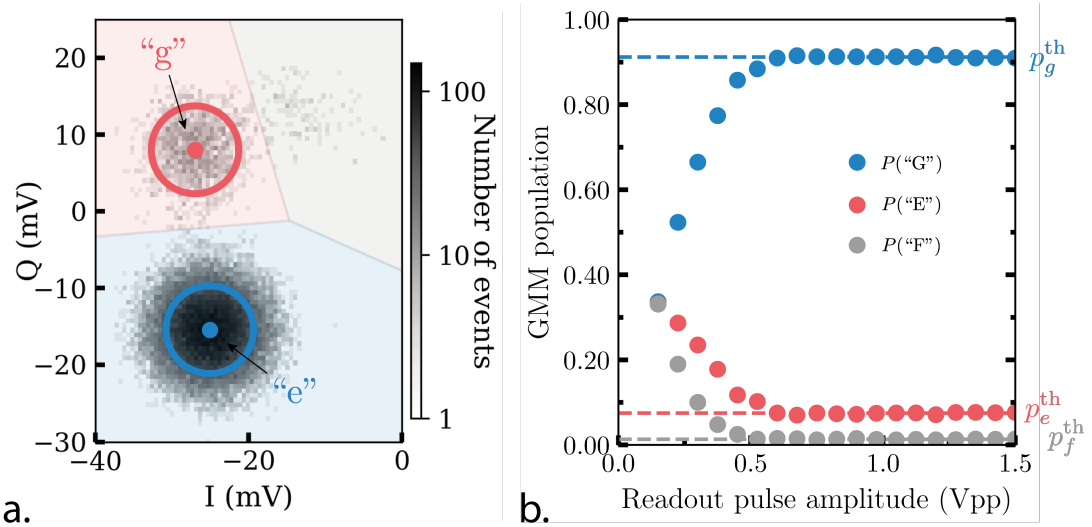

Figure 7.8: a. Histogram of the quadratures of 40000 demodulated square readout pulses. The histogram bin size is $0.31\,\mathrm{mV}^2$. Colored circles with radius $1.5\sigma_{\mathrm{IQ}}$ are shown centered on Z_g and Z_e which are materialised by blue and red points respectively. Blue, red and grey shading shows the parts of the IQ plane associated with the states $|g\rangle$, $|e\rangle$ and $|f\rangle$ by the GMM algorithm. c. Extracted populations of each qubit state using the GMM algorithm as a function of the readout pulse amplitude referred to room temperature. Horizontal dashed lines correspond to the average qubit populations above 0.8Vpp, which are equal to the qubit's thermal populations p_g^{th}, p_e^{th} and p_f^{th}.

30000 readout traces at 2Vpp. To initialise the density matrix of (7.22) we neglect the population of the $|f\rangle$ state setting

$$\rho(0) = (1 - p_e^{\mathrm{th}})\,|g\rangle\langle g| + p_e^{\mathrm{th}}\,|e\rangle\langle e| \quad .r \tag{7.24}$$

7.4.3.2 *Readout Fidelity*

The effect matrix is initialised with the information about the qubit state at time t_{d} that we gained thanks to the readout pulse. If the measurement outcome is "g" then, neglecting the effect of the $|f\rangle$ state, we initialise the effect matrix as $E(t_{\mathrm{d}}) = \mathbf{P}(|g\rangle\,|\text{"g"})\,|g\rangle\langle g| + (1 - \mathbf{P}(|g\rangle\,|\text{"g"}))\,|e\rangle\langle e|$, and similarly for "e". We thus need to first measure the readout fidelities $\mathbf{P}(|g\rangle\,|\text{"g"})$ and $\mathbf{P}(|e\rangle\,|\text{"e"})$.

For simplicity we will only detail the case $\mathbf{P}(|g\rangle\,|\text{"g"})$, but the method for $\mathbf{P}(|e\rangle\,|\text{"e"})$ is identical. To determine the probability $\mathbf{P}(|g\rangle\,|\text{"g"})$ we use Bayes' rule

$$\mathbf{P}(|g\rangle\,|\text{"g"}) = \frac{\mathbf{P}(\text{"g"}|\,|g\rangle)\mathbf{P}(|g\rangle)}{\mathbf{P}(\text{"g"})}\ , \tag{7.25}$$

where $\mathbf{P}(|g\rangle)$ is the probability of the qubit being in state $|g\rangle$ immediately before the readout and $\mathbf{P}(\text{"g"})$ is the probability of obtaining the measurement outcome "g". In practice, we set $\mathbf{P}(|g\rangle) = \mathbf{P}(\text{"G"})$, where $\mathbf{P}(\text{"G"})$ is the proportion of points in the IQ-plane within the distribution pertaining to the pointer-state of $|g\rangle$ as determined by the GMM (see Fig. 7.8a.). $\mathbf{P}(\text{"g"})$ on the other hand, is simply the proportion of

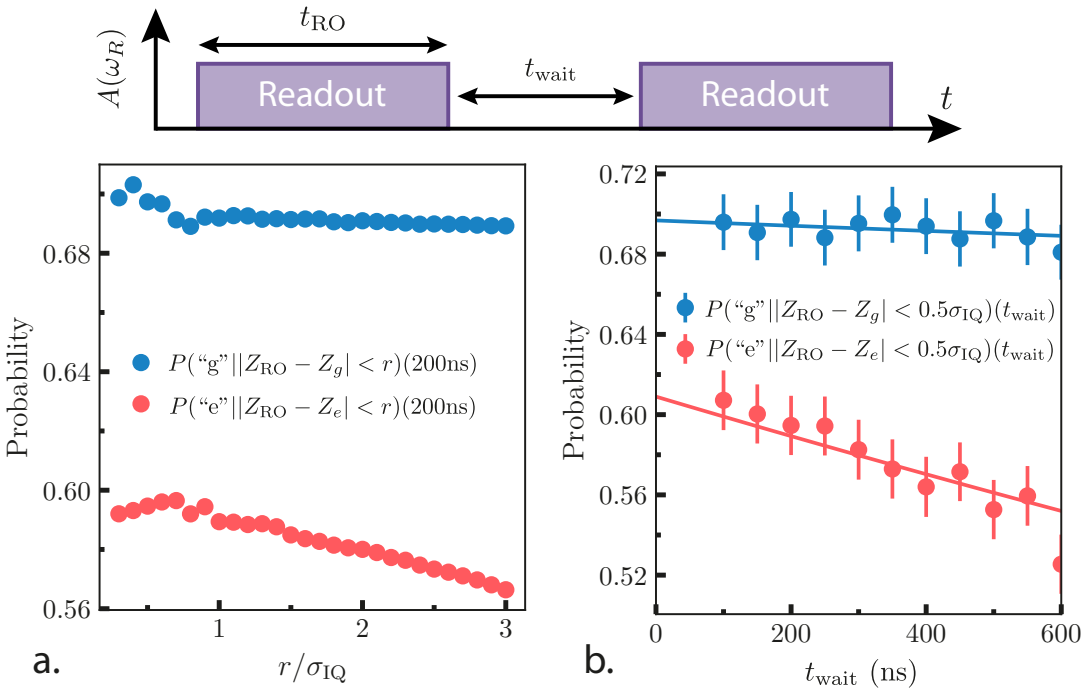

Figure 7.9: Measuring the readout fidelity a. $\mathbf{P}(\text{“x”}||Z_{\mathrm{RO}} - Z_g| < r)(200\,\mathrm{ns})$ as function of r measured in units of σ_{IQ} (x $\in$ {g, e}). b. Probability of obtaining measuremement outcome "x" in the second readout, given the knowledge that the qubit state was $|x\rangle$ immediately after the first readout (x $\in$ {g, e}. The solid lines are given by (7.29) with $T_1 = 5.5\mu\mathrm{s}$, $p_g^{\mathrm{th}} = 0.892$ and $p_e^{\mathrm{th}} = 0.088$, $\mathbf{P}(\text{“g”}||g\rangle) = 0.696$, $\mathbf{P}(\text{“e”}||e\rangle) = 0.605$ and $\mathbf{P}(\text{“g”}||e\rangle) = \mathbf{P}(\text{“e”}||g\rangle) = 0$.

measurements with outcome “g”. We calculate $\mathbf{P}(\text{“g”}||g\rangle)$ (the probability of obtaining outcome “g” knowing the qubit was in state $|g\rangle$ at the beginning of the readout) using the pulse sequence shown above the panels of Fig. 7.9 corresponding to two successive readout pulses separated by a wait time t_{wait}. Varying t_{wait} is necessary to separate potential non-QND effects of the readout from the decay of the qubit during the wait time. In Fig. 7.9a. we show the probability $\mathbf{P}(\text{“g”}||Z_{\mathrm{RO}} - Z_g| < r)(t_{\mathrm{wait}} = 200\,\mathrm{ns})$ of obtaining the outcome “g” in the second readout after waiting 200 ns between the two readouts, knowing that in the first readout, the measurement result Z_{RO} was within a circle of radius r around Z_g. As r decreases, the probability saturates

$$\lim_{r\to 0} \mathbf{P}(\text{“g”}||Z_{\mathrm{RO}} - Z_g| < r)(t_{\mathrm{wait}}) = \mathbf{P}(\text{“g”}||g\rangle)(t_{\mathrm{wait}}) \ , \tag{7.26}$$

such that at sufficiently small r, we can consider the qubit state to have remained in $|g\rangle$ throughout the entire readout pulse. This means that immediately after the readout pulse has ended, the qubit state is known to be $|g\rangle$. After the wait time between the readouts the qubit finds itself in the mixed state

$$\rho = p_g(t_{\mathrm{wait}})\,|g\rangle\langle g| + (1 - p_g(t_{\mathrm{wait}}))\,|e\rangle\langle e| \ , \tag{7.27}$$

where

$$p_g(t) = (1 - p_g^{\mathrm{th}})e^{-t/T_1} + p_g^{\mathrm{th}} \tag{7.28}$$

describes the decay of the qubit polarisation due to T_1. The probability of the outcome "g" for this mixed state is given by

$$\mathbf{P}(\text{“g”}|\,|g\rangle)(t_{\text{wait}}) = p_g(t_{\text{wait}})\mathbf{P}(\text{“g”}|\,|g\rangle) + (1-p_g(t_{\text{wait}}))\mathbf{P}(\text{“g”}|\,|e\rangle)\ . \tag{7.29}$$

In Fig. 7.9b. we show $\mathbf{P}(\text{“g”}||Z_{\text{RO}}-Z_g|<0.5\sigma_{\text{IQ}})(t_{\text{wait}}) \approx \mathbf{P}(\text{“g”}|\,|g\rangle)(t_{\text{wait}})$ as a function of t_{wait}. We choose $r=0.5\sigma_{\text{IQ}}$ because at around that level the value of $\mathbf{P}(\text{“g”}||Z_{\text{RO}}-Z_g|<r)(t_{\text{wait}})$ saturates. The variations at small r seen in Fig. 7.9a. are taken into account by the error bar on the scattered points of Fig. 7.9b. By adjusting the model of (7.29) with only two free parameters (T_1, p_g^{th} and p_e^{th} are measured independently) we can determine $\mathbf{P}(\text{“g”}|\,|g\rangle) = 0.696\pm0.002$ and $\mathbf{P}(\text{“g”}|\,|e\rangle) < 10^{-7}$. The latter value can be explained by the large $6\sigma_{\text{IQ}}$ separation between the two pointer states in the IQ-plane (see Fig. 7.8). From these values, and using (7.25) we obtain $\mathbf{P}(|g\rangle\,|\text{“g”}) \geq 97\%$. Using an identical method but for $|e\rangle$, we obtain $\mathbf{P}(\text{“e”}|\,|e\rangle) = 0.605\pm0.002$, $\mathbf{P}(\text{“e”}|\,|g\rangle) < 10^{-7}$ and $\mathbf{P}(|e\rangle\,|\text{“e”}) = 86.7\pm2.8\%$.

7.4.4 *Post-selected outgoing photon flux - part 2*

With the thermal populations and readout fidelities now determined, we can use (7.21) to reproduce the experimental results. As a reminder, the cases where the measurement outcome is "g" are given by using $E(t_{\text{d}}) = \mathbf{P}(|g\rangle\,|\text{“g”})\,|g\rangle\langle g| + (1-\mathbf{P}(|g\rangle\,|\text{“g”}))\,|e\rangle\langle e|$ and when the outcome is "e" by $E(t_{\text{d}}) = \mathbf{P}(|e\rangle\,|\text{“e”})\,|e\rangle\langle e| + (1-\mathbf{P}(|e\rangle\,|\text{“e”}))\,|g\rangle\langle g|$. This allows us to trace the solid lines in Fig. 7.7b. which reproduce the experimental results. This also works over a wide range of Rabi frequencies as shown in Fig. 7.10. Note that if there is no post-selection, the theory accounts for this by setting $E(t_{\text{d}}) = \frac{1}{2}\mathbb{1}$. We explain the discrepancies between the theory and experiment at the beginning of the 400 ns time trace by deformations of the Gaussian edged pulse in the experimental setup. Because of this, we allow ourselves a single free parameter and adjust the time delay between the experimental results and theoretical model by hand. This delay is determined empirically to be around 3 ns which is much shorter than any other characteristic times in the experiment. This small value suggests that the offset could be be partially due to an error in the calibration of the delay between the trigger of our acquision card and the arrival of the qubit pulse from the dilution refrigerator.

A last technical comment about the T_1 measurement embedded in the pulse sequence of Fig. 7.7a. is in order. We observed significant T_1 drifts during the time it took to acquire the results shown in Fig. 7.7b. and Fig. 7.10. To eliminate this effect, we measured the average T_1 over batches of 40000 iterations of the experiment by counting the number of events where the qubit started in $|g\rangle$ in the first readout and finished in $|e\rangle$ in the second. With this probability being given by $1-p_g(t=5\,\mu\text{s})$ (see (7.28)) and with all but T_1 known, this allows us to keep track of the average T_1 over the course of the experiment. Only batches with T_1 in the range $5.5\pm0.3\,\mu$s were kept.

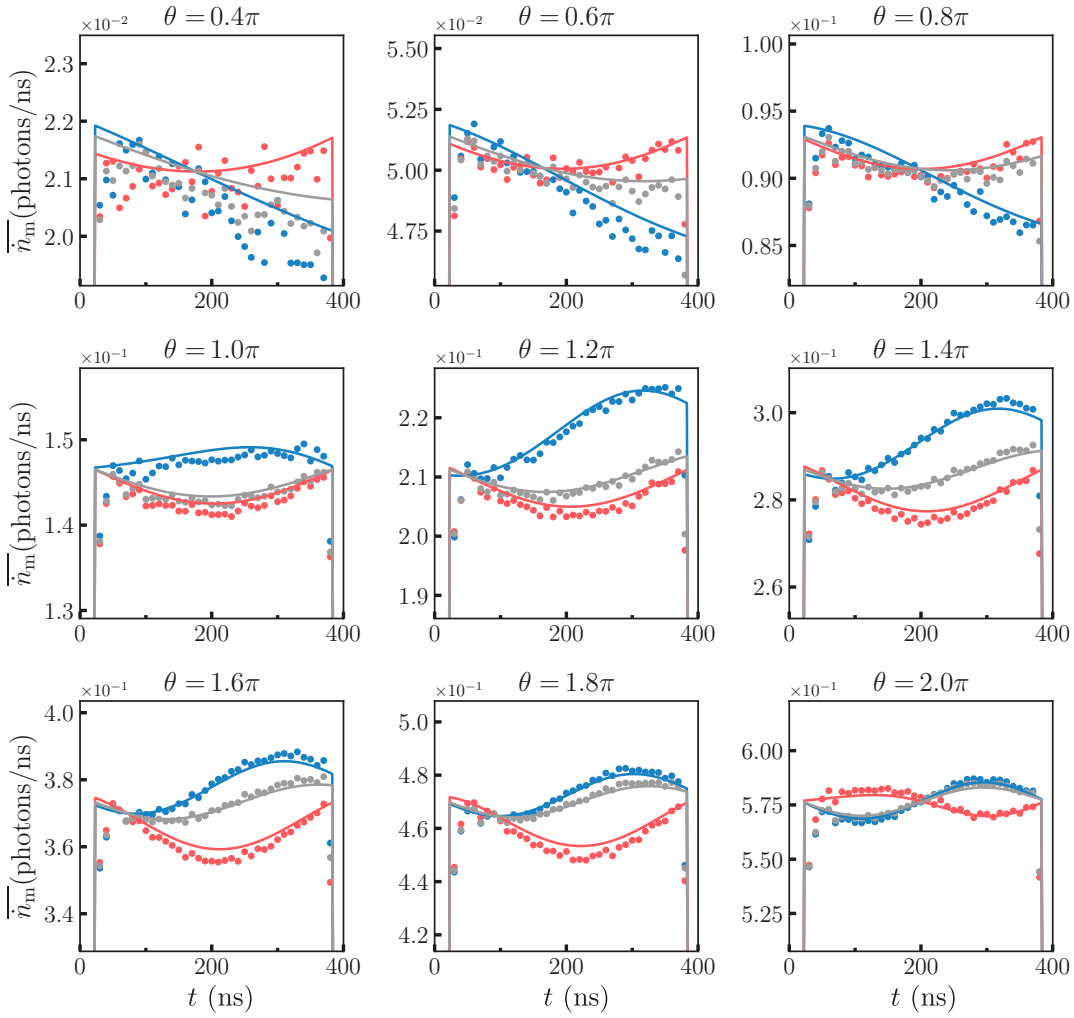

Figure 7.10: Post-selected fluorescence power for 400 ns pulses and varying Rabi frequencies Ω_a leading to a rotation angle θ after t_d. In the top left, without post-selection the qubit undergoes just over a $\pi/2$ pulse. In the bottom right, the qubit has approximately undergone a full 2π rotation before being measured. As before, grey is without post-selection, blue a measurement in "g" and red a measurement in "e"

7.4.5 *Post-selection of the total photon number*

Up until now we have considered the outgoing photon flux $\overline{\dot{n}_m}$, and although we saw that its average value depended on the result of the qubit measurement, our original goal was to detect changes in the total energy of the outgoing drive. We thus now look at the total number of photons contained in the pulse. It can be calculated as $\langle n_{out}\rangle = \int_0^{t_d} \overline{\dot{n}_m}^{E,\rho} dt$ from the measured $\overline{\dot{n}_m}$. In Fig. 7.11a, we show the square root of the measured total photon numbers $\sqrt{\langle n_{out}\rangle}$ as a function of the rotation angle in the Bloch sphere. The photon number scales as the square of the rotation angle as expected since the Rabi frequency scales as the drive amplitude. The measurement outcome-dependent change in $\langle n_{out}\rangle$ is negligible compared to the total number of photons in the pulse, as expected from the strong overlap of states $|\psi_g\rangle$ and $|\psi_e\rangle$ explained

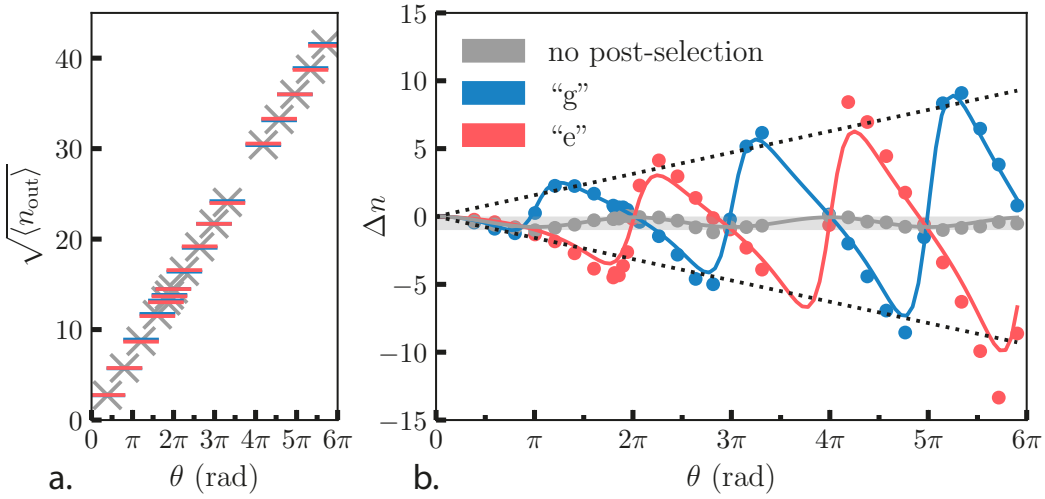

Figure 7.11: a. Square root of the measured total mean number of photons in the outgoing drive pulse as a function of the qubit rotation angle θ around $\hat{\sigma}^y$. Gray crosses correspond to no post-selection, lines to post-selection on the qubit being measured in $|g\rangle$ (blue) and $|e\rangle$ (red). For these photon numbers, the effect of post-selection is almost indistinguishable. b. Dots: measured difference Δn between the mean post-selected number of photons and the mean number of photons in the incoming drive pulse as a function of the qubit rotation angle. Colors indicate the kind of post-selection. Lines: time integrated equation (7.21). Dotted lines: guides to the eye with equation $y = \theta/2 = \sqrt{\Gamma_a t_{\rm d} n_{\rm in}}$. Shaded area: allowed range of exchanged energy without post-selection (between -1 and 0 photons).

in Sec. 7.2.

To reveal the difference between the energies of these states, we subtract the mean number of photons contained in the incoming pulse $n_{\rm in} = \int_0^{t_{\rm d}} |\alpha_{\rm in}(t)|^2 {\rm d}t$ (Fig. 7.11b). Without post-selection, the difference $\Delta n = \langle n_{\rm out}\rangle - n_{\rm in}$ oscillates between -1 and 0, as expected from the principle of energy conservation: when the qubit is excited, it extracts a photon from the pulse and when it is in the ground state the pulse energy stays unchanged. With post-selection, $\Delta n_{g,e}$ can exceed the non post-selected average value (blue and red dots out of shaded area in Fig. 7.11b), which is typical behavior for weak values [237]. The dependence of $\Delta n_{g,e}$ with the qubit rotation angle is also typical of the dependence of a weak value with its post-selection parameter as sharp slopes can be observed compared to the non post-selected case. Interestingly, one can observe that the post-selected photon number Δn_g oscillates in counter-phase with Δn_e. This reveals the two contributions to the measurement backaction exerted on the drive pulse by the qubit measurement. First, the information acquired on the qubit state distorts the probability of finding a given photon number in the drive pulse, hence producing the oscillations. Second, the qubit measurement is a destructive operation from the point of view of the drive pulse and only if the qubit is found in $|e\rangle$, it implies that the drive pulse now has one less photon.

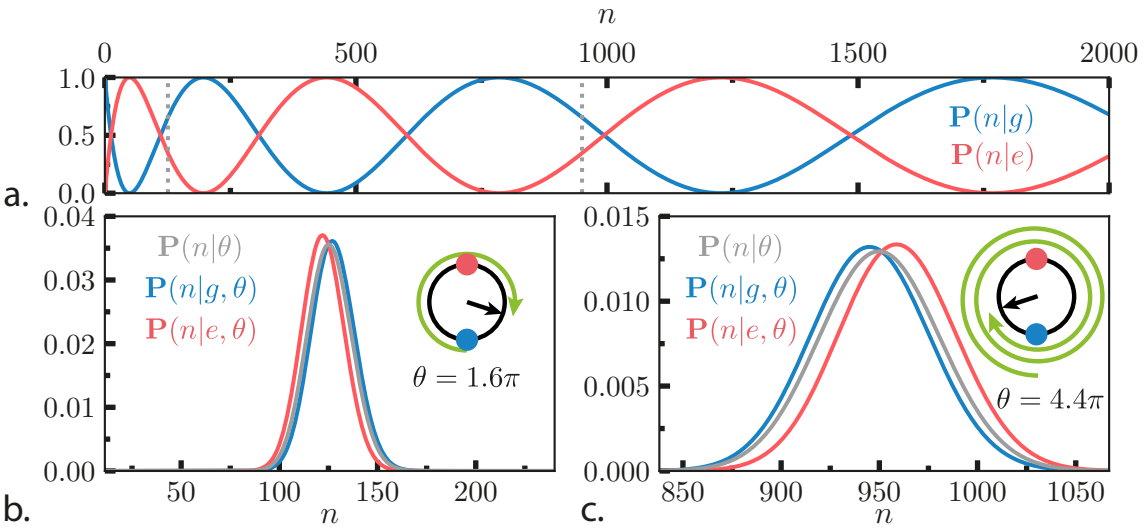

Figure 7.12: Probabilities that the drive pulse contains n photons. a. Predicted probability that the drive contains n photons conditioned on the qubit being measured in $|g\rangle$ (blue) or in $|e\rangle$ (red). Vertical grey dotted lines correspond to the Rabi rotations featured in the panels below. b & c. Probability that the drive pulse contains n photons knowing that it was prepared in a coherent state leading to a Rabi rotation of $\theta = 1.6\pi$ (b) or $\theta = 4.4\pi$ (c). Colors encode the conditional outcome of the qubit measurement: no post-selection (grey), $|g\rangle$ (blue) and $|e\rangle$ (red). Bloch representation of the qubit state after the drive pulse has left it. A green arrow represents the Rabi rotation around σ_y endured by the driven qubit. Blue and red dots indicate the $|g\rangle$ and $|e\rangle$ states.

7.5 BACKACTION OF THE QUBIT MEASUREMENT ON THE DRIVE FIELD

To better understand the origin of the oscillations in the photon number difference $\Delta n_{g,e}$, we propose a simple but enlightening model, where the drive pulse is a harmonic oscillator that is coupled to the qubit for a time t_d with a rate Γ_a. Let us assume that we measure the photon number in the drive pulse with a photon number-resolved counter and that the qubit starts in the ground state. In Fig. 7.12a, we plot the conditional probability that the incoming drive has a given number of photons n when the qubit is measured in $|g\rangle$ ($|e\rangle$) given by $\mathbf{P}(n|g) = \cos^2(\sqrt{n\Gamma_a t_\mathrm{d}})$ ($\mathbf{P}(n|e) = \sin^2(\sqrt{n\Gamma_a t_\mathrm{d}})$). This simple observation allows us to get further insight into the thermodynamic properties of the measurement backaction. In the model, for a rotation angle θ, the incoming drive pulse is in a coherent state $|\sqrt{n_\mathrm{in}}\rangle = |\theta/\sqrt{4\Gamma_a t_\mathrm{d}}\rangle$, which corresponds to a Poisson distribution of photon numbers $\mathbf{P}(n|\theta)$ with mean n_in (grey in Fig. 7.12b. & c.). The information provided by the measurement of the qubit state thus leads to new distributions, which are the products $\mathbf{P}(n|g,\theta) \propto \cos^2(\sqrt{n\Gamma_a t_\mathrm{d}})\mathbf{P}(n|\theta)$ and $\mathbf{P}(n|e,\theta) \propto \sin^2(\sqrt{n\Gamma_a t_\mathrm{d}})\mathbf{P}(n|\theta)$ (blue and red in Fig. 7.12b. & c.). The oscillations now become clear. Depending on the rotation angle, the outcome of the qubit measurement indicates that the qubit is either ahead of its average evolution (more photons than expected in the drive), or behind (less photons). In Fig. 7.12b., one can see that for $\theta = 1.6\pi$, finding the qubit in $|g\rangle$ indicates that it is ahead and thus offsets the probability distribution $\mathbf{P}(n|g,\theta)$ towards

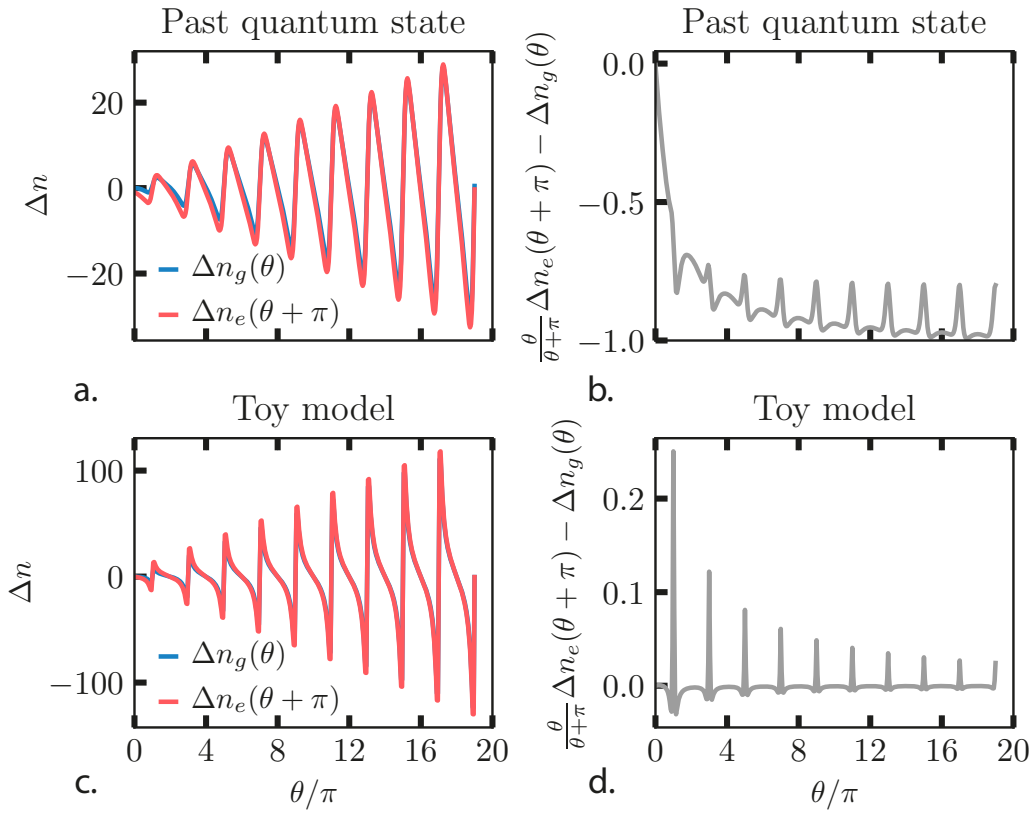

Figure 7.13: Identifying the sources of backaction. a. Comparison of the photon number differences $\Delta n_{g,e}$ for post-selection in "g" and "e" according to the predictions of (7.21) for our experiment. Δn_e is offset by π to highlight the similarity between the two cases up to a half period. b. Difference between the phase shifted and rescaled Δn_e and Δn_g. For large θ, and up to a half qubit rotation, Δn_e and Δn_g tend to differ by a single excitation. c. & d. Same as a. & b. but for the toy model presented above. Note that the difference $\frac{\theta}{\theta+\pi}\Delta n_e(\theta+\pi) - \Delta n_g(\theta)$ tends to 0 for our model.

larger photon numbers. For other angles, such as $\theta = 4.4\pi$ (Fig. 7.12c.), the same outcome reveals a qubit behind, which offsets $\mathbf{P}(n|g,\theta)$ towards smaller photon numbers. With this argument, one understands why at each half turn in the rotation angle, the situation between $|g\rangle$ and $|e\rangle$ outcomes is reversed in Fig. 7.11b. Additionally, owing to the increasing standard deviation of the Poisson distribution with the amplitude $\sqrt{n_{\text{in}}}$, the backaction on Δn increases linearly with θ (dotted lines in Fig. 7.11b).

Up to now, this model only completed the first part of the backaction: the distortion of the photon number distribution owing to the information acquired by the qubit measurement. In order to predict the measured distribution instead, one needs to take into account the fact that the qubit consumed a photon if it is measured in $|e\rangle$ and not if it is found in $|g\rangle$. To highlight this effect, we compare the phase shifted photon number differences $\Delta n_g(\theta)$ and $\Delta n_e(\theta+\pi)$ calculated both using (7.21) and our model in Fig. 7.13. For the information backaction, there is an exchange symmetry between $|g\rangle$ and $|e\rangle$ with respect to π rotations around the Bloch sphere. Thus the differences between

$\Delta n_g(\theta)$ and $\Delta n_e(\theta+\pi)$ are thus small in both models (see Fig. 7.13a. & c.). They do not overlap entirely though, because an extra π rotation requires extra photons in the field. Knowing phenomenologically that the backaction scales as $\sqrt{n_{\text{in}}} \propto \theta$, it is thus judicious to compare $\Delta n_g(\theta)$ with $\Delta n_e(\theta+\pi)$ rescaled by a factor $\frac{\theta}{\theta+\pi}$ to take the additional rotation into account. The differences $\frac{\theta}{\theta+\pi}\Delta n_e(\theta+\pi) - \Delta n_g(\theta)$ for both models are shown in Fig. 7.13b. & d. While for large θ the difference tends to go to 0 for our toy model, the limit appears to be -1 for the complete theory. This corresponds to the single photon absorbed by the qubit from the field when it is measured in $|e\rangle$ which we have not accounted for. Critically, this allows us to separate both contributions to the measurement backaction: the information update and the energy update. By measuring the qubit in either $|g\rangle$ or $|e\rangle$, we bias the probability of having a certain number of photons in the field and then subtract a single photon if the qubit was measured in $|e\rangle$.

As a further illustration that this is a useful way of thinking, we can come back to a simpler situation of a single cavity coupled to a transmission line at a rate κ which is connected to a photodetector [229]. Assuming the state inside the cavity starts in the superpostion $|\psi_i\rangle = \frac{1}{\sqrt{2}}(|k\rangle + |l\rangle)$, where $|k\rangle$ ($|l\rangle$) is the Fock state with k (l) photons inside the cavity. The probability of having n photons inside the cavity if the photodector clicks is given by Bayes' rule

$$\mathbf{P}(n|\text{“click”}) = \frac{\mathbf{P}(\text{“click”}|n)\mathbf{P}(n)}{\mathbf{P}(\text{“click”})} = \frac{n\kappa\tau\cdot(\frac{1}{2}\delta_{kn}+\frac{1}{2}\delta_{ln})}{\frac{k+l}{2}\kappa\tau}\ , \tag{7.30}$$

where τ is some time between measurements. Additionally, if a photon left the cavity, then we need to reduce the number of excitations inside by 1

$$\mathbf{P}(n|\text{“click” and } -1 \text{ photon}) = \mathbf{P}(n+1|\text{“click”}) = \frac{(n+1)\kappa\tau\cdot(\frac{1}{2}\delta_{k-1,n}+\frac{1}{2}\delta_{l-1,n})}{\frac{k+l}{2}\kappa\tau}\ . \tag{7.31}$$

This is exactly the result predicted by quantum mechanics

$$|\psi_{\text{after meas.}}\rangle = \frac{\hat{M}\,|\psi_i\rangle}{\sqrt{\langle\psi_i|\,\hat{M}^\dagger\hat{M}\,|\psi_i\rangle}} = \sqrt{\frac{k}{k+l}}\,|k-1\rangle + \sqrt{\frac{l}{k+l}}\,|l-1\rangle\ , \tag{7.32}$$

where $\hat{M} = \hat{a}$ is the Kraus operator describing the photon detection (see Appendix D). Note that the information update must be done before the energy update to obtain the correct results.

7.6 CONCLUSION

This chapter offers a new perspective on our interpretation of qubit gates. We started with a qubit and field in a separable state. After letting them interact, the qubit and field become entangled. We demonstrated this by measuring the photon flux in the outgoing drive conditioned on the outcome of a strong qubit measurement after the two finished interacting. We showed that on average a single excitation is transfered between the

drive and the qubit, but that the number of photons in the field could change by more than 1 if the qubit is measured to be in $|g\rangle$ or $|e\rangle$. This can be interpreted as the backaction of a weak measurement by the qubit on the coherent pulse. The backaction scales with the width of the photon number distribution in the incoming field and shows a certain symmetry when going through a full rotation of the qubit on the Bloch sphere. By comparing the experimentally observed backaction with a simplified model, we were able to separate the contributions of the information update and energy update on the outgoing field. The apparent ability for the field to gain or lose more than the single quantum of energy allowed by the qubit is explained by the fact that the system's starting state is not an eigenstate of the Hamiltonian, so its energy is undetermined from the beginning. Thus the energy change made evident by the projective measurement, is in fact due to a collapse of the global system wavefunction whose average energy is conserved, and not to the interaction with the measurement apparatus.

A

SOLVING THE BLOCH EQUATIONS

A.1 DYNAMICS OF THE DENSITY MATRIX

We consider a qubit undergoing Rabi oscillations. In the frame rotating at the qubit frequency ω_Q, the Hamiltonian of the system can be written $H = -\hbar\frac{\Omega}{2}\hat{\sigma}^y + \hbar\frac{\delta}{2}\hat{\sigma}^z$, where the detuning of the driving field at frequency ω_d from the qubit frequency is $\delta = \omega_Q - \omega_d$. Note that by writing the term $-\hbar\frac{\Omega}{2}\hat{\sigma}^y$ we have implicitly chosen a phase for the qubit drive. There is no loss of generality in doing this, as we can always redefine the axes of the Bloch sphere to be aligned with the phase of the drive. The Lindblad master equation defining the dynamics of the qubit density matrix ρ is given by

$$\partial_t\rho = -\frac{i}{\hbar}[\hat{H},\rho] + \frac{\Gamma_\phi}{2}D[\hat{\sigma}^z](\rho) + \Gamma_\downarrow D[\hat{\sigma}^-](\rho) + \Gamma_\uparrow D[\hat{\sigma}^+](\rho)\ . \tag{A.1}$$

Γ_ϕ is the pure dephasing rate and $\Gamma_{\uparrow,\downarrow}$ are the energy excitation ($\uparrow$) and de-excitation rates ($\downarrow$). We define the Lindblad superoperator in the standard way

$$D[L](\rho) = L\rho L^\dagger - \frac{1}{2}\rho L^\dagger L - \frac{1}{2}L^\dagger L\rho\ . \tag{A.2}$$

A.1.1 *Time dependence*

To simplify the discussion we consider the qubit drive to be at the frequency ω_Q in the following such that $\delta = 0$. Eq. (A.1) can be conveniently expressed in matrix form

$$\begin{pmatrix}\dot{\rho_{ee}} & \dot{\rho_{eg}}\\ \dot{\rho_{ge}} & \dot{\rho_{gg}}\end{pmatrix} = -\frac{\Omega}{2}\begin{pmatrix}-(\rho_{eg}+\rho_{ge}) & \rho_{ee}-\rho_{gg}\\ \rho_{ee}-\rho_{gg} & \rho_{eg}+\rho_{ge}\end{pmatrix} + \Gamma_\phi\begin{pmatrix}0 & -\rho_{eg}\\ -\rho_{ge} & 0\end{pmatrix} + \Gamma_\downarrow\begin{pmatrix}-\rho_{ee} & -\frac{1}{2}\rho_{eg}\\ -\frac{1}{2}\rho_{ge} & \rho_{ee}\end{pmatrix} + \Gamma_\uparrow\begin{pmatrix}\rho_{gg} & -\frac{1}{2}\rho_{eg}\\ -\frac{1}{2}\rho_{ge} & -\rho_{gg}\end{pmatrix}\ , \tag{A.3}$$

or, using $\Gamma_2 = \Gamma_\phi + \frac{\Gamma_1}{2}$ and in a form more tractable for subsequent calculations

$$\begin{pmatrix}\dot{\rho_{ee}}\\ \dot{\rho_{eg}}\\ \dot{\rho_{ge}}\\ \dot{\rho_{gg}}\end{pmatrix} = \begin{pmatrix}-\Gamma_\downarrow & \frac{\Omega}{2} & \frac{\Omega}{2} & \Gamma_\uparrow\\ -\frac{\Omega}{2} & -\Gamma_2 & 0 & \frac{\Omega}{2}\\ -\frac{\Omega}{2} & 0 & -\Gamma_2 & \frac{\Omega}{2}\\ \Gamma_\downarrow & -\frac{\Omega}{2} & -\frac{\Omega}{2} & -\Gamma_\uparrow\end{pmatrix}\begin{pmatrix}\rho_{ee}\\ \rho_{eg}\\ \rho_{ge}\\ \rho_{gg}\end{pmatrix}\ . \tag{A.4}$$

It is standard practice to rewrite this equation in the basis of the expectation values of the Pauli operators or, in other words, as the components of the Bloch vector

$$\langle\hat{\sigma}^x\rangle = \rho_{eg} + \rho_{ge}\ , \tag{A.5}$$

$$\langle\hat{\sigma}^y\rangle = i(\rho_{eg} - \rho_{ge})\ , \tag{A.6}$$

$$\langle\hat{\sigma}^z\rangle = \rho_{ee} - \rho_{gg}\ . \tag{A.7}$$

Remember that $\rho_{ee} + \rho_{gg} = 1$ so there is one degree of freedom less than there appears.

In this basis we can write

$$\frac{\mathrm{d}}{\mathrm{d}t}\begin{pmatrix}\langle\hat{\sigma}^x\rangle\\ \langle\hat{\sigma}^y\rangle\\ \langle\hat{\sigma}^z\rangle\end{pmatrix} = \begin{pmatrix}-\Gamma_2 & 0 & -\Omega\\ 0 & -\Gamma_2 & 0\\ \Omega & 0 & -\Gamma_1\end{pmatrix}\begin{pmatrix}\langle\hat{\sigma}^x\rangle\\ \langle\hat{\sigma}^y\rangle\\ \langle\hat{\sigma}^z\rangle\end{pmatrix} + \begin{pmatrix}0\\ 0\\ \Gamma_\uparrow - \Gamma_\downarrow\end{pmatrix} . \tag{A.8}$$

The solution to the homogeneous part of the equation is (using Mathematica)

$$\begin{pmatrix}\langle\hat{\sigma}^x\rangle(t)\\ \langle\hat{\sigma}^y\rangle(t)\\ \langle\hat{\sigma}^z\rangle(t)\end{pmatrix} = \begin{pmatrix}\frac{e^{-\frac{\Gamma_2+\Gamma_1}{2}t}}{2\Delta}\left[\Delta(e^{\frac{1}{2}\Delta t}+e^{-\frac{1}{2}\Delta t}) + (\Gamma_1-\Gamma_2)(e^{\frac{1}{2}\Delta t}-e^{-\frac{1}{2}\Delta t})\right] & 0 & -\frac{\Omega}{\Delta}e^{-\frac{\Gamma_2+\Gamma_1}{2}t}(e^{-\frac{1}{2}\Delta t}-e^{\frac{1}{2}\Delta t})\\ 0 & e^{-\Gamma_2 t} & 0\\ -\frac{\Omega}{\Delta}e^{-\frac{\Gamma_2+\Gamma_1}{2}t}(e^{\frac{1}{2}\Delta t}-e^{-\frac{1}{2}\Delta t}) & 0 & \frac{e^{-\frac{\Gamma_2+\Gamma_1}{2}t}}{2\Delta}\left[\Delta(e^{\frac{1}{2}\Delta t}+e^{-\frac{1}{2}\Delta t}) + (\Gamma_1-\Gamma_2)(e^{-\frac{1}{2}\Delta t}-e^{\frac{1}{2}\Delta t})\right]\end{pmatrix}\begin{pmatrix}x_c\\ y_c\\ z_c\end{pmatrix} , \tag{A.9}$$

where $\Delta^2 = (\Gamma_1-\Gamma_2)^2 - 4\Omega^2$ and x_c, y_c and z_c are some constants to be determined. When $|\Omega| \geq \frac{\Gamma_1-\Gamma_2}{2}$ then the solution includes under-damped oscillations

$$\begin{pmatrix}\langle\hat{\sigma}^x\rangle(t)\\ \langle\hat{\sigma}^y\rangle(t)\\ \langle\hat{\sigma}^z\rangle(t)\end{pmatrix} = \begin{pmatrix}\frac{e^{-\Gamma_R t}}{2\Delta}\left[2\Delta\cos(\Omega_R t) + 2i(\Gamma_1-\Gamma_2)\sin(\Omega_R t)\right] & 0 & -2i\frac{\Omega}{\Delta}e^{-\Gamma_R t}\sin(\Omega_R t)\\ 0 & e^{-\Gamma_2 t} & 0\\ 2i\frac{\Omega}{\Delta}e^{-\Gamma_R t}\sin(\Omega_R t) & 0 & \frac{e^{-\Gamma_R t}}{2\Delta}\left[2\Delta\cos(\Omega_R t) - 2i(\Gamma_1-\Gamma_2)\sin(\Omega_R t)\right]\end{pmatrix}\begin{pmatrix}x_c\\ y_c\\ z_c\end{pmatrix} , \tag{A.10}$$

with $\Gamma_R = \frac{\Gamma_2+\Gamma_1}{2}$ and $\Omega_R = \sqrt{\Omega^2 - \frac{(\Gamma_1-\Gamma_2)^2}{4}} = \frac{\Delta}{2i}$. Finally

$$\begin{pmatrix}\langle\hat{\sigma}^x\rangle(t)\\ \langle\hat{\sigma}^y\rangle(t)\\ \langle\hat{\sigma}^z\rangle(t)\end{pmatrix} = \begin{pmatrix}e^{-\Gamma_R t}\left[\cos(\Omega_R t) + \frac{(\Gamma_1-\Gamma_2)}{2\Omega_R}\sin(\Omega_R t)\right] & 0 & -\frac{\Omega}{\Omega_R}e^{-\Gamma_R t}\sin(\Omega_R t)\\ 0 & e^{-\Gamma_2 t} & 0\\ \frac{\Omega}{\Omega_R}e^{-\Gamma_R t}\sin(\Omega_R t) & 0 & e^{-\Gamma_R t}\left[\cos(\Omega_R t) - \frac{(\Gamma_1-\Gamma_2)}{2\Omega_R}\sin(\Omega_R t)\right]\end{pmatrix}\begin{pmatrix}x_c\\ y_c\\ z_c\end{pmatrix} , \tag{A.11}$$

The particular solution is obtained by setting the time derivative to 0

$$\begin{pmatrix}\langle\hat{\sigma}^x\rangle^p\\ \langle\hat{\sigma}^y\rangle^p\\ \langle\hat{\sigma}^z\rangle^p\end{pmatrix} = -\begin{pmatrix}-\Gamma_2 & 0 & -\Omega\\ 0 & -\Gamma_2 & 0\\ \Omega & 0 & -\Gamma_1\end{pmatrix}^{-1}\begin{pmatrix}0\\ 0\\ \Gamma_\uparrow - \Gamma_\downarrow\end{pmatrix} \tag{A.12}$$

$$= -\frac{1}{\Gamma_1\Gamma_2+\Omega^2}\begin{pmatrix}-\Gamma_1 & 0 & \Omega\\ 0 & -\frac{\Gamma_1\Gamma_2+\Omega^2}{\Gamma_2} & 0\\ -\Omega & 0 & -\Gamma_2\end{pmatrix}\begin{pmatrix}0\\ 0\\ \Gamma_\uparrow - \Gamma_\downarrow\end{pmatrix} \tag{A.13}$$

$$= \frac{1}{\Gamma_1\Gamma_2+\Omega^2}\begin{pmatrix}\Omega(\Gamma_\downarrow - \Gamma_\uparrow)\\ 0\\ \Gamma_2(\Gamma_\uparrow - \Gamma_\downarrow)\end{pmatrix} , \tag{A.14}$$

In the following we note the particular solutions, the solution to the Bloch equations in the steady-state as $(x_\infty, y_\infty, z_\infty)^T$. We can write out the solutions without taking into account the boundary conditions as

$$\langle\hat{\sigma}^x\rangle(t) = x_\infty + e^{-\Gamma_R t}\left[\cos(\Omega_R t)x_c + \frac{\sin(\Omega_R t)}{\Omega_R}\left(\frac{\Gamma_1-\Gamma_2}{2}x_c - \Omega z_c\right)\right] , \quad (A.15)$$

$$\langle\hat{\sigma}^y\rangle(t) = e^{-\Gamma_2 t}y_c , \quad (A.16)$$

$$\langle\hat{\sigma}^z\rangle(t) = z_\infty + e^{-\Gamma_R t}\left[\cos(\Omega_R t)z_c - \frac{\sin(\Omega_R t)}{\Omega_R}\left(\frac{\Gamma_1-\Gamma_2}{2}z_c - \Omega x_c\right)\right] . \quad (A.17)$$

If we know the conditions x_0, y_0 and z_0 at time 0, we can replace the constants

$$\langle\hat{\sigma}^x\rangle(t) = x_\infty + e^{-\Gamma_R t}[\cos(\Omega_R t)(x_0 - x_\infty) + \frac{\sin(\Omega_R t)}{\Omega_R}\left(\frac{\Gamma_1-\Gamma_2}{2}(x_0 - x_\infty) - \Omega(z_0 - z_\infty)\right)\Big] , \quad (A.18)$$

$$\langle\hat{\sigma}^y\rangle(t) = e^{-\Gamma_2 t}y_0 , \quad (A.19)$$

$$\langle\hat{\sigma}^z\rangle(t) = z_\infty + e^{-\Gamma_R t}[\cos(\Omega_R t)(z_0 - z_\infty) - \frac{\sin(\Omega_R t)}{\Omega_R}\left(\frac{\Gamma_1-\Gamma_2}{2}(z_0 - z_\infty) - \Omega(x_0 - x_\infty)\right)\Big] . \quad (A.20)$$

We can consider the case where qubit never has a component along the y-axis. In that case

$$\langle\hat{\sigma}^y\rangle = 0 \Leftrightarrow \rho_{eg} = \rho_{ge} , \quad (A.21)$$

$$\langle\hat{\sigma}^x\rangle = 2\rho_{eg} = 2\rho_{ge} , \quad (A.22)$$

$$\langle\hat{\sigma}^z\rangle = 2\rho_{ee} - 1 = 1 - 2\rho_{gg} . \quad (A.23)$$

This allows us to transform the solution of the Bloch equations into the solutions for the components of the density matrix

$$\rho_{ee} = \frac{1}{2}\Big\{1 + z_\infty + e^{-\Gamma_R t}[\cos(\Omega_R t)(z_0 - z_\infty) - \frac{\sin(\Omega_R t)}{\Omega_R}\left(\frac{\Gamma_1-\Gamma_2}{2}(z_0 - z_\infty) - \Omega(x_0 - x_\infty)\right)\Big]\Big\} \quad (A.24)$$

$$\rho_{eg} = \rho_{ge} = \frac{1}{2}\Big\{x_\infty + e^{-\Gamma_R t}[\cos(\Omega_R t)(x_0 - x_\infty) + \frac{\sin(\Omega_R t)}{\Omega_R}\left(\frac{\Gamma_1-\Gamma_2}{2}(x_0 - x_\infty) - \Omega(z_0 - z_\infty)\right)\Big]\Big\} \quad (A.25)$$

$$\rho_{gg} = \frac{1}{2}\Big\{1 - z_\infty - e^{-\Gamma_R t}[\cos(\Omega_R t)(z_0 - z_\infty) - \frac{\sin(\Omega_R t)}{\Omega_R}\left(\frac{\Gamma_1-\Gamma_2}{2}(z_0 - z_\infty) - \Omega(x_0 - x_\infty)\right)\Big]\Big\} \quad (A.26)$$

A.1.2 *Steady-State*

It's useful to study the steady-state solutions in more detail, in particular when $\delta \neq 0$. In that case

$$x_\infty = \lim_{t\to\infty} \langle \hat{\sigma}^x \rangle (t) = -z_{\text{th}} \frac{\Gamma_1 \Gamma_2 \Omega}{\Gamma_1(\Gamma_2^2 + \delta^2) + \Gamma_2 \Omega^2} , \tag{A.27}$$

$$y_\infty = \lim_{t\to\infty} \langle \hat{\sigma}^y \rangle (t) = -z_{\text{th}} \frac{\delta \Gamma_1 \Omega}{\Gamma_1(\Gamma_2^2 + \delta^2) + \Gamma_2 \Omega^2} , \tag{A.28}$$

$$z_\infty = \lim_{t\to\infty} \langle \hat{\sigma}^z \rangle (t) = z_{\text{th}} \frac{\Gamma_1(\Gamma_2^2 + \delta^2)}{\Gamma_1(\Gamma_2^2 + \delta^2) + \Gamma_2 \Omega^2} , \tag{A.29}$$

where z_{th} is the thermal population of the qubit $z_{\text{th}} = \frac{\Gamma_\uparrow - \Gamma_\downarrow}{\Gamma_1}$.

B

TWO CAPACITIVELY COUPLED FLUXONIUMS COUPLED TO CAVITY

A novelty of this thesis was the need for a precise knowledge of all parameters of the complex Hamiltonian

$$\hat{H} = \hat{H}_L + \hat{H}_H + \hat{H}_c + \hat{H}_{H\leftrightarrow L} + \hat{H}_{c\leftrightarrow L} + \hat{H}_{c\leftrightarrow H} \ , \tag{B.1}$$

with

$$\hat{H}_{\mathrm{H/L}} = 4E_C\hat{n}^2_{H/L} + \frac{1}{2}E_L^{(H/L)}\hat{\varphi}^2_{H/L} - E_J^{(H/L)}\cos\left(\hat{\varphi}_{H/L} - 2\pi\frac{\Phi_{\mathrm{ext},H/L}}{\Phi_0}\right) \tag{B.2}$$

$$\hat{H}_c = \hbar\omega_R\hat{a}_c^\dagger\hat{a}_c \ , \tag{B.3}$$

$$\hat{H}_{H\leftrightarrow L} = -\hbar g_{\mathrm{HL}}\hat{n}_L\hat{n}_H \ , \tag{B.4}$$

$$\hat{H}_{\mathrm{cav}\leftrightarrow H/L} = -\hbar g_c\hat{n}_{H/L}(\hat{a}_c^\dagger + \hat{a}_c) \ , \tag{B.5}$$

corresponding to two capacitively coupled Fluxoniums (indexed by H and L for low and high in reference to their frequencies ω_{01} at half flux) each coupled to the same linear resonator. The approach which was the most successful in our case is a generalisation of the technique mentioned in [97] with the addition of a state labeling technique inspired by [100].

B.1 DIAGONALISE LINEAR HAMILTONIAN

The first step involves the diagonalisation of the linear part of the Hamiltonian given explicitly by

$$\begin{aligned}\hat{H}_{\mathrm{lin}} = \ & \hbar\omega_R\hat{a}_c^\dagger\hat{a}_c + 4E_C\hat{n}_L^2 + \tfrac{1}{2}E_L^{(L)}\hat{\varphi}_L^2 + 4E_C\hat{n}_H^2 + \tfrac{1}{2}E_L^{(H)}\hat{\varphi}_L^2 \\ & -\hbar g_c\hat{n}_L(\hat{a}_c^\dagger + \hat{a}_c) - \hbar g_c\hat{n}_H(\hat{a}_c^\dagger + \hat{a}_c) - \hbar g_{\mathrm{HL}}\hat{n}_L\hat{n}_H \ .\end{aligned}$$

Because the terms pertaining to the two Fluxonium qubits are quadratic, the linear Hamiltonian can be rewritten

$$\begin{aligned}\hat{H}_{lin} = \ & \hbar\omega_R\hat{a}_c^\dagger\hat{a}_c + \hbar\omega_H\hat{a}_H^\dagger\hat{a}_H + \hbar\omega_L\hat{a}_L^\dagger\hat{a}_L \\ & -i\hbar g_c n^H_{\mathrm{ZPF}}(\hat{a}_c + \hat{a}_c^\dagger)(\hat{a}_H^\dagger - \hat{a}_H) - i\hbar g_c n^L_{\mathrm{ZPF}}(\hat{a}_c + \hat{a}_c^\dagger)(\hat{a}_L^\dagger - \hat{a}_L) \\ & +\hbar g_{\mathrm{HL}} n^L_{\mathrm{ZPF}} n^H_{\mathrm{ZPF}}(\hat{a}_H^\dagger - \hat{a}_H)(\hat{a}_L^\dagger - \hat{a}_L) \ ,\end{aligned}$$

where

$$\omega_{H/L} = \sqrt{8E_C E_L^{(H/L)}}$$

and we have defined the operators $\hat{a}_{H/L}$ and $\hat{a}^\dagger_{H/L}$ as in (3.40) and (3.41). Finding the operator transformation which makes this Hamiltonian diagonal involves the diagonalisation of the matrix M_H so that

$$\hat{H}_{\mathrm{lin}} = \frac{\hbar}{2}\hat{v}^\dagger M_H\hat{v} \ , \tag{B.6}$$

where $\hat{v}^\dagger$ is the row vector $(\hat{a}_c^\dagger\ \hat{a}_H^\dagger\ \hat{a}_L^\dagger\ \hat{a}_c\ \hat{a}_H\ \hat{a}_L)$[101]. M_H reads

$$\begin{pmatrix} \omega_R & ig_c n^H_{\text{ZPF}} & ig_c n^L_{\text{ZPF}} & 0 & -ig_c n^H_{\text{ZPF}} & -ig_c n^L_{\text{ZPF}} \\ -ig_c n^H_{\text{ZPF}} & \omega_H & -g_{\text{HL}} n^L_{\text{ZPF}} n^H_{\text{ZPF}} & -ig_c n^H_{\text{ZPF}} & 0 & g_{\text{HL}} n^L_{\text{ZPF}} n^H_{\text{ZPF}} \\ -ig_c n^L_{\text{ZPF}} & -g_{\text{HL}} n^L_{\text{ZPF}} n^H_{\text{ZPF}} & \omega_L & -ig_c n^L_{\text{ZPF}} & g_{\text{HL}} n^L_{\text{ZPF}} n^H_{\text{ZPF}} & 0 \\ 0 & ig_c n^H_{\text{ZPF}} & ig_c n^L_{\text{ZPF}} & \omega_R & -ig_c n^H_{\text{ZPF}} & -ig_c n^L_{\text{ZPF}} \\ ig_c n^H_{\text{ZPF}} & 0 & g_{\text{HL}} n^L_{\text{ZPF}} n^H_{\text{ZPF}} & ig_c n^H_{\text{ZPF}} & \omega_H & -g_{\text{HL}} n^L_{\text{ZPF}} n^H_{\text{ZPF}} \\ ig_c n^L_{\text{ZPF}} & g_{\text{HL}} n^L_{\text{ZPF}} n^H_{\text{ZPF}} & 0 & ig_c n^L_{\text{ZPF}} & -g_{\text{HL}} n^L_{\text{ZPF}} n^H_{\text{ZPF}} & \omega_L \end{pmatrix} . \tag{B.7}$$

This is possible algebraically, but involves finding the roots of 3rd order polynomials and the equations are intractable. Numerical diagonalisation of M_H yields a set of eigenoperators $\tilde{a}_X$ labelled by the set $S = \{c, H, L\}$ which are a linear combination of the original operators and their conjugates[1]. Conversely

$$\hat{a}_X = \sum_{Y \in S} \lambda_{XY} \tilde{a}_Y^\dagger + \mu_{XY}^* \tilde{a}_Y \ , \ \lambda_{XY}, \mu_{XY} \in \mathbb{C} \ . \tag{B.8}$$

In this basis the full Hamiltonian is written

$$\begin{aligned} \tilde{H} = \quad & \hbar\tilde{\omega}_R \tilde{a}_c^\dagger \tilde{a}_c + \hbar\tilde{\omega}_H \tilde{a}_H^\dagger \tilde{a}_H + \hbar\tilde{\omega}_L \tilde{a}_L^\dagger \tilde{a}_L \\ & -E_J^{(L)} \cos\left(\hat{\varphi}_L - 2\pi \tfrac{\Phi_{ext}^{(L)}}{\Phi_0}\right) - E_J^{(H)} \cos\left(\hat{\varphi}_H - 2\pi \tfrac{\Phi_{ext}^{(H)}}{\Phi_0}\right) \ , \end{aligned} \tag{B.9}$$

and we can express the phase of each qubit as a function of the new operators

$$\hat{\varphi}_X = \varphi^X_{\text{ZPF}} (\hat{a}_X^\dagger + \hat{a}_X) = \varphi^X_{\text{ZPF}} \sum_{Y \in S} c_{XY}^* \tilde{a}_Y + c_{XY} \tilde{a}_Y^\dagger \ , \tag{B.10}$$

where we have defined $c_{XY} = \lambda_{XY} + \mu_{XY}$.

B.2 CALCULATING THE MATRIX COSINE

At this point we encounter severe numerical issues simply in setting up the matrix for the cosine terms. Indeed, with the dimensions of the qubit Hilbert spaces around 20 and the cavity Hilbert space of dimension 10, we need to numerically compute the matrix cosine of a 4000×4000 matrix. This is doable, but not convenient if we want to evaluate the result of the diagonalisation at different fluxes. Thankfully, there exists an algebraic solution for the cosine matrix. We reexpress the equation for $\hat{\varphi}_X$ above as a sum of charge and phase operators. To do this we define $\theta_{XY} = \arg c_{XY}$ and continue transforming the expression

$$\begin{aligned} c_{XY}^* \tilde{a}_Y + c_{XY} \tilde{a}_Y^\dagger &= |c_{XY}| \left(e^{-i\theta_{XY}} \tilde{a}_Y + e^{i\theta_{XY}} \tilde{a}_Y^\dagger \right) \\ &= \frac{|c_{XY}| \cos\theta_{XY}}{\tilde{\varphi}_{Y,\text{ZPF}}} \tilde{\varphi}_Y + \frac{|c_{XY}| \sin\theta_{XY}}{\tilde{n}_{Y,\text{ZPF}}} \tilde{n}_Y \ . \end{aligned} \tag{B.11}$$

In the above $\tilde{\varphi}_{Y,\text{ZPF}}$ and $\tilde{n}_{Y,\text{ZPF}}$ are the zero point fluctuations of the operators $\tilde{\varphi}_Y$ and $\tilde{n}_Y$ respectively. So finally

$$\hat{\varphi}_X = \varphi^X_{\text{ZPF}} \sum_{Y \in S} \frac{|c_{XY}| \cos\theta_{XY}}{\tilde{\varphi}_{Y,\text{ZPF}}} \tilde{\varphi}_Y + \frac{|c_{XY}| \sin\theta_{XY}}{\tilde{n}_{Y,\text{ZPF}}} \tilde{n}_Y \ . \tag{B.12}$$

1 We omit the operator hat notation $\hat{\ }$ for the tilde operators for the sake of readability.

Note that the diagonalised Hamiltonian in the eigenmode basis is invariant under the redefinition of the phase of each of the operators in O. So there is a phase degree of freedom we have not yet used in this calculation. We can use it to eliminate the sine term in the expression for $\hat{\varphi}_X$. The expression for the phase operator becomes

$$\hat{\varphi}_X = \sum_{Y \in S} \frac{|c_{XY}| \cos\theta_{XY}}{\tilde{\varphi}_{Y,\mathrm{ZPF}}} \tilde{\varphi}_Y = \sum_{Y \in S} \xi_{XY} \tilde{\varphi}_Y \ . \tag{B.13}$$

B.2.1 *Phase criterion*

To eliminate the sine term we impose the following condition

$$\sin\theta_{X,Y} = 0 \Leftrightarrow \theta_{X,Y} = 0 \Leftrightarrow \lambda_{XY} + \mu_{XY} \in \mathbb{R} \ . \tag{B.14}$$

We express this as a condition on the transformation from the original operators to the operators in the normal basis. Let $\tilde{v} = A\hat{v}$, with A the matrix that diagonalises M_H. We also define the following matrix

$$K = \begin{pmatrix} 0 & \mathbb{1}_3 \\ \mathbb{1}_3 & 0 \end{pmatrix} \ , \tag{B.15}$$

and the phase matrix β which describes a transformation of the phase of the operators

$$\beta = \mathrm{diag}(e^{i\beta_c}, e^{i\beta_H}, e^{i\beta_L}, e^{-i\beta_c}, e^{-i\beta_H}, e^{-i\beta_L}) \ . \tag{B.16}$$

Noting the following identity

$$\begin{pmatrix} \hat{a}_c + \hat{a}_c^\dagger \\ \hat{a}_H + \hat{a}_H^\dagger \\ \hat{a}_L + \hat{a}_L^\dagger \\ \hat{a}_c^\dagger + \hat{a}_c \\ \hat{a}_H^\dagger + \hat{a}_H \\ \hat{a}_L^\dagger + \hat{a}_L \end{pmatrix} = (\mathbb{1} + K)\hat{v} = (\mathbb{1} + K)A^{-1}\beta\tilde{v} \ , \tag{B.17}$$

if we want $\hat{\varphi}_X = \sum_{Y \in S} \xi_{XY} \tilde{\varphi}_Y$ then we need to choose β such that the rows of the matrix $T = (\mathbb{1} + K)A^{-1}\beta$ are of the form $(\alpha_i\ \beta_i\ \gamma_i\ \alpha_i\ \beta_i\ \gamma_i)$ with $\alpha_i,\ \beta_i,\ \gamma_i \in \mathbb{C}$ and i is the row index of T. With this

$$\hat{\varphi}_H = \varphi^H_{\mathrm{ZPF}} \sum_{j=1}^{6} T_{1j} \tilde{v}_j \ , \tag{B.18}$$

$$\hat{\varphi}_L = \varphi^L_{\mathrm{ZPF}} \sum_{j=1}^{6} T_{2j} \tilde{v}_j \ . \tag{B.19}$$

B.2.2 *Cosine matrix elements*

Concretely, we now need to calculate $\cos\left(\hat{\varphi}_X - 2\pi\frac{\Phi_{\text{ext}}^{(X)}}{\Phi_0}\right)$. We use the expression for a cosine containing four different terms

$$\cos\left(\sum_{i=1}^{4}\theta_i\right) = \sum_{k=0}^{2}(-1)^k \sum_{\substack{A\subseteq\{1,2,3,4\}\\|A|=2k}} \left(\prod_{i\in A}\sin\theta_i \prod_{i\notin A}\cos\theta_i\right) , \tag{B.20}$$

so that

$$\cos\left(\hat{\varphi}_X - \varphi_{\text{ext}}\right) = \sum_{k=0}^{2}(-1)^k \sum_{\substack{A\subseteq\{c,H,L,\text{ext}\}\\|A|=2k}} \left[\left(\prod_{\substack{Y\in A\\Y\neq\text{ext}}}\sin\xi_{XY}\tilde{\varphi}_Y \prod_{\substack{Y\notin A\\Y\neq\text{ext}}}\cos\xi_{XY}\tilde{\varphi}_Y\right)\right.$$
$$\left.\cdot(\delta_{\text{ext}\in A}\sin\left(-\varphi_{\text{ext}}\right) + \delta_{\text{ext}\notin A}\cos\varphi_{\text{ext}})\right] . \tag{B.21}$$

Let's take $|\alpha,\beta,m\rangle = |\alpha\rangle\otimes|\beta\rangle\otimes|m\rangle$ as a basis of the Hilbert space $\mathcal{H} = \mathcal{H}_H\otimes\mathcal{H}_L\otimes\mathcal{H}_c$ spanned by the operators $\tilde{a}_H^\dagger\tilde{a}_H$, $\tilde{a}_L^\dagger\tilde{a}_L$, $\tilde{a}_c^\dagger\tilde{a}_c$ with eigenstates $|\alpha\rangle$, $|\beta\rangle$, $|m\rangle$. We can decompose the expression (B.21) onto this basis

$$\cos\left(\hat{\varphi}_X - \varphi_{\text{ext}}\right) = \sum_{\substack{\alpha,\alpha'\\\beta,\beta'\\m,m'}} |\alpha,\beta,m\rangle\left\langle\alpha',\beta',m'\right| \sum_{k=0}^{2}(-1)^k \sum_{\substack{A\subseteq\{c,H,L,\text{ext}\}\\|A|=2k}} \langle\alpha,\beta,m|$$
$$(\delta_{c\in A}\sin\xi_{Xc}\tilde{\varphi}_c + \delta_{c\notin A}\cos\xi_{Xc}\tilde{\varphi}_c)(\delta_{H\in A}\sin\xi_{XH}\tilde{\varphi}_H + \delta_{H\notin A}\cos\xi_{XH}\tilde{\varphi}_H)\cdot$$
$$(\delta_{L\in A}\sin\xi_{XL}\tilde{\varphi}_L + \delta_{L\notin A}\cos\xi_{XL}\tilde{\varphi}_L)(\delta_{\text{ext}\in A}\sin\left(-\varphi_{\text{ext}}\right) + \delta_{\text{ext}\notin A}\cos\varphi_{\text{ext}})\left|\alpha',\beta',m'\right\rangle \tag{B.22}$$

Note that each of the $\tilde{\varphi}_X$ act on a different part of the Hilbert space $\mathcal{H}$. Using the associativity of the product

$$\cos\left(\hat{\varphi}_X - \varphi_{\text{ext}}\right) = \sum_{k=0}^{2}(-1)^k \sum_{\substack{A\subseteq\{c,H,L,\text{ext}\}\\|A|=2k}} (\delta_{\text{ext}\in A}\sin\left(-\varphi_{\text{ext}}\right) + \delta_{\text{ext}\notin A}\cos\varphi_{\text{ext}})\cdot$$
$$\left(\delta_{H\in A}\sum_{\alpha,\alpha'}|\alpha\rangle\left\langle\alpha'\right|\left\langle\alpha\middle|\sin\xi_{XH}\tilde{\varphi}_H\middle|\alpha'\right\rangle + \delta_{H\notin A}\sum_{\alpha,\alpha'}|\alpha\rangle\left\langle\alpha'\right|\left\langle\alpha\middle|\cos\xi_{XH}\tilde{\varphi}_H\middle|\alpha'\right\rangle\right)\otimes$$
$$\left(\delta_{L\in A}\sum_{\beta,\beta'}|\beta\rangle\left\langle\beta'\right|\left\langle\beta\middle|\sin\xi_{XL}\tilde{\varphi}_L\middle|\beta'\right\rangle + \delta_{L\notin A}\sum_{\beta,\beta'}|\beta\rangle\left\langle\beta'\right|\left\langle\beta\middle|\cos\xi_{XL}\tilde{\varphi}_L\middle|\beta'\right\rangle\right)\otimes$$
$$\left(\delta_{c\in A}\sum_{l,l'}|l\rangle\left\langle l'\right|\left\langle l\middle|\sin\xi_{Xc}\tilde{\varphi}_c\middle|l'\right\rangle + \delta_{c\notin A}\sum_{l,l'}|l\rangle\left\langle l'\right|\left\langle l\middle|\cos\xi_{Xc}\tilde{\varphi}_c\middle|l'\right\rangle\right) \tag{B.23}$$

Finally, the matrix elements $\langle k|\sin\lambda\varphi|l\rangle$ and $\langle k|\cos\lambda\varphi|l\rangle$ are given by the analytical expressions ([97] and equations 7.388.6 & 7.388.7 of [238])

$$\langle k|\cos\lambda\varphi|l\rangle = \begin{cases} (-1)^{\frac{l-k}{2}}\sqrt{\frac{k!}{l!}}(\lambda\varphi_{\text{ZPF}})^{l-k}e^{-(\lambda\varphi_{\text{ZPF}})^2/2}\mathcal{L}_k^{l-k}((\lambda\varphi_{\text{ZPF}})^2) & (k+l \text{ even},\ k\leq l) \\ 0 & (k+l \text{ odd})\ ; \end{cases} \tag{B.24}$$

$$\langle k|\sin\lambda\varphi|l\rangle = \begin{cases} 0 & (k+l \text{ even}) \\ (-1)^{\frac{l-k+1}{2}}\sqrt{\frac{k!}{l!}}(\lambda\varphi_{\text{ZPF}})^{l-k}e^{-(\lambda\varphi_{\text{ZPF}})^2/2}\mathcal{L}_k^{l-k}((\lambda\varphi_{\text{ZPF}})^2) & (k+l \text{ odd},\ k\leq l)\ . \end{cases} \tag{B.25}$$

In the above formulas, $\mathcal{L}_a^b$ are the associated Laguerre polynomials.

B.3 ORDERING THE STATES

Diagonalising $\tilde{H}$ yields a list of energy eigenstates and their respective energies ordered by increasing energy. For the diagonalisation to be useful we need to assign quantum numbers belonging to the cavity and both fluxoniums to each state. To do this we first use a technique developped in [100] which uses the cavity dipole operator to identify resonator transitions. We calculate

$$\langle\psi_n|\tilde{a}_c^\dagger + \tilde{a}_c|\psi_m\rangle\ , \tag{B.26}$$

for all eigenstates $|\psi_n\rangle$ in $\mathcal{H}$. The coupling g_{cav} is weak so the operator $\tilde{a}_c^\dagger + \tilde{a}_c$ is very close to $\hat{a}_c^\dagger + \hat{a}_c$. Because of this we can restrict the numerics to the states separated in energy by a range around the experimental cavity frequency. This dramatically reduces the number of calculations from N^2 to $\Theta(N)$ (N is the dimension of $\mathcal{H}$), which is a key speed up when N is large. The calculation of these matrix elements allows us to create ladders of states corresponding to increments in the photon number in the resonator. Thus, we can already label $|\psi_n\rangle$ as $|\gamma, m\rangle$ where m is the photon number in the resonator. Assigning quantum numbers from the two Fluxonium qubits is done by comparing $|\gamma, 0\rangle$ with the product states $|\alpha\rangle\otimes|\beta\rangle\otimes|0\rangle$ obtained by direct diagonalisation of

$$\tilde{H}_H = \hbar\tilde{\omega}_H\tilde{a}_H^\dagger\tilde{a}_H - E_J^{(H)}\cos\left(\hat{\varphi}_H - 2\pi\frac{\Phi_{ext}^{(H)}}{\Phi_0}\right)\ , \tag{B.27}$$

$$\tilde{H}_L = \hbar\tilde{\omega}_L\tilde{a}_L^\dagger\tilde{a}_L - E_J^{(L)}\cos\left(\hat{\varphi}_L - 2\pi\frac{\Phi_{ext}^{(L)}}{\Phi_0}\right)\ , \tag{B.28}$$

independently. In practice we calculate the overlaps $\langle\gamma, 0|\,(|\alpha\rangle\otimes|\beta\rangle\otimes|0\rangle)$. We can again reduce the number of overlaps, by considering that the energies of the states $|\gamma, 0\rangle$ are close to those of $|\alpha\rangle\otimes|\beta\rangle\otimes|0\rangle$. This is equivalent to saying that the couplings g_c and g_{HL} are small compared to the energies of each Hamiltonian independently. This way we don't compare states which are energetically too distant.
We have obtained a labelling with quantum numbers α, β and m such that $|\psi_n\rangle = |\alpha, \beta, m\rangle$ is in fact very close to $|\alpha\rangle\otimes|\beta\rangle\otimes|m\rangle$ in the case of weak couplings.

C

FABRICATION OF TITANIUM NITRIDE DEVICES

The fabrication of the TiN hanger resonators was done in multiple steps in multiple cleanrooms.

1. High resistivity ($> 20\,000\,\Omega\,\mathrm{cm}$) Silicon (111) wafers were cleaned in acetone and IPA for 1 minute, before a plasma O_2 clean for 3 minutes.
2. The wafer were then dipped in a 5% HF solution for 1 minute before being rinsed with DI water.
3. They were then placed as fast as possible inside the sputtering machine to avoid reoxidation of the silicon substrate. Deposition was done according to the parameters mentioned in Tab. C.1.
4. The colour of the TiN films were monitored during venting of the sputtering chamber and the colour immediately after exiting the sputtering machine was recorded. This colour was not necessarily the same as inside the chamber, but that colour was difficult to determine precisely due to the UV filters on the chamber windows. The wafers were then package for transport.
5. Before spin coating with S1813 resin (10s 1000rpm (500 rpm/s), 40s 2000rpm (4000 rpm/s), 1 minute bake at 115°C) the wafers were cleaned with acetone and IPA again.
6. Optical lithography was used to pattern the wafer after which the exposed resin was developped using AZ726 MIF for 90 seconds and then rinsed in DI water.
7. The exposed TiN film was etched using an SF6 plasma taking care not to over-etch the silicon beneath.
8. The resin was the removed using acetone and IPA.
9. In certain cases the wafer was then taken for another etch with HF 5% for 1 minute and DI water rinse in a different location (INSA).

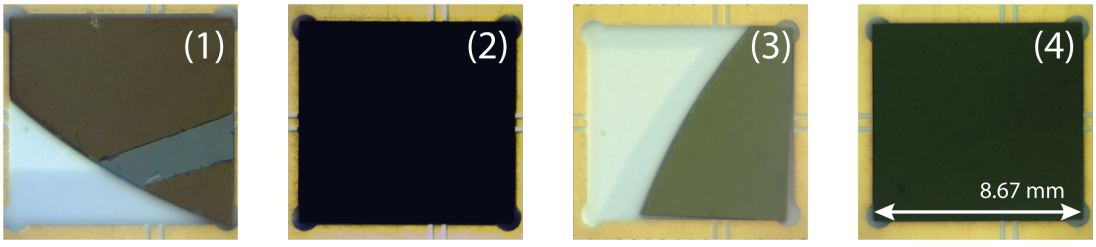

Figure C.1: Optical image of the chips labeled 1 - 4 in Tab. C.1 illustrating the different colours of TiN samples visible on 31/05/2018.

10. Finally, the wafers were diced after having been spin coated with resin for protection. A final clean with acetone and IPA was done before wirebonding.

Steps 1 to 4 were done in the cleanroom at Centrale Lyon, steps 5 - 8 and 10 at the cleanroom at the Université Claude Bernard and step 9 was done at the cleanroom at INSA Lyon.

	Fabrication details											Colour		EDX Results at. %		
Chip	Fabrication date	Pressure ($\times 10^{-3}$mbar)	Ar flow (sccm)	N_2 flow (sccm)	Target DC/RF	DC Power (W)	DC Voltage (V)*	DC Current (A)*	RF Power (W)	RF Voltage (V)*	Colour after deposition	Colour after exposure to air 31/05/2018	Ti	N	O
1	06/03/2018	9.3	50	2.5	DC	300	367	0.82	100	750	Copper	Copper	55.8	40.4	3.8
2	21/03/2018	9.3	15	2.5	DC	300	377	0.8			Green	Purple	32.7	45.6	21.8
3	12/03/2018	9.3	15	2.5	DC	300	380	0.79			Blue	Green	28.7	45.8	25.5
4	21/03/2018	9.3	50	2.5	DC	300	366	0.82			Pink	Gray	33.9	42.4	23.7
	21/03/2018	5	50	2.5	DC	300	373	0.81			Pink	Green	31.4	48.1	20.5
	15/03/2018	12	50	2.3	RF	2	60	0.03	250	320	Gold	Black	45.5	45.8	8.7
		5.1	50	3	RF	3	60	0.05	300	329	Gold		48.1	47.9	4
	09/05/2018	12	50	3	RF	3	60	0.04	303	324	Gold	Gold	34.1	52.2	13.7
	06/03/2018	9.3	50	2.5	DC	300	371	0.81	250	320	Green	Copper	41.2	40.2	18.6

Table C.1: Table summarising the principle results from the TiN fabrication project. We recorded the colour of the samples because this contained information about the stochiometry of each thin film [127].

D

PAST QUANTUM STATE FORMALISM

D.1 INTRODUCTION

The dynamics of a classical system can be described by propagating the system forwards in time from a known initial state at time t_i. If we have access to all the microscopic microstates of the system, this forwards trajectory is full reversible by propagating the perfectly known final state at time t_f backwards in time towards the intial state. For an isolated quantum system this is also the case, as the Schrödinger equation possesses time reversal symmetry. Differences arise if the quantum system is measured. In the classical case, measurement does not affect the system and does not need to be included in the dynamics, whether backwards or forwards. In the quantum case, because a measurement at time $t_M \in [t_i, t_f]$ always leads to some backaction on the state of the system, the dynamics after the measurement can only be described conditioned on the result of the measurement at time t_M. Using the density matrix and the Lindblad master equation, we can predict the probability of a certain measurement outcome at time t_M using the information about the state before the measurement. Is it possible to improve the estimation of the unknown outcome of an measurement at time t_M by also using the information about the quantum state at times $t \in [t_M, t_f]$? This is the objective of the past quantum state formalism as described in [42, 239]. The work by Gammelmark et al. introduces the pair of matrices $(\rho(t), E(t))$ which contain the observer's information about the quantum state obtained both before and after time t. $\rho(t)$ is simply the density matrix and $E(t)$ is called the effect matrix. The thesis of Quentin Ficheux [48] gives an excellent introduction to the subject complementary to the work by Gammelmark et al. Here we will simply sum up some of the main results useful for understanding the results and techniques developed in this thesis.

D.2 GENERALISED MEASUREMENTS IN QUANTUM MECHANICS

Quantum measurements, unlike their classical counterparts whose nature is fixed, belong on a spectrum, from weak to strong. At the strong end we find projective measurements, or Von Neumann measurements, which collapse the quantum state after the measurement onto one of the pointer states of the measurement operator. Stern and Gerlach's experiment measures the spin of an incoming particle strongly by encoding the measured value in the position of the particle's impact on a screen when using a large magnetic field gradient [240]. Particles with different measured spins can therefore be distinguished by comparing the positions of their impacts on the screen. At the weak end, the measurement outcome gives little information about the quantum state, which is barely disturbed by the measurement. This is the case if the magnitude of the magnetic field gradient is much smaller, only separating the spins a little, such that we cannot truely distinguish different positions on the screen. In that case the spin is not

totally projected onto a single value, but there remains some uncertainty. To describe these generalised measurements, we introduce a set of Kraus operators $\{\hat{M}_i\}$ with outcomes λ_i. All the operators $\hat{M}_i^\dagger \hat{M}_i$ are hermitian and $\sum_i \hat{M}_i^\dagger \hat{M}_i = \mathbb{1}$. The probability of each measurement outcome is

$$p_i = \mathrm{tr}\left[\hat{M}_i \rho \hat{M}_i^\dagger\right] \tag{D.1}$$

given a density matrix ρ, and immediately after a measurement with outcome λ_i the state is given by

$$\rho = \frac{\hat{M}_i \rho \hat{M}_i^\dagger}{\mathrm{tr}\left[\hat{M}_i \rho \hat{M}_i^\dagger\right]} \ . \tag{D.2}$$

D.3 FORWARD-BACKWARD ALGORITHM

In Chapter 6 we considered the probabilities $P(z_k|\,|\nu\rangle)$ of obtaining the point z_k in the IQ-plane if the qubit was in state $|\nu\rangle$. We can express this as a function of a set of Kraus operators $\{\hat{M}_z\}$ whose outcomes are all possible values z in the IQ-plane. In that case

$$P(z|\,|\nu\rangle) = \mathrm{tr}\left[\hat{M}_z\,|\nu\rangle\,\langle\nu|\,\hat{M}_z^\dagger\right] = \sum_\sigma \langle\sigma|\hat{M}_z|\nu\rangle\ \langle\nu|\hat{M}_z^\dagger|\sigma\rangle = \sum_\sigma \Big|\,\langle\sigma|\hat{M}_z|\nu\rangle\Big|^2 \ . \tag{D.3}$$

Equivalently, the probability $P(|\nu\rangle\,,k)$ of being in state $|\nu\rangle$ at time t_k is given by the diagonal elements of the density matrix at time t_k

$$P(|\nu\rangle\,,k) = \ \langle\nu|\rho(t_k)|\nu\rangle \ . \tag{D.4}$$

We are now ready to derive equation (6.39) from the Kraus matrix representation. To do that, remember that our dispersive measurement does not yield any information about the coherences of the density matrix at each time step. Thus after each measurement, the density matrix stays diagonal. In that case, to determine the density matrix $\rho(t_k^+)$ just after the measurement with outcome z at time t_k, we only need to specify

$$P(|\nu\rangle\,,k+) = \ \langle\nu|\rho(t_k^+)|\nu\rangle = \ \langle\nu|\frac{\hat{M}_z\rho(t_k^-)\hat{M}_z^\dagger}{\mathrm{tr}\left[\hat{M}_z\rho(t_k^-)\hat{M}_z^\dagger\right]}|\nu\rangle \ , \tag{D.5}$$

where $\rho(t_k^-)$ is the density matrix just before the measurement. Using the fact that ρ is diagonal, the numerator can be reduced to

$$\langle\nu|\hat{M}_z\rho(t_k^-)\hat{M}_z^\dagger|\nu\rangle = \sum_\mu \Big|\,\langle\nu|\hat{M}_z|\mu\rangle\Big|^2 P(|\mu\rangle\,,k-) \ , \tag{D.6}$$

because $\rho(t_k^-) = \sum_\mu P(|\mu\rangle\,,k-)\,|\mu\rangle\,\langle\mu|$. Equivalently, the trace becomes

$$\mathrm{tr}\left[\hat{M}_z\rho(t_k^-)\hat{M}_z^\dagger\right] = \sum_{\mu,\sigma} \Big|\,\langle\sigma|\hat{M}_z|\mu\rangle\Big|^2 P(|\mu\rangle\,,k-) = \sum_\mu P(z|\,|\mu\rangle)P(|\mu\rangle\,,k-) \ . \tag{D.7}$$

Equation (D.7) already corresponds to the denominator of (6.39). To transform (D.6) into the correct form we need to specify some assumptions about the physical model.

Subliminal to (6.39) is the assumption that the measurement record is obtained by a series of instantaneous measurements, followed by an evolution given by the transition rates. Of course this is not really the case as the cavity drive is applied continuously, so the true description of the system would have to take into account infinitesimal time steps and an evolution related to the stochastic master equation. Because we separate the measurement result from the dynamics of the qubit during the measurement, we can assume that our instantaneous measurement is quantum non-demolition. In that case, $\hat{M}_z$ is diagonal in the qubit basis [241]. So

$$\langle\nu|\hat{M}_z|\mu\rangle = \delta_{\mu,\nu}\langle\nu|\hat{M}_z|\nu\rangle \ , \tag{D.8}$$

and (D.6) becomes

$$\langle\nu|\hat{M}_z\rho(t_k^-)\hat{M}_z^\dagger|\nu\rangle = P(z|\,|\nu\rangle)P(|\nu\rangle\,,k-) \ . \tag{D.9}$$

Finally

$$P(|\nu\rangle\,,k+) = \frac{P(z|\,|\nu\rangle)P(|\nu\rangle\,,k-)}{\sum_\mu P(z|\,|\mu\rangle)P(|\mu\rangle\,,k-)} \ , \tag{D.10}$$

exactly reproducing (6.39) when taking into account the transition rates between measurements. The backwards update equation (6.40) can be determined the same way.

D.4 LINK TO THE EFFECT MATRIX

Through the example of the quantum jumps of Chapter 6 we can better understand the role of the effect matrix. When propagating forward through time the density matrix is updated by the Hamiltonian dynamics and by the information obtained in the measurement record. When the measurement efficiency and coherences of the quantum state need to be taken into account, the evolution of ρ is given by the stochastic master equation. This equation can be seen as a successive application of Kraus maps at each time step dt which take into account the Hamiltonian dynamics, dissipation and measurement record. The effect matrix also obeys a stochastic master equation, but with time propagating backwards. Thus, when there is no measurement, while ρ obeys the Lindblad master equation, E obeys

$$\partial_t E = -\frac{i}{\hbar}[E,\rho] - \sum_i D^*[\hat{L}_i](E) \tag{D.11}$$

where the adjoint of the Lindblad superoperator is

$$D^*[\hat{L}](E) = \hat{L}^\dagger E\hat{L} - \frac{1}{2}E\hat{L}^\dagger\hat{L} - \frac{1}{2}\hat{L}^\dagger\hat{L}E \ . \tag{D.12}$$

Note the change of sign with respect to the normal Lindblad equation

$$\partial_t E = -\frac{i}{\hbar}[E,\rho] + \sum_i D[\hat{L}_i](E) \ . \tag{D.13}$$

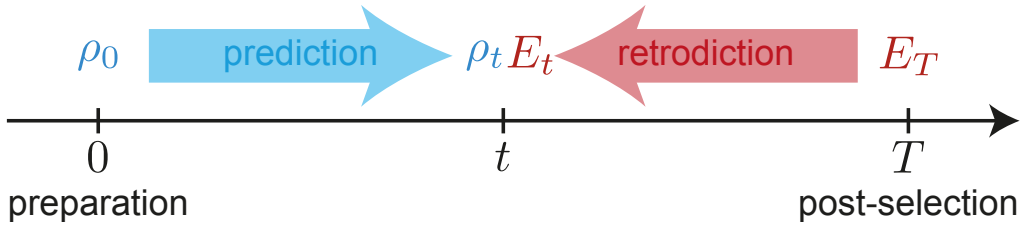

Figure D.1: The effect matrix is the dual of the density matrix propagating backwards in time. Figure taken from [48].

How can we use the effect matrix to make better predictions about measurements at past times? Given a set of measurement operators $\{\hat{M}_i\}$ the probability of a measurement outcome λ_m at time t is given by

$$P(\lambda_m) = \frac{\mathrm{tr}\left[\hat{M}_m \rho(t) \hat{M}_m^\dagger E(t)\right]}{\sum_n \mathrm{tr}\left[\hat{M}_n \rho(t) \hat{M}_n^\dagger E(t)\right]} \,. \tag{D.14}$$

If we have no information about the qubit state at future times, $E(t) = \mathbb{1}/\dim \mathcal{H}$ and we retrieve equation (D.1). $E(t)$ should therefore be interpreted as the information about the state we obtain from observation and not the state itself. In particular, $\mathrm{tr}\,[E(t)]$ is not always equal to 1.

D.5 TIME EVOLUTION OF THE EFFECT MATRIX

We solve the backward propagating Lindblad equation equivalent to A.1 for the effect matrix

$$\partial_t E = -\frac{i}{\hbar}[E, \rho] - \frac{\Gamma_\phi}{2} D^*[\hat{\sigma}^z](E) - \Gamma_\downarrow D^*[\hat{\sigma}^-](E) - \Gamma_\uparrow D^*[\hat{\sigma}^+](E) \,. \tag{D.15}$$

We can express the equations in matrix form again

$$\begin{aligned}\begin{pmatrix} \dot{E_{ee}} & \dot{E_{eg}} \\ \dot{E_{ge}} & \dot{E_{gg}} \end{pmatrix} = &-\frac{\Omega}{2}\begin{pmatrix} -(E_{eg}+E_{ge}) & E_{ee}-E_{gg} \\ E_{ee}-E_{gg} & E_{eg}+E_{ge} \end{pmatrix} - \Gamma_\phi \begin{pmatrix} 0 & -E_{eg} \\ -E_{ge} & 0 \end{pmatrix} \\ &- \Gamma_\downarrow \begin{pmatrix} E_{gg}-E_{ee} & -\frac{1}{2}E_{eg} \\ -\frac{1}{2}E_{ge} & 0 \end{pmatrix} - \Gamma_\uparrow \begin{pmatrix} 0 & -\frac{1}{2}E_{eg} \\ -\frac{1}{2}E_{ge} & E_{ee}-E_{gg} \end{pmatrix} \,,\end{aligned} \tag{D.16}$$

or in a more readable form

$$\begin{pmatrix} \dot{E_{ee}} \\ \dot{E_{eg}} \\ \dot{E_{ge}} \\ \dot{E_{gg}} \end{pmatrix} = \begin{pmatrix} \Gamma_\downarrow & \frac{\Omega}{2} & \frac{\Omega}{2} & -\Gamma_\downarrow \\ -\frac{\Omega}{2} & \Gamma_2 & 0 & \frac{\Omega}{2} \\ -\frac{\Omega}{2} & 0 & \Gamma_2 & \frac{\Omega}{2} \\ -\Gamma_\uparrow & -\frac{\Omega}{2} & -\frac{\Omega}{2} & \Gamma_\uparrow \end{pmatrix} \begin{pmatrix} E_{ee} \\ E_{eg} \\ E_{ge} \\ E_{gg} \end{pmatrix} \,. \tag{D.17}$$

Note that these equations do not the trace of E $\dot{E_{ee}} + \dot{E_{gg}} \neq 0$. In the Bloch basis we obtain

$$\frac{\mathrm{d}}{\mathrm{d}t}\begin{pmatrix} \langle\hat{\sigma}^x\rangle \\ \langle\hat{\sigma}^y\rangle \\ \langle\hat{\sigma}^z\rangle \end{pmatrix} = \begin{pmatrix} \Gamma_2 & 0 & -\Omega \\ 0 & \Gamma_2 & 0 \\ \Omega & 0 & \Gamma_1 \end{pmatrix} \begin{pmatrix} \langle\hat{\sigma}^x\rangle \\ \langle\hat{\sigma}^y\rangle \\ \langle\hat{\sigma}^z\rangle \end{pmatrix} \,. \tag{D.18}$$

To take into account the last degree of freedom we use the independent equation $\dot{E_{ee}} + \dot{E_{gg}} = (\Gamma_\downarrow - \Gamma_\uparrow)\langle\hat{\sigma}^z\rangle$, which is the time reversed equivalent of the constant term above. We already know the homogeneous solution to the Bloch equations for the density matrix, we just need to replace all the dissipation terms by their negative

$$\langle\hat{\sigma}^x\rangle(t) = e^{\Gamma_R t}\left[\cos(\Omega_R t)x_c + \frac{\sin(\Omega_R t)}{\Omega_R}\left(\frac{\Gamma_2-\Gamma_1}{2}x_c - \Omega z_c\right)\right] , \tag{D.19}$$

$$\langle\hat{\sigma}^y\rangle(t) = e^{\Gamma_2 t}y_c , \tag{D.20}$$

$$\langle\hat{\sigma}^z\rangle(t) = e^{\Gamma_R t}\left[\cos(\Omega_R t)z_c - \frac{\sin(\Omega_R t)}{\Omega_R}\left(\frac{\Gamma_2-\Gamma_1}{2}z_c - \Omega x_c\right)\right] . \tag{D.21}$$

Here again the constants correspond to the boundary conditions, this time most likely at the end of the trajectory. We can again consider the case where the qubit never has a component along the y-axis. In that case

$$E_{ee} - E_{gg} = \langle\hat{\sigma}^z\rangle , \tag{D.22}$$

$$E_{ee} + E_{gg} = (\Gamma_\downarrow - \Gamma_\uparrow)\int\langle\hat{\sigma}^z\rangle\,\mathrm{d}t + c , \tag{D.23}$$

$$E_{eg} = E_{ge} = \frac{1}{2}\langle\hat{\sigma}^x\rangle , \tag{D.24}$$

where c is a constant which depends on the boundary conditions. Solving the integral is painless by using the exponential formulas for cos and sin

$$\int e^{\Gamma t}(a\cos(\omega t) - b\sin(\omega t))\mathrm{d}t = \frac{e^{\Gamma t}}{\Gamma^2+\omega^2}\left[\cos(\omega t)(a\Gamma + b\omega) + \sin(\omega t)(a\omega - b\Gamma)\right] + c_I , \tag{D.25}$$

replacing the constants by the correct values

$$\int\langle\hat{\sigma}^z\rangle\,\mathrm{d}t = \frac{e^{\Gamma_R t}}{\Gamma_R^2+\Omega_R^2}\left[\cos(\Omega_R t)\left(z_c\Gamma_R + \frac{\Gamma_2-\Gamma_1}{2}z_c - \Omega x_c\right)\right.$$
$$\left. + \sin(\Omega_R t)\left(z_c\Omega_R - \frac{\Gamma_R}{\Omega_R}\left(\frac{\Gamma_2-\Gamma_1}{2}z_c - \Omega x_c\right)\right)\right] + c_I , \tag{D.26}$$

and

$$E_{ee} + E_{gg} = \frac{e^{\Gamma_R t}(\Gamma_\downarrow - \Gamma_\uparrow)}{\Gamma_R^2+\Omega_R^2}\left[\cos(\Omega_R t)\left(z_c\Gamma_2 - \Omega x_c\right)\right.$$
$$\left. + \frac{\sin(\Omega_R t)}{\Omega_R}\left(\left(\Omega_R^2 - \Gamma_R\frac{\Gamma_2-\Gamma_1}{2}\right)z_c + x_c\Gamma_R\Omega\right)\right] + c_I , \tag{D.27}$$

$$E_{ee} - E_{gg} = e^{\Gamma_R t}\left[\cos(\Omega_R t)z_c - \frac{\sin(\Omega_R t)}{\Omega_R}\left(\frac{\Gamma_2-\Gamma_1}{2}z_c - \Omega x_c\right)\right] , \tag{D.28}$$

$$E_{eg} = E_{ge} = \frac{1}{2}e^{\Gamma_R t}\left[\cos(\Omega_R t)x_c + \frac{\sin(\Omega_R t)}{\Omega_R}\left(\frac{\Gamma_2-\Gamma_1}{2}x_c - \Omega z_c\right)\right] . \tag{D.29}$$

D.6 WEAK VALUES

In Chapter 7 we use the past quantum state formalism to predict the expectation value of an operator at time t post-selected on the results of a strong measurement at time

$t_m > t$ and with knowledge of the qubit starting state. This expectation value of an operator $\hat{o}$ conditioned on the measurement result λ at t_m is given by

$$\langle \hat{o} \rangle_\lambda = \frac{\mathrm{tr}\left[E_\lambda(t)\hat{o}\rho(t)\right]}{\mathrm{tr}\left[E_\lambda(t)\rho(t)\right]} \ . \tag{D.30}$$

This is called the weak value of $\hat{o}$ [237].

BIBLIOGRAPHY

[1] *The Nobel Prize in Physics 1972*. en-US (Cited on page 1).

[2] *The Nobel Prize in Physics 1956*. en-US (Cited on page 1).

[3] E. Schrödinger. "Are there quantum jumps ?: part ii*." In: *The British Journal for the Philosophy of Science* 3.11 (Nov. 1952). Publisher: The University of Chicago Press, pp. 233–242 (Cited on page 1).

[4] *The Nobel Prize in Physics 2012*. en-US (Cited on page 1).

[5] D. J. Wineland, R. E. Drullinger, and F. L. Walls. "Radiation-Pressure Cooling of Bound Resonant Absorbers." In: *Physical Review Letters* 40.25 (June 1978). Publisher: American Physical Society, pp. 1639–1642 (Cited on page 1).

[6] Michael Tinkham. *Introduction to Superconductivity*. Courier Corporation, 2004 (Cited on pages 2, 9).

[7] Uri Vool and Michel Devoret. "Introduction to quantum electromagnetic circuits." en. In: *International Journal of Circuit Theory and Applications* 45.7 (2017), pp. 897–934 (Cited on pages 2, 15, 41, 81, 161).

[8] David Pozar. *Microwave Engineering*. Wiley, 2011 (Cited on pages 2, 11, 26, 41, 42, 76).

[9] Brian Josephson. *The Discovery of Tunnelling Supercurrents*. Nobel Lecture. 1973 (Cited on pages 2, 12).

[10] John M. Martinis, Michel H. Devoret, and John Clarke. "Energy-Level Quantization in the Zero-Voltage State of a Current-Biased Josephson Junction." In: *Physical Review Letters* 55.15 (Oct. 1985). Publisher: American Physical Society, pp. 1543–1546 (Cited on page 2).

[11] L. DiCarlo et al. "Demonstration of two-qubit algorithms with a superconducting quantum processor." en. In: *Nature* 460.7252 (July 2009). Number: 7252 Publisher: Nature Publishing Group, pp. 240–244 (Cited on pages 3, 51).

[12] Shay Hacohen-Gourgy et al. "Quantum dynamics of simultaneously measured non-commuting observables." en. In: *Nature* 538.7626 (Oct. 2016), pp. 491–494 (Cited on page 3).

[13] Z. K. Minev et al. "To catch and reverse a quantum jump mid-flight." en. In: *Nature* 570.7760 (June 2019), pp. 200–204 (Cited on page 3).

[14] Paul Benioff. "The computer as a physical system: A microscopic quantum mechanical Hamiltonian model of computers as represented by Turing machines." en. In: *Journal of Statistical Physics* 22.5 (May 1980), pp. 563–591 (Cited on page 3).

[15] Richard P. Feynman. "Simulating physics with computers." en. In: *International Journal of Theoretical Physics* 21.6 (June 1982), pp. 467–488 (Cited on page 3).

[16] A. Wallraff et al. "Strong coupling of a single photon to a superconducting qubit using circuit quantum electrodynamics." en. In: *Nature* 431.7005 (Sept. 2004). Number: 7005 Publisher: Nature Publishing Group, pp. 162–167 (Cited on pages 3, 34).

[17] Alexandre Blais et al. "Cavity quantum electrodynamics for superconducting electrical circuits: An architecture for quantum computation." In: *Physical Review A* 69.6 (June 2004). Publisher: American Physical Society, p. 062320 (Cited on page 3).

[18] Jens Koch et al. "Charge-insensitive qubit design derived from the Cooper pair box." In: *Physical Review A* 76.4 (Oct. 2007). Publisher: American Physical Society, p. 042319 (Cited on pages 3, 13, 32, 34, 47, 53, 77).

[19] Vladimir B. Braginsky, Yuri I. Vorontsov, and Kip S. Thorne. "Quantum Nondemolition Measurements." en. In: *Science* 209.4456 (Aug. 1980). Publisher: American Association for the Advancement of Science Section: Articles, pp. 547–557 (Cited on page 3).

[20] A. A. Clerk et al. "Introduction to quantum noise, measurement, and amplification." In: *Reviews of Modern Physics* 82.2 (Apr. 2010). Publisher: American Physical Society, pp. 1155–1208 (Cited on pages 3, 34, 40, 41, 75, 77, 161, 162).

[21] Y. Nakamura, Yu A. Pashkin, and J. S. Tsai. "Coherent control of macroscopic quantum states in a single-Cooper-pair box." en. In: *Nature* 398.6730 (Apr. 1999). Number: 6730 Publisher: Nature Publishing Group, pp. 786–788 (Cited on pages 3, 33).

[22] S. Kuhr et al. "Ultrahigh finesse Fabry-Pérot superconducting resonator." In: *Applied Physics Letters* 90.16 (Apr. 2007). Publisher: American Institute of Physics, p. 164101 (Cited on page 3).

[23] Frank Arute et al. "Quantum supremacy using a programmable superconducting processor." en. In: *Nature* 574.7779 (Oct. 2019), pp. 505–510 (Cited on page 3).

[24] T. L. Nguyen et al. "Towards Quantum Simulation with Circular Rydberg Atoms." In: *Physical Review X* 8.1 (Feb. 2018). Publisher: American Physical Society, p. 011032 (Cited on page 3).

[25] H. Häffner, C. F. Roos, and R. Blatt. "Quantum computing with trapped ions." en. In: *Physics Reports* 469.4 (Dec. 2008), pp. 155–203 (Cited on page 3).

[26] Hui Wang et al. "Boson Sampling with 20 Input Photons and a 60-Mode Interferometer in a $1{0}^{14}$-Dimensional Hilbert Space." In: *Physical Review Letters* 123.25 (Dec. 2019). Publisher: American Physical Society, p. 250503 (Cited on page 3).

[27] Daniel Loss and David P. DiVincenzo. "Quantum computation with quantum dots." In: *Physical Review A* 57.1 (Jan. 1998). Publisher: American Physical Society, pp. 120–126 (Cited on page 3).

[28] B. Roussel et al. "Processing Quantum Signals Carried by Electrical Currents." In: *PRX Quantum* 2.2 (May 2021). Publisher: American Physical Society, p. 020314 (Cited on page 3).

[29] P. Campagne-Ibarcq et al. "Quantum error correction of a qubit encoded in grid states of an oscillator." en. In: *Nature* 584.7821 (Aug. 2020). Bandiera_abtest: a Cg_type: Nature Research Journals Number: 7821 Primary_atype: Research Publisher: Nature Publishing Group Subject_term: Quantum information;Quantum mechanics;Qubits Subject_term_id: quantum-information;quantum-mechanics;qubits, pp. 368–372 (Cited on pages 3, 53).

[30] Raphaël Lescanne et al. "Exponential suppression of bit-flips in a qubit encoded in an oscillator." en. In: *Nature Physics* 16.5 (May 2020). Number: 5 Publisher: Nature Publishing Group, pp. 509–513 (Cited on pages 3, 53).

[31] P. Magnard et al. "Microwave Quantum Link between Superconducting Circuits Housed in Spatially Separated Cryogenic Systems." In: *Physical Review Letters* 125.26 (Dec. 2020). Publisher: American Physical Society, p. 260502 (Cited on page 3).

[32] Vladimir E. Manucharyan et al. "Fluxonium: Single Cooper-Pair Circuit Free of Charge Offsets." en. In: *Science* 326.5949 (Oct. 2009). Publisher: American Association for the Advancement of Science Section: Report, pp. 113–116 (Cited on pages 4, 35–37, 39, 48).

[33] Aaron Somoroff et al. "Millisecond coherence in a superconducting qubit." In: *arXiv:2103.08578 [cond-mat, physics:quant-ph]* (Mar. 2021). arXiv: 2103.08578 (Cited on pages 4, 43, 44, 64, 66, 109, 121).

[34] Daria Gusenkova et al. "Quantum non-demolition dispersive readout of a superconducting artificial atom using large photon numbers." In: *arXiv:2009.14785 [cond-mat, physics:quant-ph]* (Sept. 2020). arXiv: 2009.14785 (Cited on pages 4, 5, 107, 121, 138, 143–145, 151).

[35] Laura Cardani et al. "Reducing the impact of radioactivity on quantum circuits in a deep-underground facility." In: *arXiv:2005.02286 [cond-mat, physics:physics, physics:quant-ph]* (May 2020). arXiv: 2005.02286 (Cited on pages 4, 67, 92).

[36] Antti P. Vepsäläinen et al. "Impact of ionizing radiation on superconducting qubit coherence." en. In: *Nature* 584.7822 (Aug. 2020). Number: 7822 Publisher: Nature Publishing Group, pp. 551–556 (Cited on pages 4, 92).

[37] U. Vool et al. "Non-Poissonian Quantum Jumps of a Fluxonium Qubit due to Quasiparticle Excitations." In: *Physical Review Letters* 113.24 (Dec. 2014). Publisher: American Physical Society, p. 247001 (Cited on pages 5, 42, 121, 143, 145, 151).

[38] Quentin Ficheux et al. "Fast logic with slow qubits: microwave-activated controlled-Z gate on low-frequency fluxoniums." In: *arXiv:2011.02634 [cond-mat, physics:quant-ph]* (Nov. 2020). arXiv: 2011.02634 (Cited on pages 5, 51, 109, 121, 151).

[39] H. M. Wiseman. "Weak values, quantum trajectories, and the cavity-QED experiment on wave-particle correlation." In: *Physical Review A* 65.3 (Feb. 2002). Publisher: American Physical Society, p. 032111 (Cited on pages 5, 164).

[40] Cyril Elouard et al. "The role of quantum measurement in stochastic thermodynamics." en. In: *npj Quantum Information* 3.1 (Mar. 2017), pp. 1–10 (Cited on pages 6, 154, 155).

[41] Alexia Auffèves. "A short story of quantum and information thermodynamics." In: *SciPost Physics Lecture Notes* (Mar. 2021). arXiv: 2102.00920, p. 27 (Cited on pages 6, 154).

[42] Søren Gammelmark, Brian Julsgaard, and Klaus Mølmer. "Past Quantum States of a Monitored System." In: *Physical Review Letters* 111.16 (Oct. 2013). Publisher: American Physical Society, p. 160401 (Cited on pages 6, 127, 141, 164, 191).

[43] Steven Girvin. "Circuit QED: Superconducting Qubits Coupled to Microwave Photons." In: Oxford University Press, 2011 (Cited on pages 7, 13, 35, 38, 80).

[44] Alexandre Blais et al. "Circuit Quantum Electrodynamics." In: *arXiv:2005.12667 [quant-ph]* (May 2020). arXiv: 2005.12667 (Cited on pages 7, 18).

[45] P. Krantz et al. "A quantum engineer's guide to superconducting qubits." In: *Applied Physics Reviews* 6.2 (June 2019). Publisher: American Institute of Physics, p. 021318 (Cited on pages 7, 61).

[46] G. Wendin. "Quantum information processing with superconducting circuits: a review." en. In: *Reports on Progress in Physics* 80.10 (Sept. 2017). Publisher: IOP Publishing, p. 106001 (Cited on page 7).

[47] Q. Ficheux et al. "Dynamics of a qubit while simultaneously monitoring its relaxation and dephasing." en. In: *Nature Communications* 9.1 (May 2018). Number: 1 Publisher: Nature Publishing Group, pp. 1–6 (Cited on page 8).

[48] Quentin Ficheux. "Quantum Trajectories with Incompatible Decoherence Channels." en. PhD thesis. École normale supérieure - ENS PARIS, Dec. 2018 (Cited on pages 8, 141, 161, 191, 194).

[49] Claude Cohen-Tannoudji, Bernard Biu, and Franl Laloë. *Quantum Mechanics*. Vol. I & II. Wiley, 1991 (Cited on page 9).

[50] Pascal Degiovanni et al. *Physique quantique, information et calcul*. fr. Publication Title: Physique quantique, information et calcul. EDP Sciences, Jan. 2021 (Cited on page 9).

[51] Jack Ekin. *Experimental Techniques for Low-Temperature Measurements: Cryostat Design, Material Properties and Superconductor Critical-Current Testing*. Publication Title: Experimental Techniques for Low-Temperature Measurements. Oxford University Press (Cited on pages 9, 65, 99).

[52] Johannes M. Fink. "Quantum nonlinearities in strong coupling circuit QED." en. Accepted: 2017-06-13T11:55:44Z. Doctoral Thesis. ETH Zurich, 2010 (Cited on pages 14, 73).

[53] G. J. Dolan. "Offset masks for lift-off photoprocessing." In: *Applied Physics Letters* 31.5 (Sept. 1977). Publisher: American Institute of Physics, pp. 337–339 (Cited on page 14).

[54] Peter Hänggi, Peter Talkner, and Michal Borkovec. "Reaction-rate theory: fifty years after Kramers." In: *Reviews of Modern Physics* 62.2 (Apr. 1990). Publisher: American Physical Society, pp. 251–341 (Cited on page 20).

[55] G. Lindblad. "On the generators of quantum dynamical semigroups." en. In: *Communications in Mathematical Physics* 48.2 (June 1976), pp. 119–130 (Cited on page 20).

[56] Moein Malekakhlagh. "Heisenberg-Langevin Formalism for Open Circuit-QED Systems." PhD Thesis. Princeton, 2017 (Cited on page 22).

[57] C. W. Gardiner and M. J. Collett. "Input and output in damped quantum systems: Quantum stochastic differential equations and the master equation." In: *Physical Review A* 31.6 (June 1985). Publisher: American Physical Society, pp. 3761–3774 (Cited on page 22).

[58] P. Campagne-Ibarcq. "Measurement backaction and feedback in superconducting circuits." PhD Thesis. ENS Paris, 2015 (Cited on pages 22, 86, 130).

[59] András Gyenis et al. "Moving beyond the transmon: Noise-protected superconducting quantum circuits." In: *arXiv:2106.10296 [quant-ph]* (June 2021). arXiv: 2106.10296 (Cited on pages 32, 34, 35, 39, 53).

[60] M. H. Devoret, A. Wallraff, and J. M. Martinis. "Superconducting Qubits: A Short Review." In: *arXiv:cond-mat/0411174* (Nov. 2004). arXiv: cond-mat/0411174 (Cited on page 33).

[61] D. Vion et al. "Manipulating the Quantum State of an Electrical Circuit." en. In: *Science* 296.5569 (May 2002). Publisher: American Association for the Advancement of Science Section: Report, pp. 886–889 (Cited on pages 33, 34).

[62] Chenlu Wang et al. "Transmon qubit with relaxation time exceeding 0.5 milliseconds." In: *arXiv:2105.09890 [quant-ph]* (May 2021). arXiv: 2105.09890 (Cited on pages 34, 64–66).

[63] A. A. Houck et al. "Controlling the Spontaneous Emission of a Superconducting Transmon Qubit." In: *Physical Review Letters* 101.8 (Aug. 2008). Publisher: American Physical Society, p. 080502 (Cited on pages 34, 86).

[64] Daoquan Zhu et al. "Quantum computing with superconducting circuits in the picosecond regime." In: *arXiv:2101.05810 [quant-ph]* (Jan. 2021). arXiv: 2101.05810 (Cited on page 35).

[65] M. Werninghaus et al. "Leakage reduction in fast superconducting qubit gates via optimal control." en. In: *npj Quantum Information* 7.1 (Jan. 2021). Number: 1 Publisher: Nature Publishing Group, pp. 1–6 (Cited on page 35).

[66] Vladimir E. Manucharyan. "Superinductance." PhD Thesis. Yale, 2012 (Cited on pages 35, 37, 38, 109, 151).

[67] Ivan V. Pechenezhskiy et al. "The superconducting quasicharge qubit." en. In: *Nature* 585.7825 (Sept. 2020). Number: 7825 Publisher: Nature Publishing Group, pp. 368–371 (Cited on pages 35, 36, 39, 53, 55, 56).

[68] M. Peruzzo et al. "Surpassing the Resistance Quantum with a Geometric Superinductor." In: *Physical Review Applied* 14.4 (Oct. 2020). Publisher: American Physical Society, p. 044055 (Cited on pages 35, 36).

[69] M. H. Devoret, Steven Girvin, and Robert Schoelkopf. "Circuit-QED: How strong can the coupling between a Josephson junction atom and a transmission line resonator be?" en. In: *Annalen der Physik* 16.10-11 (2007). _eprint: https://onlinelibrary.wiley.com/doi/p pp. 767–779 (Cited on page 36).

[70] C. Rolland et al. "Antibunched Photons Emitted by a dc-Biased Josephson Junction." In: *Physical Review Letters* 122.18 (May 2019). Publisher: American Physical Society, p. 186804 (Cited on page 36).

[71] Nathanaël Cottet. "Energy and information in fluorescence with superconducting circuits." PhD Thesis. ENS Paris, Sept. 2018 (Cited on pages 37, 158, 161).

[72] Carsten Hutter et al. "Josephson junction transmission lines as tunable artificial crystals." In: *Physical Review B* 83.1 (Jan. 2011). Publisher: American Physical Society, p. 014511 (Cited on page 37).

[73] Lukas Grünhaupt. "Granular Aluminium Superconductors." PhD thesis. Karlsruhe Institute of Technology (KIT), June 2019 (Cited on pages 37, 42, 65, 73).

[74] Lukas Grünhaupt et al. "Granular aluminium as a superconducting material for high-impedance quantum circuits." en. In: *Nature Materials* 18.8 (Aug. 2019). Number: 8 Publisher: Nature Publishing Group, pp. 816–819 (Cited on pages 37, 39, 40, 43, 62, 67).

[75] T. M. Hazard et al. "Nanowire Superinductance Fluxonium Qubit." In: *Physical Review Letters* 122.1 (Jan. 2019). Publisher: American Physical Society, p. 010504 (Cited on pages 37, 39).

[76] Long B. Nguyen. "Towards the Fluxonium Quantum Processor." PhD Thesis. University of Maryland, 2020 (Cited on page 38).

[77] Helin Zhang et al. "Universal Fast-Flux Control of a Coherent, Low-Frequency Qubit." In: *Physical Review X* 11.1 (Jan. 2021). Publisher: American Physical Society, p. 011010 (Cited on pages 39, 40, 44, 56, 74, 76, 109).

[78] A. Kou et al. "Simultaneous Monitoring of Fluxonium Qubits in a Waveguide." In: *Physical Review Applied* 9.6 (June 2018). Publisher: American Physical Society, p. 064022 (Cited on page 39).

[79] Long B. Nguyen et al. "High-Coherence Fluxonium Qubit." In: *Physical Review X* 9.4 (Nov. 2019). Publisher: American Physical Society, p. 041041 (Cited on pages 40, 43, 53, 54, 64, 66, 93, 94, 123).

[80] Nicholas Masluk. "Reducing the losses of the fluxonium artificial atom." PhD Thesis. 2012 (Cited on pages 41, 42).

[81] John M. Martinis et al. "Decoherence in Josephson Qubits from Dielectric Loss." In: *Physical Review Letters* 95.21 (Nov. 2005). Publisher: American Physical Society, p. 210503 (Cited on page 41).

[82] Ioan M. Pop et al. "Coherent suppression of electromagnetic dissipation due to superconducting quasiparticles." en. In: *Nature* 508.7496 (Apr. 2014). Number: 7496 Publisher: Nature Publishing Group, pp. 369–372 (Cited on pages 42, 43, 78, 79, 92, 145).

[83] K. Serniak et al. "Hot Nonequilibrium Quasiparticles in Transmon Qubits." In: *Physical Review Letters* 121.15 (Oct. 2018). Publisher: American Physical Society, p. 157701 (Cited on pages 42, 92).

[84] J. Aumentado et al. "Nonequilibrium Quasiparticles and $2e$ Periodicity in Single-Cooper-Pair Transistors." In: *Physical Review Letters* 92.6 (Feb. 2004). Publisher: American Physical Society, p. 066802 (Cited on page 42).

[85] P. J. de Visser et al. "Number Fluctuations of Sparse Quasiparticles in a Superconductor." In: *Physical Review Letters* 106.16 (Apr. 2011). Publisher: American Physical Society, p. 167004 (Cited on page 42).

[86] V. F. Maisi et al. "Excitation of Single Quasiparticles in a Small Superconducting Al Island Connected to Normal-Metal Leads by Tunnel Junctions." In: *Physical Review Letters* 111.14 (Oct. 2013). Publisher: American Physical Society, p. 147001 (Cited on page 42).

[87] X. Y. Jin et al. "Thermal and Residual Excited-State Population in a 3D Transmon Qubit." In: *Physical Review Letters* 114.24 (June 2015). Publisher: American Physical Society, p. 240501 (Cited on pages 42, 91).

[88] Leonid I. Glazman. "Bogoliubov Quasiparticles in Superconducting Qubits." In: 2019 (Cited on page 42).

[89] G. Catelani et al. "Relaxation and frequency shifts induced by quasiparticles in superconducting qubits." In: *Physical Review B* 84.6 (Aug. 2011). Publisher: American Physical Society, p. 064517 (Cited on pages 42, 92).

[90] Tenghui Wang and Alibaba Quantum Laboratory. "Experimental realization of ultra-high fidelity qubit operations with tunable fluxonium qubits." In: *Bulletin of the American Physical Society*. American Physical Society (Cited on pages 44, 51).

[91] Guanyu Zhu et al. "Circuit QED with fluxonium qubits: Theory of the dispersive regime." In: *Physical Review B* 87.2 (Jan. 2013). Publisher: American Physical Society, p. 024510 (Cited on pages 45, 128).

[92] Raphaël Lescanne et al. "Escape of a Driven Quantum Josephson Circuit into Unconfined States." In: *Physical Review Applied* 11.1 (Jan. 2019). Publisher: American Physical Society, p. 014030 (Cited on pages 46, 121, 143).

[93] Zlatko K. Minev et al. "Energy-participation quantization of Josephson circuits." In: *arXiv:2010.00620 [cond-mat, physics:quant-ph]* (Feb. 2021). arXiv: 2010.00620 (Cited on pages 47, 82, 84).

[94] Mario F. Gely and Gary A. Steele. "QuCAT: quantum circuit analyzer tool in Python." en. In: *New Journal of Physics* 22.1 (Jan. 2020). Publisher: IOP Publishing, p. 013025 (Cited on page 47).

[95] *scqubits/scqubits*. original-date: 2016-05-05T19:25:12Z. Apr. 2021 (Cited on page 47).

[96] Simon E. Nigg et al. "Black-Box Superconducting Circuit Quantization." In: *Physical Review Letters* 108.24 (June 2012). Publisher: American Physical Society, p. 240502 (Cited on pages 47, 80, 82).

[97] W. C. Smith et al. "Quantization of inductively shunted superconducting circuits." In: *Physical Review B* 94.14 (Oct. 2016). Publisher: American Physical Society, p. 144507 (Cited on pages 48, 49, 181, 185).

[98] J. R. Johansson, P. D. Nation, and Franco Nori. "QuTiP: An open-source Python framework for the dynamics of open quantum systems." en. In: *Computer Physics Communications* 183.8 (Aug. 2012), pp. 1760–1772 (Cited on page 48).

[99] J. R. Johansson, P. D. Nation, and Franco Nori. "QuTiP 2: A Python framework for the dynamics of open quantum systems." en. In: *Computer Physics Communications* 184.4 (Apr. 2013), pp. 1234–1240 (Cited on page 48).

[100] Martin Spiecker. "Fabrication and design of a fluxonium qubit with a granular aluminum superinductance." MA thesis. Karlsruhe: Karlsruhe Institute of Technology (KIT), 2018 (Cited on pages 49, 181, 185).

[101] Yoel Tikochinsky. "On the diagonalization of the general quadratic Hamiltonian for coupled harmonic oscillators." In: *Journal of Mathematical Physics* 20.3 (Mar. 1979). Publisher: American Institute of Physics, pp. 406–408 (Cited on pages 49, 182).

[102] R. C. Bialczak et al. "Quantum process tomography of a universal entangling gate implemented with Josephson phase qubits." en. In: *Nature Physics* 6.6 (June 2010). Number: 6 Publisher: Nature Publishing Group, pp. 409–413 (Cited on page 51).

[103] Jerry M. Chow et al. "Microwave-activated conditional-phase gate for superconducting qubits." en. In: *New Journal of Physics* 15.11 (Nov. 2013). Publisher: IOP Publishing, p. 115012 (Cited on page 51).

[104] Jerry M. Chow et al. "Simple All-Microwave Entangling Gate for Fixed-Frequency Superconducting Qubits." In: *Physical Review Letters* 107.8 (Aug. 2011). Publisher: American Physical Society, p. 080502 (Cited on page 51).

[105] Haonan Xiong et al. "Arbitrary controlled-phase gate on fluxonium qubits using differential ac-Stark shifts." In: *arXiv:2103.04491 [cond-mat, physics:quant-ph]* (Mar. 2021). arXiv: 2103.04491 (Cited on page 51).

[106] Austin G. Fowler et al. "Surface codes: Towards practical large-scale quantum computation." In: *Physical Review A* 86.3 (Sept. 2012). Publisher: American Physical Society, p. 032324 (Cited on page 53).

[107] Andrew N. Cleland. "An Introduction to the Surface Code." In: Oxford University Press, 2019 (Cited on page 53).

[108] Jérémie Guillaud and Mazyar Mirrahimi. "Repetition Cat Qubits for Fault-Tolerant Quantum Computation." In: *Physical Review X* 9.4 (Dec. 2019). Publisher: American Physical Society, p. 041053 (Cited on page 53).

[109] N. Earnest et al. "Realization of a $\mathrm{\ensuremath{\Lambda}}$ System with Metastable States of a Capacitively Shunted Fluxonium." In: *Physical Review Letters* 120.15 (Apr. 2018). Publisher: American Physical Society, p. 150504 (Cited on pages 53–55, 109).

[110] Yen-Hsiang Lin et al. "Demonstration of Protection of a Superconducting Qubit from Energy Decay." In: *Physical Review Letters* 120.15 (Apr. 2018). Publisher: American Physical Society, p. 150503 (Cited on pages 54, 109).

[111] András Gyenis et al. "Experimental Realization of a Protected Superconducting Circuit Derived from the 0–$\ensuremath{\pi}$ Qubit." In: *PRX Quantum* 2.1 (Mar. 2021). Publisher: American Physical Society, p. 010339 (Cited on pages 56–59).

[112] Alexei Kitaev. "Protected qubit based on a superconducting current mirror." In: *arXiv:cond-mat/0609441* (Sept. 2006). arXiv: cond-mat/0609441 (Cited on page 56).

[113] Konstantin Kalashnikov et al. "Bifluxon: Fluxon-Parity-Protected Superconducting Qubit." In: *PRX Quantum* 1.1 (Sept. 2020). Publisher: American Physical Society, p. 010307 (Cited on page 56).

[114] Agustin Di Paolo. "Qubit supraconducteurs protégés basés sur des modes à haute impédance." PhD Thesis. Université de Sherbrooke, 2020 (Cited on pages 56–59).

[115] Eyob A. Sete et al. "Charge- and Flux-Insensitive Tunable Superconducting Qubit." In: *Physical Review Applied* 8.2 (Aug. 2017). Publisher: American Physical Society, p. 024004 (Cited on page 61).

[116] V. Bouchiat et al. "Josephson junctions and superconducting quantum interference devices made by local oxidation of niobium ultrathin films." In: *Applied Physics Letters* 79.1 (June 2001). Publisher: American Institute of Physics, pp. 123–125 (Cited on page 62).

[117] Patrick Winkel et al. "Implementation of a Transmon Qubit Using Superconducting Granular Aluminum." In: *Physical Review X* 10.3 (Aug. 2020). Publisher: American Physical Society, p. 031032 (Cited on page 62).

[118] J. Basset et al. "High kinetic inductance microwave resonators made by He-Beam assisted deposition of tungsten nanowires." In: *Applied Physics Letters* 114.10 (Mar. 2019). Publisher: American Institute of Physics, p. 102601 (Cited on pages 62, 63, 65).

[119] P. Bonnet et al. "Strongly non-linear superconducting silicon resonators." In: *arXiv:2101.11125 [cond-mat]* (Jan. 2021). arXiv: 2101.11125 (Cited on pages 62, 63, 65).

[120] Hélène le Sueur et al. "Microscopic charged fluctuators as a limit to the coherence of disordered superconductor devices." In: *arXiv:1810.12801 [cond-mat]* (Oct. 2018). arXiv: 1810.12801 (Cited on pages 62, 63, 65).

[121] E. Dumur et al. "Epitaxial Rhenium Microwave Resonators." In: *IEEE Transactions on Applied Superconductivity* 26.3 (Apr. 2016). Conference Name: IEEE Transactions on Applied Superconductivity, pp. 1–4 (Cited on pages 62, 63, 65).

[122] A. Megrant et al. "Planar superconducting resonators with internal quality factors above one million." In: *Applied Physics Letters* 100.11 (Mar. 2012). Publisher: American Institute of Physics, p. 113510 (Cited on pages 63, 65, 66, 69).

[123] J. M. Kreikebaum et al. "Optimization of infrared and magnetic shielding of superconducting TiN and Al coplanar microwave resonators." en. In: *Superconductor Science and Technology* 29.10 (Aug. 2016). Publisher: IOP Publishing, p. 104002 (Cited on pages 63, 66, 67).

[124] A. Bruno et al. "Reducing intrinsic loss in superconducting resonators by surface treatment and deep etching of silicon substrates." In: *Applied Physics Letters* 106.18 (May 2015). Publisher: American Institute of Physics, p. 182601 (Cited on pages 63, 65, 66).

[125] J.G. Kroll et al. "Magnetic-Field-Resilient Superconducting Coplanar-Waveguide Resonators for Hybrid Circuit Quantum Electrodynamics Experiments." In: *Physical Review Applied* 11.6 (June 2019). Publisher: American Physical Society, p. 064053 (Cited on pages 63, 67).

[126] G. Calusine et al. "Analysis and mitigation of interface losses in trenched superconducting coplanar waveguide resonators." In: *Applied Physics Letters* 112.6 (Feb. 2018). Publisher: American Institute of Physics, p. 062601 (Cited on pages 62, 63, 65, 66).

[127] S. Ohya et al. "Room temperature deposition of sputtered TiN films for superconducting coplanar waveguide resonators." en. In: *Superconductor Science and Technology* 27.1 (Dec. 2013). Publisher: IOP Publishing, p. 015009 (Cited on pages 63, 65, 66, 69, 189).

[128] Abigail Shearrow et al. "Atomic layer deposition of titanium nitride for quantum circuits." In: *Applied Physics Letters* 113.21 (Nov. 2018). Publisher: American Institute of Physics, p. 212601 (Cited on pages 63, 66).

[129] Lukas Grünhaupt et al. "An argon ion beam milling process for native AlOx layers enabling coherent superconducting contacts." In: *Applied Physics Letters* 111.7 (Aug. 2017). Publisher: American Institute of Physics, p. 072601 (Cited on pages 63, 65).

[130] Ani Nersisyan et al. "Manufacturing low dissipation superconducting quantum processors." In: *arXiv:1901.08042 [physics, physics:quant-ph]* (Jan. 2019). arXiv: 1901.08042 (Cited on pages 63–66).

[131] J. Verjauw et al. "Investigation of microwave loss induced by oxide regrowth in high-Q Nb resonators." In: *arXiv:2012.10761 [cond-mat, physics:physics, physics:quant-ph]* (Dec. 2020). arXiv: 2012.10761 (Cited on pages 63, 65, 66).

[132] M. Virginia P. Altoé et al. "Localization and reduction of superconducting quantum coherent circuit losses." In: *arXiv:2012.07604 [cond-mat, physics:quant-ph]* (Dec. 2020). arXiv: 2012.07604 (Cited on pages 63, 66).

[133] Cécile Xinqing Yu et al. "Magnetic field resilient high kinetic inductance superconducting niobium nitride coplanar waveguide resonators." In: *Applied Physics Letters* 118.5 (Feb. 2021). Publisher: American Institute of Physics, p. 054001 (Cited on pages 63, 65).

[134] S. E. de Graaf et al. "Galvanically split superconducting microwave resonators for introducing internal voltage bias." In: *Applied Physics Letters* 104.5 (Feb. 2014). Publisher: American Institute of Physics, p. 052601 (Cited on page 63).

[135] Alexander P. M. Place et al. "New material platform for superconducting transmon qubits with coherence times exceeding 0.3 milliseconds." en. In: *Nature Communications* 12.1 (Mar. 2021). Number: 1 Publisher: Nature Publishing Group, p. 1779 (Cited on pages 64–66).

[136] Chad Rigetti et al. "Superconducting qubit in a waveguide cavity with a coherence time approaching 0.1 ms." In: *Physical Review B* 86.10 (Sept. 2012). Publisher: American Physical Society, p. 100506 (Cited on page 64).

[137] Z. Wang et al. "Cavity Attenuators for Superconducting Qubits." In: *Physical Review Applied* 11.1 (Jan. 2019). Publisher: American Physical Society, p. 014031 (Cited on pages 64–67, 91).

[138] Oliver Dial et al. "Bulk and surface loss in superconducting transmon qubits." en. In: *Superconductor Science and Technology* 29.4 (Mar. 2016). Publisher: IOP Publishing, p. 044001 (Cited on pages 64, 66).

[139] R. Barends et al. "Coherent Josephson Qubit Suitable for Scalable Quantum Integrated Circuits." In: *Physical Review Letters* 111.8 (Aug. 2013). Publisher: American Physical Society, p. 080502 (Cited on pages 64, 66, 76).

[140] Alexander Stehli et al. "Coherent superconducting qubits from a subtractive junction fabrication process." In: *Applied Physics Letters* 117.12 (Sept. 2020). Publisher: American Institute of Physics, p. 124005 (Cited on page 64).

[141] Jonathan J. Burnett et al. "Decoherence benchmarking of superconducting qubits." en. In: *npj Quantum Information* 5.1 (June 2019). Number: 1 Publisher: Nature Publishing Group, pp. 1–8 (Cited on pages 64, 65).

[142] Alexander Melville et al. "Comparison of Dielectric Loss in Titanium Nitride and Aluminum Superconducting Resonators." In: *Applied Physics Letters* 117.12 (Sept. 2020). arXiv: 2007.07338, p. 124004 (Cited on pages 65, 66).

[143] Jiansong Gao et al. "Experimental evidence for a surface distribution of two-level systems in superconducting lithographed microwave resonators." In: *Applied Physics Letters* 92.15 (Apr. 2008). Publisher: American Institute of Physics, p. 152505 (Cited on page 65).

[144] *Ta CPW resonators measured in October 2020 at ENS Lyon.* Oct. 2020 (Cited on page 65).

[145] Lukas Grünhaupt et al. "Loss Mechanisms and Quasiparticle Dynamics in Superconducting Microwave Resonators Made of Thin-Film Granular Aluminum." In: *Physical Review Letters* 121.11 (Sept. 2018). Publisher: American Physical Society, p. 117001 (Cited on page 65).

[146] F. Levy-Bertrand et al. "Electrodynamics of granular aluminum from superconductor to insulator: Observation of collective superconducting modes." In: *Physical Review B* 99.9 (Mar. 2019). Publisher: American Physical Society, p. 094506 (Cited on page 65).

[147] W. Woods et al. "Determining Interface Dielectric Losses in Superconducting Coplanar-Waveguide Resonators." In: *Physical Review Applied* 12.1 (July 2019). Publisher: American Physical Society, p. 014012 (Cited on pages 65, 66).

[148] John M. Martinis and A. Megrant. "UCSB final report for the CSQ program: Review of decoherence and materials physics for superconducting qubits." In: *arXiv:1410.5793 [cond-mat, physics:quant-ph]* (Oct. 2014). arXiv: 1410.5793 (Cited on pages 62, 65, 66).

[149] Daniel L. Creedon et al. "High Q-factor sapphire whispering gallery mode microwave resonator at single photon energies and millikelvin temperatures." In: *Applied Physics Letters* 98.22 (May 2011). Publisher: American Institute of Physics, p. 222903 (Cited on page 65).

[150] Daniel Tennant. *Investigation into Charge Noise in a Tantalum Transmon on Sapphire Substrate across Higher Energy Levels*. Mar. 2021 (Cited on page 66).

[151] J. Wenner et al. "Surface loss simulations of superconducting coplanar waveguide resonators." In: *Applied Physics Letters* 99.11 (Sept. 2011). Publisher: American Institute of Physics, p. 113513 (Cited on page 66).

[152] *Cramming More Power Into a Quantum Device*. en-US. Mar. 2019 (Cited on page 66).

[153] Jay Gambetta. *Breaking through the millisecond barrier with our single junction transmon @IBMResearch https://t.co/WlmCUvONtg*. en. Tweet. May 2021 (Cited on page 67).

[154] K. Borisov et al. "Superconducting granular aluminum resonators resilient to magnetic fields up to 1 Tesla." In: *Applied Physics Letters* 117.12 (Sept. 2020). Publisher: American Institute of Physics, p. 120502 (Cited on page 67).

[155] N. Samkharadze et al. "High-Kinetic-Inductance Superconducting Nanowire Resonators for Circuit QED in a Magnetic Field." In: *Physical Review Applied* 5.4 (Apr. 2016). Publisher: American Physical Society, p. 044004 (Cited on page 67).

[156] Marta Pita-Vidal et al. "A gate-tunable, field-compatible fluxonium." In: *Physical Review Applied* 14.6 (Dec. 2020). arXiv: 1910.07978, p. 064038 (Cited on page 67).

[157] Sihao Huang et al. "Microwave Package Design for Superconducting Quantum Processors." In: *PRX Quantum* 2.2 (Apr. 2021). Publisher: American Physical Society, p. 020306 (Cited on pages 67, 70).

[158] Srivatsan Chakram et al. "Seamless high-Q microwave cavities for multimode circuit QED." In: *arXiv:2010.16382 [cond-mat, physics:quant-ph]* (Nov. 2020). arXiv: 2010.16382 (Cited on page 67).

[159] Kurtis Geerlings. "Improving Coherence of Superconducting Qubits and Resonators." PhD Thesis. Yale, 2013 (Cited on page 68).

[160] S. Probst et al. "Efficient and robust analysis of complex scattering data under noise in microwave resonators." In: *Review of Scientific Instruments* 86.2 (Feb. 2015). Publisher: American Institute of Physics, p. 024706 (Cited on page 69).

[161] M. S. Khalil et al. "An analysis method for asymmetric resonator transmission applied to superconducting devices." In: *Journal of Applied Physics* 111.5 (Mar. 2012). Publisher: American Institute of Physics, p. 054510 (Cited on page 69).

[162] Zlatko K Minev et al. *Qiskit Metal: An Open-Source Framework for Quantum Device Design & Analysis*. 2021 (Cited on page 70).

[163] Vinay Ambegaokar and Alexis Baratoff. "Tunneling Between Superconductors." In: *Physical Review Letters* 10.11 (June 1963). Publisher: American Physical Society, pp. 486–489 (Cited on page 73).

[164] Alexandre Blais. "Qubit Readout in circuit QED (Lecture Notes)." In: 2019 (Cited on page 74).

[165] A. O. Caldeira and A. J. Leggett. "Influence of Dissipation on Quantum Tunneling in Macroscopic Systems." In: *Physical Review Letters* 46.4 (Jan. 1981). Publisher: American Physical Society, pp. 211–214 (Cited on page 75).

[166] *LD dilution refrigerator measurement system*. en-US (Cited on page 77).

[167] Moein Malekakhlagh, Alexandru Petrescu, and Hakan E. Türeci. "Cutoff-Free Circuit Quantum Electrodynamics." In: *Physical Review Letters* 119.7 (Aug. 2017). Publisher: American Physical Society, p. 073601 (Cited on page 80).

[168] Firat Solgun, David W. Abraham, and David P. DiVincenzo. "Blackbox quantization of superconducting circuits using exact impedance synthesis." In: *Physical Review B* 90.13 (Oct. 2014). Publisher: American Physical Society, p. 134504 (Cited on page 80).

[169] Ronald M. Foster. "A Reactance Theorem." en. In: *Bell System Technical Journal* 3.2 (1924). _eprint: https://onlinelibrary.wiley.com/doi/pdf/10.1002/j.1538-7305.1924.tb01358.x, pp. 259–267 (Cited on page 81).

[170] Zlatko K. Minev et al. *pyEPR: The energy-participation-ratio (EPR) open- source framework for quantum device design*. May 2021 (Cited on page 82).

[171] Jay Gambetta et al. "Qubit-photon interactions in a cavity: Measurement-induced dephasing and number splitting." In: *Physical Review A* 74.4 (Oct. 2006). Publisher: American Physical Society, p. 042318 (Cited on page 91).

[172] A. A. Clerk and D. Wahyu Utami. "Using a qubit to measure photon-number statistics of a driven thermal oscillator." In: *Physical Review A* 75.4 (Apr. 2007). Publisher: American Physical Society, p. 042302 (Cited on page 91).

[173] R. Barends et al. "Minimizing quasiparticle generation from stray infrared light in superconducting quantum circuits." In: *Applied Physics Letters* 99.11 (Sept. 2011). Publisher: American Institute of Physics, p. 113507 (Cited on pages 91, 92, 103).

[174] Antonio D. Córcoles et al. "Protecting superconducting qubits from radiation." In: *Applied Physics Letters* 99.18 (Oct. 2011). Publisher: American Institute of Physics, p. 181906 (Cited on pages 91, 92, 103).

[175] Leonid I. Glazman and Gianluigi Catelani. "Bogoliubov Quasiparticles in Superconducting Qubits." In: *arXiv:2003.04366 [cond-mat, physics:quant-ph]* (Apr. 2021). arXiv: 2003.04366 (Cited on page 92).

[176] D. Ristè et al. "Millisecond charge-parity fluctuations and induced decoherence in a superconducting transmon qubit." en. In: *Nature Communications* 4.1 (May 2013). Number: 1 Publisher: Nature Publishing Group, p. 1913 (Cited on page 92).

[177] Hanhee Paik et al. "Observation of High Coherence in Josephson Junction Qubits Measured in a Three-Dimensional Circuit QED Architecture." In: *Physical Review Letters* 107.24 (Dec. 2011). Publisher: American Physical Society, p. 240501 (Cited on page 92).

[178] C. Macklin et al. "A near–quantum-limited Josephson traveling-wave parametric amplifier." en. In: *Science* 350.6258 (Oct. 2015). Publisher: American Association for the Advancement of Science Section: Report, pp. 307–310 (Cited on pages 94, 123, 158).

[179] S. Krinner et al. "Engineering cryogenic setups for 100-qubit scale superconducting circuit systems." en. In: *EPJ Quantum Technology* 6.1 (Dec. 2019). Number: 1 Publisher: SpringerOpen, pp. 1–29 (Cited on page 99).

[180] F. P. Milliken et al. "50 characteristic impedance low-pass metal powder filters." In: *Review of Scientific Instruments* 78.2 (Feb. 2007). Publisher: American Institute of Physics, p. 024701 (Cited on page 102).

[181] D. F. Santavicca and D. E. Prober. "Impedance-matched low-pass stripline filters." en. In: *Measurement Science and Technology* 19.8 (June 2008). Publisher: IOP Publishing, p. 087001 (Cited on page 102).

[182] K. Serniak et al. "Direct Dispersive Monitoring of Charge Parity in Offset-Charge-Sensitive Transmons." In: *Physical Review Applied* 12.1 (July 2019). Publisher: American Physical Society, p. 014052 (Cited on page 103).

[183] T. Walter et al. "Rapid High-Fidelity Single-Shot Dispersive Readout of Superconducting Qubits." In: *Physical Review Applied* 7.5 (May 2017). Publisher: American Physical Society, p. 054020 (Cited on page 107).

[184] K. Geerlings et al. "Demonstrating a Driven Reset Protocol for a Superconducting Qubit." In: *Physical Review Letters* 110.12 (Mar. 2013). Publisher: American Physical Society, p. 120501 (Cited on page 107).

[185] P. Magnard et al. "Fast and Unconditional All-Microwave Reset of a Superconducting Qubit." In: *Physical Review Letters* 121.6 (Aug. 2018). Publisher: American Physical Society, p. 060502 (Cited on page 109).

[186] D.J. Egger et al. "Pulsed Reset Protocol for Fixed-Frequency Superconducting Qubits." In: *Physical Review Applied* 10.4 (Oct. 2018). Publisher: American Physical Society, p. 044030 (Cited on page 109).

[187] M. Pechal et al. "Microwave-Controlled Generation of Shaped Single Photons in Circuit Quantum Electrodynamics." In: *Physical Review X* 4.4 (Oct. 2014). Publisher: American Physical Society, p. 041010 (Cited on page 109).

[188] Jani Tuorila et al. "Efficient protocol for qubit initialization with a tunable environment." en. In: *npj Quantum Information* 3.1 (July 2017). Number: 1 Publisher: Nature Publishing Group, pp. 1–12 (Cited on page 109).

[189] Hsiang-Sheng Ku. *Toward an ultra-high fidelity and scalable fluxonium quantum processor*. Mar. 2021 (Cited on page 109).

[190] F. Pedregosa et al. "Scikit-learn: Machine Learning in Python." In: *Journal of Machine Learning Research* 12 (2011), pp. 2825–2830 (Cited on pages 117, 166).

[191] Daniel Sank et al. "Measurement-Induced State Transitions in a Superconducting Qubit: Beyond the Rotating Wave Approximation." In: *Physical Review Letters* 117.19 (Nov. 2016). Publisher: American Physical Society, p. 190503 (Cited on pages 121, 144, 151).

[192] Th. K. Mavrogordatos et al. "Simultaneous Bistability of a Qubit and Resonator in Circuit Quantum Electrodynamics." In: *Physical Review Letters* 118.4 (Jan. 2017). Publisher: American Physical Society, p. 040402 (Cited on page 121).

[193] E. Ginossar et al. "Protocol for high-fidelity readout in the photon-blockade regime of circuit QED." In: *Physical Review A* 82.2 (Aug. 2010). Publisher: American Physical Society, p. 022335 (Cited on pages 121, 143).

[194] Moein Malekakhlagh, Alexandru Petrescu, and Hakan E. Türeci. "Lifetime renormalization of weakly anharmonic superconducting qubits. I. Role of number nonconserving terms." In: *Physical Review B* 101.13 (Apr. 2020). Publisher: American Physical Society, p. 134509 (Cited on pages 121, 144).

[195] Alexandru Petrescu, Moein Malekakhlagh, and Hakan E. Türeci. "Lifetime renormalization of driven weakly anharmonic superconducting qubits. II. The readout problem." In: *Physical Review B* 101.13 (Apr. 2020). Publisher: American Physical Society, p. 134510 (Cited on pages 121, 144, 151).

[196] Sander Weinreb, Joseph C. Bardin, and Hamdi Mani. "Design of Cryogenic SiGe Low-Noise Amplifiers." en. In: *IEEE Transactions on Microwave Theory and Techniques* 55.11 (Nov. 2007). Number: 11, pp. 2306–2312 (Cited on page 123).

[197] Maxime Boissonneault, J. M. Gambetta, and Alexandre Blais. "Dispersive regime of circuit QED: Photon-dependent qubit dephasing and relaxation rates." In: *Physical Review A* 79.1 (Jan. 2009). Publisher: American Physical Society, p. 013819 (Cited on pages 128, 143).

[198] Maxime Boissonneault, J. M. Gambetta, and Alexandre Blais. "Improved Superconducting Qubit Readout by Qubit-Induced Nonlinearities." In: *Physical Review Letters* 105.10 (Sept. 2010). Publisher: American Physical Society, p. 100504 (Cited on page 129).

[199] Jay Gambetta et al. "Quantum trajectory approach to circuit QED: Quantum jumps and the Zeno effect." In: *Physical Review A* 77.1 (Jan. 2008). Publisher: American Physical Society, p. 012112 (Cited on page 130).

[200] T. Rybarczyk et al. "Forward-backward analysis of the photon-number evolution in a cavity." In: *Physical Review A* 91.6 (June 2015). Publisher: American Physical Society, p. 062116 (Cited on page 141).

[201] Christine Guerlin et al. "Progressive field-state collapse and quantum non-demolition photon counting." en. In: *Nature* 448.7156 (Aug. 2007). Bandiera_abtest: a Cg_type: Nature Research Journals Number: 7156 Primary_atype: Research Publisher: Nature Publishing Group, pp. 889–893 (Cited on page 141).

[202] J. E. Johnson et al. "Heralded State Preparation in a Superconducting Qubit." In: *Physical Review Letters* 109.5 (Aug. 2012). Publisher: American Physical Society, p. 050506 (Cited on page 143).

[203] D. H. Slichter et al. "Measurement-Induced Qubit State Mixing in Circuit QED from Up-Converted Dephasing Noise." In: *Physical Review Letters* 109.15 (Oct. 2012). Publisher: American Physical Society, p. 153601 (Cited on page 143).

[204] C. M. Wilson et al. "Dressed relaxation and dephasing in a strongly driven two-level system." In: *Physical Review B* 81.2 (Jan. 2010). Publisher: American Physical Society, p. 024520 (Cited on page 143).

[205] Eyob A. Sete, Jay M. Gambetta, and Alexander N. Korotkov. "Purcell effect with microwave drive: Suppression of qubit relaxation rate." In: *Physical Review B* 89.10 (Mar. 2014). Publisher: American Physical Society, p. 104516 (Cited on page 143).

[206] Pierre Six et al. "Parameter estimation from measurements along quantum trajectories." In: *arXiv:1503.06149 [quant-ph]* (Mar. 2015). arXiv: 1503.06149 (Cited on page 145).

[207] P. W. Anderson. "More Is Different." en. In: *Science* 177.4047 (Aug. 1972). Publisher: American Association for the Advancement of Science Section: Articles, pp. 393–396 (Cited on page 154).

[208] Sophia Kivelson and Steven A. Kivelson. "Defining emergence in physics." en. In: *npj Quantum Materials* 1.1 (Nov. 2016). Bandiera_abtest: a Cc_license_type: cc_by Cg_type: Nature Research Journals Number: 1 Primary_atype: Reviews Publisher: Nature Publishing Group, pp. 1–2 (Cited on page 154).

[209] Koji Maruyama, Franco Nori, and Vlatko Vedral. "Colloquium: The physics of Maxwell's demon and information." In: *Reviews of Modern Physics* 81.1 (Jan. 2009). Publisher: American Physical Society, pp. 1–23 (Cited on page 154).

[210] R. Landauer. "Irreversibility and Heat Generation in the Computing Process." In: *IBM Journal of Research and Development* 5.3 (July 1961). Conference Name: IBM Journal of Research and Development, pp. 183–191 (Cited on page 154).

[211] Charles Bennett. "The Thermodynamics of Computation - a Review." In: *International Journal of Theoretical Physics* 21.12 (1982) (Cited on page 154).

[212] A. Einstein. "Über die von der molekularkinetischen Theorie der Wärme geforderte Bewegung von in ruhenden Flüssigkeiten suspendierten Teilchen." en. In: *Annalen der Physik* 322.8 (1905). _eprint: https://onlinelibrary.wiley.com/doi/pdf/10.1002/andp.190532 pp. 549–560 (Cited on page 154).

[213] Nathanaël Cottet et al. "Observing a quantum Maxwell demon at work." In: *Proceedings of the National Academy of Sciences* 114.29 (July 2017), pp. 7561–7564 (Cited on page 155).

[214] Y. Masuyama et al. "Information-to-work conversion by Maxwell's demon in a superconducting circuit quantum electrodynamical system." en. In: *Nature Communications* 9.1 (Mar. 2018). Number: 1 Publisher: Nature Publishing Group, p. 1291 (Cited on page 155).

[215] Baldo-Luis Najera-Santos et al. "Autonomous Maxwell's demon in a cavity QED system." In: *Physical Review Research* 2.3 (July 2020). Publisher: American Physical Society, p. 032025 (Cited on page 155).

[216] Alberto Ronzani et al. "Tunable photonic heat transport in a quantum heat valve." en. In: *Nature Physics* 14.10 (Oct. 2018). Number: 10 Publisher: Nature Publishing Group, pp. 991–995 (Cited on page 155).

[217] Jorden Senior et al. "Heat rectification via a superconducting artificial atom." en. In: *Communications Physics* 3.1 (Feb. 2020). Number: 1 Publisher: Nature Publishing Group, pp. 1–5 (Cited on page 155).

[218] P. Kammerlander and J. Anders. "Coherence and measurement in quantum thermodynamics." en. In: *Scientific Reports* 6.1 (Feb. 2016). Number: 1 Publisher: Nature Publishing Group, p. 22174 (Cited on page 155).

[219] Philippe Faist et al. "The minimal work cost of information processing." en. In: *Nature Communications* 6.1 (July 2015). Number: 1 Publisher: Nature Publishing Group, p. 7669 (Cited on page 155).

[220] Fabien Clivaz et al. "Unifying paradigms of quantum refrigeration: Fundamental limits of cooling and associated work costs." In: *Physical Review E* 100.4 (Oct. 2019). Publisher: American Physical Society, p. 042130 (Cited on page 155).

[221] Shishir Khandelwal et al. "Critical heat current for operating an entanglement engine." en. In: *New Journal of Physics* 22.7 (July 2020). Publisher: IOP Publishing, p. 073039 (Cited on page 155).

[222] Massimiliano Esposito, Upendra Harbola, and Shaul Mukamel. "Nonequilibrium fluctuations, fluctuation theorems, and counting statistics in quantum systems." In: *Reviews of Modern Physics* 81.4 (Dec. 2009). Publisher: American Physical Society, pp. 1665–1702 (Cited on page 155).

[223] Michele Campisi, Peter Hänggi, and Peter Talkner. "Colloquium: Quantum fluctuation relations: Foundations and applications." In: *Reviews of Modern Physics* 83.3 (July 2011). Publisher: American Physical Society, pp. 771–791 (Cited on page 155).

[224] Michael Moskalets and Géraldine Haack. "Heat and charge transport measurements to access single-electron quantum characteristics." en. In: *physica status solidi (b)* 254.3 (2017). _eprint: https://onlinelibrary.wiley.com/doi/pdf/10.1002/pssb.201600616, p. 1600616 (Cited on page 155).

[225] Zheng Tan et al. "Alternative experimental ways to access entropy production." In: *arXiv:2012.13640 [quant-ph]* (May 2021). arXiv: 2012.13640 (Cited on page 155).

[226] Cyril Elouard et al. "Extracting Work from Quantum Measurement in Maxwell's Demon Engines." In: *Physical Review Letters* 118.26 (June 2017). Publisher: American Physical Society, p. 260603 (Cited on page 156).

[227] Andrew N. Jordan et al. "Anatomy of fluorescence: quantum trajectory statistics from continuously measuring spontaneous emission." en. In: *Quantum Studies: Mathematics and Foundations* 3.3 (Sept. 2016), pp. 237–263 (Cited on page 156).

[228] Claude Cohen-Tannoudji, Jacques Dupont-Roc, and Gilbert Grynberg. *Atom-Photon Interactions: Basic Processes and Applications*. Wiley, 1998 (Cited on page 156).

[229] Serge Haroche and Jean-Michel Raimond. *Exploring the Quantum. Atoms, Cavities and Photons*. Oxford Graduate Texts. Oxford University Press, 2006 (Cited on pages 157, 174).

[230] S. J. van Enk and H. J. Kimble. "On the classical character of control fields in quantum information processing." In: *arXiv:quant-ph/0107088* (July 2001). arXiv: quant-ph/0107088 (Cited on page 157).

[231] O. Astafiev et al. "Resonance Fluorescence of a Single Artificial Atom." en. In: *Science* 327.5967 (Feb. 2010). Publisher: American Association for the Advancement of Science Section: Report, pp. 840–843 (Cited on page 161).

[232] A. A. Abdumalikov et al. "Dynamics of Coherent and Incoherent Emission from an Artificial Atom in a 1D Space." In: *Physical Review Letters* 107.4 (July 2011). Publisher: American Physical Society, p. 043604 (Cited on page 161).

[233] Yong Lu et al. "Characterizing decoherence rates of a superconducting qubit by direct microwave scattering." en. In: *npj Quantum Information* 7.1 (Feb. 2021). Number: 1 Publisher: Nature Publishing Group, pp. 1–9 (Cited on page 161).

[234] T. Hönigl-Decrinis et al. "Two-Level System as a Quantum Sensor for Absolute Calibration of Power." In: *Physical Review Applied* 13.2 (Feb. 2020). Publisher: American Physical Society, p. 024066 (Cited on page 161).

[235] Mankei Tsang. "Optimal waveform estimation for classical and quantum systems via time-symmetric smoothing." In: *Physical Review A* 80.3 (Sept. 2009). Publisher: American Physical Society, p. 033840 (Cited on page 164).

[236] Maria Maffei, Cyril Elouard, and Alexia Auffèves (Cited on page 166).

[237] Justin Dressel et al. "Colloquium: Understanding quantum weak values: Basics and applications." In: *Reviews of Modern Physics* 86.1 (Mar. 2014). Publisher: American Physical Society, pp. 307–316 (Cited on pages 171, 196).

[238] I. S. Gradshteyn and I. M. Ryzhik. *Table of Integrals, Series, and Products*. en. Elsevier, 1980 (Cited on page 185).

[239] Mankei Tsang. "Time-Symmetric Quantum Theory of Smoothing." In: *Physical Review Letters* 102.25 (June 2009). Publisher: American Physical Society, p. 250403 (Cited on page 191).

[240] Walther Gerlach and Otto Stern. "Der experimentelle Nachweis der Richtungsquantelung im Magnetfeld." de. In: *Zeitschrift für Physik* 9.1 (Dec. 1922), pp. 349–352 (Cited on page 191).

[241] M. Hatridge et al. "Quantum Back-Action of an Individual Variable-Strength Measurement." en. In: *Science* 339.6116 (Jan. 2013). Publisher: American Association for the Advancement of Science Section: Report, pp. 178–181 (Cited on page 193).